A244023

UNITED STATES AIR FORCE

GRADUATE STUDENT RESEARCH PROGRAM

1990

PROGRAM TECHNICAL REPORT

UNIVERSAL ENERGY SYSTEMS, INC.

VOLUME 2 OF 3

PROGRAM DIRECTOR, U. E. S.
RODNEY C. DARRAH

PROGRAM ADMINISTRATOR, U. E. S.
SUSAN K. ESPY

PROGRAM MANAGER, A. F. O. S. R.
LT. COL. CLAUDE CAVENDER

SUBMITTED TO
AIR FORCE OFFICE OF SCIENTIFIC RESEARCH
BOLLING AIR FORCE BASE
WASHINGTON, DC

DECEMBER 1990

REPORT DOCUMENTATION PAGE

Form Approved
OMB No. 0704-0188

1. AGENCY USE ONLY (Leave blank)	2. REPORT DATE	3. REPORT TYPE AND DATES COVERED
	5 June 1991	Annual/Final 1 Sep 89-31 Aug 90

4. TITLE AND SUBTITLE
United States Air Force Graduate Student Research Program
1990 Volume 2083
Program Technical Report (w/atch. 1 & 2)

5. FUNDING NUMBERS
F49620-88-C-0053

6. AUTHOR(S)
Mr Rodney Darrah

7. PERFORMING ORGANIZATION NAME(S) AND ADDRESS(ES)
Universal Energy Systems (UES)
4401 Dayton-Xenia
Dayton OH 45432

8. PERFORMING ORGANIZATION REPORT NUMBER
AFOSR-TR- 91 0968

9. SPONSORING/MONITORING AGENCY NAME(S) AND ADDRESS(ES)
AFOSR/NI
Bldg 410
Bolling AFB DC 20332-6448
Lt Col V. Claude Cavender

10. SPONSORING/MONITORING AGENCY REPORT NUMBER

11. SUPPLEMENTARY NOTES

12a. DISTRIBUTION/AVAILABILITY STATEMENT
UNLIMITED

12b. DISTRIBUTION CODE

13. ABSTRACT (Maximum 200 words)

The Summer Faculty Research Program (SFRP) was initiated in 1982. The Graduate Student Research Program (GSRP) is an adjunct effort to the Summer Faculty Research Program. Its purpose is to provide opportunities for selected graduate students to perform summer research at Air Force laboratories with supervising professors who hold concurrent SFRP appointments or with Air Force researchers.

The program is available to graduate students enrolled in either Masters Degree or Doctorate Programs. It has proven especially beneficial to the students who are starting their academic research programs.

14. SUBJECT TERMS
91 1223 194

15. NUMBER OF PAGES

16. PRICE CODE

17. SECURITY CLASSIFICATION OF REPORT	18. SECURITY CLASSIFICATION OF THIS PAGE	19. SECURITY CLASSIFICATION OF ABSTRACT	20. LIMITATION OF ABSTRACT
UNCLASSIFIED	UNCLASSIFIED	UNCLASSIFIED	UL

UNITED STATES AIR FORCE

GRADUATE STUDENT RESEARCH PROGRAM

1990

PROGRAM TECHNICAL REPORT

UNIVERSAL ENERGY SYSTEMS, INC.

VOLUME II of III

Program Director, UES
Rodney C. Darrah

Program Administrator, UES
Susan K. Espy

Program Manager, AFOSR
Lt. Col. Claude Cavender

Submitted to

Air Force Office of Scientific Research

Bolling Air Force Base

Washington, DC

December 1990

TABLE OF CONTENTS

PREFACE

The United States Air Force Graduate Student Resarch Program (USAF-GSRP) is conducted under the United Air Force Summer Faculty Research Program. The program provides funds for selected graduate students to work at an appropriate Air Force facility with a supervising professor who holds a concurrent Summer Faculty Research Program appointment or with a supervising Air Force Engineer/Scientist. This is accomplished by the students being selected on a nationally advertised competitive basis for a ten-week assignment during the summer intersession period to perfrom research at Air Force laboratories/centers. Each assignment is in a subject area and at an Air Force facility mutually agreed upon by the students and the Air Force. In addition to compensation, travel and cost of living allowances are also paid. The USAF-GSRP is sponsored by the Air Force Office of Scientific Research, Air Force Systems Command, United States Air Force, and is conducted by Universal Energy Systems, Inc.

The specific objectives of the 1990 USAF-GSRP are:

(1) To provide a productive means for the graduate students to participate in research at Air Force Laboratories/Centers;

(2) To stimulate continuing professional association among the graduate students and their professional peers in the Air Force;

(3) To further the research objectives of the United States Air Force;

(4) To enhance the research productivity and capabilities of the graduate students especially as these relate to Air Force technical interests.

During the summer of 1990, 121-graduate students participated. These researchers were assigned to 23 USAF laboratories/centers across the country. This three volume document is a compilation of the final reports written by the assigned students members about their summer research efforts.

LIST OF 1990 PARTICIPANTS

NAME / ADDRESS	DEGREE, SPECIALTY, LABORATORY ASSIGNED
Ben Abbott Vanderbilt University Electrical Engineering Dept. Nashville, TN 37240 (615) 343-8302	Degree: MS Specialty: Computer Engineering Assigned: Arnold Engineering Development Center
Gregory Addington Colorado - Boulder, Univ. of Campus Box 429, Dept. of Aerospace Eng. Boulder, CO 80310 (303) 492-7559	Degree: BS Specialty: Aerospace Engineering Assigned: Frank J. Seiler Research Lab.
Magna Altamirano New Orleans, Univ. of Lakefront New Orleans, LA 70148 (504) 286-6652	Degree: BS Specialty: Civil Engineering Assigned: Flight Dynamics Laboratory
Joseph Baldonado California State Univ. Dept. of Mechanical Eng. Long Beach, CA 90840 (213) 985-5471	Degree: BS Specialty: Electrical Engineering Assigned: Astronautics Laboratory
Theodore Bapty Vanderbilt University Electrical Eng. Dept. Nashville, TN 37240 (615) 322-3455	Degree: BS Specialty: Computer Engineering Assigned: Arnold Engineering Development Center
Janis Beaird Alabama, Univ. of A.B. Moore Hall, Box 870312 Tuscaloosa, AL 35487 (205) 348-6075	Degree: MS Specialty: Physiology Assigned: School of Aerospace Medicine

NAME / ADDRESS	DEGREE, SPECIALTY, LABORATORY ASSIGNED	
Joseph Bernardo Scranton, Univ. of Chemistry Dept. Scranton, PA 18510 (717) 961-6286	Degree: Specialty: Assigned:	BS Biochemistry Engineering & Services Ctr.
Laura Bernhofen Syracuse U. Crouse-Hinds School of Mgmt. Syracuse, NY 13210 (315) 475-1418	Degree: Specialty: Assigned:	MS Statistics Human Resources Laboratory Manpower & Personnel Div.
Ronald Blume Tennessee, Univ. & Space Inst. Aerospace Eng. Dept. Tullahoma, TN 37388 (615) 455-0631	Degree: Specialty: Assigned:	BS Aerospace Engineering Arnold Engineering Development Center
Andrew Bonas Duke University Dept. of Civil Eng. PO Box 4264DS Durham, NC 27706 (919) 684-1670	Degree: Specialty: Assigned:	BS Civil Engineering Occupational & Environmental Health Laboratory
George Boynton Miami, Univ. of Dept. of Physics, PO Box 248046 Coral Gables, FL 33124 (305) 284-2323	Degree: Specialty: Assigned:	MS Physics Armament Laboratory
Dora Brenner Auburn University Dept. of Zoology & Wildlife Auburn, AL 36830 (205) 844-9245	Degree: Specialty: Assigned:	MS Chemistry School of Aerospace Medicine
Thomas Broersma Texas-Austin, Univ. of EDB 244 Austin, TX 78712 (512) 471-4285	Degree: Specialty: Assigned:	MS Arts School of Aerospace Medicine

NAME / ADDRESS	DEGREE, SPECIALTY, LABORATORY ASSIGNED	
Joseph Brogan Scranton, Univ. of Dept. of Biology Scranton, PA 18510 (717) 961-6338	Degree: Specialty: Assigned:	BS Biochemistry School of Aerospace Medicine
Robert Byers Texas A&M Univ. Aerospace Eng. Dept. College Station, TX 77843 (409) 845-0745	Degree: Specialty: Assigned:	MS Aerospace Engineering Astronautics Laboratory
Eric Byrne Kansas State Univ. 234 Nichols Hall Manhattan, KS 66502 (913) 532-6350	Degree: Specialty: Assigned:	MS Computer Science Avionics Laboratory
Jordan Cahn Univ. of Tennessee Space Inst. Dept. of Applied Mathematics Tullahoma, TN 37388 (615) 455-0631	Degree: Specialty: Assigned:	BS Aerospace Engineering Arnold Engineering Development Center
Ann Canfield Utah State Univ. Dept. of Instructional Technology Logan, UT 84321 (801) 752-1398	Degree: Specialty: Assigned:	BS Instructional Technology Human Resources Laboratory Training Systems
Robert Carlin New York at Buffalo, Univ. of Mechanical & Aerospace Eng. Buffalo, NY 14261 (716) 636 4006	Degree: Specialty: Assigned:	BS Aerospace Engineering Frank J. Seiler Research Lab.
Leonard Carter Boston Univ. 705 Commonwealth Ave. Boston, MA 02215 (617) 353-5611	Degree: Specialty: Assigned:	MS Engineering Geophysics Laboratory

NAME / ADDRESS	DEGREE, SPECIALTY, LABORATORY ASSIGNED	
Frank Chavez Arizona State Univ. Dept. of Mech. & Aerospace Eng. Tempe, AZ 85287 (602) 965-3291	Degree: Specialty: Assigned:	BS Aerospace Engineering Flight Dynamics Laboratory
Alan Coleman Indiana Univ. of Pennsylvania Dept. of Physics Wey. Hall Indiana, PA 15705 (412) 357-2370	Degree: Specialty: Assigned:	BS Physics Electronic Technology Lab.
Tammie Confer Akron, Univ. of Dept. of Physics Akron, OH 44325 (216) 375-7078	Degree: Specialty: Assigned:	BS Physics Electronic Technology Lab.
Rand Conger Washington S. Univ. Dept. of Mech. & Materials Eng Pullman, WA 99163 (509) 332-1622	Degree: Specialty: Assigned:	BS Aerodynamics Frank J. Seiler Research Lab.
Brian Cull Kent State Univ. Kent Campus E Main and Lincoln Kent, OH 44242 (216) 672-2880	Degree: Specialty: Assigned:	BS Physics Materials Laboratory
Gary Cunning Colorado-Colorado Spr., Univ. of PO Box 7150 Colorado Springs, CO 80933 (719) 548-0602	Degree: Specialty: Assigned:	BS Electrical Engineering Frank J. Seiler Research Lab.
James Day Kentucky, Univ. of Dept. of Physics, Room 177 Lexington, KY 40506 (606) 257-1397	Degree: Specialty: Assigned:	BS Physics Geophysics Laboratory

NAME / ADDRESS	DEGREE, SPECIALTY, LABORATORY ASSIGNED	
Melissa Dittmer New Mexico, Univ. of Dept. of Physics & Astronomy Albuquerque, NM 87131 (505) 277-6088	Degree: Specialty: Assigned:	BS Physics Weapons Laboratory
Christina Estep Virginia Poly. Inst. & S. Univ. Dept. of Engineering Mechanics Blacksburg, VA 24060 (703) 951-0563	Degree: Specialty: Assigned:	BS Mechanical Engineering Aerospace Medical Research Laboratory
Joan Estes St. Mary's Univ. 1830 Bandera #826 San Antonio, TX 78228 (512) 436-2613	Degree: Specialty: Assigned:	BS Psychology Wilford Hall Medical Center
Paul Fayfich Texas-Austin, Univ. of College of Education Austin, TX 78712 (512) 471-5211	Degree: Specialty: Assigned:	MS Operations Research Human Resources Laboratory Manpower & Personnel Div.
Michael Findler Arizona State Univ. Computer Science Dept. Tempe, AZ 85387 (602) 965-3190	Degree: Specialty: Assigned:	MS Computer Science Avionics Laboratory
James Fitzgerald New Jersey, S. Univ. of Dept. of Biology 202 Boyden Hall Newark, NJ 07102 (201)648-1076	Degree: Specialty: Assigned:	BS Biology School of Aerospace Medicine
Blaise Fitzpatrick Rhode Island, Univ. of Civil and Envir. Eng. Kingston, RI 02881 (401) 792-2692	Degree: Specialty: Assigned:	BS Civil Engineering Engineering & Services Ctr.

NAME / ADDRESS	DEGREE, SPECIALTY, LABORATORY ASSIGNED	
Kenneth Fleming Rensselaer Poly. Inst. Dept. of Psychology Troy, NY 12180 (518) 276-6000	Degree: Specialty: Assigned:	BS Psychology Human Resources Laboratory Operations Training Division
Patrick Fourspring Pennsylvania S. Univ. 211-16 Easterly Parkway State College, PA 16801 (814) 867-3602	Degree: Specialty: Assigned:	MS Structural Engineering Flight Dynamics Laboratory
Joan Fuller Birmingham-Southern College P O Box 670 BSC Birmingham, AL 35254 (205) 780-4231	Degree: Specialty: Assigned:	BS Chemistry Frank J. Seiler Research Lab.
Robert Gabruk Virginia Poly. Inst. Dept. of Mechanical Eng. Blacksburg, VA 24061 (703) 231-7295	Degree: Specialty: Assigned:	BS Mechanical Engineering Aero Propulsion Laboratory
Shawn Gaffney Notre Dame, Univ. of Dept. of Electrical & Comp. Eng. Notre Dame, IN 46556 (219) 239-7596	Degree: Specialty: Assigned:	BS Physics Weapons Laboratory
Andrew Galasso Worcester Poly. Inst. Dept. of Physics Worcester, MA 01609 (508) 831-5313	Degree: Specialty: Assigned:	BS Physics Rome Air Development Ctr.
Michael Geer Pennsylvania State Univ. Civil Engineering Dept. State College, PA 16801 (814) 863-0576	Degree: Specialty: Assigned:	BS Civil Engineering Weapons Laboratory

NAME / ADDRESS	DEGREE, SPECIALTY, LABORATORY ASSIGNED	
James Golden Tennessee Space Inst., Univ. of Dept. of Aerospace Eng. Tullahoma, TN 37388 (615) 455-0631	Degree: Specialty: Assigned:	MS Computer Science Arnold Engineering Development Center
Ellen Goldey Miami Univ. Dept. of Zoology Oxford, OH 45056 (513) 529-3184	Degree: Specialty: Assigned:	MS Zoology Aerospace Medical Research Laboratory
Randy Gove Alabama, Univ. of Dept. of Physics Huntsville, AL 35899 (205) 895-6276	Degree: Specialty: Assigned:	BS Physics Armament Laboratory
Thomas Haas Kentucky, Univ. of Dept. of Electrical Eng. Lexington, KY 40502 (606) 257-2943	Degree: Specialty: Assigned:	BS Electrical Engineering Materials Laboratory
David Harper Bowling Green S. Univ. Dept. of Psychology Bowling Green, OH 43402 (419) 372-2301	Degree: Specialty: Assigned:	BS Psychology Aerospace Medical Research Laboratory
Craig Harwood North Carolina S. Univ. Dept. of Civil Eng., 208 Mann Raleigh, NC 27695 (919) 737-2331	Degree: Specialty: Assigned:	BS Civil Engineering Flight Dynamics Laboratory
Dollena Hawkins Tennessee Tech. Univ. Box 5054 TTU Cookeville, TN 38505 (615) 372-3441	Degree: Specialty: Assigned:	BS Mechanical Engineering Arnold Engineering Development Center

NAME / ADDRESS	DEGREE, SPECIALTY, LABORATORY ASSIGNED
Gregory Herdt Denver, Univ. of Dept. of Engineering Denver, CO 80208 (303) 871-2102	Degree: BS Specialty: Materials Science Assigned: Astronautics Laboratory
John Holman Iowa, Univ. of W35 Seashore Hall Iowa City, IA 52242 (319) 335-2502	Degree: MS Specialty: Sociology Assigned: Human Resources Laboratory Manpower & Personnel Div.
Michael Houts Massachusetts Inst. of Tech. 77 Massachusetts Ave. Rm. 24-302 Cambridge, MA 02139 (617) 253-3720	Degree: BS Specialty: Nuclear Engineering Assigned: Weapons Laboratory
Tonia Howe Wright S. Univ. Applied Behavioral Science Dept. Dayton, OH 45435 (513) 873-2089	Degree: BS Specialty: Psychology Assigned: Human Resources Laboratory Logistics & Human Factors
Johnny Hurtado Texas A&M Univ. Dept. of Aerospace Engineering College Station, TX 77840 (409) 846-9583	Degree: BS Specialty: Aerospace Engineering Assigned: Astronautics Laboratory
Leonard Isaacs Wyoming, Univ. of 804 University #1 Laramie, WY 82070 (307) 766-4221	Degree: BS Specialty: Mathematics Assigned: Armament Laboratory
Stacey Johnson Meharry Medical College 944 21st Ave. N. Apt. 109 Nashville, TN 37208 (615) 320-5484	Degree: BS Specialty: Biology Assigned: Wilford Hall Medical Center

NAME / ADDRESS	DEGREE, SPECIALTY, LABORATORY ASSIGNED
Lisa Jones Meharry Medical College 1005 D.B. Todd Blvd. Nashville, TN 37208 (615) 327-6000	Degree: BS Specialty: Biology Assigned: School of Aerospace Medicine
Susan Jones St. Mary's Univ. One Camino Santa Maria San Antonio, TX 78284 (512) 436-3011	Degree: BS Specialty: Psychology Assigned: Wilford Hall Medical Center
Christopher Kardish Florida, Univ. of 300 MEB/CIMAR Gainesville, FL 32611 (904) 392-0814	Degree: MS Specialty: Mechanical Engineering Assigned: Engineering & Services Ctr.
George Kim Trinity Univ. 715 Stadium Dr. San Antonio, TX 78284 (512) 736-7231	Degree: BS Specialty: Biology Assigned: School of Aerospace Medicine
James Kime Alabama, Univ. of Box 870312 Tuscaloosa, AL 35487 (205) 348-6075	Degree: BS Specialty: Fitness Management Assigned: School of Aerospace Medicine
Everett King Alabama, Univ. of 4527 18th Ave. East Tuscaloosa, AL 35405 (205) 556-1654	Degree: BS Specialty: Aerospace Engineering Assigned: Arnold Engineering Development Center
John Klinge Colorado, Univ. of Campus Box 429 Boulder, CO 80309 (303) 492-7559	Degree: BS Specialty: Physics Assigned: Frank J. Seiler Research Lab.

NAME / ADDRESS	DEGREE, SPECIALTY, LABORATORY ASSIGNED
Christopher Kocher Illinois, Univ. of 216 Talbot Lab 104 S. Wright St. Urbana, IL 61801 (217) 333-2322	Degree: MS Specialty: Mechanical Engineering Assigned: Astronautics Laboratory
Thomas Kuchar Boston Univ. 725 Commonwealth Ave. Boston, MA 02215 (617) 353-4884	Degree: MS Specialty: Physics Assigned: Geophysics Laboratory
David LaGraffe Syracuse Univ. 201 Physics Bldg. Syracuse, NY 13244 (315) 443-5966	Degree: MS Specialty: Physics Assigned: Rome Air Development Ctr.
Peter LaRose Northwestern Univ. 2145 Sheridan Rd. Evanston, IL 60208 (708) 491-7848	Degree: BS Specialty: Mathematics Assigned: Aero Propulsion Laboratory
John Lair New Orleans, Univ. of Dept. of Mech. Eng. Lake Front Cam New Orleans, LA 70148 (504) 286-6652	Degree: BS Specialty: Mechanical Engineering Assigned: Flight Dynamics Laboratory
Davis Lange Arizona, Univ. of Optical Sciences Center Tucson, AZ 85721 (602) 621-9104	Degree: BS Specialty: Electrical Engineering Assigned: Armament Laboratory
Richard Lareau Worcester Poly. Inst. 100 Institute Rd. Worcester, MA 01609 (508) 831-5000	Degree: BS Specialty: Electrical Engineering Assigned: Rome Air Development Ctr.

NAME / ADDRESS	DEGREE, SPECIALTY, LABORATORY ASSIGNED
James Lasche (To Be Determined)	Degree: BS Specialty: Optics Assigned: Weapons Laboratory
Jeffery Layne Ohio State Univ. 205 Dreese Laboratories Columbus, OH 43210 (614) 292-2572	Degree: BS Specialty: Electrical Engineering Assigned: Avionics Laboratory
Minh Le Calif.-Long Beach, S. Univ. of Mechanical Eng. Dept. Long Beach, CA 90840 (213) 985-4407	Degree: BS Specialty: Chemical Engineering Assigned: Astronautics Laboratory
Teresa Lee Western Illinois Univ. Dept. of Sociology Macomb, IL 61455 (309) 298-1056	Degree: MS Specialty: Sociology Assigned: Aerospace Medical Research Laboratory
Toby Martin Illinois, Univ. of Dept. of Aeronautical Eng. Champaign, IL 61820 (217) 351-1935	Degree: BS Specialty: Aeronautical Engineering Assigned: Weapons Laboratory
Margo McDowell Nebraska, University of Civil Engineering Lincoln, NE 68588 (402) 472-2354	Degree: BS Specialty: Mechanical Engineering Assigned: Materials Laboratory
Michael Montegut Rensselaer Poly. Inst. Psychology Dept. Troy, NY 12180 (518) 276-6472	Degree: BS Specialty: Psychology Assigned: Human Resources Laboratory Operations Training Division

NAME / ADDRESS	DEGREE, SPECIALTY, LABORATORY ASSIGNED	
John Moore Texas-Austin, Univ. of Dept. of Elect. Eng. 3914 Ave D Austin, TX 78751 (512) 458-9674	Degree: Specialty: Assigned:	MS Electromagnetic Rome Air Development Ctr.
Kyle Nash Alabama, Univ. of Dept. of Aerospace Eng. Tuscaloosa, AL 35405 (205) 556-2842	Degree: Specialty: Assigned:	BS Aerodynamics Arnold Engineering Development Center
Kelly Neville Rice University Dept. of Psychology Houston, TX	Degree: Specialty: Assigned:	BS Psychology School of Aerospace Medicine
Keith Newman Pennsylvania State Univ. 209 Steidle Bldg. University Park, PA 16802 (814) 865-5446	Degree: Specialty: Assigned:	MS Metallurgical Engineering Materials Laboratory
Hung Nguyen California State Univ. Mechanical Eng. Dept. Long Beach, CA 90840 (213) 985-4111	Degree: Specialty: Assigned:	BS Mechanical Engineering Astronautics Laboratory
John Noto Tufts Univ. Dept. of Physics & Astronomy Medford, MA 02155 (617) 628-5000	Degree: Specialty: Assigned:	BS Physics Geophysics Laboratory
Allen Olheiser North Dakota State Univ. 1017 N. 10 Street Fargo, ND 58102 (701) 237-4636	Degree: Specialty: Assigned:	BS Computer Engineering Aero Propulsion Laboratory

NAME / ADDRESS	DEGREE, SPECIALTY, LABORATORY ASSIGNED	
Kristina Pawlikowski Ohio S. Univ. Dept. of Civil Eng. Columbus, OH 43212 (614) 299-9323	Degree: Specialty: Assigned:	BS Civil Engineering Flight Dynamics Laboratory
Tanya Payne New Mexico, Univ. of Psychology Dept. Albuquerque, NM 87131 (505) 277-4805	Degree: Specialty: Assigned:	BS Psychology Weapons Laboratory
Christine Perry Pennsylvania S. Univ. Dept. of Aerospace Eng. State College, PA 16801 (814) 867-7877	Degree: Specialty: Assigned:	BS Aerospace Engineering Astronautics Laboratory
James Perry Florida Inst. of Tech. 150 West University Blvd. Melbourne, FL 32901 (407) 768-8000	Degree: Specialty: Assigned:	BS Electrical Engineering Avionics Laboratory
Brett Pokines New York, State Univ. of 1068 Richmond Quad Buffalo, NY 14260 (716) 636-5541	Degree: Specialty: Assigned:	BS Mechanical Engineering Frank J. Seiler Research Lab.
George Proicou Ohio State Univ. Biomedical Center 270 Bevis Hall Columbus, OH 43210 (614) 292-5570	Degree: Specialty: Assigned:	BS Aeronautical Engineering School of Aerospace Medicine
Jenny Rawson Washington S. Univ. Dept. of Elect. & Comp. Eng. Pullman, WA 99164 (509) 335-6602	Degree: Specialty: Assigned:	MS Electrical Engineering Flight Dynamics Laboratory

NAME / ADDRESS	DEGREE, SPECIALTY, LABORATORY ASSIGNED
Keith Redmill Ohio State Univ. Dept. of Elect. Eng. 201 Dreese Lab Columbus, OH 43210 (614) 292-2572	Degree: BS Specialty: Electrical Engineering Assigned: Flight Dynamics Laboratory
Mary Reid Arizona, Univ. of Shantz Blvd. #429 Tucson, AZ 85721 (602) 621-1646	Degree: BS Specialty: History Assigned: Engineering & Services Ctr.
Brahm Rhodes Boston Univ. Aero/Mech. Office 110 Cummington Boston, MA 02215 (617) 353-1285	Degree: MS Specialty: Mechanical Engineering Assigned: Geophysics Laboratory
Edward Riegelsberger Ohio State Univ. Dept. of Electrical Eng. Columbus, OH 43201 (614) 291-0899	Degree: BS Specialty: Electrical Engineerig Assigned: Aerospace Medical Research Laboratory
Joseph Rigney Case Western Reserve Univ. Cleveland Hts., OH 44106 (216) 321-1114	Degree: BS Specialty: Materials Science Assigned: Materials Laboratory
Dawnlee Roberson Texas-San Antonio, Univ. of SB 3.01.37 San Antonio, TX 78228 (512) 691-5665	Degree: BS Specialty: Biology Assigned: School of Aerospace Medicine
Robyn Robinson Meharry Medical College 1005 D.B. Todd Blvd. Nashville, TN 37208 (615) 327-6413	Degree: BS Specialty: Biology Assigned: School of Aerospace Medicine

NAME / ADDRESS	DEGREE, SPECIALTY, LABORATORY ASSIGNED
Steve Romaniuk South Florida, Univ. of Dept. of Computer Science Tampa, FL 33620 (813) 974-3921	Degree: MS Specialty: Computer Science Assigned: Avionics Laboratory
Arthur Ryan Wright State Univ. Dept. of Psychology Dayton, OH 45435 (513) 873-2451	Degree: BS Specialty: Psychology Assigned: Aerospace Medical Research Laboratory
Robert Sabatini Scranton, Univ. of Dept. of Biology Scranton, PA 18510 (717) 961-6117	Degree: BS Specialty: Biology Assigned: School of Aerospace Medicine
Gregory Schoeppner Ohio State Univ. 470 Hitchcock Hall Columbus, OH 43210 (614) 292-2771	Degree: MS Specialty: Civil Engineering Assigned: Flight Dynamics Laboratory
John Sebghati Tennessee Space Inst. Box 55 Tullahoma, TN 37388 (615) 454-1087	Degree: BS Specialty: Aerospace Engineering Assigned: Arnold Engineering Development Center
Charles Shank Syracuse Univ. Dept. of Elec. & Computer Eng. Syracuse, NY 13210 (315) 443-4229	Degree: BS Specialty: Electrical Engineering Assigned: Rome Air Development Ctr.
David Shehee Eastern Kentucky Univ. Chemistry Dept. Richmond, KY 40475 (606) 677-1456	Degree: BS Specialty: Chemistry Assigned: Aero Propulsion Laboratory

NAME / ADDRESS	DEGREE, SPECIALTY, LABORATORY ASSIGNED	
Scott Short Dayton, Univ. of 300 College Park Dayton, OH 45469 (513) 229-2627	Degree: Specialty: Assigned:	MS Material Science Materials Laboratory
Sveta Singh Texas-San Antonio, Univ. of Dept. of Life Sciences San Antonio, TX 78285 (512) 691-5493	Degree: Specialty: Assigned:	BS Biology School of Aerospace Medicine
Janet Solomon Alabama, Univ. of Health & Human Perform. Box 870312 Tuscaloosa, AL 35487 (205) 348-6075	Degree: Specialty: Assigned:	MS Physiology School of Aerospace Medicine
Carol Soule Georgia, Univ. of Dept. of Educational Psychology Athens, GA 30602 (404) 542-4110	Degree: Specialty: Assigned:	MS Educational Psychology Human Resources Laboratory Manpower & Personnel Div.
Thomas Starchville Pennsylvania State Univ. Dept. of Aerospace Eng. University Park, PA 16802 (814) 865-2569	Degree: Specialty: Assigned:	BS Aerospace Engineering Astronautics Laboratory
Anne Stephenson Dayton, Univ. of Aerospace Engineering Dept. Dayton, OH 45469 (513) 228-3891	Degree: Specialty: Assigned:	BS Aerospace Engineering Flight Dynamics Laboratory
Julia Stephenson North Texas, Univ. of 505 Eagle #8 Denton, TX 76201 (817) 565-3110	Degree: Specialty: Assigned:	BS Economics Human Resources Laboratory Training Systems

NAME / ADDRESS	DEGREE, SPECIALTY, LABORATORY ASSIGNED	
Velma Velazquez Wright State Univ. Dept. of Psychology Dayton, OH 45435 (513) 873-2391	Degree: Specialty: Assigned:	BS Psychology Human Resources Laboratory Logistics & Human Factors
Andrew Walsh Colorado State Univ. Dept. of Civil Eng. Fort Collins, CO 80523 (303) 491-6603	Degree: Specialty: Assigned:	BS Civil Engineering Engineering & Services Ctr.
Jennifer Wang Rensselaer Poly. Inst. Computer Science Dept. Troy, NY 12180 (518) 276-8291	Degree: Specialty: Assigned:	BS Computer Science Human Resources Laboratory Operations Training Division
Christopher Wanstall Alabama, Univ. of Dept. of Engineering Mechanics Tuscaloosa, AL 35487 (205) 348-7241	Degree: Specialty: Assigned:	BS Oceanography Armament Laboratory
Grant Watson Florida Inst. of Tech. 150 West University Melbourne, FL 32901 (407) 768-8000	Degree: Specialty: Assigned:	BS Mechanical Engineering Arnold Engineering Development Center
Melody Welch Texas A&M Univ. Dept. of Biology 715 Stadium Dr. San Antonio, TX 78212 (512) 736-7231	Degree: Specialty: Assigned:	BS Biology School of Aerospace Medicine
David Welter Dayton, Univ. of Dept. of Mechanical Eng. 300 College Park Drive Dayton, OH 45469 (513) 229-2875	Degree: Specialty: Assigned:	BS Mechanical Engineering Aero Propulsion Laboratory

NAME / ADDRESS	DEGREE, SPECIALTY, LABORATORY ASSIGNED	
William Wilk Alabama, Univ. of Dept. of Aerospace Engineering Tuscaloosa, AL 35486 (205) 348-7987	Degree: Specialty: Assigned:	BS Aerospace Engineering Arnold Engineering Development Center
William Yee Ohio State Univ. 142 Townshend Hall 1885 Neil Ave. Columbus, OH 43210 (614) 292-1123	Degree: Specialty: Assigned:	BS Psychology Aerospace Medical Research Laboratory
Timothy Young Central Florida, Univ. of MEAS Dept., Box 25000 Orlando, FL 32816 (407) 275-2416	Degree: Specialty: Assigned:	BS Mechanical Engineering Aero Propulsion Laboratory

PARTICIPANT LABORATORY ASSIGNMENT

C. PARTICIPANT LABORATORY ASSIGNMENT (Page 1)

1990 USAF/UES GRADUATE STUDENT RESEARCH PROGRAM

AERO PROPULSION LABORATORY (WRDC/APL)
(Wright-Patterson Air Force Base)

1. Robert Gabruk
2. Peter LaRose
3. Allen Olheiser
4. David Shehee
5. David Welter
6. Timothy Young

ARMAMENT LABORATORY (ATL)
(Eglin Air Force Base)

1. George Boynton
2. Randy Gove
3. Leonard Isaacs
4. Davis Lange
5. Christopher Wanstall

HARRY G. ARMSTRONG AEROSPACE MEDICAL RESEARCH LABORATORY (AAMRL)
(Wright-Patterson Air Force Base)

1. Christina Estep
2. Ellen Goldey
3. David Harper
4. Teresa Lee
5. Edward Riegelsberger
6. Arthur Ryan
7. William Yee

ARNOLD ENGINEERING DEVELOPMENT CENTER (AEDC)
(Arnold Air Force Base)

1. Ben Abbott
2. Theodore Bapty
3. Ronald Blume
4. Jordan Cahn
5. James Golden
6. Dollena Hawkins
7. Everett King
8. Kyle Nash
9. John Sebghati
10. Grant Watson
11. William Wilk

ASTRONAUTICS LABORATORY (AL)
(Edwards Air Force Base)

1. Joseph Baldonado
2. Robert Byers
3. Gregory Herdt
4. Johnny Hurtado
5. Christopher Kocher
6. Minh Le
7. Hung Nguyen
8. Christine Perry
9. Thomas Starchville

AVIONICS LABORATORY (Avionics Laboratory)
(Wright-Patterson Air Force Base)

1. Eric Byrne
2. Michael Findler
3. Jeffrey Layne
4. James Perry
5. Steve Romaniuk

C. PARTICIPANT LABORATORY ASSIGNMENT (Page 2)

ELECTRONIC TECHNOLOGY LABORATORY (ETL)
(Wright-Patterson Air Force Base)

1. Alan Coleman
2. Tammie Confer

ENGINEERING AND SERVICES CENTER (ESC)
(Tyndall Air Force Base)

1. Joseph Bernardo
2. Blaise Fitzpatrick
3. Christopher Kardish
4. Mary Reid
5. Andrew Walsh

FLIGHT DYNAMICS LABORATORY (FDL)
(Wright-Patterson Air Force Base)

1. Magna Altamirano
2. Frank Chavez
3. Patrick Fourspring
4. Craig Harwood
5. John Lair
6. Kristina Pawlikowski
7. Jenny Rawson
8. Keith Redmill
9. Gregory Schoeppner
10. Anne Stephenson

FRANK J. SEILER RESEARCH LABORATORY (Frank J. Seiler Research Lab.)
(USAF Academy)

1. Gregory Addington
2. Robert Carlin
3. Rand Conger
4. Gary Cunning
5. Joan Fuller
6. John Klinge
7. Brett Pokines

GEOPHYSICS LABORATORY (Geophysics Laboratory)
(Hansom Air Force Base)

1. Leonard Carter
2. James Day
3. Thomas Kuchar
4. John Noto
5. Brahm Rhodes

HUMAN RESOURCES LABORATORY
(Brooks, Williams and Wright-Patterson Air Force Bases)

1. Laura Bernhofen
2. Ann Canfield
3. Paul Fayfich
4. Kenneth Fleming
5. John Holman
6. Tonia Howe
7. Michael Montegut
8. Carol Soule
9. Julia Stephenson
10. Velma Velazquez
11. Jennifer Wang

C. PARTICIPANT LABORATORY ASSIGNMENT (Page 3)

MATERIALS LABORATORY (ML)
(Wright-Patterson Air Force Base)

1. Broam Cull
2. Thomas Haas
3. Margo McDowell
4. Keith Newman
5. Joseph Rigney
6. Scott Short

OCCUPATIONAL AND ENVIRONMENT HEALTH LABORATORY (OEHL)
(Brooks Air Force Base)

1. Andrew Bonas

ROME AIR DEVELOPMENT CENTER (Rome Air Development Center)
(Griffiss Air Force Base)

1. Andrew Galasso
2. David LaGraffe
3. Richard Lareau
4. John Moore
5. Charles Shank

SCHOOL OF AEROSPACE MEDICINE (School of Aerospace Medicine)
(Brooks Air Force Base)

1. Janis Beaird
2. Dora Brenner
3. Thomas Broersma
4. Joseph Brogan
5. James Fitzgerald
6. Lisa Jones
7. George Kim
8. James Kime
9. Kelly Neville
10. George Proicou
11. Dawnlee Roberson
12. Robyn Robinson
13. Robert Sabatini
14. Sveta Singh
15. Janet Solomon
16. Melody Welch

WEAPONS LABORATORY (Weapons Laboratory)
(Kirtland Air Force Base)

1. Melissa Dittmer
2. Shawn Gaffney
3. Michael Geer
4. Michael Houts
5. James Lasche
6. Toby Martin
7. Tanya Payne

WILFORD HALL MEDICAL CENTER (Wilford Hall Medical Center)
(Lackland Air Force Base)

1. Joan Estes
2. Stacey Johnson
3. Susan Jones

PAGES _____

ARE

MISSING

IN

ORIGINAL

DOCUMENT

Volume I
Engineering and Services Center

Frank J. Seiler Research Laboratory

Volume I

Volume II
Wright Research Development Center
Aero Propulsion Laboratory

Volume II
Flight Dynamics Laboratory

Materials Laboratory

Volume II

Volume III
Human Systems Divisions Laboratories
Harry G. Armstrong Aerospace Medical Research Laboratory

Human Resources Laboratory

Volume III

Volume III

Volume III
Wilford Hall Medical Center

1990 USAF-UES SUMMER FACULTY RESEARCH PROGRAM

GRADUATE STUDENT RESEARCH PROGRAM

Sponsored by the

AIR FORCE OFFICE OF SCIENTIFIC RESEARCH

Conducted by the

Universal Energy Systems, Inc.

FINAL REPORT

Characterization of the Flowfield of a Dump Combustor

Prepared by:	Robert S. Gabruk
Academic Rank:	Master of Science student
Department and	Mechanical Engineering
University:	Virginia Polytechnic Institute & State Universtiy
Research Location:	USAF/POPT Wright-Patterson AFB Dayton, OH 45433
USAF Researcher:	Abdollah Nejad
Date:	11/6/90
Contract No.:	F49620-88-C-0053

CHARACTERIZATION OF THE FLOWFIELD OF A DUMP COMBUSTOR

BY

ROBERT S. GABRUK

ABSTRACT

To provide quality benchmark data (that can be used in numerical simulation comparisons) and to examine the effects of combustion and on a typical ramjet engine flowfield, a water-cooled, stainless steel dump combustor model was developed. A two-component Laser Doppler Anemometer (LDA) was used to measure the mean and turbulent velocities in the axial and tangential directions and provide a comparison between combusting and isothermal flows.

The results showed some significant differences between the reacting and nonreacting flows. The most significant effect was the difference between the inherent recirculation regions for each case. Combustion decreased the length of the region (from 6.75 step heights to 3.5 step heights from the dump plane), while increasing the maximum negative velocities. This made for a more compact, but stronger, recirculation region. Since the recirculation region acts as the main flame holder and is a major source of turbulence, the changes in this region significantly altered the dump combustor flowfield.

ACKNOWLEDGEMENT

The research effort presented here was sponsored by the Air Force Systems Command and the Air Force Office of Scientific Research. Universal Energy Systems also deserves recognition for providing all of the information necessary for a comfortable and productive research session. This project would not have been possible without the support of Abdollah Nejad and Saad Ahmed. They provided the tools and encouragement needed to carry out the research effort.

I. INTRODUCTION

Detailed experimental studies must be carried out before the accuracy of a numerical simulation can be determined. The application of mathematical methods to complex turbulent flowfields continues to be the focus of many current studies, as numerical modeling of turbulent flows provides a more cost-efficient and time-saving method of engineering design. Most of the past studies have concentrated on understanding the behavior of turbulent flows and improving the accuracy of the computational modeling. Lower order numerical models require various assumptions in the solution of the Navier-Stokes equations, and experimental data must be available to determine the validity of these assumptions.

One focus of these experimental and numerical studies has been on sudden expansion (or dump) combustors, typically found in many air-breathing propulsion systems, and in particular, the ramjet engine. Ramjets are used in unison with rocket boosters to provide integral propulsion systems for missiles. The rocket booster is designed to provide the necessary propulsion in the initial stage of flight, with the ramjet engine taking over as the propulsion system once the rocket reaches the required flight speed. The basic configuration of a ramjet engine is that of a dump combustor. Therefore, much can be learned about the ramjet through studies on a sudden expansion combustor. The flowfield of a dump combustor

is a complex combination of turbulent fuel-air mixing, flow separation, flow recirculation, flow reattachment, and various other flow phenomena, as shown in Fig. 1.

Past studies have concentrated mainly on isothermal (cold) flows through dump combustors. Therefore, a significant amount of detailed flowfield data is readily available for cold flows only. In addition, most of the prior studies on actual dump combustors have been limited to measurements of quantities such as combustion efficiency and velocity measurements were not available.

My research interests are in the area of internal flows, both with and without combustion. During the summer previous to this research session, I was involved with this same research project. While working on the project, I helped characterize the stability of the dump combustor and take some preliminary data.

II. OBJECTIVES OF THE RESEARCH EFFORT:

This thesis documents a study done on combusting flow through a dump combustor with zero inlet swirl. (In future experiments, the effects of inlet swirl on the flowfield will be studied). Velocity measurements (both mean and turbulent) are provided by a Laser Doppler Anemometer (LDA) and are the major point of information.

The main goal of this research effort was to provide a benchmark set of LDA flowfield data that could be used in comparisons with numerical simulation. Numerical modeling can be an extremely valuable research tool because, if a particular flowfield can be mapped on a computer rather than in a test lab, both time and money can be saved. However, in order to test these models, quality experimental data is needed for comparison. A secondary goal of this research effort was to study the effects of heat release, mixing processes, and chemical reactions on the flowfield of a ramjet engine.

III.

a. All experiments were conducted in a water-cooled stainless steel model of a ramjet dump combustor as shown schematically in Figs. 2 and 3. The combustor wall contained a high-quality quartz window for optical access to the flow. Since the dump plane (or piston, as shown in Fig. 3) was mounted on precision rails, it could be positioned at any axial location relative

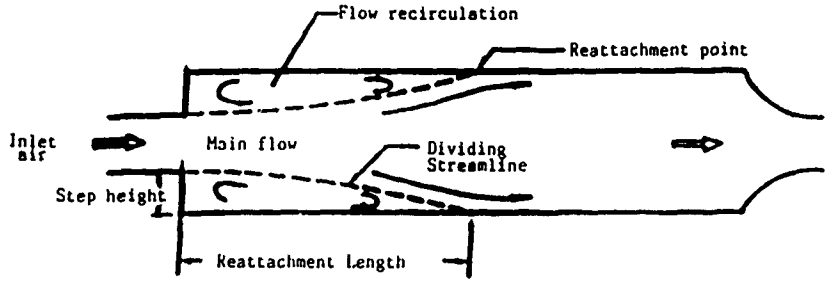

Fig. 1 Schematic illustration of a dump combustor flowfield.

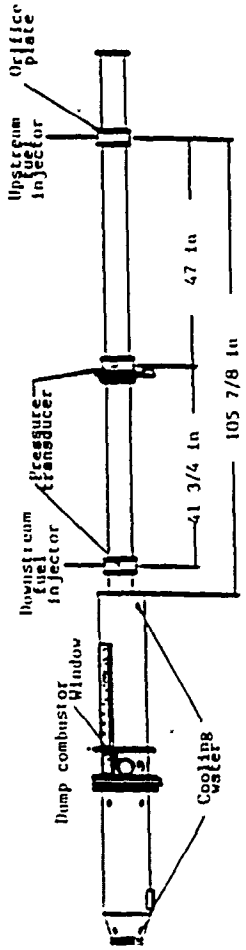

Fig. 2 Overall view of inlet duct and dump combustor.

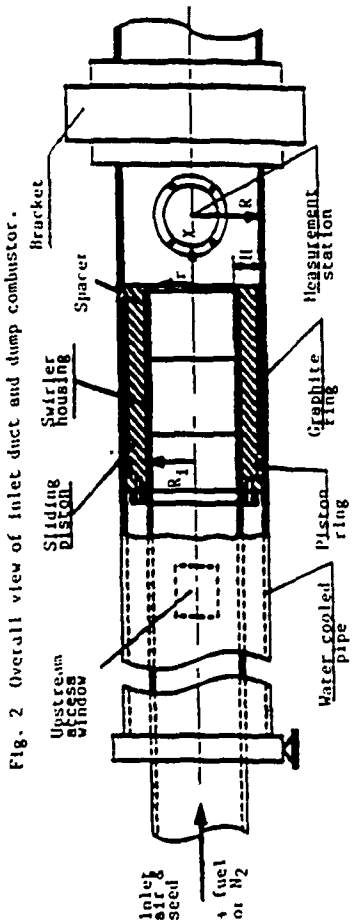

Fig. 3 Cross sectional view of dump combustor.

to the window. This provided a good way to take LDA measurements at any axial location downstream of the dump plane. The inlet duct also contained a high-quality quartz window in order to obtain inlet flow conditions. The jacket outlet temperature was constantly monitored to ensure that the water temperature was well below boiling.

The rig was of the same basic design as the plexiglass model used in the nonreacting studies of Favaloro et al. (1). A 4-inch diameter inlet duct supplied air to a 6-inch diameter combustor. This corresponds to a 2.25 area ratio. The combustor, which had a 6-inch long exit nozzle with 60% area reduction, had a maximum length of 63 3/4 inches when the piston was at full stroke. The inlet air was supplied by high pressure compressors to achieve a 60 ft/sec average velocity, corresponding to a 1.18×10^5 Reynolds number. Inlet pressures and temperatures were ambient (80 F,14.7 psia). A screen (flame arrester) was located 18 1/4 inches upstream of the dump plane to guard against flashback.

A two-component, frequency-shifted, backscatter LDA system was used to obtain mean velocity and turbulence data. TiO_2 particles were used as the seeder. Stored data rates ranged from 100 to 1000 per second for isothermal flows and 15 to 500 for combusting flows, using a 20 usec coincident window.

b. With the experimental rig configured as such, various mean and turbulent velocity data were taken. This information will

help accomplish the research goals of providing a set of data that can be used both to compare with numerical simulations and to make general conclusions as to the effects of heat release on the dump combustor flowfield. The data includes the inlet velocity profile, which is a point of information neglected in some other experiments. All velocity results have been normalized with the average inlet duct velocity (Uref). Although obtained in this study, the mean tangential velocity and Reynolds stress data are not presented here. The reason for not presenting this data is that in an absence of inlet swirl, these values should theoretically be equal to zero.

The inlet velocity profile (at 10 step heights upstream of the dump plane) is shown in Fig. 4. Both the streamwise mean and turbulent velocities (normalized with the average inlet duct velocity) are shown. As can be seen from the figure, the mean velocities are fairly symmetrical about the inlet duct centerline and the turbulent velocities hold approximately constant at 15 percent of the average inlet duct velocity.

Centerline mean velocity and turbulence results (for both reacting and nonreacting cases) are shown in Figs. 5-7. These figures were designed to illustrate the effects of heat release on the flowfield of the dump combustor. Figure 5 shows a gradual decay of cold flow centerline axial velocity

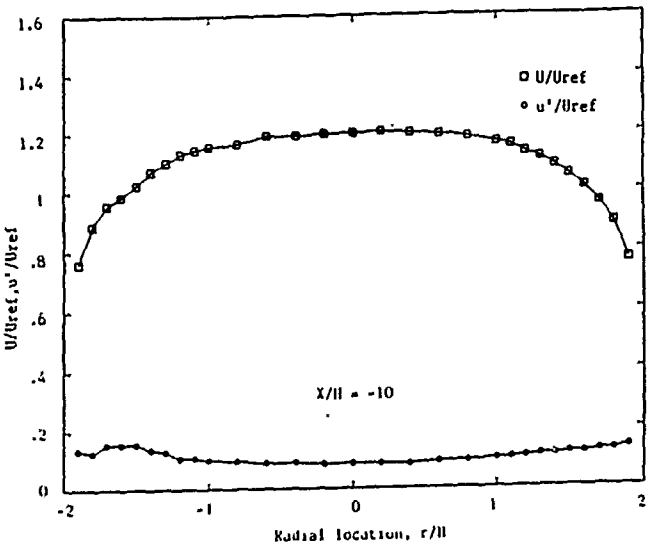

Fig. 4 Inlet velocity profiles

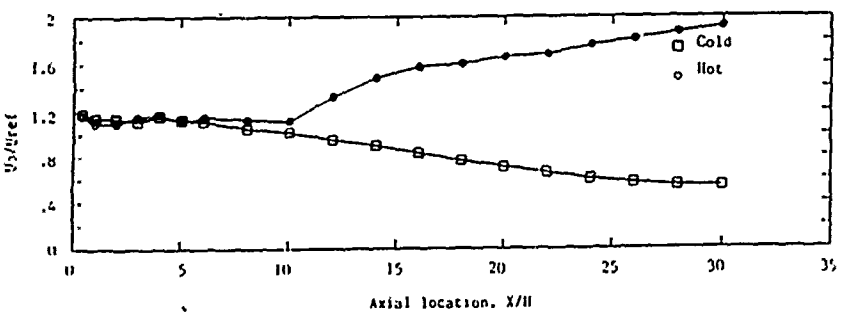

Fig. 5 Centerline mean axial velocity.

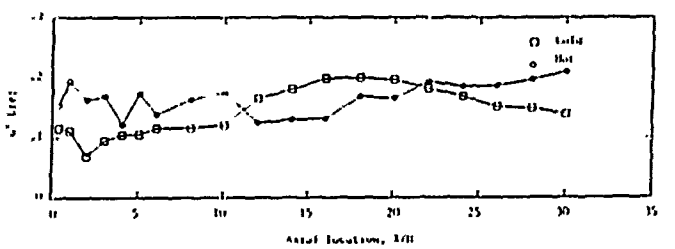

Fig. 6 Centerline distribution of axial turbulence.

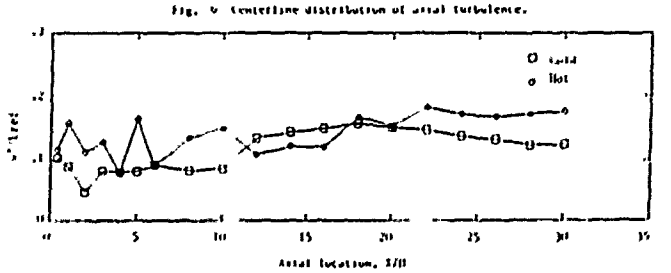

Fig. 7 Centerline distribution of tangential turbulence.

throughout the length of the combustor. This is consistent with mass continuity principles, i.e., when given constant density, an increase in flow area will cause a decrease in flow velocity.

The cold flow centerline axial and tangential turbulence intensity (Figs. 6 and 7), on the other hand, increased in the downstream direction until approximately 18 step heights. This increase in turbulence intensity was due to the convection and diffusion of high turbulent energy created in the shear layer during flow separation. After 18 step heights, however, the velocities decreased as the flow became more developed. The maximum turbulence level (based on inlet duct average velocity) was about 20 percent at 18 step heights from the dump.

One important observation of the turbulent velocity data is the fact that the axial turbulence levels were always greater than the corresponding tangential levels (Figs. 6 and 7), however, the general trend (of turbulence level with axial location) was almost identical. This is an important observation since this means that the flow demonstrates little turbulence isotropicity. Since many numerical models assume turbulence isotropicity, this puts the validity of the results of these models in question.

At first glance (at Figs. 5-7), one might be inclined to hypothesize that heat release had little effect on the mean

centerline velocity in axial locations less than approximately 10 step heights from the dump plane. However, the similarity between the hot and cold flow velocities is due to the lack of combustion that occurred in the high speed potential core in the center of the flowfield. The potential core is a region of the flow where the inlet centerline velocity is maintained. The length of the potential core was on the order of 9 to 10 step heights for the reacting case and 7 to 8 step heights for the nonreacting flow.

After the end of the non-combusting potential core, heat release had a significant effect in the center of the combustor flowfield. Figures 5-7 illustrate these differences. After X/H = 10, the mean axial velocities (for the reacting case) began to increase. Conservation of mass principles support the results of this study. At X/H = 10, the time mean average flame front penetrated into the potential core and combustion effects began. At the point where heat release effects started, an increase of velocity should occur since the temperature increased (which causes a density decrease).

The difference between the hot and cold flow turbulence intensities in the potential core can be attributed to the fact that the reacting flow had a more intense corner recirculation region (discussed later in this section). This more intense recirculation region had a higher turbulent

energy, so more turbulence was convected into the potential core.

Outside of the potential core, the reacting flow turbulence levels showed a sharp decline just across the flame front and then a gradual rise throughout the remainder of the combustor as the turbulent velocities expanded (increased as the density decreased) with the mean velocities. The flame front is a region of high turbulence, so the sharp decline in turbulence from a location on (or very near) the flame front to a location outside of the flame front is not unexpected.

Profiles of mean velocities at various axial locations are presented in Fig. 8. More detailed profiles are shown in Appendix B. The numbers (0,1,2) shown on the abscissa represent origins for each velocity profile. For example, the first zero marks the origin for the profile taken 0.38 step heights from the dump plane. Any part of the velocity curves located to the left of the zero tick are negative velocities and those to the right are positive velocities. Velocities were measured from the centerline to one-tenth of an inch from the combustor wall. This figure (8) shows the evolution of mean axial velocity with radial location.

At axial locations of 0.38 to 10 step heights from the dump plane, there is very little difference between the nonreacting and reacting cases in the potential core (r/H is less than 1). This is what would be expected since there was

very little combustion occurring in the high speed core near the dump plane.

At axial locations greater than (about) 10 step heights, however, the velocities near the centerline began to deviate from each other. This marked the end of the potential core flow (at X/H = 9-10) of the reacting flow, and the effects of heat release began.

There was a significant difference, on the other hand, between the hot and cold flow mean axial velocities outside of the potential core (r/H greater than 2). This became even more apparent as the flow progressed downstream. At axial locations less than 4 step heights from the dump, the high shear region between the potential core and the recirculation region (near the combustor wall) could be clearly identified. The shear region could be identified by the region of flow with the highest velocity gradient. Measurements near the combustor wall showed rapid velocity decay and a small region of flow reversal in the corner recirculation zone. The corner recirculation region can be clearly identified in Fig. 8 and in a contour plot of constant velocity lines (Fig. 9).

The levels in Fig. 9 identify locations in the flowfield that have the same mean velocity. For example, the lines with the number 7 attached to them represent locations in the flow where the velocity was equal to the inlet centerline mean velocity (hence, UMEA for level 7 is equal to 1.00). Level

2 indicates the zero velocity contour. An extrapolation of the zero velocity line to the combustor wall defines the reattachment point. The distance from the dump plane to the reattachment point is the recirculation length. Note that the zero velocity line is different from the dividing streamline (not represented in the figure) and they only intersect at the separation and reattachment points.

As can be seen from the contour plot, the recirculation length was much shorter for the reacting flow, although the maximum negative velocity was greater. For the hot flow, the recirculation length was approximately 3.5 step heights from the dump plane, opposed to 6.75 for the cold.

Table I gives a comparison of the corner recirculation zone (CRZ) length for a number of studies. Although not shown in the table, Pitz and Daily (2) also reported results showing a similar trend for reattachment with combustion. However, their experiments were performed on reacting turbulent flows after a reward-facing step. The variance in the results of Table I can be attributed to fuel type, equivalence ratio, and inlet flow conditions. As mentioned earlier, most previous studies do not include inlet velocity profiles, so it is difficult to conclude how the aforementioned factors affect corner recirculation zone length.

TABLE I

CORNER RECIRCULATION ZONE LENGTH

Reference	CRZ Length(X/H)	Diameter Ratio	Phi	Fuel
current study	6.7	1.5	0.00	
current study	3.5	1.5	0.65	propane
Nejad et al.(3)	8.2	1.5	0.00	
Nejad et al.(3)	3.7	1.5	0.65	propane
Stevenson et al.(4)	8.6	2.0	0.00	
Stevenson et al.(4)	7.4	2.0	0.28	propane
Smith and Giel(5)	4.0	2.0	0.00	
Smith and Giel(5)	8.0	2.0	0.12	hydrogen
Schulz(6)	1.0	10.0	0.00	

A decrease in corner recirculation zone length with combustion was not reported by all researchers. Smith and Giel (5) found the corner recirculation zone length to increase with combustion, however, their experiments were not performed in a true dump combustor. Their combustor had a high velocity annulus air jet that expanded into a central low velocity fuel stream. Schulz (6) found no significant change in length while studying a sudden-expansion combustor with a diameter ratio of 10, which is very large for aerospace applications.

The turbulent velocity profiles are shown in Figs. 10 and 11. Although a direct comparison between Figs. 10 and 11 is somewhat difficult, one should try to recognize that the axial

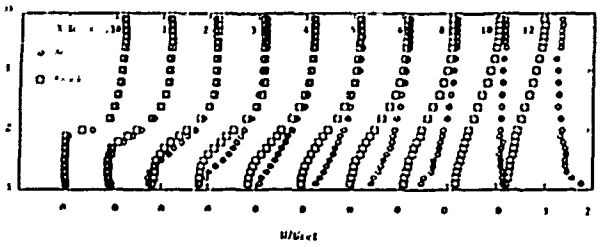

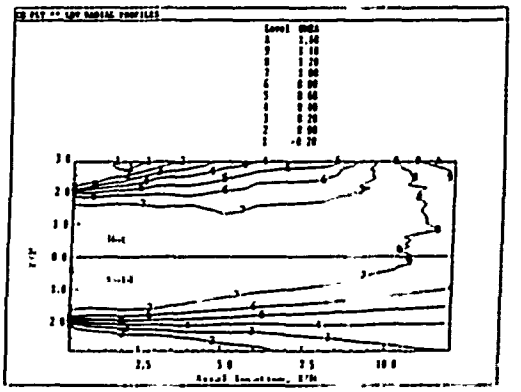

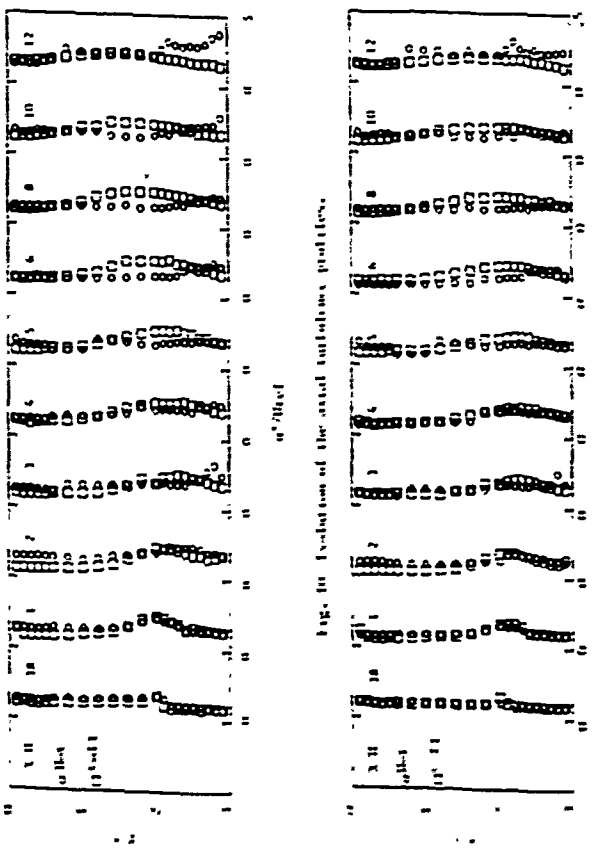

turbulent velocities were generally greater than the corresponding tangential turbulent velocities, although the maximum turbulence levels occurred at the same radial position. Furthermore, in the beginning region of the core flow (where X/H is less than 5), heat release had only a small effect on both the axial and tangential turbulent intensities, with the exceptions of intensities at X/H = 1 and 2. At these locations, the mean axial velocities (Fig. 8) were at their peak negative values. Therefore, these locations (X/H = 1 and 2) mark the most intense region of the recirculation zone. Hence, more turbulent energy is convected into the core at these axial locations.

In the vicinity of the high shear region there is a significant difference between reacting and nonreacting turbulence levels. As the flow progressed downstream from the dump plane, the location of the maximum turbulence level (which usually corresponds with the high shear region) shifted towards the wall much sooner for the reacting flow. Since the shear region roughly coincides with the dividing streamline, this suggests a smaller recirculation region.

Further downstream, where X/H is greater than 4, combustion decreased the turbulent levels. This is not a surprise since the recirculation zone length for the reacting case was only 3.5 step heights, while recirculation continued until nearly 7 step heights for the nonreacting case. After

the flame front penetrated the potential core, at locations after 10 step heights from the dump, the axial and tangential turbulent velocities expanded (increased as the density decreased) along with the mean velocities.

The turbulent levels near the combustor wall also seem to be affected by combustion, with an apparent increase at some downstream locations (where X/H is greater than 6). One possible explanation for this is that the turbulent boundary layer created along the combustor wall after the reattachment point was much more intense for the reacting flow. Not only were the mean velocities greater (at these locations) for the reacting case, but so was the distance from the reattachment point. This means that the boundary layer had more "time" to grow and become more intense. Some of the turbulent energy was being convected radially inward from the boundary layer, which is expected to be very thin at locations shortly after the reattachment point, and appeared as an increase in turbulence in the near wall region.

VI. RECOMMENDATIONS:

a. The mean and turbulent velocity data presented here will be useful in comparisons with numerical models. The inlet velocity profiles provide the initial conditions needed for the numerical code. Furthermore, the velocity data will determine the validity of some of the assumptions used in the mathematical simulation.

b. Detailed temperature measurements that are coincident with LDA velocity measurements should be taken. A dump combustor flowfield temperature map would not only help identify regions of flow such as the potential core and recirculation region, but it would also be useful in numerical modeling.

REFERENCES

1 Favaloro, S.C., Nejad, A.S., and Vanka, S.P., "An Experimental and Computational Investigation of Isothermal Swirling Flow in an Axisymmetric Dump Combustor," AIAA 89-0620, 1989.

2 Pitz, R.W. and Daily, J.W., "Combustion in a Turbulent Mixing Layer Formed at a Rearward-Facing Step," AIAA Journal, Vol. 21, Nov. 1983, pp.1565-1570.

3 Nejad, A.S., Ahmed, S.A., Roe, L.A., and Gabruk, R.S., "Experimental Studies of Reactive and Non-Reactive Flows in Dump Combustors," ASME Journal, 90-GT-82, 1990.

4 Stevenson, W.H., Gould, R.D., and Thompson, H.D., "Laser Velocity Measurements and Analysis in Turbulent Flows with Combustion," Part II, AFWAL-TR-82-2076, 1983.

5 Smith, G.D. and Giel, T.V., "An Experimental Investigation of Reactive, Turbulent, Recirculating Jet Mixing," AEDC-TR-79-79, May 1980.

6 Schulz, R.J., "An Investigation of Ducted, Two-stream, Variable Density, Turbulent Jet Mixing wiht Recirculation," AEDC-TR-76-152, AFOSR-TR-76-187, ADA 034537, 1977.

1990 USAF-UES SUMMER FACULTY RESEARCH PROGRAM/

GRADUATE STUDENT RESEARCH PROGRAM

Sponsored by the

AIR FORCE OFFICE OF SCIENTIFIC RESEARCH

Conducted by the

Universal Energy Systems, Inc.

FINAL REPORT

"CHAOTIC" MICROFAUCETS AND THE PREDICTION OF DROPLET DISTRIBUTIONS

Prepared by:	P. Gavin LaRose
Academic Rank:	Graduate Student
Department and	Applied Mathematics and Engineering Sciences
University:	Northwestern University
Research Location:	WRDC/POSF Wright Patterson AFB Dayton, OH 45433
USAF Researcher:	Dr. W. M. Roquemore
Date:	August 15, 1990
Contract Number:	F49620-85-C-0013

"CHAOTIC" MICROFAUCETS AND THE PREDICTION OF DROPLET DISTRIBUTIONS

by

P. Gavin LaRose

ABSTRACT

The existence of chaos in dripping faucets has been studied in some detail by several researchers. The behavior of a single hole drop producing nozzle with aperture diameter of about fifty microns, or microfaucet, was investigated to determine whether or not chaos is similarly found in this system. Three methods were used to determine the existence of chaos in the microfaucet. The results were ambiguous, and it seemed likely that the experiment was complicated by the presence of noise, possibly due to mechanical vibrations. Mass flow rates obtained with the Phase/Doppler measurement system were checked for consistancy with calibrated flow rates for the system with good results. The evaluation of the theory of Li and Tankin predicting drop size distributions and velocity distributions was considered but rendered impossible by experimental complications.

I. INTRODUCTION

The chaotic aspects of a dripping faucet system were examined in some detail by Shaw, et. al. [1,2] and Calahan, et. al. [3]. They found that at low fluid flow rates drops fall from a faucet aperture periodically, and that with increasing flow rate a series of period doublings are seen culminating with the appearance of chaos.

In work with spray nozzles Tankin and Li developed an entropy and conservation law based theory predicting drop size distributions and velocity distributions [4,5]. This was tested using a commercial spray nozzle and a Phase/Doppler measurement system manufactured by Aerometrics [6]. Overall agreement was determined to be quite good, but their results were plagued by significant discrepancies between the mass flow calculated by the Phase/Doppler system and that measured in calibrating the nozzle.

As chaos has strong roots in entropy, and as the work of Tankin and Li is based on entropy, it was expected that their theory should be able to predict the drop distributions for a single hole drop producing nozzle with small aperture diameter that generated a single stream of drops with diameters of 50 to 300 microns (a microfaucet). The microfaucet system should thus provide a simplest case scenario to evaluate both the mass flow rate measured by the Phase/Doppler and the drop distribution predictions of Li and Tankin's theory.

II. OBJECTIVES

My work this summer was concerned with the investigation of various aspects of a microfaucet with an aperture diameter of about fifty microns. It was expected that this would reproduce at least some of the characteristics and in particular the chaotic aspects of the systems studied by Shaw and Calahan. Visual inspection of the behavior of drops produced by the nozzle seemed to verify this, as at lower flow rates a periodic regime was observed that was replaced by aperiodicity as the flow rate was increased. The first objective in the analysis of the microfaucet was thus the verification or disproving of the existence of chaos in system. Second and third

objectives were the investigation of the consistency of the mass flow rate measured by the Phase/Doppler with a calibration value and the evaluation of the drop prediction theory of Li and Tankin.

Figures 1 and 2 show the drop nozzle and experimental set up used.

III.a. PHASE SPACE ANALYSIS (DETERMINATION OF CHAOS)

Several methods were employed to determine the existence or nonexistence of chaos in the microfaucet system, the first being the examination of two and three dimensional plots of the times separating adjacent drops in the drop stream. These phase space plots were expected to be the most important indicator of chaotic or non-chaotic behavior in the system, and were obtained through a phase space reconstruction technique described by Crutchfield, et. al. [7] The sequence of drop separation times t1, t2,... was used to make an N-dimensional representation of the data by grouping the times into N-tuples, (t1, t2, ..., tN), (tN+1, ..., t2N), ... and then plotting these points in N-space. For periodic drop rates the resulting graph should clearly consist of only one point; after period doubling two points should appear, and so on. Aperiodic data should appear as a scatterplot in the absence of chaos and should have some distinguishable shape if it is indeed chaotic.

Plots of drop diameters against drop velocities were also examined, as were plots of diameters, velocities and drop separation times against elapsed time.

III.b. RESULTS OF PHASE SPACE ANALYSIS

Figures 3-6 show the results of the phase space reconstruction plots for four representative data sets obtained from the microfaucet system; Figures 7-10 show plots of drop separation times against elapsed time for the same data. The periodic data (Fig. 2, 7) appeared precisely as expected, but this was not the case for the other data sets. It was thought at first that the so called "semi-periodic" and "multiply-periodic" (Fig. 3, 8; 4, 9) data might be evidence of some stage of period doubling in the system, but as the additional frequencies both fail to alternate with the original

frequency and are not the right frequencies to be period doubled this possibility was discounted. It seemed more likely that these and other similar data sets were actually essentially periodic, probably with some external noise. The appearance of a large number of drops with near zero separation in the "multiply-periodic" data was and remains the subject of questions of validity and significance. Similar drops were apparent in the aperiodic data sets (see Fig. 5).

The appearance of the phase space plots of the aperiodic data is represented in Fig. 5 and 10. It was observed that as the flow rate through the microfaucet was increased the line(s) of drops with near zero separation became less distinct. At the same time the time separation between the drops decreased, resulting in a migration of points from the outer edge of the wedge of points seen in Fig. 5 to the inner corner; because of this the horizontal and vertical edges of the wedge became more distinct. With the exception of the line of points with near zero separation these plots appeared to be scatterplots; the concentration of points in the midst of the random looking wedge in Fig. 5 was only apparent in that data set and was thought to be a remnant of the periodic flow. In any event the plots of the aperiodic runs fail to reproduce the results of the faucet experiments of Shaw [1] and Calahan [3], and with the exclusion of the bands of points near zero, Fig. 10 (showing drop separation times vs run time) most closely resembles a plot Calahan obtained illustrating noisy data. Some effort was put forth in an attempt to determine if the closely spaced drops had any consistent distinguishing characteristic (eg. high velocity, large diameter, etc.), but none was discovered.

The plots of velocities revealed another peculiarity of the data obtained, namely the existence of a large number of drops in the aperiodic runs with negative (i.e. upwards) velocities. Had the number of points involved been smaller and the diameters of the drops in question been uniformly small, this could have been a feature of the drop break-up mechanism, but as there were a significant number of large (200 micron or larger) diameter drops with these velocities this was impossible. It was also discovered following the acquisition of data that the Phase/Doppler system used

was giving some incorrect diameter information, which to a greater or lesser extent calls into question the validity of the data in general.

Thus this phase of the analysis arrived at few conclusions. The fact that the periodic flows appeared as they should provides some support for the validity of the time data for the other runs. However, the aperiodic flows fail to conclusively indicate the presence of chaos in the system, and due to ambiguities on account of the closely falling drops it is similarly not obvious that its existence is disproved. In any event it seems likely that significant noise exists in the system, perhaps due to vibrations. Due to the small scale and hence potential sensitivity of the system it was also thought possible (though highly unlikely) that the aperiodic data could be indicative of a fourth or higher dimensional chaotic system, probably obscured by noise.

IV.a. LYAPUNOV EXPONENT CALCULATION (DETERMINATION OF CHAOS)

The second approach taken to determine the existence of chaos in the microfaucet system was the calculation of the largest Lyapunov exponent associated with the various data sets collected. Lyapunov exponents measure the divergence of points initially close together in phase space; thus a chaotic system is characterized by a positive exponent while predictable systems have non-positive exponents. The calculation of the Lyapunov exponents was accomplished through the use of computer code formulated by Wolf, et. al. [8].

IV.b. RESULTS OF THE LYAPUNOV EXPONENT CALCULATION

As was expected, the Lyapunov exponents calculated for all of the periodic or near periodic data sets were negative, while those for the aperiodic sets were positive. The values calculated were, however, much larger than the exponents for a number of known chaotic maps. Further, the significance of the positive exponents was not clear. If the aperiodic runs were chaotic a positive exponent would be expected, but if they were merely random (non-chaotic) a positive exponent might still be reasonable because the

unpredictability in the system suggests some form of divergence in phase space. It should also be noted that the accuracy of the results obtained using the computer code on random data is in itself questionable.

Thus the calculation of the Lyapunov exponents proved inconclusive in the determination of chaos in the microfaucet system.

Va. POWER SPECTRUM ANALYSIS (DETERMINATION OF CHAOS)

The final technique used to address the issue of the existence of chaos in the system was the determination of the power spectra for the microfaucet data, with consideration being given to the trends expected for the period doubling route to chaos. For periodic data the spectrum should have a single frequency spike; period doubled data should have two spikes, etc. Chaotic data, characterized by an infinite number of frequencies, should appear as broad band noise above which should project the remnants of the taller spikes from the first couple of frequencies.

V.b. RESULTS OF POWER SPECTRUM ANALYSIS

The power spectra for the periodic and "semi-periodic" data appeared as expected, with frequencies corresponding to the main concentrations of points in the drop separation time plots shown in Fig. 3 and 4. The spectra for the aperiodic data appeared as noise, which was also expected from previous analysis. The "multiply-periodic" runs, however, appeared more interesting: at lower frequencies, spikes in the spectra showed up as expected, but when the region of examination was expanded to look for those points with near zero separation (at frequencies of about 10^5), graphs as that shown in Figure 11 were seen. This result appeared only in the "multiply-periodic" data sets, and while it is difficult to attribute great significance to the oscillations due to their extremely small amplitude, they are at the same time puzzling.

It should be noted that the presence of noise decreases the number of period doublings that one can expect to see as a system moves through period doubling to chaos; thus the possibility exists

that the lack of a period doubled data set may be attributable to the noise that seems evident in the microfaucet system.

VI.a. ANALYSIS OF PHASE/DOPPLER MASS FLOW RATES

The next issue addressed was that of the validity of the Phase/Doppler measured mass flow rate. To test this the drop nozzle was run for approximately 45 minutes and the drop stream collected. During this time several sets of data were taken using the Phase/Doppler equipment. It was then possible to compare the volume flow rate found from the collected fluid with that calculated by the Phase/Doppler, as well as with that calculated from a summation of volumes over all drops counted by the Phase/Doppler. These comparisons were made both including and excluding an internal correction to the number of drops registered by the Phase/Doppler. For the test the drop nozzle was run in its periodic regime, and validation rates of 99% or better were obtained.

VI.b. RESULTS OF MASS FLOW ANALYSIS

The results of these comparisons were quite good. Discrepancies between the hand measured volume flow rate and the Phase/Doppler calculated values were limited to about 15%, and with the inclusion of the indicated correction made by the software this was reduced to about 8%. As diameter varies as the cube root of volume, these discrepancies were indicative of diameter measurement errors of only 2% to 2.5%. This led to the conclusion that there was no significant problem with the numbers calculated by the Phase/Doppler equipment.

VII.a. EVALUATING THE DROP DISTRIBUTION THEORY

Finally, it had been hoped to use the data obtained from the microfaucet to test the drop distribution theory of Tankin and Li, and it was with this in mind that the drop nozzle aperture was chosen to be small. Drops from larger diameter nozzles are seen to oscillate due to surface tension effects following separation in the drop breakup region; as the diameter measurements calculated by the Phase/Doppler equipment are predicated on the assumption of

spherical drops this can result in inaccurate diameter estimates. Although it is possible to avoid this problem by acquiring data further from the drop break up region, this is not desirable as information on small drops that agglomerate with larger ones is lost. Velocity measurements also become more complicated as the effects of air resistance must be accounted for. It was hoped that with the implementation of a small aperture drop nozzle the oscillations of drops leaving the break up region would be reduced sufficiently to allow accurate diameter measurements.

VII.b. RESULTS OF THE THEORY EVALUATION

This phase of analysis remained incomplete, as photographs of the drop stream revealed that even with a 50 micron nozzle aperture drops separated with significant oscillations. Further, as the microfaucet itself appeared not to be characterized by regions of clearly chaotic behavior one of the initial premises for its selection as a good test of the theory was potentially eliminated.

VIII. RECOMMENDATIONS

The continued investigation of the existence of chaos in the microfaucet system merits some thought. A primary consideration is the elimination of external noise (vibration) from the system, by appropriately suspending the drop nozzle set up or basing the experiment on a vibration/noise free support. The results previously obtained should then be checked against those found in this noise free system. It is further expected that the issue of pendant drop separation vs. rod breakup is of significance; the distinction between these two modes of drop formation is illustrated in Figure 12. With smaller drop nozzle apertures, higher flow rates result in a fluid rod that emanates from the nozzle and then breaks up due to instabilities to external influences, as shown in the figure. Since these external influences are likely to be noisy (i.e. essentially random) it is expected that this mode of break up should not result in chaos. Rod breakup was observed in some if not all of the aperiodic data from the microfaucet. On the other hand, pendant drops are formed at the nozzle aperture and it seems likely that this mode of drop formation

results in the periodic drop frequencies observed as well as the period doubling to chaos found by Shaw and Calahan. It does not appear likely that rod breakup should be responsible for the formation of periodic drops and thus the possibility of examining aperiodic flow rates immediately following the periodic flows is one to address in subsequent analysis of the system.

Despite the apparent lack of success in the use of the microfaucet to test the drop distribution theory of Tankin and Li, there were two suggestions for improvements or modifications that might make the system usable. The first of these is the implementation of drop nozzles with smaller diameter apertures, in the hopes that this will sufficiently reduce drop size and hence oscillation so that the Phase/Doppler equipment can be used to obtain reliable diameter data. The second hinges on the observation that in the regions of near periodic flow there was less drop oscillation and additionally that for these flows no very small drops were produced that might agglomerate with larger drops as they fell. Thus in this case it becomes possible to gather data lower in the drop stream where drop oscillations have died out and after accounting for the effects of air resistance possibly compare results with those predicted by the drop distribution theory.

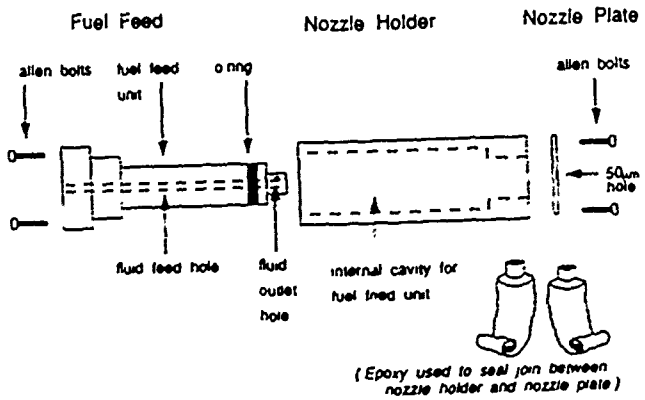

Figure 1.
The Drop Nozzle used in the experiments.

Figure 2. The experimental set up. The Phase/Doppler hardware was connected to the photomultiplier tube, which was set to accept images of the Helium Neon laser beam as it was projected through the drop stream. Not shown are optical elements used to produce the shadowgraph projections.

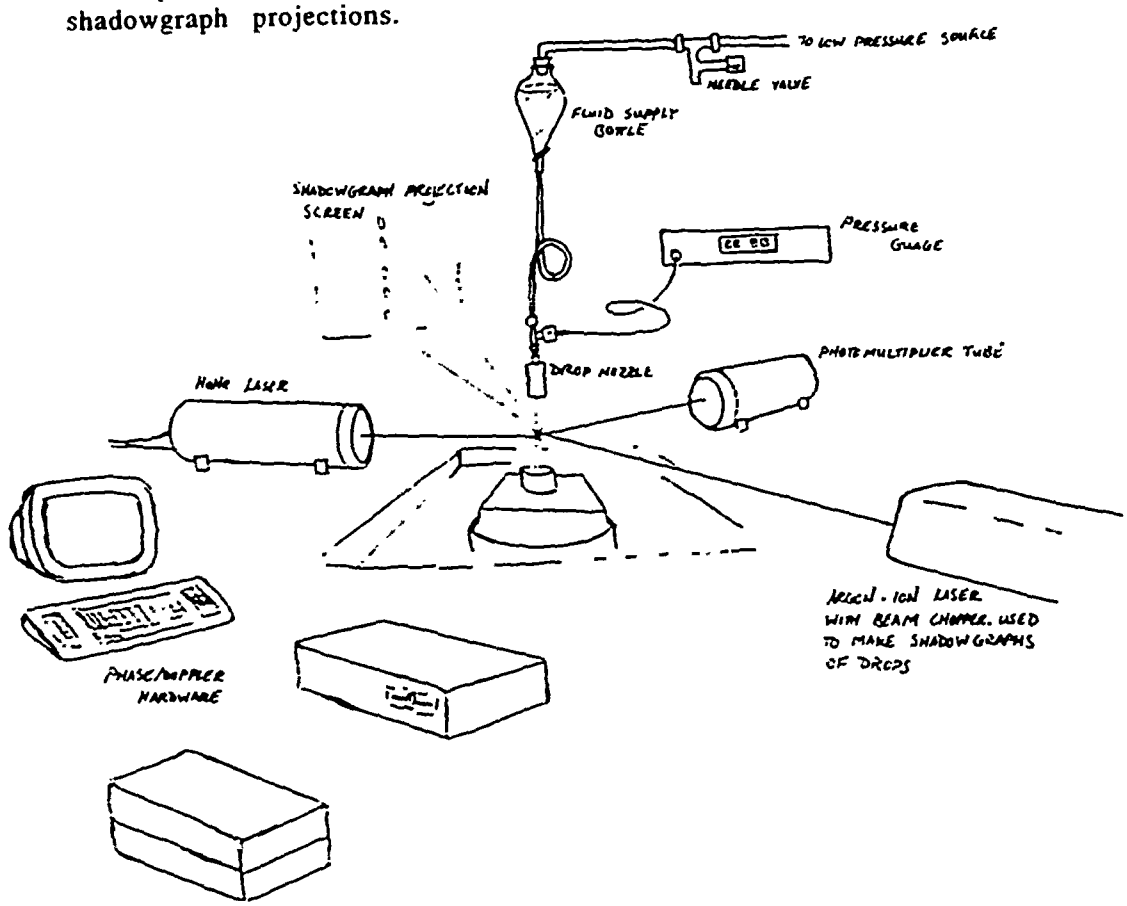

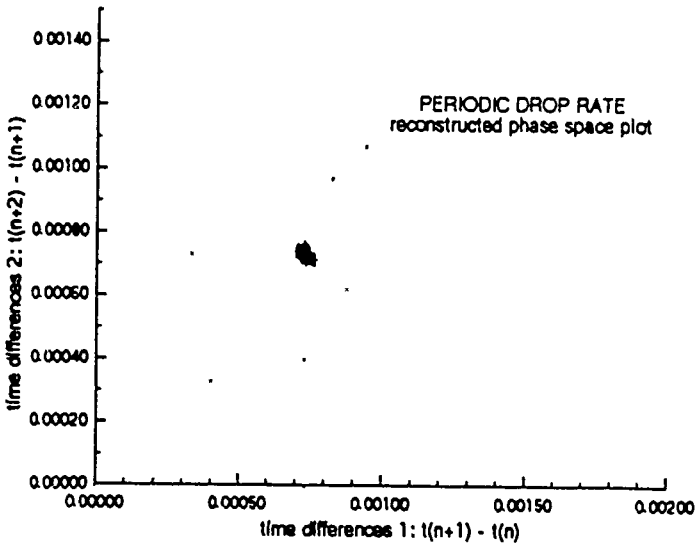

Figure 3. Phase space reconstruction plot of a periodic data set.

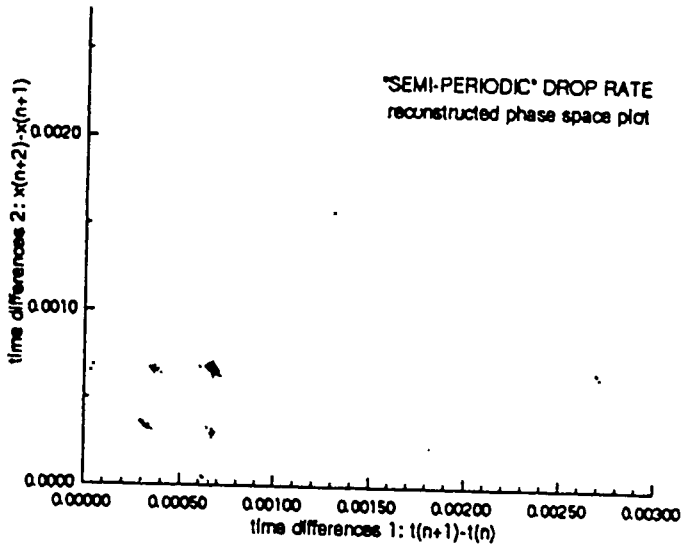

Figure 4. Phase space reconstruction plot of a nearly periodic data set, called "semi - periodic".

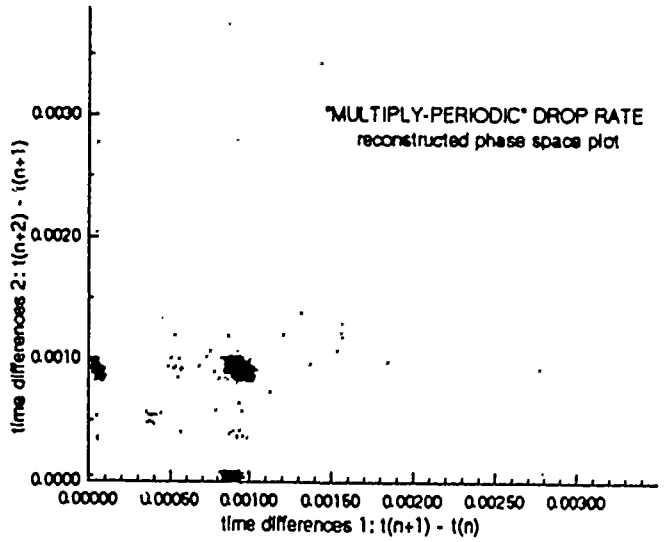

Figure 5. Phase space reconstruction plot of a nearly periodic data set, called "multiply - periodic".

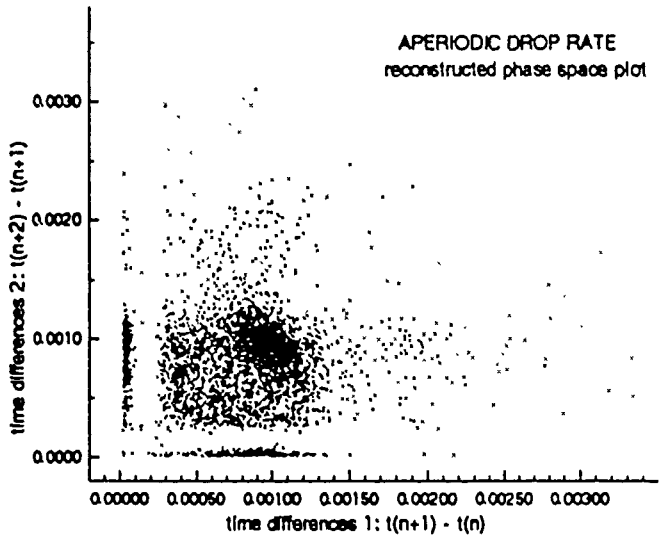

Figure 6. Phase space reconstruction plot of an aperiodic data set.

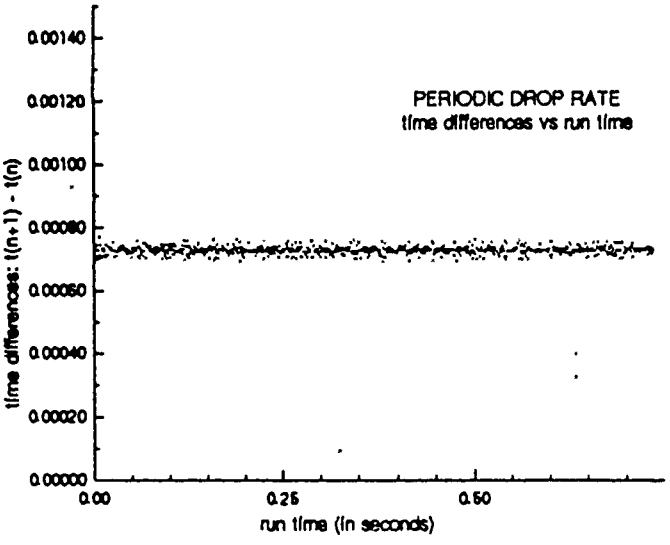

Figure 7. Plot of time differences vs. time for the periodic data set.

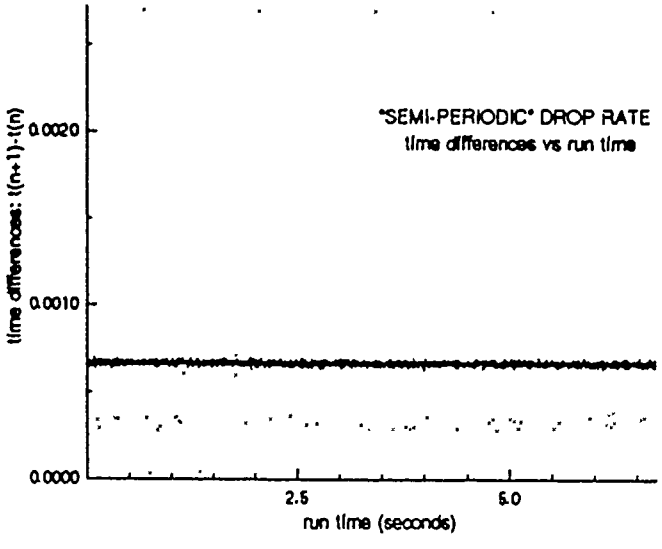

Figure 8. Plot of time differences vs. time for the so called "semi - periodic" data set.

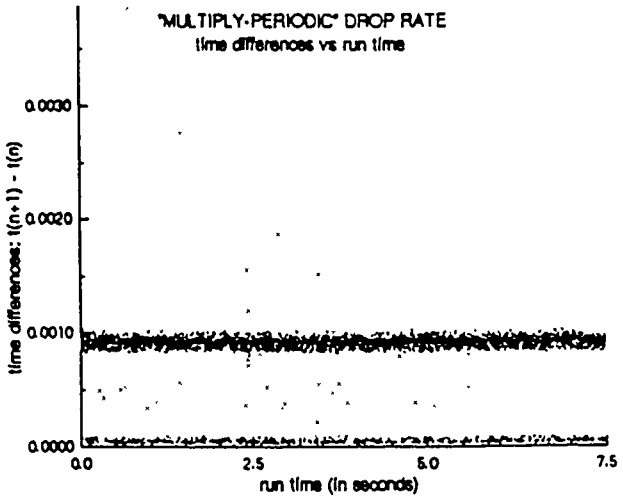

Figure 9.
Plot of time differences vs. time for the so called "multiply - periodic" data set.

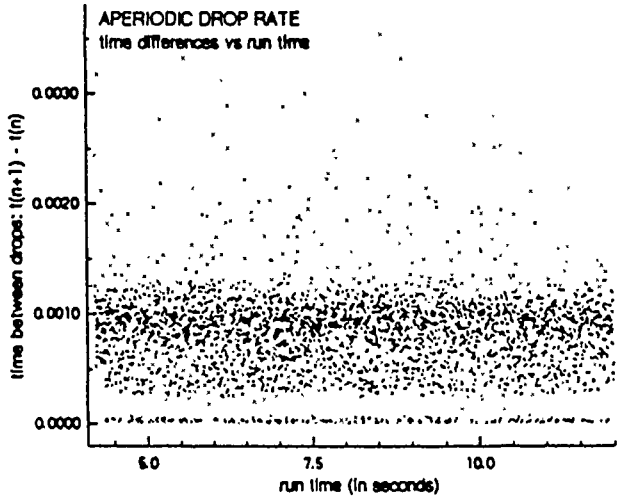

Figure 10.
Plot of time differences vs. time for the aperiodic data set.

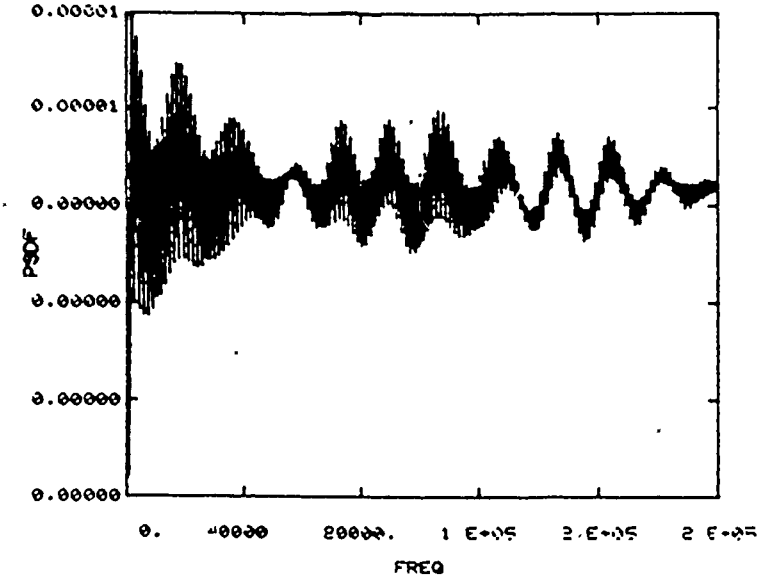

Figure 11.
Power spectrum for the "multiply - periodic" data set.

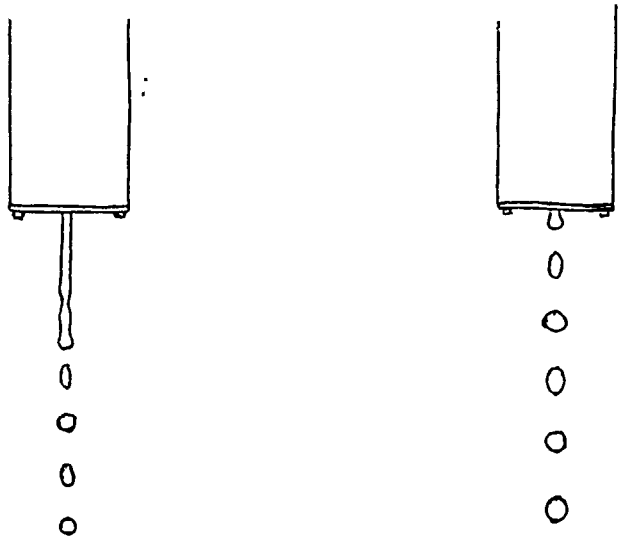

Figure 12. Diagram on left illustrates rod break up; that on the right shows pendant drop break up.

ACKNOWLEDGEMENTS

Thanks are due to the Air Force Office of Scientific Research for sponsorship of this research, and to Universal Energy Systems for the administration of the Graduate Student Research Program.

But a fraction of the work accomplished would have actually been completed were it not for the extensive aid and assistance of those at Wright Patterson Air Force Base with whom I had the privilege and pleasure to work for the summer, in particular Dr. W.M. Roquemore, Dr. T. Jackson, Dr. J. Dressler, Ms. Cindy Obringer, Mr. Gary Switzer, Dr. J. Erdie of the University of Dayton and of course Dr. R. Tankin of Northwestern University.

Thanks to all.

REFERENCES

1. Shaw, Robert, The Dripping Faucet as a Model Chaotic System, Santa Cruz, California, Aerial Press Inc. 1984.

2. Crutchfield, J.P., Farmer, J.D., Packard, N.H., and Shaw, R.S., "Chaos," Scientific American, December 1986, pp. 46-57.

3. Calahan, R.F., Leidecker, H., and Calahan, G.D., "Chaotic Rhythms of a Dripping Faucet," Computers in Physics, July/August 1990, pp. 368-382.

4. Li, X., and Tankin, R., "Droplet Size Distribution: A Derivation of a Nukiyama-Tanasawa Type Distribution Function," Combustion Science and Technology, Volume 56, 1987, pp. 65-76.

5. Li, X., and Tankin, R., "Derivation of Droplet Size Distributions in Sprays Using Information Theory," Combustion Science and Technology, Volume 60, 1988, pp. 345-357.

6. Li, X., Chin, L.P., Tankin, R., Jackson, T., Stutrud, J., and Switzer, G., "Comparison Between Theory and Experiments for Sprays from a Pressure Atomizer, Submitted for Publication.

7. Crutchfield, J.P., Farmer, J.D., Packard, N.H., and Shaw, R.S., "Geometry from a Time Series," Physical Review Letters, September 1, 1980, pp. 712-716.

8. Wolf, Swift, Swinney and Vastano, "Determining Lyapunov Exponents from a Time Series," Physica, Vol16D, 1985, pp. 285-317.

1990 USAF-UES SUMMER FACULTY RESEARCH PROGRAM/

GRADUATE STUDENT RESEARCH PROGRAM

Sponsored by the

AIR FORCE OFFICE OF SCIENTIFIC RESEARCH

Conducted by the Universal Energy Systems, Inc.

FINAL REPORT

AIRCRAFT HVDC POWER SYSTEM - STABILITY ANALYSIS

Prepared by:	K. Sankara Rao, Ph.D. and Allen Olheiser, B. S.
Academic Rank:	Professor
Department and	Electrical and Electronics Engineering Department
University:	North Dakota State University, Fargo, North Dakota
Research Location:	WRDC/POOC1, Wright Patterson Air Force Base
USAF Researcher:	Joe Weimer
Date:	September 7, 1990
Contract Number:	F49620-88-C-0053

Same Report as
Prof. K. Sankara Rao
(Report # 82)

1990 USAF-UES SUMMER FACULTY RESEARCH PROGRAM/

GRADUATE STUDENT RESEARCH PROGRAM

Sponsored by the

AIR FORCE OFFICE OF SCIENTIFIC RESEARCH

Conducted by the

Universal Energy Systems, Inc.

FINAL REPORT

Analysis of Thermal Oxidation of Jet Fuels

Prepared by:	David Shehee
Academic Rank:	Graduate Student
Department and	Chemistry
University	Eastern Kentucky University
Research Location:	WRDC/POSF Wright Patterson AFB Dayton, Ohio 45433
USAF Researcher:	W. M. Roquemore
DATE:	7 Nov 90
Contract No:	F49620-88-C-0053

Analysis of Thermal Oxidation of Jet Fuels

by

David Shehee

ABSTRACT

Thermal oxidation products from jet fuels will be formed in the presence of fuel and oxygen at elevated temperatures. Development of fuels that will not form solid residues depends on the development of a method to analyze the rate of oxidation of fuels. Gravimetric determination of fuel residues was imprecise and very time consuming. Gas Chromatography-Mass Spectrometry of oxidation products yields a great deal of fundamental information but is too specific to be used as a rapid method for determining the rate of oxygen. Fourier Transform Infrared Spectroscopy is not specific and gives integrated signals for classes of oxygen products that will give rapid analytical results for rates of oxygen. Preliminary results indicate that the Fourier Transform Infrared Spectroscopy method should be developed as an analytical tool to determine oxygen rates for fuel.

Acknowledgements

I would like to thank the Air Force Systems Command and the Air Force Office of Scientific Research for our research this summer. I would also like to thank Universal Energy Systems for the administrative and directional help they provided.

This summer was a rewarding experience for several different reasons. Dr. Schulz was especially helpful and provided an enjoyable working atmosphere as well as support and encouragement. In addition I would like to thank four employees of the Air Force, including Steve Anderson, Ellen Steward, Mel Roquemore and Ed Pitzer for their guidance and assistance. Lastly, I would like to thank Dan Dannichek for his assistance helping us get situated.

I. INTRODUCTION:

I am a graduate student at Eastern Kentucky University working toward an M. S. degree in Chemistry under the direction of Dr. William D. Schulz. My B. S. degree (Chemistry major) is from Berea College, Berea, Ky. Dr. Schulz was already doing research on thermal oxidation of jet fuels[1] when I started my research program and I decided to pursue research on analysis of thermal oxidation products from jet fuel.

Concern for the oxidative stability of jet fuels is evident in the literature. A 1974 Russian article[2] lists 122 references. A 1986 review by Taylor and Frankenfeld[3] contains 55 "representative, rather than all inclusive" references. Aircraft malfunction caused by fuel oxidation includes effects ranging from synthetic seal and O-ring failure caused by hydroperoxides[4] to clogged injection nozzles and fouled heat exchanger surfaces[5] due to surface deposits of gums and particulates. The fuel deterioration problem is very complex. Although hydroperoxide formation is certainly the first step of the oxidation process, different mechanistic steps can become more important to product formation at different temperatures. As temperatures increase pyrolytic reactions begin to contribute to deterioration and finally predominate at about 500°C.[6] The composition of the fuel is, of course, the determining stability factor, but it is also important for solvent properties in gum and particulate formation from oxidized species.

The chemistry of alkane (parafin) oxidation is well defined[4] as is that of less stable species such as cycloalkanes and tetralins.[1] If oxygen is present, even pure aliphatic compounds will oxidize to form insoluble species at temperatures as low as 100°C. The implication of this is, that regardless of fuel quality, thermal oxidative stability in air over the 100°C-400°C range can only be improved by use of antioxidants, surface deactivators, anticoagulants and other additives.

In order to test the effectiveness of fuel additives, it is necessary to use a standardized thermal stress test and uniform fuel samples. Dr. Schulz had developed a simple, inexpensive flask test for thermal oxidation and a surrogate JP-8 fuel[1] in previous work. The flask test is very similar in principle to the British flask test[7] for thermal oxidation and seems well suited to both the study of thermal oxidation and to the development of methods of analysis of thermal oxidation. Because I had experience with the surrogate and the flask test, I was chosen to work at the WRDC/POSF laboratory on the thermal oxidation and additive problem.

II. OBJECTIVES OF THE RESEARCH EFFORT:

The objectives were twofold. The principle objective was to develop a rapid, reliable and inexpensive method of analysis for the extent of oxidation of thermally stressed fuel. The secondary objective was to use the analytical method to measure the kinetics of thermal oxidation for the surrogate JP-8 as a "baseline" and then to measure oxidation kinetics for the surrogate with selected additives.

III. Analysis of extent of oxidation of fuels.

a. Filtration.

Oxidation products are frequently measured by ASTM D-2274. This test involves filtration of solids and classification of solid as "gums" or "residues" depending upon solubility in specified solvents. We thought to increase the speed and reliability of this test by the use of state-of-the-art filtration. "Anotop™ 25 plus" filter cartridges, 25mM., 0.2mM inorganic membrane, with a glass fiber prefilter gave good results in preliminary tests and blank tests. When we attempted to filter and weigh real oxidation products, results were at first encouraging, but extensive experimentation showed that we could not achieve reliable constant weights for the filters plus fuel residues when dripping with a stream of warm nitrogen. Since this was the only drying method usable with plastic cartridge type filters we abandoned the method.

b. GC-MS Analysis of Oxidation Products.

We obtained sufficient concentration and isolation of oxidation products from fuels by the use of silica gel solid phase extraction cartridges (Supelco, Inc., Bellefonte, Pa.) to get gas chromatographic separation, and mass spectrometric identification of the products. The products identified included a very wide range of alcohols, aldehydes and ketones, as well as a small concentration of alkenes and some non-volitile compounds. The identification of these products is fundamental to the study of gum and residue formation from fuels and vital in the explanation of solid formation but it is so specific that it is not easy to compare rates of oxidations of different fuels and this is not a rapid method to determine oxidation rates on a routine basis.

c. Fourier transform infrared spectroscopy of oxidation products

Although may studies of jet fuel oxidation are aimed at solid products, the formation of the solids generally requires relatively long time periods. It is our feeling that the tendency of a fuel to form solid products can be determined from the formation of precursor oxidation products, such as alcohols and aldehydes, in a fairly short time. Fourier transform infrared (FTIR) analysis provides a means of determining the amount of such products formed from the integration of absorbances caused by O - H and C = O stretching. The integration gives a quantitative measure of compound group (alcohol, carbonyl) rather than specific compounds such as GC-

MS. F.T.I.R. is also amenable to automatable programed analysis of reaction with accessories such as attemated total reflectance (ATR) flow cells or in situ ATR probes coupled to the spectrophotometer by fiber optics.

We have done preliminary experiments with FTIR, using fixed path length cells and the results are very encouraging. Our initial experiments were based on comparison of oxidation products at hour or more intervals and we observed dramatic increase in the O - H absorbance at first and the decrease in the O - H absorbance and an increase in the C = O absorbance.

Our data is not comprehensive enough to obtain reaction rate at this time but we believe that this method, used with more rapid sampling and more sophisticated samples cells can be developed to give oxidation rates very quickly and with high precision. Such rates can then be used to judge either fuel quality or the effectiveness of antioxidants.

Recommendations

Attenuated total reflectance flow cells and deep immersion probes for FTIR are commercially available. We recommend that the FTIR analysis of oxidation products be continued, possibly at first with flow cell, because of lower cost, and ultimately with an automated sampling program utilizing a deep immersion probe.

We also recommend that the study of the mechanism of the oxidation process by GC-MS analysis of oxidation products be continued. The information gained by this process, enhanced by information on the nature of solid deposits obtained by pyrolysis-GC-MS will ultimately produce knowledge of which chemical reactions must be blocked to prevent solids formation from the thermal oxidation of jet fuels.

REFERENCES

(1) Schulz, W. D., "Oxidative Thermal Degradation Studies of a Surrogate JP-8 with a Modified Thermal Precipitation Apparatus" Final Report; Contract F49620-88-C-0053, WRDC/POSF, W.P.A.F.B., August 1989.

(2) Bol'shakov, G. F., "The Physico-Chemical Principles of the Formation of Deposits in Jet-Fuels," FTD-MT-24-416-74 Translation, April 1974

(3) Taylor, W. F., and Frankenfeld, J. W., "Chemistry and Mechanism of Distallate Fuel Stability," Proceeding 2nd International Conference on Long Term Storage Stabilities of Liquid Fuels, S.W.R.I., San Antonio, Texas. Vol. 2, pp. 496-511

(4) Fodor, G. E., Naegel, D. W. and Kohl, K. B., "Peroxide Formation in Jet Fuels," Energy and Fuels, Vol. 2, pp. 729-734 (1988)

(5) Reddy, K. T., and Cernansky, N. P., J. Propulsion. Vol. 5, No. 1, pp. 6-13, Jan-Feb 1989

(6) Hazlett, R. N., Hall, J. N. and Matson, M., Ind. Eng. Chem. Prod. Res. Dev. Vol. 16, No. 2, pp. 171-177 (1977)

(7) Kendall, D. R., Clark, R. H. and Stevenson, P. A., "The Influence of Polar Compounds on the Stability of Jet Fuel." Proceeding 2nd International Conference on Long Term Storage Stabilities of Liquid Fuels, S.W.R.I., San Antonio, Texas. Vol. 2, pp. 694-705

1990 USAF-UES SUMMER FACULTY RESEARCH PROGRAM/

GRADUATE STUDENT RESEARCH PROGRAM

Sponsored by the

AIR FORCE OFFICE OF SCIENTIFIC RESEARCH

Conducted by the

Universal Energy Systems, Inc.,

FINAL REPORT

EFFECT OF EVAPORATION ON THE DRIVING CAPILLARY PRESSURE IN CAPILLARY PUMPED AEROSPACE THERMAL MANAGEMENT SYSTEMS

Prepared by:	Kevin P. Hallinan, Ph.D. / David Welter
Academic Rank:	Assistant Professor / Graduate Student
Department and University:	Mechanical and Aerospace Engineering University of Dayton
Research Location:	Aero Propulsion Laboratory Wright-Patterson AFB Wright-Patterson AFB, OH 45433
USAF Researcher:	Michael Morgan
Contract No:	F49620-85-C-0013

Same Report as
Prof. Kevin Hallinan
(Report # 80)

A Computer Simulation of Thermionic Convertor Performance of Tungsten(110) and Rhenium(0001) Cesium Diminiodes

by

Timothy Joseph Young

ABSTRACT

A one-dimensional, time dependant computer simulation of Thermionic Energy Conversion (TEC) performance was evaluated. The output of the TEC simulation, in the form of current density versus voltage (J-V) curves, was compared to experimentally generated output from preferentially oriented, single crystalline tungsten, W(110), and rhenium, Re(0001), emitters with niobium collectors in cesium diminiodes.

The TEC computer simulation code calculates the output voltage corresponding to an operational current density. Emitter, collector, and cesium reservoir temperatures, electrode spacing, and material parameters are input to characterize the model. A batch-driven, DOS level loop and several auxiliary FORTRAN programs control the main TEC programs.

For the diminiode computer simulations it was found that the effective bare work functions must be varied to allow the short-circuit current densities to approximate those of the experimental data. J-V shapes, Boltzmann slopes, saturation features, and open-circuit voltages were then compared for similarities. Of all simulations, only seven W(110) cases and one Re(0001) case displayed good comparative results with the experimental data.

USAF-UES SUMMER FACULTY RESEARCH PROGRAM/

GRADUATE STUDENT RESEARCH PROGRAM

Sponsored by the

AIR FORCE OFFICE OF SCIENTIFIC RESEARCH

Conducted by the

Universal Energy Systems, Inc.

FINAL REPORT

A Computer Simulation of Thermionic Convertor Performance of Tungsten(110) and Rhenium(0001) Cesium Diminiodes

Prepared by:	Timothy Joseph Young
Academic Rank:	Graduate Student
Department and	Department of Mechanical Engineering and Aerospace Sciences
University:	University of Central Florida
Research Location:	Wright Research and Development Center
	Thermionics Laboratory / POOC-2
	Wright-Patterson AFB, Dayton, Ohio 45433
USAF Researcher:	Dr. M.L. Ramalingam
Date:	30 September 1990
Contract No.:	F49620-88-C-0053

I. INTRODUCTION

Thermionic energy conversion (TEC) is a method for converting heat directly into electrical energy through thermionic electron emission. The most basic thermionic convertor would consist of an emitter connected to a heat source and a collector connected to a heat sink separated by an interelectrode space with leads connecting these electrodes to an electrical load, and a vacuum enclosure. The interelectrode space is generally filled with a suitable rarefied vapor. The temperature difference between the electrodes provides the potential for electron flow through the load.

Future space power applications require reliable and efficient electrical generation systems. Thermionic convertors are simple, small volume, light weight, modular, and have no moving parts. The high temperature operation and high output power density of TEC has applications in nuclear electric propulsion and cycle topping in addition to solar and radioisotopic power generation.

The Thermionics Laboratory of the Aero Propulsion and Power Laboratory, Wright Research and Development Center at Wright-Patterson Air Force Base is concerned with many areas of thermionics, including the experimental and computer simulated characterization of TEC. For all thermionic diode uses, effective materials and operating conditions are essential. But the development of improved vapor convertors means extensive testing of promising electrode materials operating in various ranges of temperatures and spacings. An effective TEC computer simulation would allow the performance characteristics of various diode models to be evaluated prior to costly and time consuming fabrication and testing.

II. OBJECTIVES OF THE RESEARCH EFFORT

TEC must produce higher output power densities at lower operating temperatures to further the lifetime of the convertor components. In the performance mapping of thermionic convertors, computerized data acquisition has been used to record current density versus voltage (J-V) data. But as convertor conditions change and as electrodes yield better performance the range of operating conditions for thermionic systems becomes broader. Computer TEC simulation would allow untested combinations of TEC parameters to be evaluated with promising models cataloged for further examination.

My assignment as a participant in the 1990 Graduate Student Research Program (GSRP) was to determine if the Georgia Institute of Technology TEC Code Version 1.1 would accurately calculate the J-V characteristics of a one-dimensional cesium vapor thermionic convertor. The code, in previous versions, had been used by Main[1] and VanDam and Ramalingam[2] for TEC simulation. During my 1990 GSRP, simulations were performed to model cesium vapor filled diminiodes with W(110) and Re(0001) emitter electrodes and polycrystalline niobium collectors.

The TEC code was found to be very sensitive to the temperature (pressure) of the cesium reservoir and to the product of the cesium pressure and the interelectrode spacing. This sensitivity limited the number of experimental cases that could be modelled using the code.

III. DIMINIODE DESCRIPTION AND EXPERIMENTAL PROCEDURE

Diminiodes are fixed- or variable-gap cesium vapor filled thermionic diodes. They employ planar miniature emitters and guarded collectors. Diminiodes, from two (di) miniature (mini) electrodes (odes), allow the thermionic evaluation of small pieces of rare solids or specimens grown from single crystals. Relative to conventional research diodes, the advantages of the diminiode are simplicity, smallness, precision, ease of fabrication, ruggedness, and parts interchangeability.

As Figure 3.1 shows, the circular electrodes are separated by an interelectrode gap containing cesium vapor[3]. The diameter of the emitter, collector, and collector guard are 0.635, 0.457, and 0.635 centimeters respectively. The surfaces of the electrodes were lapped and polished smooth and flat to 10^{-5} millimeter. This was followed by a cleaning and degassing prior to attachment to the diode.

Blackbody holes and thermocouples allow doubly measured temperatures for the emitter, collector, and cesium reservoir. The emitter is heated through electron bombardment while cooling coils control the temperature of the collector and cesium reservoir assemblies. The temperature of the external tungsten-lined hohlraum is related to that of the blackbody hole in the emitter near its surface. The collector and cesium reservoir temperatures are measured using sheathed chromel-alumel thermocouples. The maximum uncertainty associated with the observed temperatures is 10 K. This includes

the accuracy of the NIST calibrated tungsten lamp, the optical pyrometer, and the effective emissivity of the blackbody hohlraums.

The experimental J-V characteristics of the diminiodes were obtained by Tsao[4]. The current developed in the diodes was measured by the voltage drop across a 0.01 Ω, low inductance, precision shunt. The area of the collector face determined the current density. The output voltage was measured using the sheaths of the emitter and collector as potential probes. The table below lists the ranges of temperatures for which experimental J-V characteristics were obtained for the diminiodes.

	W(110)	Re(0001)
T_E	1700-1900 K	1700-1900 K
T_C	700-1000 K	650-1000 K
T_R	500-800 K	450-850 K

IV. TEC SIMULATION CODE DESCRIPTION AND OPERATION

The Georgia Tech TEC simulation codes use time dependant analysis of plasma parameters to calculate the thermionic output of diode models. The purpose of the programs is to estimate convertor performance and J-V characteristics, to reproduce trends due to changes in electrode temperatures and materials, cesium temperature (pressure), and interelectrode spacing, and to provide further understanding of the mechanisms which determine convertor performance.

The TEC initialization program first prompts the user for the emitter temperature (T_E), collector temperature (T_C), cesium pressure (P) or reservoir temperature (T_R), interelectrode gap thickness (d), the effective bare emitter work function (ϕ_o), and the operating current density (J). The cesiated electrode work functions (ϕ_E and ϕ_C) are then calculated for these conditions. The cesium pressure or temperature is calculated from an equation from Hatsopoulus and Gyftopoulos[5]. Several program operational and output variables are then input along with the end time. The end time determines whether the program will calculate output voltages that have converged to steady-state values at the operating current density.

The actual TEC-plasma computations are then initiated. The TEC calculating program begins by computing, at the operational current density, a value of the output voltage at time zero. The program then marches through time calculating revised output voltages at each step until it reaches the end time. The operational current density and end time output voltage together provide a discrete point in the simulation J-V curve.

At the Wright-Patterson Thermionics Laboratory, auxiliary FORTRAN and DOS-level Batch programs were created to allow the calculation of output voltages across a user specified range of operational current densities. This allows J-V simulation data to be tabulated in an output file in a form ready for plotting. On its own, the Georgia Tech TEC program has no provision for incrementing the operational current density after an output voltage has been calculated. The TEC program calculates a J-V pair and then terminates.

V. WORK FUNCTION MODELS

This latest version of the TEC code utilizes FORTRAN functions from Rasor Associates, Inc. to calculate the cesiated emitter and collector work functions. The theoretical basis for these calculations was developed by Rasor and Warner[6].

For the computer simulation the cesiated emitter work function is dependant upon the emitter temperature, the cesium reservoir temperature, and the effective bare emitter work function of the emitter surface. The effective bare work function (ϕ_o) is not the same as the bare work function (ϕ) measured in a vacuum. Theoretically ϕ_o is related to the experimentally obtained saturation current density J_S and T_E (in amp/cm^2 and degrees K, respectively) through the equation below[7]:

$$\phi_o = \frac{T_E}{11,606} Ln\left[\frac{120\ T_E^2}{J_S}\right] \quad eV \qquad (1)$$

From the Rasor and Warner theory the cesiated work function is calculated from an equation of the form $\phi_E = \phi_o - \Delta\phi$. The program calculates and refines a value for $\Delta\phi$ and uses a recommended average value of ϕ_o to find ϕ_E. The recommended average value of ϕ_o for several materials is given in the table below[8]:

EFFECTIVE BARE WORK FUNCTION (eV)	MATERIAL
4.78	Tungsten
4.88	Tungsten(110)
5.16	CVD Rhenium
5.56	Rhenium(0001)

The value of ϕ_E for a given ϕ_O, if plotted versus T_E/T_R, produces S-shaped Rasor curves. The calculated values for ϕ_E (Figures 5.1 and 5.2) show the same general relationship as experimental results, namely that:

$$\phi_E \approx f\left(\frac{T_E}{T_R}\right) \qquad (2)$$

This theory for calculating ϕ_E is inaccurate, however, for simultaneously high ϕ_O and low values of T_E/T_R (such as $\phi_O \geq 5.5$ and $T_E/T_R \leq 2.5$).

The work function for the polycrystalline niobium collector is determined from the following empirical relation:

$$\phi_C = 4.0392 + \left(\frac{T_C}{T_R}\right)\left[0.7595\left(\frac{T_C}{T_R}\right) - 2.7653\right] \qquad (3)$$

This formulation is good only for the range of $1.0 < T_C/T_R < 2.3$ (Figure 5.3). The output voltage is equal to the difference between ϕ_E and ϕ_C if there is no arc drop nor lead losses. As a result, it is beneficial to have a lower collector work function even though this would seem to increase the back emission.

VI. RESULTS AND DISCUSSION

In order to verify the convergence of the output voltage calculations, a family of time dependant J-V curves was produced. Figure 6.1 shows the transient nature of the TEC code. At an end time of 500 or less the space-charge limited, Boltzmann, and saturation regions are all present. At higher end times the program breaks down and will

not calculate in the space-charge-limited regime. For the W(110) and Re(0001) diminiode simulations end times of 500 or greater were used to provide non-transient output voltages. For 500 iterations or less, the computer simulation shows exaggerated current densities. This is a consequence of the inaccurate evaluations of the ion/electron collision cross-sections. However, the program is able to predict the onset of true ignition after the solutions to the non-linear equations have converged.

Of the thirty-nine W(110) and forty-one Re(0001) experimentally measured diminiode J-V data sets, only thirteen W(110) and one Re(0001) computer simulations were produced. Several experiments did not produce positive power and were not simulated as we are not interested in energy expended on the diode. The TEC-plasma calculation portion of the code is very sensitive to the cesium reservoir temperature (pressure) and to the product of the cesium pressure and the interelectrode spacing (P•d). The experimental data had T_R in the range of 450-850 K. The TEC program, however, only calculated for T_R = 550 or 600 K where the cesium pressure was calculated to be 0.96 and 3.55 torr respectively. The reason for using this restricted range of cesium pressure is that all diodes built so far have exhibited peak performance in the P•d product range of 15 to 25 mil•torr. With interelectrode spacings of 0.23 mm (~9 mil) and 0.48 mm (~19 mil) for the W(110) and Re(0001) diodes, the P•d product ranged from about eight to sixty-eight mil•torr.

Figures 6.2-14 compare W(110) diminiode experimental data with two separate simulations. The original simulation used the recommended ϕ_O value of 4.88 eV. By manipulating the value of ϕ_O the second simulation J-V curve was made to have approximately the same short-circuit current density as the experimental data. In Figures 6.2-8 the second simulations with revised ϕ_O's have better comparative Boltzmann and saturation mode characteristics than those in Figures 6.9-14. As can be seen in these figures, the simulation with the lower ϕ_E appears to be closer to the experimental output. In essence, this is a direct consequence of the increase in arc drop that may have resulted from excessive evaporation of the emitter surface or inadequate coverage of cesium on both the emitter and collector surfaces. Either way, there is a tendency for the emitter surface to assume a lower ϕ_E. The best simulations seem to occur at high ϕ_E and

low ϕ_C (as shown in Figure 6.6) where the output voltage is a maximum. This indicates the inaccuracies that are confronted by the code at low voltage output levels.

Figure 6.9 is a classic case where the low ϕ_E simulates the space-charge limited operation as well as the initial Boltzmann slope very well but predicts early saturation. The higher ϕ_E simulates the experimental results well at higher current densities but the simulation is poor at the foot of the curve. Thus we see that the transition region between space-charge limited mode and ignited mode needs additional consideration in the computer model.

Figure 6.15 compares the experimental and simulated J-V curves for a Re(0001) diminiode. As with the W(110) comparison, the first simulation uses the recommended ϕ_o value for Re(0001) of 5.56 eV. The second uses a revised value to match short-circuit current densities.

In the simulation of the W(110) and Re(0001) diminiodes, however, it was found that the recommended ϕ_o values did not allow the program to effectively simulate the characteristics of the experimental data. For the relatively good W(110) simulations (Figures 6.2-8), the mean and sample standard deviation of the ϕ_o's was 4.72 and 0.23 eV, respectively. This compares favorably with thermionic emission work function data from Fomenko for W(110) in which ϕ ranged from 4.58 to 5.33 eV[9]. Although ϕ and ϕ_o are not the same, their values are approximately equivalent.

There are several reasons why the diminiode emitter work function may not be equal to its tabulated value, necessitating different ϕ_o's for effective simulation. The emitter surface may have become coated with an oxide of cesium or niobium or it may have been depleted. Oxygen on the emitter surface could either raise of lower the work function depending upon where it settles. If the cesium adsorption coverage is reduced by surface contamination the capability to ionize the plasma is also reduced. This effect would increase over time as the adsorbed surface area is decreased. Emitter and collector surface evaporation could also affect the values of the work functions.

VII. RECOMMENDATIONS

Future direction for thermionic energy conversion points to lower operating temperatures for extended diode lifetimes. The TEC programs provide the researcher with

a tool for improving the understanding of the ignited cesium vapor diode by investigating previously untested operating combinations. The computer simulated TEC current density and voltage output was compared to experimental diminiode data. This reexamination indicated the variance in bare emitter work function necessary to approximately match short-circuit current densities. Even this matching did not, however, guarantee that the other salient features of the J-V curves (Boltzmann slope, saturation characteristics, space-charge-limited mode features) would be similar between the simulation and experiment.

Areas of improvement for the Version 1.1 of the Georgia Tech TEC simulation code include:

1) error checking to eliminate the frequent abrupt terminations of the code requiring rebooting of the computer,
2) better connection between the Boltzmann and the saturation region models to eliminate "knee's" in the J-V curves,
3) calculations of the ion/electron collision cross-section,
4) evaluation of electron temperatures and densities and ion temperatures and densities,
5) recompilation of the code for 32-bit 80386 PC, 68030 Mac, or mainframe computers for faster execution time, and
6) the incorporation into the main TEC code the functions performed by the auxiliary FORTRAN and Batch programs to further streamline the operation of the code.

ACKNOWLEDGMENTS

I would like to thank the Air Force Office of Scientific Research and the Air Force Systems Command for their support and sponsorship of this research effort. I would also like to thank Universal Energy Systems for their assistance in this program.

I would especially like to thank those people at the Thermionics Laboratory who guided and assisted me. Drs. Mysore L. Ramalingam and Bang-Hung Tsao of Universal Energy Systems provided both technical and philosophical support. Without Brian Donovan the computers and my research would not have been "up and running." The excitement of J. Steven Cloyd for Static Energy Conversion technologies further encouraged me. Overall, the people and environment of the Wright Research and Development Center's Aero Propulsion and Power Laboratory provided me with a rewarding experience.

REFERENCES

1. Main, G.L. "Emitter Sheath Effects On Thermionic Convertor Performance." Ph.D. dissertation, Princeton University, 1984.

2. VanDam, S.A. and M.L. Ramalingam. "Application of a One-Dimensional TEC Code to the Characterization of a Lanthanum-Hexaboride Diode," 25th Proc. Intersociety Energy Conversion Engineering Conference, Vol.2, 1990: 346-351.

3. Morris, J.F., A.L. Smith, and E.J. Manista. "Thermionic Performance of a Variable-Gap Cesium Diminiode With a 110-Single-Crystalline-Tungsten Emitter and a Polycrystalline-Niobium Collector." NASA Technical Memorandum X-2953, 1974.

4. Tsao, B.H. "High Temperature Thermionics." Ph.D. dissertation, Arizona State University, 1989.

5. Hatsopoulus, G.N. and E.P. Gyftopoulos. Thermionic Energy Conversion. Vol.I: Processes and Devices. Cambridge, Mass.: MIT Press, 1973.

6. Rasor, N.S. and C. Warner. "Correlation of Emission Processes for Adsorbed Alkali Films on Metal Surfaces," Journal of Applied Physics, Vol.35, 1964: 2589-2600.

7. Hatsopoulus, G.N. and E.P. Gyftopoulos. Thermionic Energy Conversion. Vol.II: Theory, Technology, and Application. Cambridge, Mass.: MIT Press, 1979.

8. McVey, J.B. "TECMDL Ignited Mode Planar Thermionic Convertor Computer Model." Software users' manual. Rasor Associates, Inc., Aug. 1988.

9. Fomenko, V.S. Handbook of Thermionic Properties. Ed. G.V. Samsomov. New York: Plenum Press Data Division, 1966.

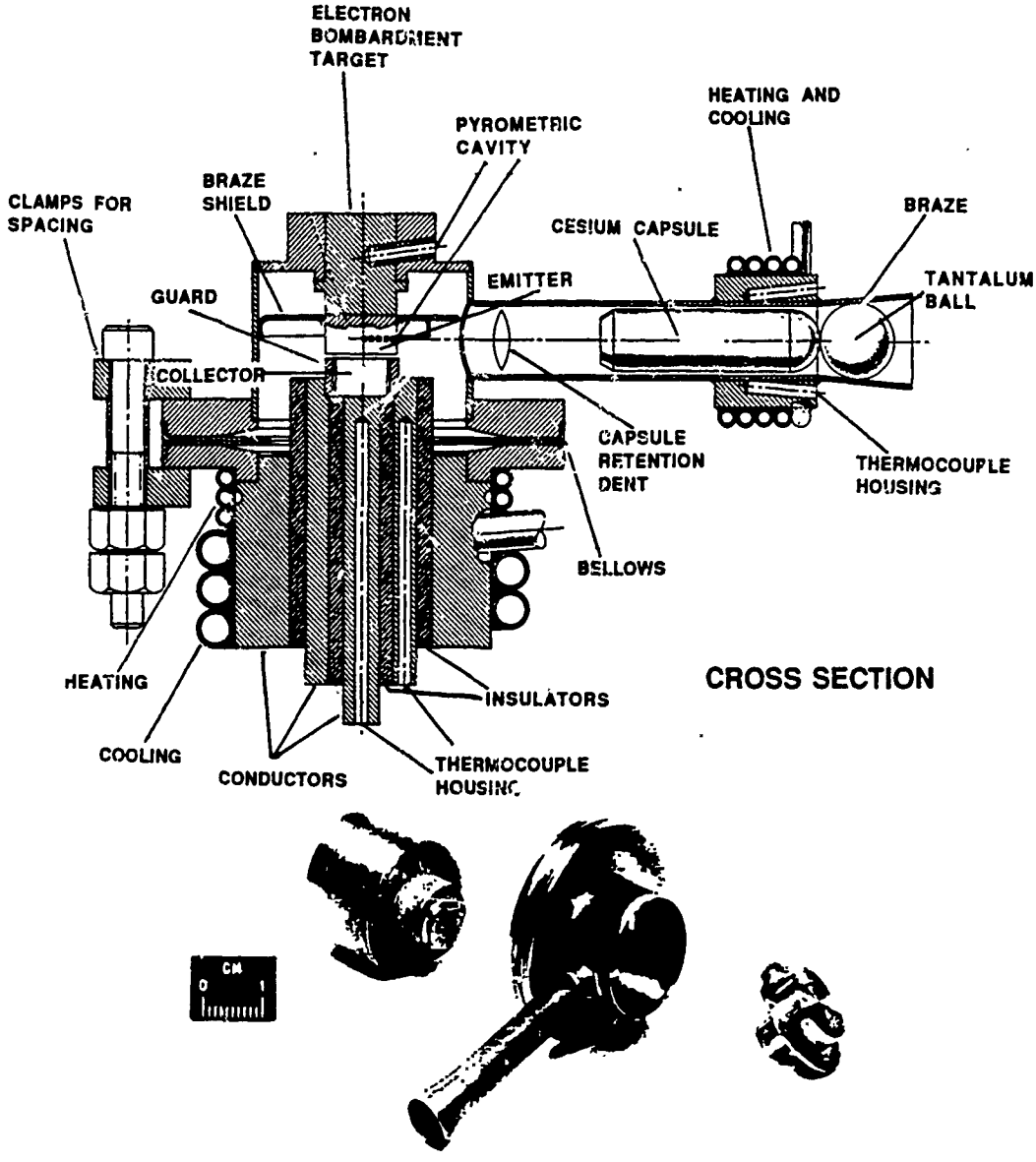

COLLECTOR, ENVELOPE, AND EMITTER SECTIONS
OF A VARIABLE-GAP DIMINIODE

FIGURE 3.1: VARIABLE-GAP DIMINIODE

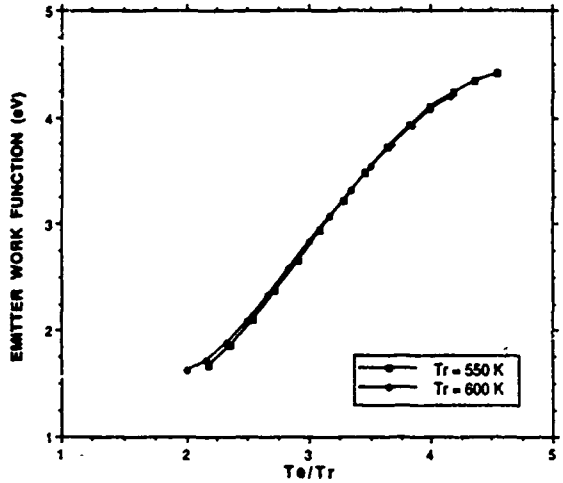

FIGURE 5.1: CESIATED EMITTER WORK FUNCTION MODEL FOR BARE EMITTER WORK FUNCTION OF 4.55 eV

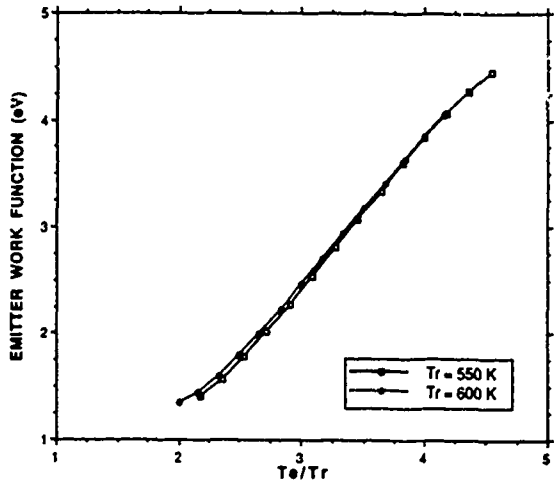

FIGURE 5.2: CESIATED EMITTER WORK FUNCTION MODEL FOR BARE EMITTER WORK FUNCTION OF 5.00 eV

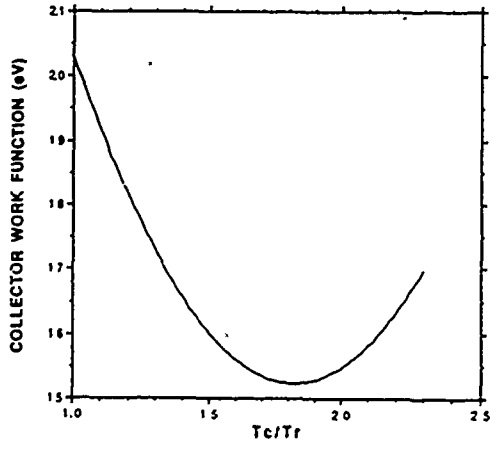

FIGURE 5.3: EMPIRICAL FORMULATION FOR THE NIOBIUM COLLECTOR WORK FUNCTION

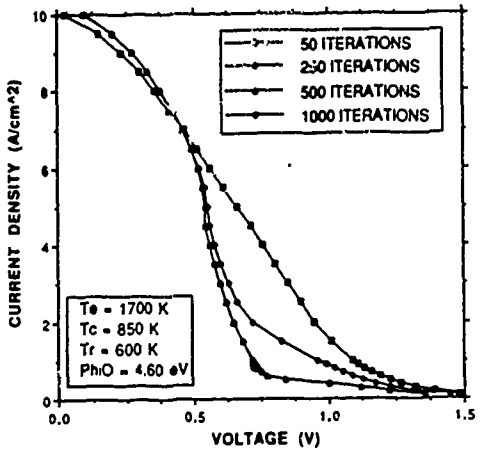

FIGURE 6.1: CONVERGENCE COMPARISON OF ITERATIVE TEC CODE

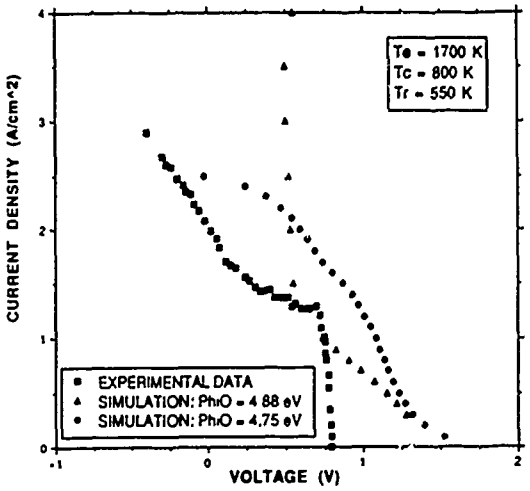

FIGURE 6.2: COMPARISON OF TEC COMPUTER SIMULATIONS WITH EXPERIMENTAL DATA

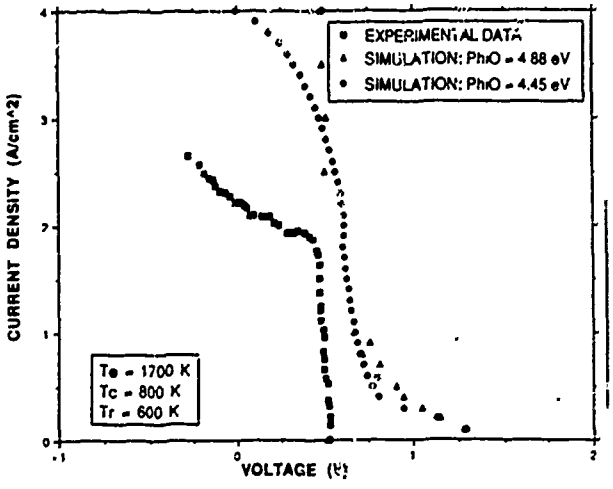

FIGURE 6.3: COMPARISON OF TEC COMPUTER SIMULATIONS WITH EXPERIMENTAL DATA

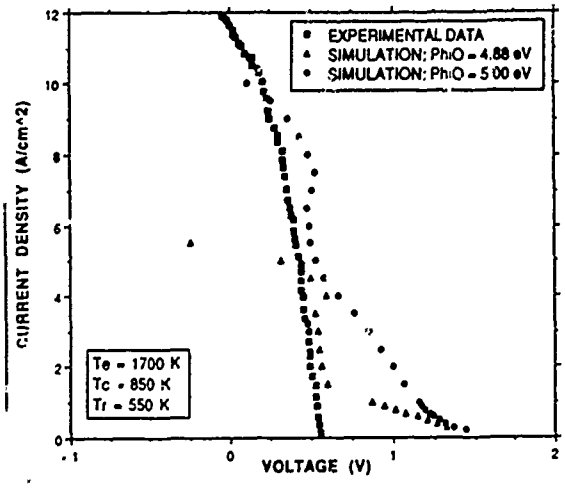

FIGURE 6.4: COMPARISON OF TEC COMPUTER SIMULATIONS WITH EXPERIMENTAL DATA

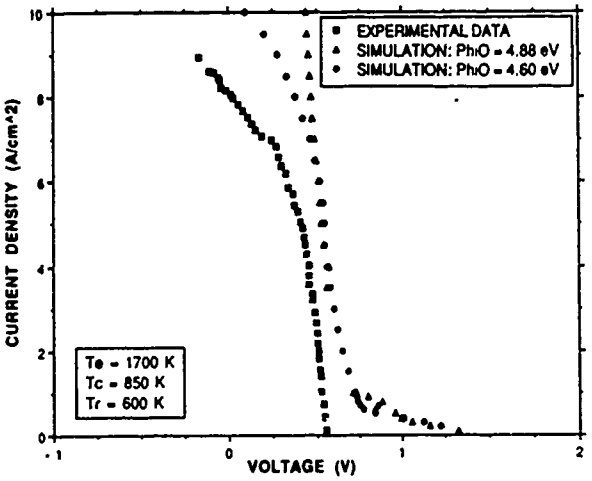

FIGURE 6.5: COMPARISON OF TEC COMPUTER SIMULATIONS WITH EXPERIMENTAL DATA

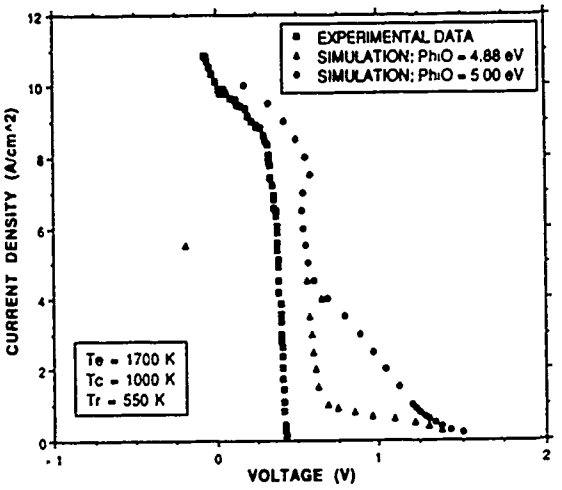

FIGURE 6.6: COMPARISON OF TEC COMPUTER SIMULATIONS WITH EXPERIMENTAL DATA

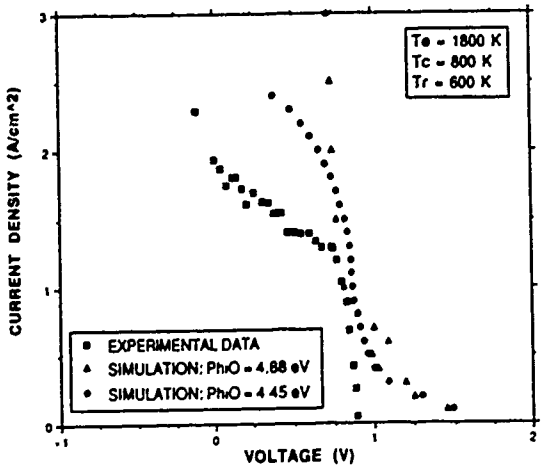

FIGURE 6.7: COMPARISON OF TEC COMPUTER SIMULATIONS WITH EXPERIMENTAL DATA

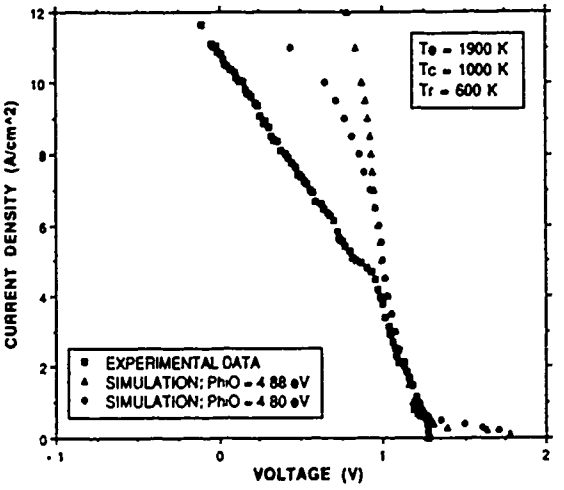

FIGURE 6.8: COMPARISON OF TEC COMPUTER SIMULATIONS WITH EXPERIMENTAL DATA

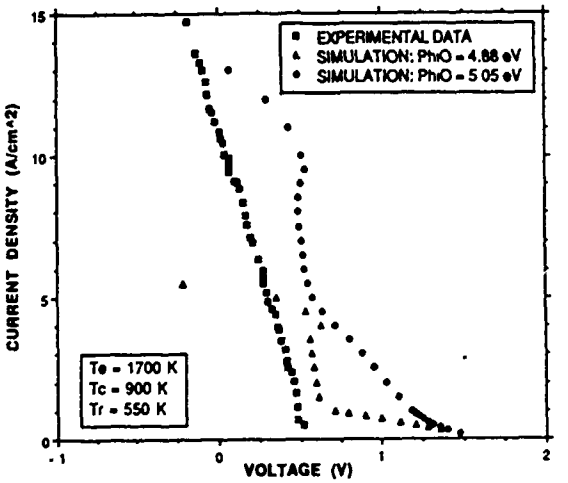

FIGURE 6.9: COMPARISON OF TEC COMPUTER SIMULATIONS WITH EXPERIMENTAL DATA

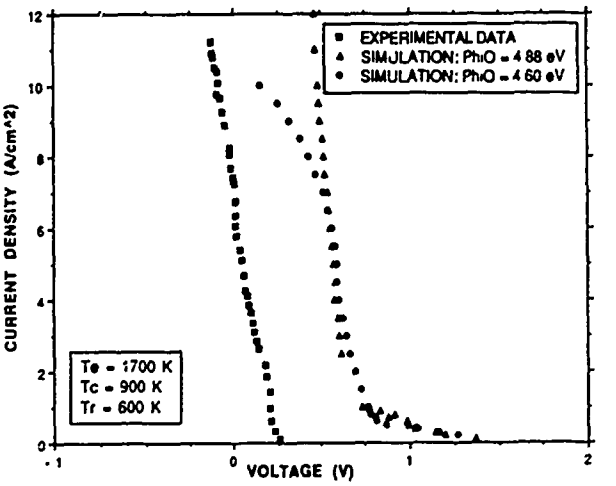

FIGURE 6.10: COMPARISON OF TEC COMPUTER SIMULATIONS WITH EXPERIMENTAL DATA

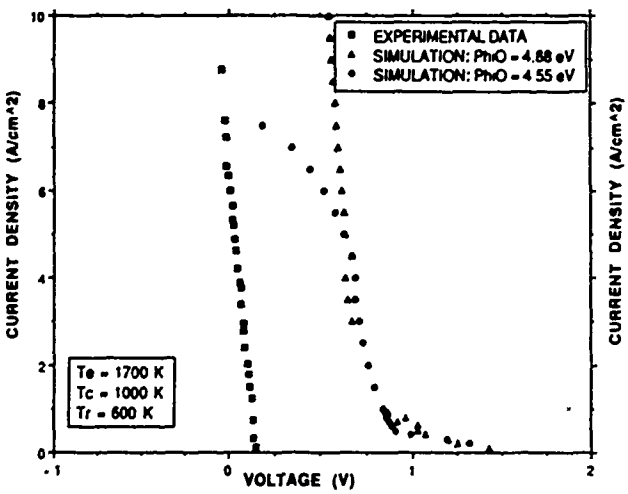

FIGURE 6.11: COMPARISON OF TEC COMPUTER SIMULATIONS WITH EXPERIMENTAL DATA

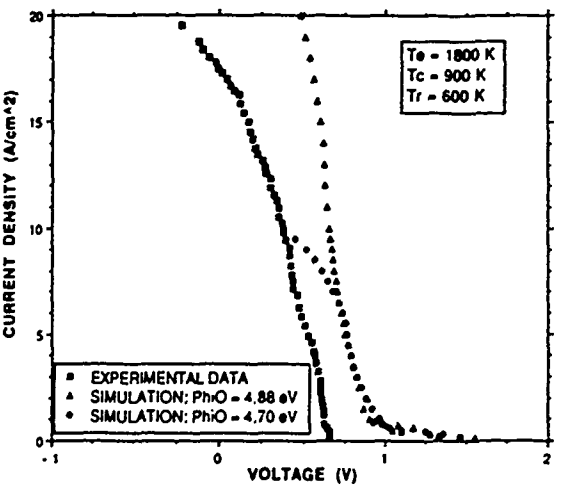

FIGURE 6.12: COMPARISON OF TEC COMPUTER SIMULATIONS WITH EXPERIMENTAL DATA

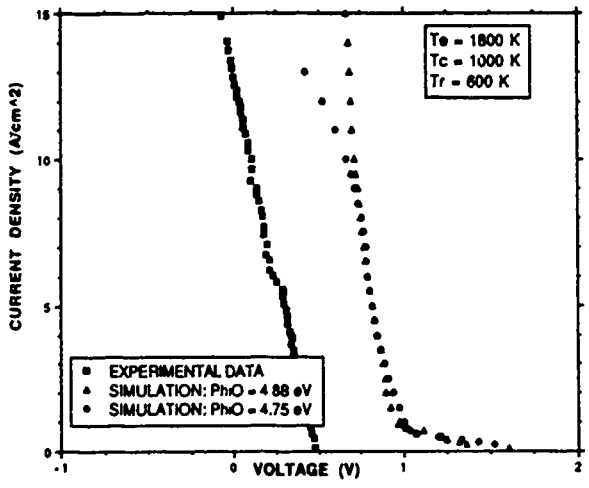

FIGURE 6.13: COMPARISON OF TEC COMPUTER SIMULATIONS WITH EXPERIMENTAL DATA

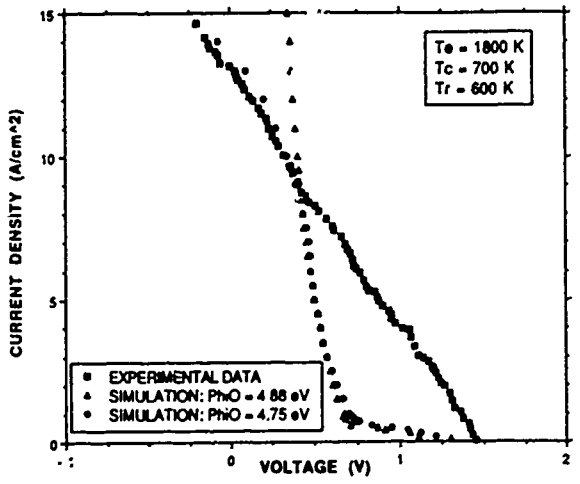

FIGURE 6.14: COMPARISON OF TEC COMPUTER SIMULATIONS WITH EXPERIMENTAL DATA

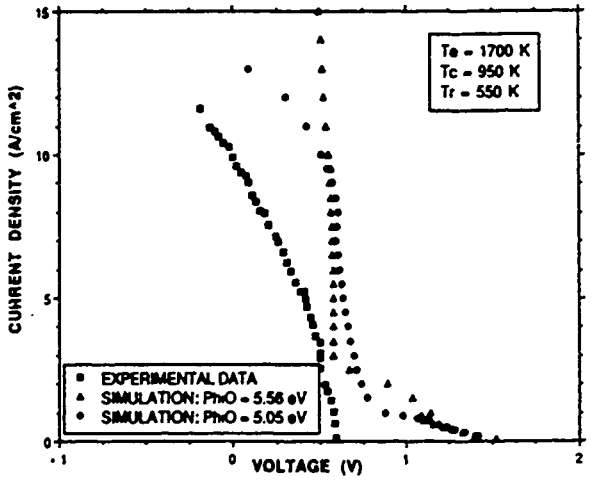

FIGURE 6.15: COMPARISON OF TEC COMPUTER SIMULATIONS WITH EXPERIMENTAL DATA

1990 USAF-UES SUMMER FACULTY RESEARCH PROGRAM/

GRADUATE STUDENT RESEARCH PROGRAM

Sponsored by the

AIR FORCE OFFICE OF SCIENTIFIC RESEARCH

Conducted by the

Universal Energy Systems, Inc.

FINAL REPORT

Overview of a Software Re-engineering Process Model

Prepared by :	Eric J. Byrne
Academic Rank :	PhD Student
Department and	Department of Computing and Information Sciences
University :	Kansas State University
Research Location :	Software Concepts Group WRDC/AAAF-3 Wright-Patterson Air Force Base Dayton, Ohio
USAF Researcher :	Robert Harris
Date :	August 10, 1990
Contract No :	F49620-88-C-0053

Overview of a Software Re-engineering Process Model

by

Eric J. Byrne

ABSTRACT

With the DoD selection of Ada as a standard programming language, many software projects are faced with the problem of how to translate existing systems into Ada. Automatic translators are available but produce poor quality Ada code. Traditional redesign and re-implementation can produce high-quality Ada systems, but this approach is seen as too expensive to be practical.

This report describes a new process model for re-engineering existing systems into Ada. The model is based on design recovery, redesign and re-implementation. An initial design is created by recovering an existing system's design using software reverse engineering techniques. The recovered design then becomes the basis for the redesign activities. The process model can be treated as a preliminary requirement specification for a re-engineering environment. Automation of the process will make it economical, plus provide the benefits usually associated with software forward engineering environments.

1. Introduction

Ada was developed by the DoD to solve the problem of the lack of commonality among major DoD systems. The DoD has issued policy statements requiring the use of Ada for all new starts and for all major system upgrades for mission-critical systems. In addition, the use of Ada for non-mission-critical systems is strongly encouraged [DoD 87a], [DoD 87b].

The Software Concepts Group (WRDC/AAAF-3) at Wright-Patterson Air Force Base focuses on identifying and developing software engineering technologies that support the development and maintenance of real-time, embedded software systems for avionics. Because the DoD Ada mandate calls for systems undergoing major upgrades to be rewritten in Ada, this group is evaluating technologies that support this task.

My research interests are in the area of software engineering particularly software maintenance and reverse engineering. Translating an existing system into high-quality Ada requires not just a language conversion, but also redesigning the system to take advantage of modern development techniques and the Ada style of programming. This can be accomplished by re-engineering the system. Rather than starting from requirements the current

system's design can be reconstructed using software reverse engineering techniques. I am investigating this technology and the Software Concepts Group is interested in its application.

2. Objectives of the Research Effort:

This report gives an overview of a process model for software re-engineering. Re-engineering software involves implementing software in a new form. For this report, we are concerned with two issues: re-implementing an existing system in Ada, and how to redesign the system to take advantage of modern design techniques. The result of the re-engineering effort is to be a high-quality system, written in Ada, with the functionality of the original system.

A problem with redesigning a system is that the requirements may not be fully known. Typically, the system has evolved over a period of years. One solution is to recover the design for the system directly from the source code. This can be accomplished using software reverse engineering techniques.

Chikofsky and Cross best defined reverse engineering [Chikofsky 90] as:

> the process of analyzing a subject system to

identify the system's components and their interrelationships and create representations of the system in another form or at a higher level of abstraction.

The important point is that software reverse engineering examines source code, it does not change it. RE-ENGINEERING IS NOT A REVERSE ENGINEERING ACTIVITY. However, reverse engineering can serve as an important first step in a re-engineering effort.

The re-engineering process model presented is a summary of work done over the summer period. Details are given in the report "A Software Re-engineering Process Model Based on Reverse Engineering" [Byrne 90a]. Another objective of this effort was to identify commercial tools for software reverse engineering and review current reverse engineering research. These reviews are given in the report "A Survey of Literature and Commercial Tools for Software Reverse Engineering" [Byrne 90b].

The overview of the re-engineering process model is given in the next section. Concluding the report are recommendations for further work.

3. A Re-engineering Process Model

The issue is to define the re-engineering process. The

selected approach to re-engineering an existing system is to redesign and re-implement. A design for the existing system will be recovered using reverse engineering techniques and this design will serve as the starting point for the redesign effort.

3.1. Process Model : Top-Level

The first step in defining the re-engineering process model is to define the inputs and outputs. Consider the re-engineering process as a black box. What are its inputs and outputs? Stated differently, what does it use and what does it generate? Figure 1 shows a context diagram for the re-engineering process. (Circles represent processes or tasks. Arrows show the flow of data between processes.)

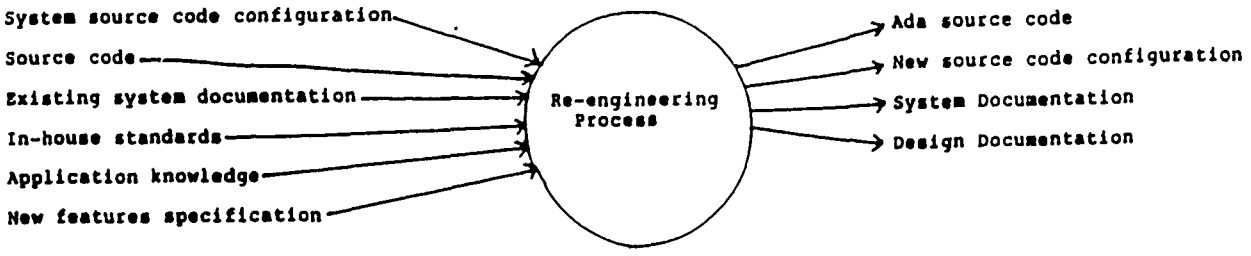

Figure 1 : Context Diagram for Re-engineering Process

Inputs

System source code configuration
Source code
Existing documentation
In-house standards
Application knowledge
New features specification

System source code configuration : The re-engineering process must be able to handle large systems. Locating a system's components may involve hundreds of files scattered across many directories.

Source code : The source code is the most important input to the re-engineering process. The information contained in the source code is need for the design recovery step.

Existing documentation : Any documentation for the system may contain useful information that is still valid. Any valid information contained in these documents will be useful during the design recovery step.

In-house standards : An organization may have several standards. One for source code, for design representations, and another for documentation contents and format. These standards will be used to verify that the products of the re-engineering process conform to the organization's standards.

Application knowledge : This knowledge can be used to

understand the existing system. The knowledge can be used during the design recovery stage and the redesign stage. Application knowledge includes an understanding of the application domain, system history, reason for the system, etc.

New features specification : It may be necessary to add new features or change current features. This input is a specification, in some form, stating what is to be added to, deleted from, or changed in the system.

Outputs

Ada source code
New source code configuration
System documentation
Design documentation

Ada source code : The primary result of the re-engineering process is the generated Ada source code. This becomes the new version of the system, replacing the older version used as input to the process.

New source code configuration : For large systems it is not enough to just generate source code. The code must be well organized. This includes organizing the code into files.

System documentation : This is documentation at the program level. It will include a data dictionary of program

items such as files, procedures, variables, and data structures. Procedure information will include name, purpose, parameters, declaration location, who-calls, etc. Information about variables will include name, data type, range of values, purpose, where-declared, where-used, where-set, etc. The exact information recorded will be decided by the organization directing the re-engineering effort.

Design documentation : This will consist of both high-level and detailed design information. The representation of the information in these documents is not important now. This documentation should also include a record of design decisions made during the redesign process.

3.2. Defining the Process Model

The next step is to define the top-level tasks of the re-engineering process. The above description treated the process as a black box, accepting inputs and somehow generating output. What are the steps of the process? How do they work together to implement the process? One possible selection of high-level tasks is:

Source code analysis
Design recovery
Information Inspection
Redesign
Re-implement
New source code analysis
Generate documentation

These are the high-level tasks of the re-engineering process. Each task, in turn, is composed of subtasks. A description of each task is given below. A description of subtasks is given in [Byrne 90a] . Figure 2 shows a Data-Flow Diagram for the re-engineering process.

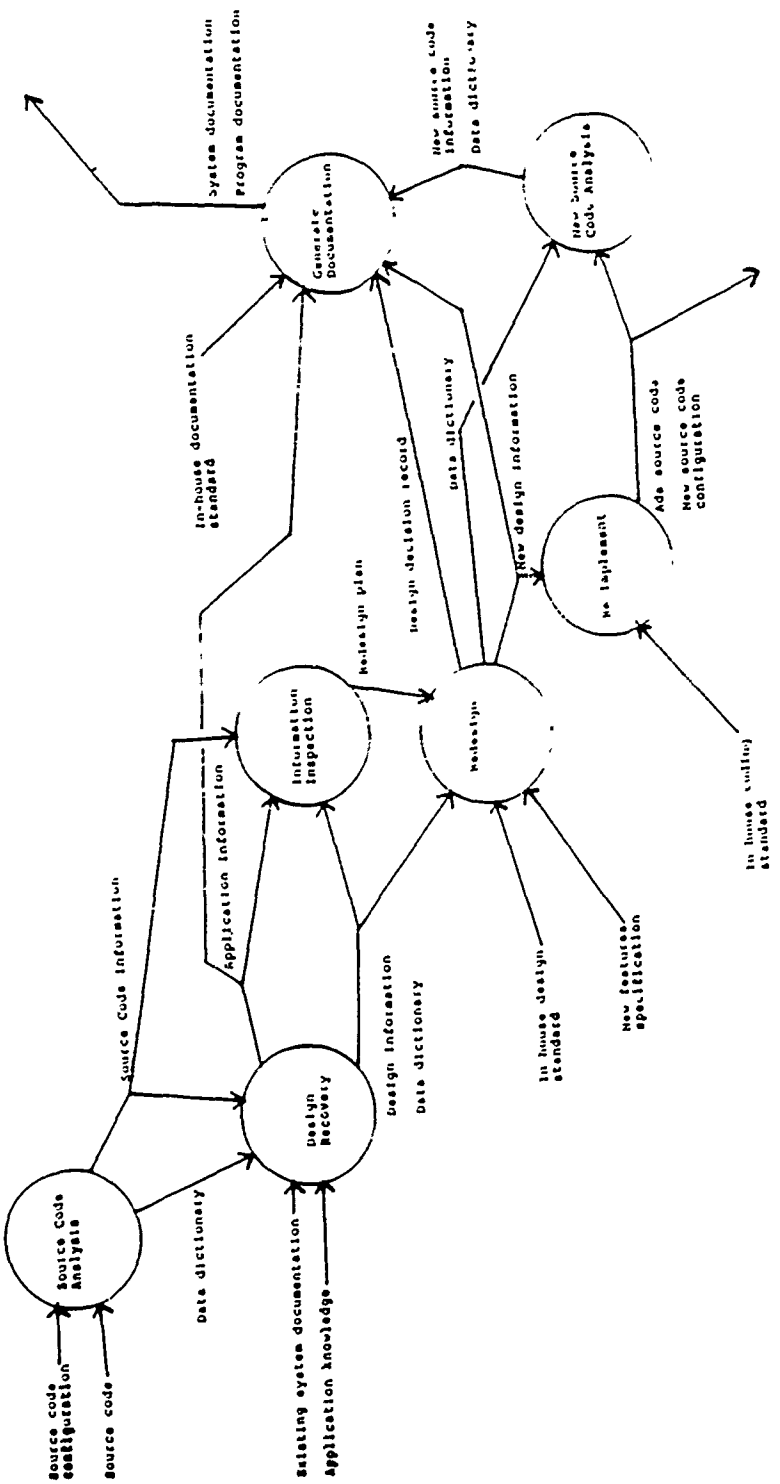

Figure 2 : Re-engineering process Data-Flow Diagram

3.2.1. TASK: Source code analysis

Inputs

System source code configuration
Source code

These inputs have been described previously.

Outputs

Source code information
Data dictionary

Source code information : This is the result of analyzing the system source code. This information gives a detailed description of the existing system.

Data dictionary : This contains an entry for each program item such as procedures, variables, data structures, and procedure parameters. This includes cross-reference information for each item.

TASK DESCRIPTION : This task is the first step in the re-engineering process. The source code is analyzed and information from it collected. A data dictionary is created that contains information about each program item. This includes cross-reference information such as where-declared, where-called for procedures, and where-used and where-set information for variables.

3.2.2. TASK: Design Recovery

Inputs

Source code information
Data dictionary
Existing system documentation
Application knowledge

These inputs have been described previously.

Outputs

Design information
Data dictionary
Application information

Design information : This is the design information reconstructed by the design recovery task. This should include both detailed and high-level design representations.

Data dictionary: The dictionary will be updated to record design information associated with program items. This includes information such as the purpose of a function or significance of data items.

Application information : This information is more abstract. This includes notes about program items recorded by a programmer, information extracted from existing documents, and information about the application domain or how the system operates within that domain. This information may include the motivation for

developing the system, history, future plans, etc. It is information about the system that can be collected and is important for understanding the system.

TASK DESCRIPTION : During this step the source code information and other information sources are used to recover the design. The recovered design must express the current system architecture and the system's functionality. Detailed design information must express processing steps, but must avoid implementation details. Not only is a design reconstructed, but any information about the application should also be recovered and recorded. The result of this step is information.

3.2.3. TASK: Information Inspection

Inputs

Source code information
Design information
Data dictionary
Application information

These inputs have been described previously.

Output

Redesign plan

Redesign plan : The result of examining the source code and design information is a plan for redesigning the system. This specifies changes that must be made to the

existing design.

TASK DESCRIPTION : This step is for planning the changes to be made and prepares for the redesign step. The system information must be examined. What are the external interfaces to the system? How can access to them be modularized? What possible subsystems can be identified? What data does the system use? Can it be organized better? What machine dependencies are present in the system? How can the system be protected from them? These are a few examples of the questions that must be asked.

The answers to these questions will be used to construct a plan for redesigning the system. The plan is not expected to be complete. The redesign phase is iterative. The information inspection reviews the current state of the design. Then design changes will be made. Then the new current state of the design will need to be reviewed and a further redesign plan constructed. This iteration will continue until the new design is considered complete.

3.2.4. TASK: Redesign

Inputs

Redesign plan
Design information
New features specification
In-house design standard
Data Dictionary

The inputs have been described previously.

Outputs

New design information
Design decision record
Data Dictionary

New design information : The redesign task generates a new design for the system. This information represents the new design.

Design decision record : This is a log of design decisions made during the redesign activities. The redesign plan can serve as a starting point. This record should contain the reasons for each change to the design and a list of all changes.

Data dictionary : This will have changed to reflect changes to the design. After redesign the data dictionary will document the new design and not the original.

TASK DESCRIPTION : The redesign phase uses the recovered design as a starting point for the redesign work. The redesign plan specifies changes to make to the design to

produce a new and hopefully better design. All levels of the design can be changed. Program items can be added, deleted, or changed. New features can be added. A record of all changes must be kept. This will be helpful to the maintenance programmers trying to understand the new version of the system.

3.2.5. TASK: Re-implement

Inputs

New design information
In-house coding standard

The input has been described previously.

Outputs

Ada source code
New source code configuration

These outputs have been described previously.

TASK DESCRIPTION : This step generates the new version of the system written in Ada. The new design is used to guide the creation of the Ada code. As part of this task a new source file configuration is created to receive the source code.

3.2.6. TASK: New source code analysis

Inputs

Data dictionary
New source code configuration
Ada source code

These inputs have been described previously.

Outputs

New source code information
Data dictionary

These outputs have been described previously. The data dictionary is updated to hold program level information such as where-used and where-set for variables.

TASK DESCRIPTION : This task analyzes the new source code and generates program information from it. This information will be used to generate new source code documentation.

3.2.7. TASK: Generate documentation

Inputs

New design information
New source code information
Application information
Design decision record
Data Dictionary
In-house documentation standard

These inputs have been described previously.

Outputs

System documentation
Design documentation

These outputs have been described previously.

TASK DESCRIPTION : This step collects all information about the application, the new design, and new source code and organizes it into documents. The documents must conform to the organization's standards.

4. Recommendations

A process for re-engineering has been defined. This process relies on software reverse engineering to recover a system design. The recovered design is then used as the basis for the re-engineering activity. The issue of generating accurate documentation for the new system was also addressed.

The next step is the selection of design representations for both detailed and high-level design documentation. Given this, algorithms for design recovery need to be developed. At the same time, algoirthms to support the inspection of program and design information can be developed. Automation of all the process steps also needs to be addressed.

ACKNOWLEDGEMENTS

I wish to thank the Air Force Systems Command and the Air Force Office of Scientific Research for sponsorship of this research. Universal Energy Systems must be mentioned for their concern and help in all administrative aspects of this program. I also wish to thank Robert Harris and Otheus Jackson of the Software Concepts Group for their support.

References

[Byrne 90a] Byrne, Eric J., A Software Re-engineering Process Model Based on Reverse Engineering, Internal Report, U.S. Air Force, WRDC/AAAF-3, Wright-Patterson Air Force Base.

[Byrne 90b] Byrne, Eric J., A Survey of Literature and Commercial Tools for Software Reverse Engineering, Internal Report, U.S. Air Force, WRDC/AAAF-3, Wright-Patterson Air Force Base.

[Chikofsky 90] Chikofsky, Elliot J., Cross, James H., "Reverse Engineering and Design Recovery: A Taxonomy," IEEE Software, Vol. 7, No. 1, January 1990, pp. 13 - 17.

[DoD 87a] DoD Directive 3405.2, "Use of Ada in Weapon Systems," March 30, 1987.

[DoD 87b] DoD Directive 3405.1, "Computer Programming Language Policy," April 2, 1987.

1990 USAF-UES SUMMER FACULTY RESEARCH PROGRAM/

GRADUATE STUDENT RESEARCH PROGRAM

Sponsored by the

AIR FORCE OFFICE OF SCIENTIFIC RESEARCH

Conducted by the

Universal Energy Systems, Inc.

FINAL REPORT

Laser Communications: Extending the Envelope

(Airy Disk and Angle of Incidence Measurements)

Prepared by:	Michael James Findler
Academic Rank:	Doctoral Candidate
Department and University:	Department of Computer Science Arizona State University
Research Location:	WRDC/AAAI-2 Wright Patterson AFB, OH 45433
USAF Researcher:	Gary D. Wilkins
Date:	3 August 1990
Contract No:	F49620-88-C-0053

Laser Communications: Extending the Envelope

(Airy Disk and Angle of Incidence Measurements)

by

Michael J. Findler

ABSTRACT

Two problems requiring research in order to optimize laser communications are: (1) assuring the proper system parameters exist for various atmospheric conditions due to thermal blooming, air eddies, etc. and (2) locating the laser beam transmission to optimize reception of the information. This summer research program was a look at trying to solve and automate these problems. These two problems were investigated in our three experiments: image enhancement, Airy disk measurements, and angle of incidence measurements

ACKNOWLEDGMENTS

I wish to thank Air Force Systems Command and the Air Force Office of Scientific Research for sponsorship of this research. Universal Energy Systems must be mentioned for their concern and help to me in all administrative and directional aspects of this program.

Further, I would like to thank Diane Summers, Frank Hutson, Lt Greg Toussaint and Claudia Duncan (WRDC/AAAI) for their support, encouragement and and a truly enjoyable working atmosphere. I would especially like to thank Gary Wilkins (WRDC/AAAI-2) for his help and guidance in overcoming many of the technical roadblocks. Uttam Sengupta (Arizona State University) gave freely of his X-Windows programming expertise. David Tsui (WRDC/AAAT-2) was very helpful in guiding me through the intricacies of bridge and the local VAX systems. Finally, Teri W. Miller, to whom I am eternally indebted.

I. INTRODUCTION:

Airborne laser communications are coming. This we know. However, implementing autonomous laser communications is still a thing of the future. Two problems in this area that we have looked at are the acquisition and tracking of laser communications and optimizing laser transmissions based upon the current existing weather conditions. These two problems were investigated in our three experiments: image enhancement, Airy disk measurements, and angle of incidence measurements

The Communication Technology Group (WRDC/AAAI-2) of the Information Transmission Branch at Wright Patterson Air Force Base is very interested in Laser Communications. Particularly, since laser communications are very secure compared to radio frequency communications. The only way to intercept a laser communique is by being in the line-of-sight of the transmission ray.

This work is a continuation of work originally started by Mr Wilkins while he was stationed at Rome Air Development Center (RADC) at the Verona Test Site Advanced Optical Test Site. While Mr Wilkins was there, he experimented in determining r_0 directly by using a telescope, a few optical instruments, a photo-multiplier tube, a spinning reticle wheel, an analog to digital converter, and a computer. "The Atmospheric Phase Coherence Length, r_0 (also known as the diffraction limited aperture of the atmosphere, or Fried's parameter), is one of the basic parameters used to determine the performance of optical imaging systems when viewed through the atmosphere." [WILKINS] This experiment was successful in determining r_0. However, the difficulty of correctly calibrat-

ing the instruments was difficult in the laboratory and nearly impossible under actual conditions.

Prior to Mr. Wilkins' work at RADC, the Navy had attempted to measure the r_0 by taking a photograph of the laser transmission. The technician would then painstakingly measure the size of the laser image and then compute the area of the Airy disk which is directly proportional to r_0. Turn around time was in minutes and hours and was subject to human error.

My research areas of interest have been in the areas of artificial intelligence and computer graphics (scientific visualization). Additionally, I am interested in user friendly interfaces.

The paper will be divided up as follows. Section II will describe the objectives of the research effort as described in the letter to UES submitted during the fifth week of the period. Section III describes the hardware and software platforms. Section IV recounts the image processing effort. The next section (V) reports on the r_0 experiments. Section VI describes the Angle of Incidence programming effort. Although each of these experiments may seem disjoint, the general opinion in the lab is that they can be combined to be a very powerful acquisition and tracking system for laser communications. Section VII will discuss possible future efforts with these tools as building blocks. Finally, Section VIII will be conclusions.

II. OBJECTIVES OF THE RESEARCH EFFORT:

Mr Wilkins and I were interested in the viability of laser communications. The research I did fell into two categories. Given a laser transmitter and receiver pair:

A) Determin from which direction the source laser is coming from and to automate the optimal laser reception.

B) Determine the r_0 of the current atmospheric conditions to automate the parameters for optimal laser transmission. This entails some digital processing.

The general approach was to do a literature search of the current research capabilities and to implement those that appear potentially applicable. The interactive user interface was done in X-Windows.

III. MATERIALS:

The programs were implemented on a Digital Equipment Corporation VAXstation 3 in C with the graphical user interface using X-Windows.

The hardware platform included a Univision Display Controller (UDC-500) with an Intel 82786 graphics coprocessor. Univision supplied a Software Development Support

Library (SDSL). Unfortunately, the software supplied by Univision did not meet our needs for the experiments, so the device drivers had to be rewritten by the lab personnel.

We used three different cameras, depending on our needs. The Fairchild Charged Coupled Device (CCD) camera was used to explore edge detection image enhancement algorithms. The Videk Series 5000 camera was used primarily as an attachment to our Celestron telescope for remote image processing, including the laser site located on New Germany Trebein Road (five miles away). Finally, the Cidek CID 2710 camera modified by the Environmental Research Institute of Michigan (ERIM) was used to determine the potential use of a wide field-of-view (FOV) holographic lens.

Note: Univision's SDSL was written for an older version of Videk camera and the new programmers at Univision were not familiar enough with the program to modify it for the new camera. Because of the problems with the Univision documentation, we had to trace the camera/graphics board DB-37 interface connector with an oscilloscope to determine the origin of the control siginals. We discovered that according to the Univision's documentation a couple of the wires were crossed. Therefore, we had to painstakingly go through each register bit by bit to create our own documentation before completing some of our experiments.

IV. IMAGE PROCESSING:

According to [GREEN], there are basically two types of image processing techniques, subjective and quantitative. We used only subjective processing techniques. Subjective processing is usually trial and error processing that the observer uses to rid the initial picture of noise. Success is based on the ability of the observer to detect relevant information on the image. While using the Fairchild, large vertical lines of noise (possibly due to a poor electrical connection) were evident near the edges of the picture. To rid the image of these vertical lines I used a couple of spatial filtering techniques: averaging over three and five pixels, and a fourier filter. Combining these techniques gave the best subjective image.

The pixel averaging algorithms can be described mathematically as

$$P_{new}(i) = \frac{\sum_{j=-k}^{k} p_{old}(i-j)}{2k+1} \qquad (3\text{-}1)$$

where $(2k + 1)$ is the number of pixels to average, p_{old} is the old value of the pixel of interest, and p_{new} is the new value to be computed. Intuitively, one can think of this operation as "fuzzing up" the picture. This broadens edges, making them clearer to the observer. Obviously, (2k + 1) is and odd number of pixels. If one wanted to do an even number of pixels, then one could drop $p_{old}(0)$ from (3-1).

The fourier filter is a weighted two dimensional averaging function. The filter is going to be 3x3, 5x5, 7x7, etc. Again, the number of pixels involved is odd. A 3x3 filter would have the following coefficients:

1	2	1
2	4	2
1	2	1

(3-2)

This is then applied to the area of interest by use of the following formula:

$$P_{new}(i,j) = \frac{\sum_{row=-1}^{1} \sum_{col=-1}^{1} p(i+row, j+col)\, coeff(i+row, j+col)}{\sum_{row=-1}^{1} \sum_{col=-1}^{1} coeff(i+row, j+col)} \qquad (3\text{-}3)$$

The formula may be extended to larger filters.

Besides needing to clean up the image from noise, we wanted to detect where the laser Airy disk was located. This requirement led to the experiments in edge detection. All the different edge detectors behaved similarly, which can be described intuitively as exaggerating the surface normals. If two adjacent points belong to the same surface, then they would typically have nearly the same normals. However, adjacent points that do not belong to the same surface would be expected to have very different normals. The edge detectors all take advantage of this concept.

The four edge detector matrices were 3x3 and symmetrical about each axis. Lt Toussaint supplied the information for the Sobel, Robert and Linear algorithms. Briefly, each algorithm uses matrix templates, for example, the Linear edge detection templates are:

Vertical			Horizontal		
-1	0	1	-1	-1	-1
-1	0	1	0	0	0
-1	0	1	1	1	1

Diagonal (Upper Lt - Lower Rt)			Diagonal (Lower Lt - Upper Rt)		
0	1	1	1	1	0
-1	0	1	1	0	-1
-1	-1	0	0	-1	-1

(3-4)

The edges that are detected are along the zero axis of the matrix. Now, using these templates, plug each into the equation (3-3) to get $p_{edge}(i,j)$. This will give four values that describe the surface normal near the pixel of interest. However, the values may be positive or negative. If we determine the magnitude of the vectors utilizing

$$P_{new}(i,j) = \sqrt{\sum_{edge=1}^{4} p_{edge}(i,j)^2} \quad , \qquad (3\text{-}5)$$

then we have a value that represents the intensity of the pixels surrounding the area of interest. If $p_{new}(i,j)$ is small (near zero), the area surrounding the pixel of interest "appears" to be on the the same surface. However, the larger the $p_{new}(i,j)$, the larger the intensity contrast and the more probable that the pixel of interest lies upon an edge between two surfaces. The image will thus be mostly dark except near edges of surfaces where it will be brighter.

I extended the Linear algorithm (and combined it with Sobel's operators) to be more heavily weighted, and called it the Linear Squared operator. The Linear Squared algorithm used the four templates shown in (3-6) which exaggerates the intensity in the direction perpendicular to the zero axis, thereby, being more sensitive to less defined edges.

Vertical

-1	0	1
-2	0	2
-1	0	1

Horizontal

-1	-2	-1
0	0	0
1	2	1

Diagonal (Upper Lt - Lower Rt)

0	1	2
-1	0	1
-2	-1	0

Diagonal (Lower Lt - Upper Rt)

2	1	0
1	0	-1
0	-1	-2

(3-6)

Sobel's filter was the same as the Linear Squared filter except that it only uses the vertical and horizontal templates. Robert's operator was

$$mag_1(i,j) = p(i,j) - p(i+1,j+1) \qquad (3\text{-}7)$$

$$mag_2(i,j) = p(i+1,j) - p(i,j+1) \qquad (3\text{-}8)$$

and then

$$P_{new}(i,j) = \sqrt{mag_1(i,j)^2 + mag_2(i,j)^2} \qquad (3\text{-}9)$$

Equations (3-7) and (3-8) are the determinant of the 2x2 matrix inscribed by the pixels $p(i,j)$, $p(i+1,j+1)$. The best images were produced by the Linear Squared algorithm while the worst images were produced by the Sobel algorithm.

V. AIRY DISK (r_0) MEASUREMENTS

As mentioned previously, this work is a offshoot of Mr Wilkins' efforts at Rome Air Development Center. Mr Wilkins was disappointed in the bulkiness of his spinning reticle wheel experiment. So he suggested modernizing the Navy photograph method. (Refer to [WILKINS] for details about the mathematical treatment of r_0.)

$$r_0 \leq Diameter_{telescope} = \frac{2.44 * wave\_length_{laser} * focal\_length_{telescope}}{diameter_{Airy\_disk}} \qquad (4\text{-}1)$$

All the values on the right side of the equation of (4-1) are constants except the diameter of the Airy disk. We can determine the diameter of the Airy disk in the laser image by counting the pixels between the edges. This value is in pixels, but the Videk camera documentation claims its pixel size is 6.8 microns on each side. It is relatively simple to convert the pixel diameter count to diameter in microns. Thus we can determine the r_0 value quickly.

"The Airy disk contains approximately 86% of the light." [WILKINS] On the computer image, this was the area turned bright white by the collimated laser stationed five miles away. During optimal times of observation, the Airy disk was relatively constant. During hot days, thermal eddies and other atmospheric conditions would cause the Airy disk to range from good to non-existent.

VI. ANGLE OF INCIDENCE MEASUREMENTS

The Cidek camera that we used for this experiment contained a column of bad pixels, and thus had to be sent back to the manufacturer. However, before it was sent back we had worked with the camera enough to know what we wanted to do is feasible. The Cidek camera had a wide field-of-view (FOV) holographic lens mounted. [TAI] This lightweight, flat, compact lens had the equivalent FOV as a 45 degree "fish eye" lens with less than half the bulk and weight. We used a 850 nanometers λ narrow pass filter to block out any extraneous noise.

The program to find the laser image on the screen was straight forward. Since we had the narrow pass filter mounted on the camera, the background was nearly black and the laser image was nearly white and the size was approximately 4 pixels. We grabbed the image from the Cidek using the Univision frame grabber. Then, we looked at every pixel and compared it to a threshold value. If the pixel was below the threshold, then the laser had not lit that pixel. Otherwise, if the pixel was above the threshold, then we had found our laser.

Now that we know the location of the laser in pixel coordinates *(x,y)*, then all we have to do is convert it to an angle in the x and y directions. First, we assume the center of the pixel screen is perpendicular to the z-axis at the origin. Let us say the pixel plane has hize (max_x , max_y), for us $max_x = 512$ and $max_y = 450$. Then the midpoint of the pixel screen is defined by

$$half_x = max_x / 2 \qquad \text{and} \qquad half_y = max_y / 2. \tag{5-1}$$

It then follows that

$$x_{adjusted} = x_{actual} - half_x \qquad \text{and } y_{adjusted} = y_{actual} - half_y. \tag{5-2}$$

If the angle visible to the camera is α (for us $\alpha = 45$), then the conversion factor from pixels to degrees is

$$angle_x = (\alpha / max_x) * x_{adjusted} \quad \text{and}$$

$$angle_y = (\alpha / max_y) * y_{adjusted} \ . \tag{5-3}$$

This information can the be used in a feedback loop controling stepping motors to adjust the receiver for optimal reception.

VII. FUTURE DIRECTIONS:

During the summer, Mr Wilkins and I discussed several possible future directions of this research. I think the most interesting possibilities are in the angle of incidence experiments. However, this implies using some of the information learned from the other two areas.

For the angle of incidence problem, we have shown that two stationary laser receiver-transmitter pairs can optimize their reception and transmission with little difficulty. Each receiver-transmitter pair optimizes itself independently with two degrees of freedom (x and y). However, if at least one of the pairs is on a moving platform, the problem gets much more difficult. Let us look at some of the different cases.

Case 1: Target stationary, Source moving

This is similar to both images being stationary, but because of the movement of this case (and all the other cases), there may be the need to hand off the communications duties to another receiver-transmitter pair. The problem has three degrees of freedom (x, y, z) to describe the Target location. Input from a flight control computer should provide enough information to know the Source position.

Case 2: Target moving (constant speed), Source stationary

In this case, the Source will need two images of Target to extrapolate the straight line course. However, Source will need a third image if Target is traveling along a curved course at constant speed. Therefore, Sources problem requires solving with four degrees of freedom (x, y, z and time). The sampling frequency is only dependent on the speed of the Target and is not too critical.

Case 3: Both Target and Source moving (constant speeds)

The Source pair must solve a seven degrees of freedom problem ($(x, y, z)_{source}$, $(x, y, z)_{target}$, and $time_{target}$). The coordinates of the Target cannot be predicted accurately, so the time and coordinates of the Target combine to give a probability distribution to where the Target might be. The Source may still miss.

Case 4: Both Target and Source moving (non-constant speeds)

Since both coordinates of Source and Target are only able to be predicted within a given accuracy (never absolute), then the problem has an eight degrees of freedom ($(x, y, z)_{source}$, $time_{source}$, $(x. y. z)_{target}$, and $time_{target}$). Both of the coordinate systems are predictions, even though the Source has more information about itself to make its predictions accurate. If the sampling frequency is high enough the problems associated with acceleration can be discarded as being inconsequential.

To solve these different cases with enough speed to be able to discard case four implies a solution in hardware. I am convinced that the rapid sampling frequency can be

achieved by designing a neural network or expert system to quickly do the processing of the image.

VIII. CONCLUSIONS:

Based on the experiments at WRDC/AAAI-2, the potential of airborne, autonomous, fast laser communications is tremendous. Acquisition and tracking have been the major obstacles to achieving such communications, but with the advent of massively parallel neural networks, the obstacles seem less intimidating. Airborne laser communications are coming. This we know.

REFERENCES

Conference and Technical Reports:

1 Andrews, Harry C., Tutorial and Selected Papers in Digital Image Processing, (various authors), IEEE Inc., New York, NY 1978.

2. Tai, A., Eisman, M. and Neagle, B., "Holographic Lens for Wide FOV Laser Receiver," Computer and Optically Formed Holographic Optics, Ivan Cindrich, Sing H. Lee, Editors, Proc. SPIE 1211, pp. 238-246 (1990).

3. Wilkins, Gary D., "Measurement of the Atmospheric Phase Coherence Length, r_0," In-house report RADC-TR-86-192, December 1986.

Textbooks:

1. Barnoski, Michael K., Fundamentals of Optical Fiber Communications, New York, Academic Press, Inc., 1976.

2. Cathey, W. Thomas, Optical Information Processing and Holography, New York, John Wiley and Sons, 1974.

3. Gagliardi, Robert M. and Karp, Sherman, Optical Communications, New York, John Wiley and Sons, 1976.

4. Goodman, Joseph W., Introduction to Fourier Optics, New York, McGraw-Hill Book Co., 1968.

5. Green, William B., Digital Image Processing: A Systems Approach, New York, Van Nostrand Reinhold, 1989.

6. Hall, Ernest L., Computer Image Processing and Recognition, New York, Academic Press, Inc., 1979.

7. Yaroslavsky, L. P., Digital Image Processing, New York, Springer-Verlag, 1985.

1990 USAF-UES SUMMER FACULTY RESEARCH PROGRAM/

GRADUATE STUDENT RESEARCH PROGRAM

Sponsored by the

AIR FORCE OFFICE OF SCIENTIFIC RESEARCH

Conducted by the

Universal Energy Systems, Inc.

FINAL REPORT

Integrated Terrain Access and Retrieval System Processor Loading

Prepared by:	Jeffery R. Layne
Academic Rank:	Graduate Student
Department and University:	Electrical Engineering The Ohio State University
Research Location:	WRDC/AAAS-3 Wright Patterson AFB Wright Patterson, Ohio 45433
USAF Researcher:	David A. Zann
Date:	31 Aug 90
Contract No:	F49620-85-C-0013

Integrated Terrain Access and Retrieval System Processor Loading

by

Jeffery R. Layne

ABSTRACT

By monitoring signals sent to the discrete output register, the loading for all five processors of the Integrated Terrain Access and Retrieval System was determined. Four of the processors were tested while driving ITARS with the "SCAN" flight simulation program. The Users Processor was tested when driving ITARS with the "Robust Demo" while performing a Terrain Following/ Terrain Avoidance algorithm. Also by monitoring signals sent to the discrete output register, I identified the subroutine which was overloading the Point Feature processor.

I. INTRODUCTION:

As a Palace Knight selectee and a future employee of the Wright Research and Development Center, my participation in the Graduate Student Research Program was intended to provide training for work in the Avionics Laboratory. This experience will enable me to structure a graduate curriculum that provides the best possible training for a successful career with the U.S. Air Force.

Working with the Technology Applications Group of AAAS, I was assigned to work on the Integrated Terrain Access and Retrieval System. The Integrated Terrain Access and Retrieval System (ITARS) is an avionics computer system that serves as a data base manager for compressed map data collected by the Digital Mapping Agency (DMA). In operation, the ITARS unit generates three simultaneous moving map displays in real time while providing terrain and feature data to external users. The moving map displays generated by ITARS contain information about the terrain elevation, area features such as vegetation or water, and linear features such as airports and bridges. The moving maps help reduce the workload on the pilot by eliminating paper charts that produce only static images of a rapidly changing situation. External users can access the digital terrain data from ITARS via the MIL-STD-1553B data bus thus freeing other systems of the task of storing and managing their own map data. For example, in the Integrated Test Bed Facility, a Microvax uses data from ITARS

to run a terrain following/terrain avoidance (TF/TA) algorithm.

The various tasks performed by ITARS are broken down and executed by five Fairchild F9450 microprocessors. The F9450 is a 16 bit microprocessor which implements the complete MIL-STD-1750A instruction set. The functions performed by these processors include the following: 1) Point Feature Processor (PFG) - responsible for retrieving point features from Regional Mass Memory (RMM) and sending them to the display buffer at a 10 hz rate; 2) Area Linear Feature Decompaction Processor (ALF) - responsible for the decompaction of area features data stored in RMM; 3) Terrain Decompaction Processor (TER) - responsible for the decompaction of terrain elevation data in RMM; 4) Controller Processor (CRL) - controls the function of the PFG, ALF, and TER processor; and 5) the User Processor (USP) - responsible for handling user request via the 1553B data bus.

II. OBJECTIVE OF THE RESEARCH EFFORT:

In order to assess the future growth capabilities of the ITARS unit, it is important to know the loading of each processor. Currently, the point features do not keep up with the terrain on the display screens. Therefore, the Point Feature Processor is suspected to be overloaded. My assignment was to determine the processor loading imposed upon each processor and to determine why the point features

do not keep up with the terrain on the display screen.

III. METHOD OF ANALYSIS:

Currently, the programs for four of the five processors within ITARS operate on an interrupt basis. Essentially, these processors execute a continuous loop referred to as the idle task. Figure 3-1a shows the idle task for the TER processor. The CRL, ALF, and USP processors execute similar idle tasks. When an interrupt occurs, the processor exits the idle task and executes an interrupt service routine (ISR). After servicing the interrupt, the program returns to the idle task as though nothing had occurred.

Determining the percentage of time that the processor spends servicing ISR routines should provide a good indication of the loading imposed upon the processor. Using equation 3-2, this percentage can be calculated by monitoring the number of times that the idle task loop is executed in a loaded and unloaded condition. The unloaded count can be obtained by simply altering the program code to mask out all interrupts.

$$\% \text{ loading} = \frac{Cu - Cl}{Cu} * 100\% \qquad \text{(Equation 3-2)}$$

Cu - # of idle task loops that the processor executes during unloaded condition for a set time frame

Cl - # of idle task loops that the processor executes during loaded condition for a set time frame

```
*************************************************************
************          idle task                      *******
*************************************************************
*       LOWEST PRIORITY BACKGROUND IDLE TASK.  JUST LOOPS   *
*       AND SEND OUT HARDWARE SIGNAL (MONITOR WITH SCOPE).  *
*************************************************************

        MODULE  START
        DEFINE  START'IDLE'TSK
        REFER   TOGGLE'DESCRETE  "TOGGLE DESCRETE SIGNAL"

START'IDLE'TSK  NOP

*********  WAIT FOR INTERRUPTS    ************

NXINTR  LD      ##1,R2

        CALL    @-R15,TOGGLE'DESCRETE

        NOP

        NOP

        NOP

        BR      NXINTR          ;WAIT FOR NEXT INTR

        END
```

figure 3-1a - idle task for the TER processor

```
*************************************************************
*******             TOGGLE'DESCRETE                 **********
*************************************************************
*      WILL TOGGLE BIT OR BITS SPECIFIED IN R2 IN THE       *
*      OUTPUT DESCRETE REGISTER.                            *
*************************************************************

      DEFINE  TOGGLE'DESCRETE

TOGGLE'DESCRETE ;
        PUSHM   R2,R1

        XIO     R2,##OD             ;SET SPECIFIED BIT TO 1

        NOP                         ;DELEY

        NOP

        NOP

        LD      ##0,R1

        XIO     R1,##OD             ;SET IT BACK TO 0

        POPM    R2,R1

        RET     @+R15

        PAGE
```

figure 3-1b - toggle'descrete subroutine

There are two possible methods of counting the idle task loops. The first involves adding a counter variable to the programming code which could be incremented every time the idle task loop is executed. However, obtaining the counters value from memory would be very difficult.

The second method involves using the discrete output register. The discrete output register was provided to control events outside of the processor. However, it is not used within ITARS. The idle task code for the TER and ALF call a procedure named toggle'discrete(1) every time the idle task loop has occurred. This routine sends the value passed (in this case 1) to the discrete output and then resets it back to zero (refer to fig 3-1b). This results in a pulse at the least significant bit of the discrete output register. The discrete output is accessible for monitoring with test equipment through the backplane of ITARS. The photo in figure 3-3 is an example oscilloscope trace showing the toggling bit of the TER processor in an unloaded condition. Since a call to the toggle'discrete routine can be added to the idle task routine for the USP and CRL processor, this would provide an easy method for counting idle task loops for all four processors. As will be demonstrated, a similar method can be used for the PFG processor.

IV. COUNTING PULSES:

Counting the pulses was first attempted by using the

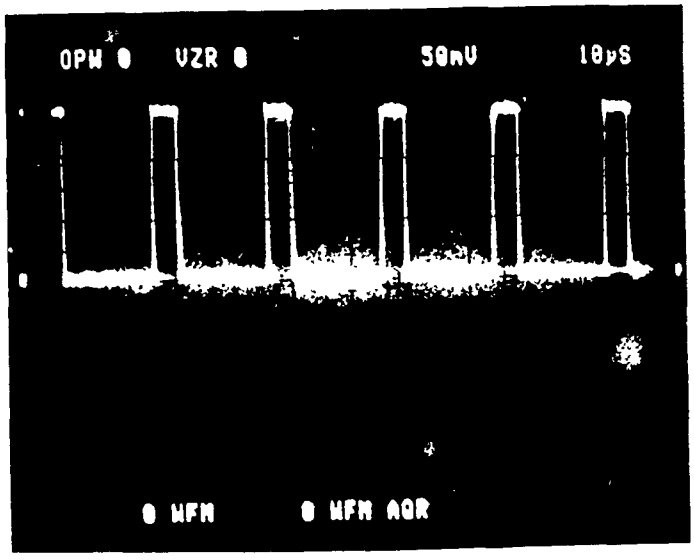

figure 3-3 - unloaded toggle discrete bit of the TER

Tektronics 7854 sampling oscilloscope. However, this method had several problems. First, some of the ISR occurred too quickly and infrequently to be registered on the oscilloscope display. Displaying longer ISR's resulted in aliasing errors. The sampling scope takes only 512 samples per frame. Thus, the slow trace speed required to view the longer IRS resulted in toggles not being sampled. The missing toggles (aliasing) appeared as interrupt processing when actually none had occurred. Also, I felt that one scope trace was too short of a time frame to be representative of what the processors were doing.

The Tektronics DC 503 Universal Counter proved to be the better tool for making the measurements. Using the totalizer

function, I could reset a counter which would begin counting pulses for a 30 Sec time frame. The final pulse count is shown on the LED display.

V. SCAN PROGRAM:

For the purpose of making measurements, ITARS was driven by an IBM personal computer running a program called "SCAN". SCAN is a simple BASIC language program that sends latitude, longitude, and altitude information to ITARS over the 1553B communications bus.

The SCAN program allows the user to alter the speed, heading, and altitude of the aircraft. Unfortunately, the SCAN speed does not represent a true aircraft speed. However by monitoring changes in latitude during a 30 second time frame while flying north at given scan speeds, I was able to calculate the associated aircraft speed. Note in figure 5-1 that the aircraft speed seems to saturate at a scan speed of 300.

The SCAN program simulates speed by sending updated position at a constant rate while varying the displacement for increases or decreases in speed. Since the update rate is constant, this seems to indicate that ITARS performance saturates at this speed. However, I was unable to prove this.

SCAN SPEED STUDY

LATITUDE SPEED: HEADING = 0 FOR 30 SECOUNDS

SCAN SPEED	CHANGE IN LAT (DEG)	ACTUAL SPEED (MPH)
30	.0206	169.85
60	.0411	338.87
90	.0633	521.91
120	.0767	632.39
150	.0881	726.38
300	.1836	1513.77
420	.1816	1497.28
600	.1875	1545.93

NOTE: 1 DEG LATATUDE REPRESENTS 68.708 STATUTE MILES

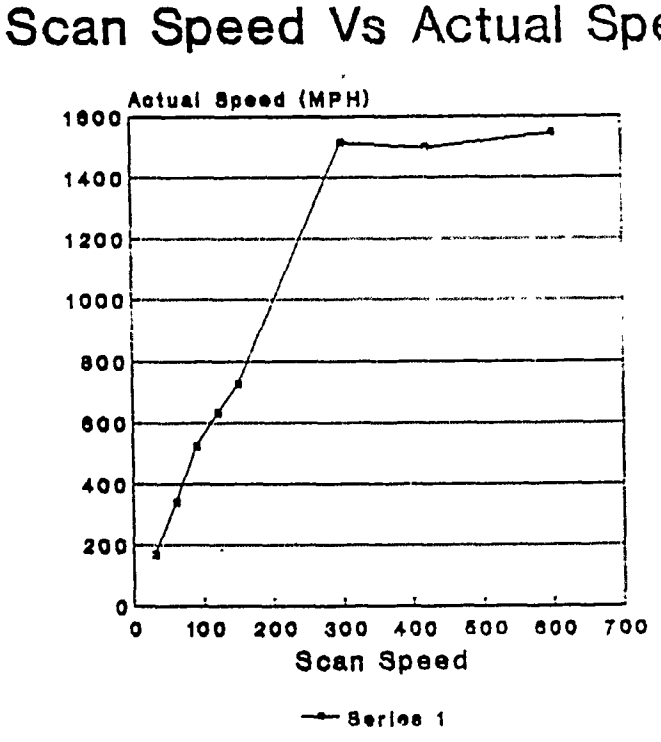

figure 5-1

While driving ITARS in the SCAN configuration, no data is being sent to external users. However, the ITARS display is configured similar to an external user requiring data at a 10 hz rate. The maximum rate in which an external user can access the data is 2 hz. Therefore, the ITARS display serves as the primary user of the system and should impose the largest loading on the CRL, TER, ALF, and PFG processors. Since the USP is responsible solely for handling user request, the SCAN program imposes no loading on the USP processor.

VI. LOADING FOR THE TER, ALF, AND THE CRL PROCESSORS:

In order to create a worst case scenario, the SCAN program was set at a heading of 45 degrees and a speed of 210 (approximately 1000 MPH based on scan speed study). A 45 degree heading imposes the most loading because both the top and right side of the display screen need to be updated every time the aircraft moves.

Five 30 second pulse counts were collected for the TER, ALF, and CRL processors both in a loaded and unloaded state. After averaging the loaded and unloaded pulse counts, a loading was calculated for each processor. The data in figure 6-1 shows that the loading for the TER, ALF, and CRL processors is 23.76%, 14.27%, and 10.98% respectfully. From this information, you can conclude that these processors probably are not overloaded and are candidate for adding

DATE: 7/18/90 REV: 7/26/90
NOTE: ALL MEASUREMENTS WERE TAKEN WHEN FLYING AT A 45 DEG HEADING AND A SCAN SPEED OF 210

CONTROLLER PROCESSOR (XA18)

MEASUREMENT	IDLE COUNT	LOADED COUNT	
1:	1475009	1313161	
2:	1473438	1311701	
3:	1476207	1314631	
4:	1471926	1312239	
5:	1478588	1313526	
MEAN	1475034	1313052	% LOADING 10.98

AREA FEATURE DECOMPACTION PROCESSOR (XA24)

MEASUREMENT	IDLE COUNT	LOADED COUNT	
1:	1493519	1314800	
2:	1495083	1304991	
3:	1485864	1320903	
4:	1494259	1152183	
5:	1487163	1298951	
MEAN	1491178	1278366	% LOADING 14.27

TERRAIN DECOMPACTION PROCESSOR (XA26)

MEASUREMENT	IDLE COUNT	LOADED COUNT	
1:	1486592	1035033	
2:	1487143	1214731	
3:	1491352	1072386	
4:	1492650	1152629	
5:	1493109	1206177	
MEAN	1490169	1136191	% LOADING 23.76

POINT FEATURE PROCESSOR (XA20)

MEASUREMENT	IDLE COUNT	LOADED COUNT	
1:	1574566	68919	
2:	1573850	49497	
3:	1575004	45293	
4:	1574500	52624	
5:	1572208	55729	
MEAN	1574026	54412	% LOADING 96.54

figure 6-1 - loading imposed on ITARS processors

future capabilities to the ITARS unit.

VII. LOADING FOR THE PFG PROCESSOR:

The program code for the PFG is structured somewhat differently than the other four processors. Similar to the other processors, the program performs a continuous loop. However, within the loop a call is made to a subroutine called msg'compare. Also, within the loop a flag is checked to see if certain conditions are met. Under certain conditions, the program exits the loop and calls three other subroutines which perform the functions of memory management, feature load, and generate display list. The frame interrupt and the message interrupt are the two primary ISR's that can suspend execution of the basic subroutines (see the Flow Diagram for PFG figure 7-1).

In order to obtain an unloaded pulse count for the PFG processor, the following modifications of the program code were required: 1) all interrupts were masked out; 2) the condition for exiting the msg'compare loop was forced to be false all of the time; 3) the msg'compare routine was commented out of the code; and 4) a call to the toggle discrete subroutine was inserted in the basic msg'compare loop. For the loaded count everything was restored back to the original condition except the toggle discrete call was left in the code.

FEATURE GENERATOR PROCESSOR CONTROL FLOW DIAGRAM

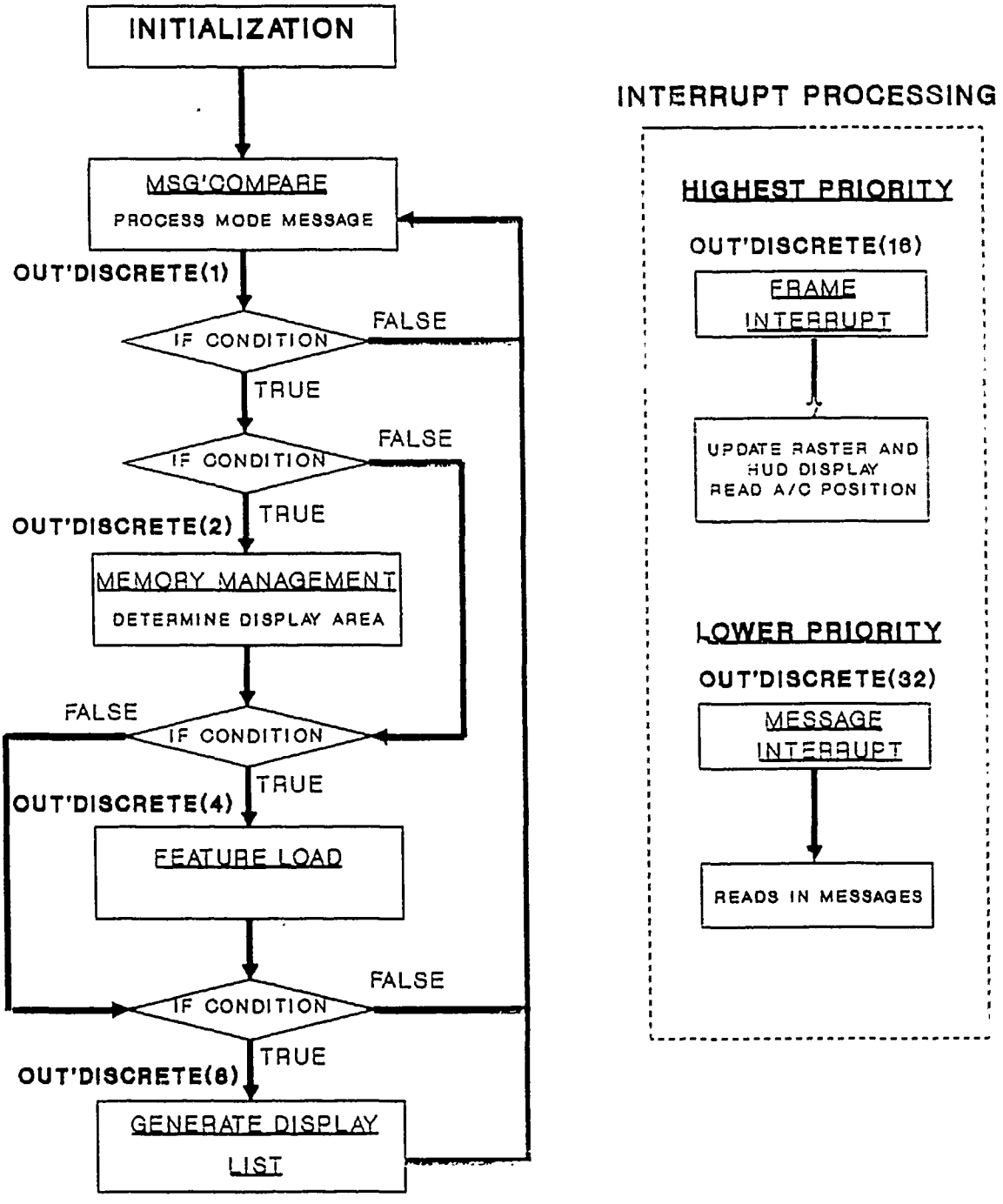

figure 7-1

Using the program SCAN set for the same heading of 45 degrees and SCAN speed of 210, a very large loading of 96.54% was obtained for the PFG (see figure 6-1). Since this processor is operating under such a large loading, I would not recommend using it to add future capabilities to the ITARS unit.

VIII. PFG PROCESSOR OVERLOAD:

Due to the very large loading found on the PFG processor and the jerky movement of the point features with respect to the terrain on the display screen, further investigation of the PFG processor was necessary. Therefore, I devised a scheme to determine which subroutine is imposing the greatest amount of loading on the PFG processor.

Essentially this involved creating a subroutine called out'discrete (see figure 8-1). This routine is very similar to the toggle discrete subroutine, except the value is sent to the discrete output and held constant instead of resetting it back to zero. A call to the out'discrete subroutine was inserted before each call to a major subroutine in the PFG processor. By setting a different bit and resetting all other bits of the discrete output when I entered a new subroutine, I would be able to isolate the routine that was overloading the processor. The Flow Diagram for the PFG (figure 7-1) shows the calls made to the out'discrete before each main subroutine. The discrete output register was

```
*****************************************************************
*****              OUT'DISCRETE                          ********
*****************************************************************
*      WILL SET THE BIT OR BITS SPECIFIED IN R2                 *
*      IN THE OUTPUT DESCRETE REGISTER.                         *
****************** ******************************************

        DEFINE  OUT'DISCRETE

OUT'DISCRETE    ;
        PUSHM   R2,R1

        XIO     R2,##OD             ;SET OD to R2

        POPM    R2,R1

        RET     @+R15

        PAGE
```

figure 8-1 - out'discrete subroutine

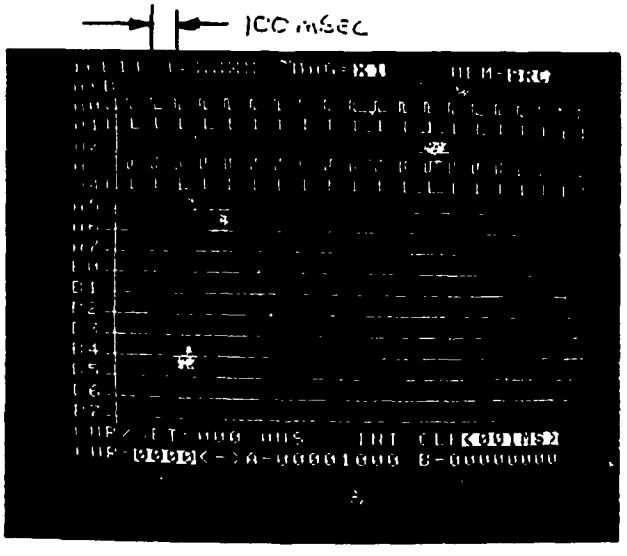

figure 8-2 - out discrete only basic point features

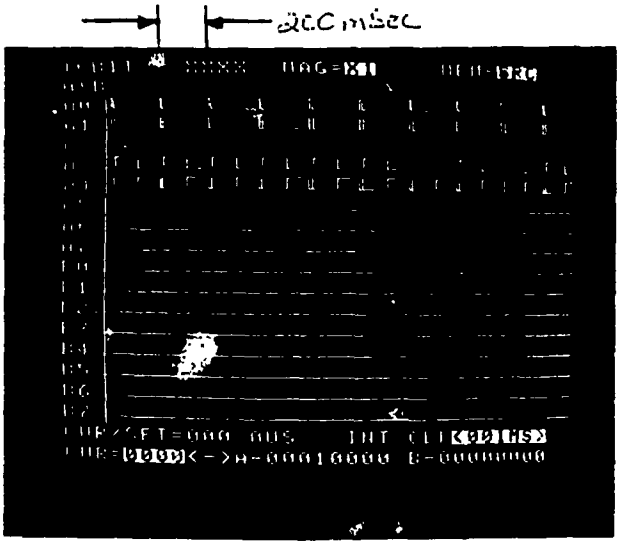

figure 8-3 - out discrete with some non-basic point features

A0 - MSG'COMPARE LOOP
A1 - MEMORY MANAGEMENT SUBROUTINE
A2 - FEATURE LOAD SUBROUTINE
A3 - GENERATE DISPLAY LIST SUBROUTINE
A4 - FRAME INTERRUPT
A5 - MESSAGE INTERRUPT

monitored using the Dolch LAM 3250 Logic Analyzer.

This test method works well except for one minor problem. An ISR does not reset the discrete output back to the original value of the routine in which it had interrupted. However, this can be accounted for by realizing that the discrete output is changed for an ISR only when the interrupted subroutine has finished executing.

As mentioned before, the PFG is responsible for updating the display at a 10 hz rate (every 100 milliseconds). The photo in figure 8-2 shows the discrete output register when only the basic point features (the aircraft symbol and the position text) are shown on the display screen. Note that the update frame interrupt ("A4") is interrupting the msg'compare loop approximately every 100 milliseconds as expected. Following a frame interrupt, the memory management ("A1") and the generate display list ("A3") subroutines are executed. Measurements show that the frame interrupt service routine and the memory management subroutine have a very short execution time of about 2.5 milliseconds each. The generate display list subroutine requires the most amount of execution time (approximately 80 milliseconds). However, all subroutines are executed within the required 100 milliseconds frame rate.

The photo in figure 8-3 shows the output discrete register

when an average number of point features are displayed on the screen. This photo illustrates the problem that I referred to before. Some of the frame interrupts ("A4") appear to require a long time to execute. In this case the subroutine generate display list overlaps the frame interrupt. However realizing that the output discrete register for an interrupt does not change until the interrupted routine has finished executing, you see that the generate display list subroutine is actually the one requiring all of the time. The frame interrupt and the memory management routine still seem to require about 2.5 milliseconds to execute. However the generate display list subroutine now requires about 180 milliseconds to execute. The time required to generate the display list seems to be proportional to the number of point features that are being displayed. When a large number of point features are displayed, I have witnessed execution times as large as 350 milliseconds. This results in the display list being updated at a much slower rate of 5 hz, 3.3 hz or 2.5 hz depending on the number of update frames that the task overlaps. The time line shown in figure 8-4 may better explain what should occur and what is actually occurring within ITARS.

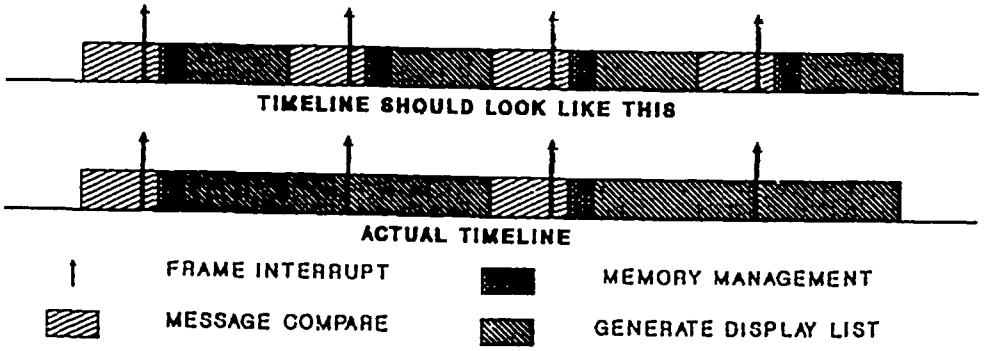

figure 8-4 - time line for the PFG processor

IX. LOADING FOR THE USP PROCESSOR:

Using the SCAN program to drive ITARS, I have determined the processor loading for four of the five microprocessors within ITARS. Unfortunately, the USP processor does not perform any task during the execution of the SCAN program. However, it would be interesting to know the loading of USP processor when operating during routine user request. Therefore, the loading was determined while running the Terrain Following/ Terrain Avoidance algorithm on the Robust Demo PC.

Based on known threats, preprogramed pop up threats, and the terrain, these routines use a cost/benefit analysis to calculate the best route for aircraft to follow in order to avoid detection. This involves flying at low altitudes and using the terrain to block potential radar.

DATE: 8/16/90
NOTE: ALL MEASUREMENTS WERE TAKEN WHEN THE ROBUST DEMO WAS FLYING AT A 45 DEG HEADING AND A SPEED OF 400 NAUTICAL MILES/HOUR. THE TF/TA ALGORITHM WAS ACTIVE.

USER PROCESSOR (XA22)

MEASUREMENT	IDLE COUNT	LOADED COUNT	
1:	1696072	409597	
2:	1697645	422465	
3:	1691271	422221	
4:	1694293	415296	
5:	1696459	430975	
MEAN	1695148	420111	% LOADING 75.22

figure 9-1 - loading measurements for the USP processor

In order to create a worst case scenario, the data request rate was set at the maximum of 2 hertz. Also, the heading was set for 45 degrees and speed was set at 400 knots. The table in figure 9-1 shows the loading for the USP processor to be 75.22 %. Based on this data, I would not recommend adding many additional users to the ITARS unit.

X. RECOMMENDATION:

a) It should be determined why the speed of the aircraft saturates out at a scan speed of 300. This could be a serious limitations for some of the Air Force's high speed aircraft.

b) Efforts should be made to speed up the generate display list subroutine of the PFG processor. There are several potential method of doing this. Since the subroutine performs many sine and cosine calculations, some time may be gained by creating faster algorithms for these functions. Also, it may be possible to speed up the routine by completely rewriting the Jovial Language programing code in Assembly Language. The most drastic and costly method would be replacing the microprocessor with a faster version.

1990 USAF-UES SUMMER FACULTY RESEARCH PROGRAM/

GRADUATE STUDENT RESEARCH PROGRAM

Sponsored by the

AIR FORCE OFFICE OF SCIENTIFIC RESEARCH

Conducted by the

Universal Energy Systems, Inc.

FINAL REPORT

PROBABILISTIC IR EVIDENCE ACCUMULATION

Prepared by:	Dr. R. H. Cofer and Jim Perry
Academic Rank:	Associate Professor and Research Assistant
Department and	Electrical Engineering and Computer Engineering
University:	Florida Institute of Technology
Research Location:	WPAFB, WRDC/AARA, ATR Branch
USAF Researcher:	Jim Leonard
Date:	September 22, 1990
Contract No:	F49620-88-C-0053

Same Report as
Prof. R. H. Cofer
(Report # 88)

1990 USAF-UES SUMMER FACULTY RESEARCH PROGRAM/

GRADUATE STUDENT RESEARCH PROGRAM

Sponsored by the

AIR FORCE OFFICE OF SCIENTIFIC RESEARCH

Conducted by the

Universal Energy Systems, Inc.

FINAL REPORT

Machine Learning Applied to High Range Resolution Radar Returns

Prepared by:	Lawrence O. Hall and Steve G. Romaniuk
Academic Rank:	Assistant Professor and Research Assistant
Department and	Computer Science and Engineering
University:	University of South Florida
Research Location:	WPAFB, WRDC/AARA, ATR Branch
USAF Researcher:	Jim Leonard
Date:	August 6, 1990
Contract No:	F49620-88-C-0053

Same Report as
Prof. Lawrence Hall
(Report # 90)

1990 USAF-UES SUMMER FACULTY RESEARCH PROGRAM

Sponsored by the

AIR FORCE OFFICE OF SCIENTIFIC RESEARCH

Conducted by the

Universal Energy Systems, Inc.

FINAL REPORT

Electronic structure and deep impurity levels in GaAs related compound semiconductors and superlattices

Prepared by:	Devki N. Talwar and Alan Coleman
Academic Rank:	Assistant Professor and Graduate Student
Department and	Department of Physics
University	Indiana University of Pennsylvania
Research Location:	Electronic Technology Laboratory
	ELRA/WRDC, Wright Patterson Air
	Force Base, Ohio, 45433
USAF Researcher	Dr. M. O. Manasreh
Date:	Sept. 27, 1990
Contract No:	F49620-88-C-0053

Same Report as
Prof. Devki Talwar
(Report # 97)

1990 USAF-UES SUMMER FACULTY RESEARCH PROGRAM/
GRADUATE STUDENT RESEARCH PROGRAM

Sponsored by the
AIR FORCE OFFICE OF SCIENTIFIC RESEARCH
Conducted by the
Universal Energy Systems, Inc.

FINAL REPORT

Surface Studies Using Scanning Tunneling Microscopy

Prepared by:	Tammie S. Confer
Academic Rank:	Graduate Student
Department and	Physics Department
University:	University of Akron
Research Location:	WDRC/ELOT
	Wright-Patterson AFB, OH 45433
USAF Researcher	Jeff L. Brown
Date:	17 Sept 90
Contract No:	F49620-88-C-0053

Surface Studies Using Scanning Tunneling Microscopy

by

Tammie S. Confer

ABSTRACT

A series of experiments were performed with a scanning tunneling microscope to determine its applicability to measuring surface roughness. Si, GaAs, and Au samples were imaged. Reliable and reproducible images of the Au sample were obtained, while those of Si and GaAs were less reliable. Since both Si and GaAs easily oxidize in air and the microscope used imaged only under ambient conditions, attempts were made to passivate these surfaces; Si by hydrogen termination and GaAs by low-temperature MBE growth. The Si images were noisy and the microscope tip touched the surface while imaging GaAs, making images from each sample difficult to interpret. Large area images of Au showed a bowing effect due to the tip moving along a spherical surface while imaging large areas. This is a non-linear effect produced by the tube-type piezoelectric scanner and can be corrected with appropriate image software.

ACKNOWLEDGEMENTS

I wish to thank the Air Force Systems Command and the Air Force Office of Scientific Research for sponsorship of this research, and Universal Energy Systems for their work in the administrative aspects of the program. In particular, I would like to thank Donald Peacock and Milton Danishek for their concern and guidance.

I would like to express my gratitude to Jeff Brown, for his support and encouragement of this project, as well as to everyone in ELOT for providing an open and enjoyable working atmosphere. Art Becraft must be acknowledged for his rapid work in the construction of the vibrational isolation apparatus. Chris Bozata graciously gave of his time in the semiconductor processing clean room to aid in the etching of the silicon samples. In addition, I would like to thank Dr. Peter Henriksen for providing the evaporated gold samples, and for his suggestions and comments on this project.

I. INTRODUCTION:

An objective of the Electro-optics Techniques and Applications Branch of the Electro-optics Division at WPAFB is to develop non-destructive techniques of evaluating semiconductor materials. One technique currently under study utilizes results obtained from monochromatic light scattering measurements. It is assumed that light scattered from a semiconductor consist of two components; that scattered by topological features of the surface and that scattered from subsurface features. If one is able to account for the component scattered by surface features, then the remaining component contains information of subsurface properties of the material, thus providing a non-destructive technique for materials evaluation.

Scanning tunneling microscopy provides detailed information of the surface topology of metals and semiconductors. Properly interpreted, this information can be used to account for diffusely and specularly reflected radiation from a surface which then can br subtracted from the total scattered radiation. The remaining scattered radiation is due to subsurface features and can be related to electronic properties of the scattering material; thus a non-destructive evaluation of those properties.

The STM can be operated in two modes; one with constant tunneling current and the other with constant tip height. In the constant current mode, the tip scans the surface, with the aid of a piezoelectric tube, while monitoring the tunneling current. Due to the exponential dependence of the tunneling current to the tip-sample separation, the current is held constant by adjusting the height of the tip above the surface through a feedback system. An image is formed by

plotting the feedback voltage (tip height) as a function of tip position.

In the constant height mode, the tip is scanned across the surface at a constant height while the tunneling current is plotted as a function of tip position. In this mode, the feedback loop only responds to gradual changes in the tip-sample height. Since the tip does not need to be vertically displaced, images obtained using the constant height mode may be obtained at a fast scan rate. This aids in imaging atomic features since faster scans are less susceptable to noise and thermal drift.

II. OBJECTIVES

A commercial STM, manufactured by Digital Instruments, Santa Barbara, California, was to be used to measure surface topology of conducting and semiconducting materials of interest to WRDC/ELOT. Since this particular STM, a Nanascope II, only operates in air and is not vacuum compatible, the project was limited to samples which could be imaged under ambient conditions. My work involved using the STM to determine the surface roughness of gallium arsenide (GaAs), silicon (Si), and gold (Au). Results of surface roughness data obtained by STM measurements are to be compared to data obtained by a variable angle scatterometer(VAS) measurements. The overall objective is to use the surface roughness data obtained from STM measurements to account for radiation which is reflected from surface features of a light scatterer.

III. ACCOMPLISHMENTS

A. INSTRUMENT INSTILATION

Initially, the problem of vibration isolation for the scanning head had to be addressed. This system was new and only a few images of highly oriented pyrolytic graphite (HOPG) and a gold grating used in calibrating the scanning heads were imaged. For vibrational isolation, the scanning head apparatus was suspended from a frame using elastic cords. The frame was constructed at a table level height in order to conveniently change the scanning heads, tips, and samples. This is also desirable since the initial or coarse approach of the tip to the sample is performed manually. The coarse adjustment is monitored visually with a microscope until the image of the tip reflected from the sample surface almost meets the tip. A stepper motor is then used to lower the tip until tunneling occurs. This vibration isolation system was tested by imaging HOPG. Clear, repeatable images were obtained with atomic resolution using the constant height mode down to a scan size of 2x2 nm. In addition, atomic resolution of graphite was observed in the constant current mode down to a 7x7 nm scan size.

B. TIPS

To continue the work on image quality, tips of different materials were investigated. The materials used in this investigation were platinum-iridium (PtIr), platinum-rhodium (PtRh), palladium (Pd), gold (Au), and tungsten (W). The PtIr tips manufactered by Digitital Instruments are mechanically formed. They were cut at about a 45 degree angle while gently pulling the wire. PtRh, Pd and Au tips were formed in a similar manner from 0.01" diameter wire. Tips were initial checked with an optical microscope for defects. Tips that

appeared to be sharp were then used to image HOPG. Atomic resolution was obtained using each the different materials. Good tips were consistently made using PtRh and Pd wire. An exceptional image of HOPG was obtained using a Pd tip as shown in Fig. 1. The top image is a large-area scan of graphite revealing a large step on the surface. The lower right corner edge of the surface of this step shows three atomic layers. The bottom image is a 2x2 nm scan of HOPG clearly showing hexagonal structure. Also note, three atoms of the hexagon appear lower than the other three due to the bonding of these atoms to those in the plane directly below.

There was some difficulty in forming a good Au tip. The difficulty arose from the softness of Au. Observation showed that these tips tended to be longer and flimsier then the tips formed from PtRh or Pd wire. The atomic scale images obtained using the Au tips were generally noisier, probably due to vibration of the filamentary tip.

While investigating different tips, the different scanning heads for the Nanoscope II were examined also. The instrument was purchased with three different scan heads. The A head is capable of imaging with atomic resolution and has a maximum scan area of 700x700 nm. The G head has a maximum scan size of 80x80 μm. Both of these heads are placed on the base which holds the sample. The sample can be no larger than 2x2 mm due to the sample holder. For samples larger than 2 inches, the E head can be used. The E head is a stand-alone head that rests on three feet placed directly onto the sample. A large gold diffraction grating was imaged using the stand alone head as shown in Fig. 2.

B. SAMPLES

1. Silicon

Previous publications have shown that silicon can be imaged in air by using a hydrofluoric acid etch technique which removes the native oxide layer and hydrogen terminates the dangling bonds on the surface. In the semiconductor-processing clean room at WPAFB, a silicon wafer was cleaned using a standard solvent cleaning procedure and dried with nitrogen gas. This sample was placed in a plasma asher to remove organic contaminants. After this procedure the wafer was imaged using the stand alone head. The minimum scan size with definable features was 750x750 nm using a 0.1nA tunneling current and -2.5 volt bias, however this scan was unstable. As described in literature and through private communication, organic contamination has been a major problem in using the HF etch. The unstable areas in the image are probably due to surface contaminants.

2. GaAs

Recent work at WPAFB has suggested that a low temperature capped, MBE grown, GaAs sample is free of surface states and ohmic contacts can be deposited directly on the surface. The STM images of a freshly prepared sample of GaAs shown definable feature down to a 67x67 nm area. Figure 3 shows an area imaged over a six minute period. Except for slight thermal drift, the image is repeatable. Large surface features are repeated although the edges of these features are not well defined. Successive images of this sample revealed similar features. Since GaAs does oxidize in air and the images obtained are somewhat unstable, more information is needed for interpretation.

3. Gold

In order to correlate STM measurement of surface roughness to results obtainable by light scattering, a thermally evaporated gold sample was used. The image of gold shown in Fig. 4 clearly shows cluster formation.

The initial plan was to obtain multiple 80x80 μm scans covering about the same surface area as illuminated by the scatterometer. In these images a noticeable spherical bow appeared due to the bending radius of the piezoelectric tube. This spherical surface is related to the tip being pulled away from the surface at the edges of the scan. The roughness measurements obtained using these scans are obviously affected by the bowing of image and is not related to the real surface.

In order to observe any change in the roughness measured, a number of scans of the same area were repeated using different scans sizes. The results are tabulated below. The first column in the table records the length of one side of a square scan. The second column describes the range of the height of the scan, denoted z, and the standard deviation, denoted σ, using the entire image. Results in the third and fourth columns are an average of 5 measurements of one quarter of the area of the original scan. These measurements were taken in each quadrant of the image with the fifth measurement taken at the center. The remaining four columns are results using a lowpass filtered image.

Surface Roughness of Evaporated Gold on Glass

scan	unfiltered data				filtered data			
size	total scan		averaged		total scan		averaged	
	z	σ	z	σ	z	σ	z	σ
50000			40.34	4.46			27.78	3.10
32000	52.05	4.99	39.23	4.66	41.52	4.25	27.61	3.90
16000	52.67	2.81	27.54	2.69	39.33	1.83	18.67	1.71
8000	25.02	1.65	16.17	1.63	8.47	0.79	7.81	0.78
4000	16.83	1.35	14.48	1.32	7.88	0.87	6.54	0.84
2000	14.46	1.31	12.79	1.29	8.29	0.95	7.24	0.93
400	10.89	0.97	8.28	0.97	7.42	0.92	6.17	0.93
400	8.92	0.94	7.04	0.93	6.47	0.89	5.62	0.88
200	6.33	0.90	5.02	0.91	5.74	0.88	4.55	0.89
100	4.63	0.76	3.91	0.68	4.95	0.73	3.34	0.66

(all values measured in nanometers)

The decreasing values of the deviation with decreasing scan size are probably due to bowing of the image. The smaller scans show less change in the standard deviation and may be a better indicator of the surface roughness. However, in this case, the sample size is small compared to the area used with the scatterometer. Whether the small STM image is indicative of a larger surface area is still an open question.

The image bow is noticeable in the 50x50 nm, although it was not as dominant as in the larger scans. Figures 5 and 6 show lineplots of these scans. The lineplots in Fig. 5 do not reveal the clusters of gold although these clusters are visible on screen with the use of color. Diagonal scratches in the glass substrate are noticeable. These scratches contribute to the surface roughness. In the smaller scans, the area imaged was in between the scratches. The fractal nature of gold cluster formation can be observed in the scans

with varying sizes. The 400x400 nm scan of Fig. 6 clearly shows cluster formation. The top image is a repeated scan of the area enclosed in the box on the lower image. The hillock with vertical indent is clearly visible in both images.

IV. RECOMMENDATIONS

1. Care should be taken when interpreting STM images. The image actually represents the local charge density of states accessible to tunneling electrons. In the case of GaAs this is not the same as surface topology.

2. An atomic force microscope (AFM) uses the same software and electronic circuitry as an STM, however it images by moving a stylus across a surface while maintaining constant force between the stylus and sample. An AFM can be used to obtain topographical images of nonconducting surfaces, thus eliminating problems encountered with oxide layers on a surface. It would be interesting to compare both types of images and their relationship to the light scatter signal.

3. Further analysis can be done on the roughness measurements of the gold sample by correcting for the arc motion of the tip over the sample.

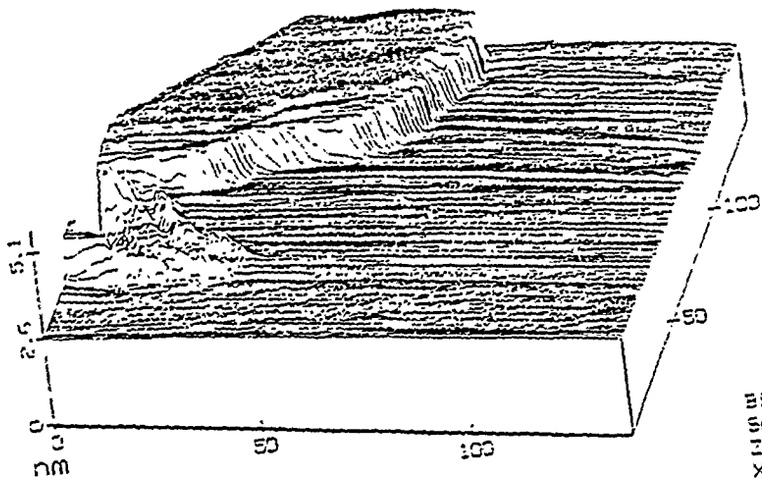

Nanoscope II
Parameters:

Bias	16.2 mV
Setpoint	1.4 nA
I	5.1 A/ln(I)
XY	19.8 A/V
Samples	400/scan

Graphite surface using PtIr tip, head A
Data taken Wed Jun 06 13:49:00 1990

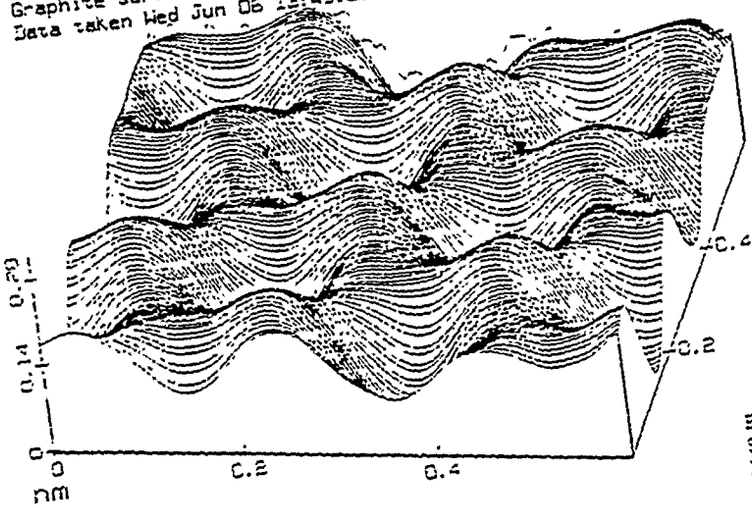

Nanoscope II
Parameters:

Bias	16.5 mV
Setpoint	1.9 nA
I	5.1 A/ln(I)
XY	19.8 A/V
Samples	200/scan

HOP Graphite
Data taken Tue Jul 17 11:28:20 1990
Buffer 2(PDS.001((I)), Rotated 180°, XY axes (nm), I axis (nm)

Figure 1

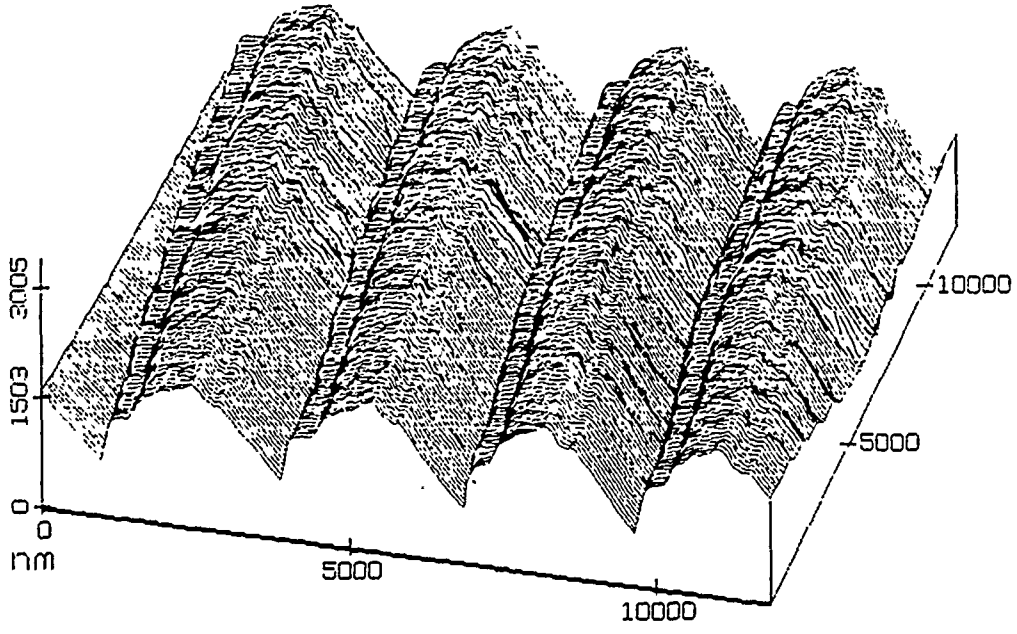

Au Diffraction Grating (using head E, stand alone)

Figure 2

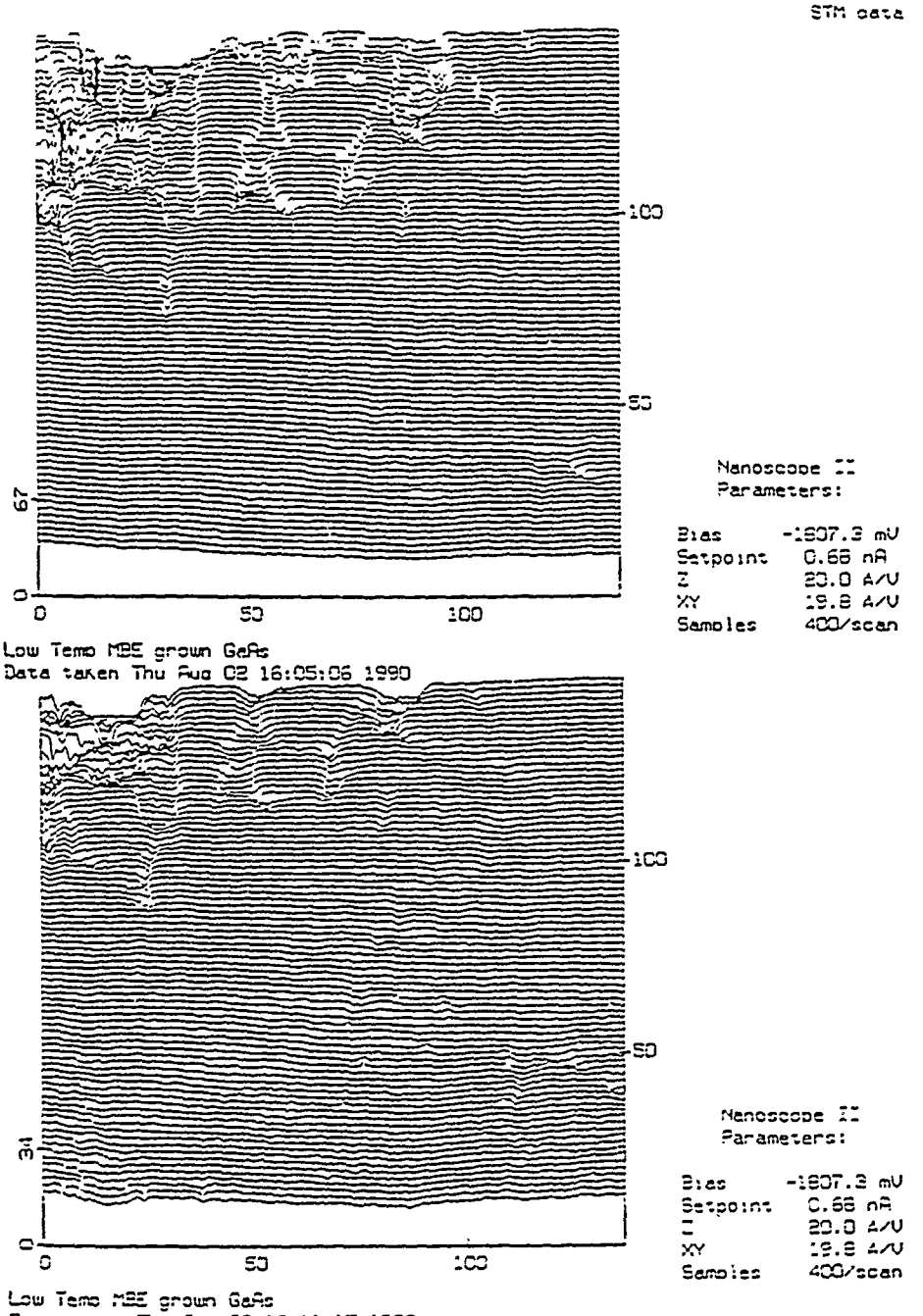
STM data
100
50
67
0
0
50
100
Nanoscope II
Parameters:
Bias -1807.3 mV
Setpoint 0.66 nA
Z 20.0 A/V
XY 19.8 A/V
Samples 400/scan
Low Temp MBE grown GaAs
Data taken Thu Aug 02 16:05:06 1990
100
50
34
0
0
50
100
Nanoscope II
Parameters:
Bias -1807.3 mV
Setpoint 0.66 nA
Z 20.0 A/V
XY 19.8 A/V
Samples 400/scan
Low Temp MBE grown GaAs
Data taken Thu Aug 02 16:11:15 1990
Buffer 2(G3.004), Rotated 270°, XY axes (nm), Z axis (nm)

Figure 3

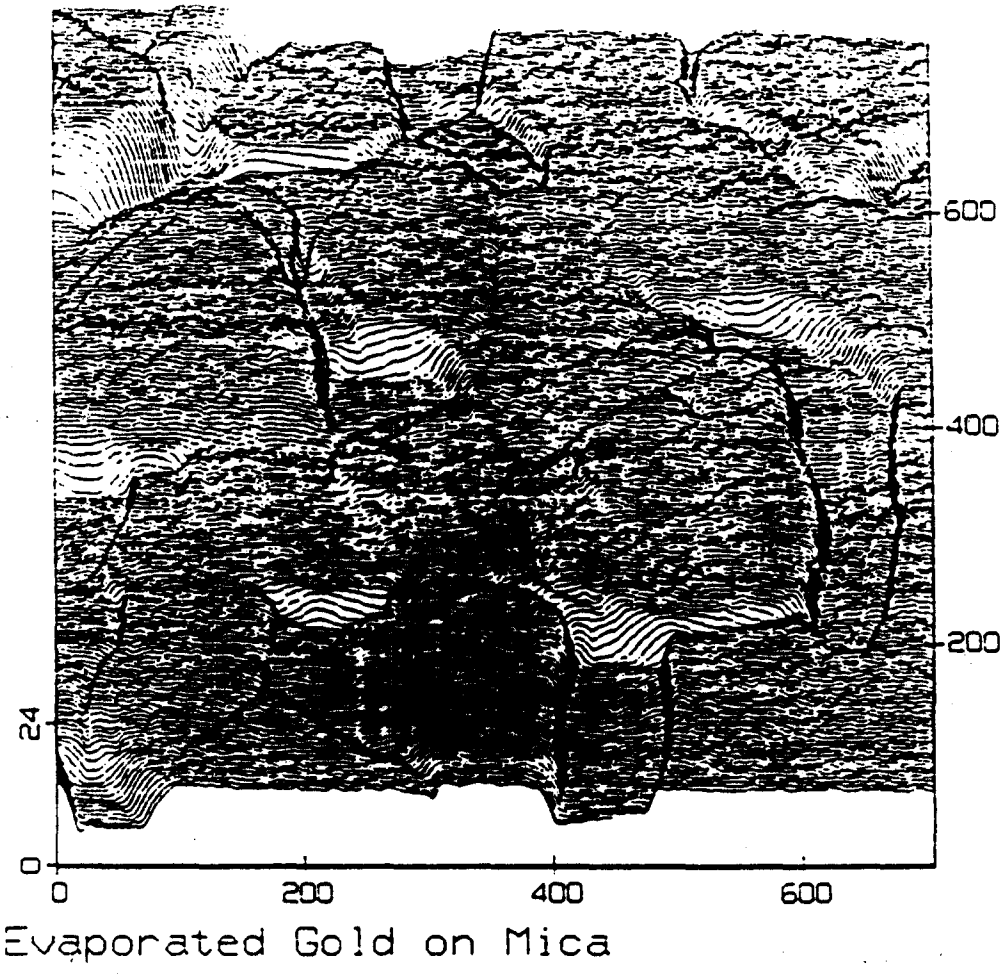

Figure 4

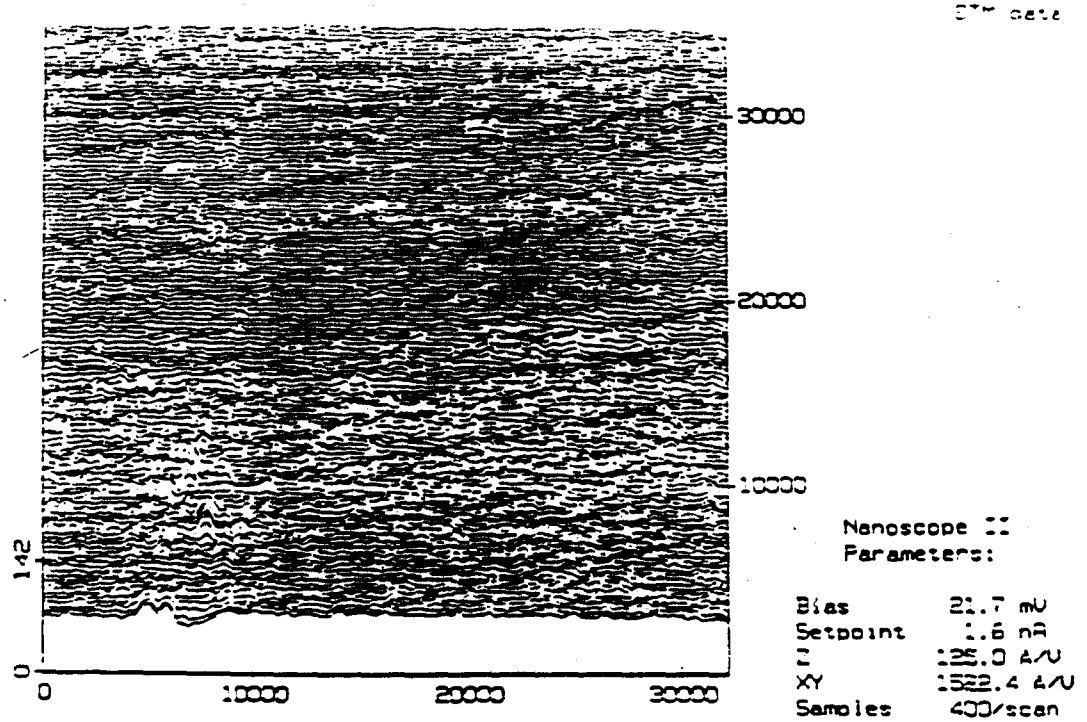
30000
20000
10000
142
0
0
10000
20000
30000
Nanoscope II
Parameters:
Bias 21.7 mV
Setpoint 1.6 nA
Z 125.0 A/V
XY 1522.4 A/V
Samples 400/scan
Evaporated Au on Glass
Data taken Thu Aug 16 17:25:13 1990

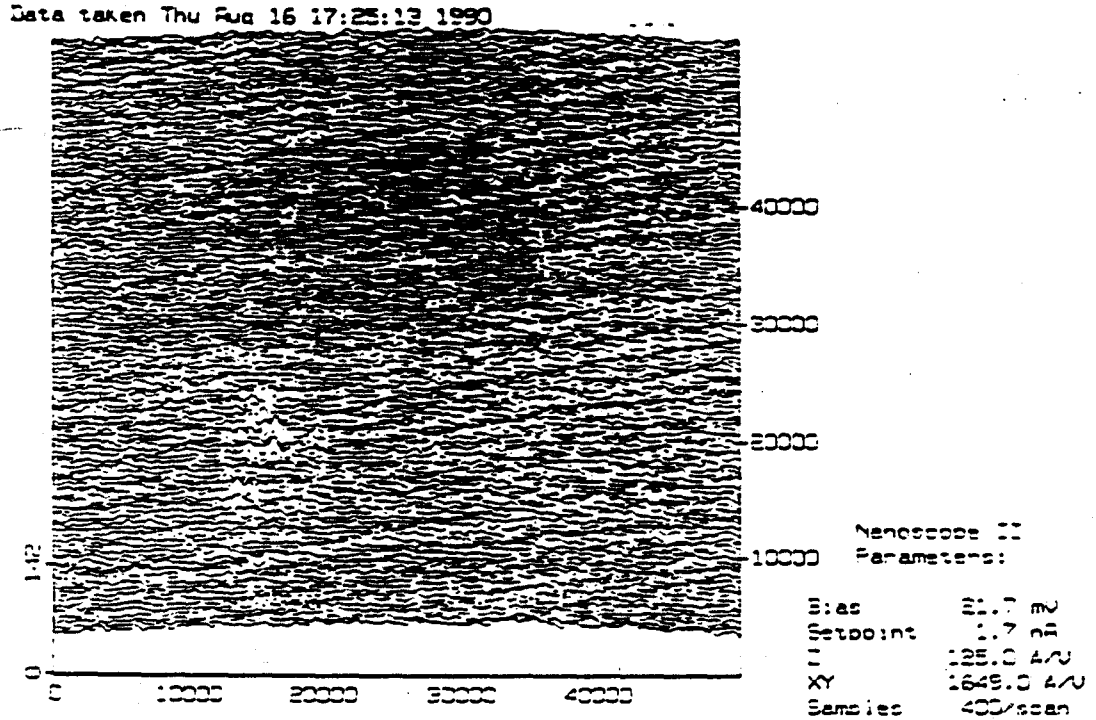
40000
30000
20000
10000
142
0
0
10000
20000
30000
40000
Nanoscope II
Parameters:
Bias 21.7 mV
Setpoint 1.7 nA
Z 125.0 A/V
XY 1649.0 A/V
Samples 400/scan
Evaporated Au on Glass
Data taken Thu Aug 16 17:34:03 1990

Figure 5

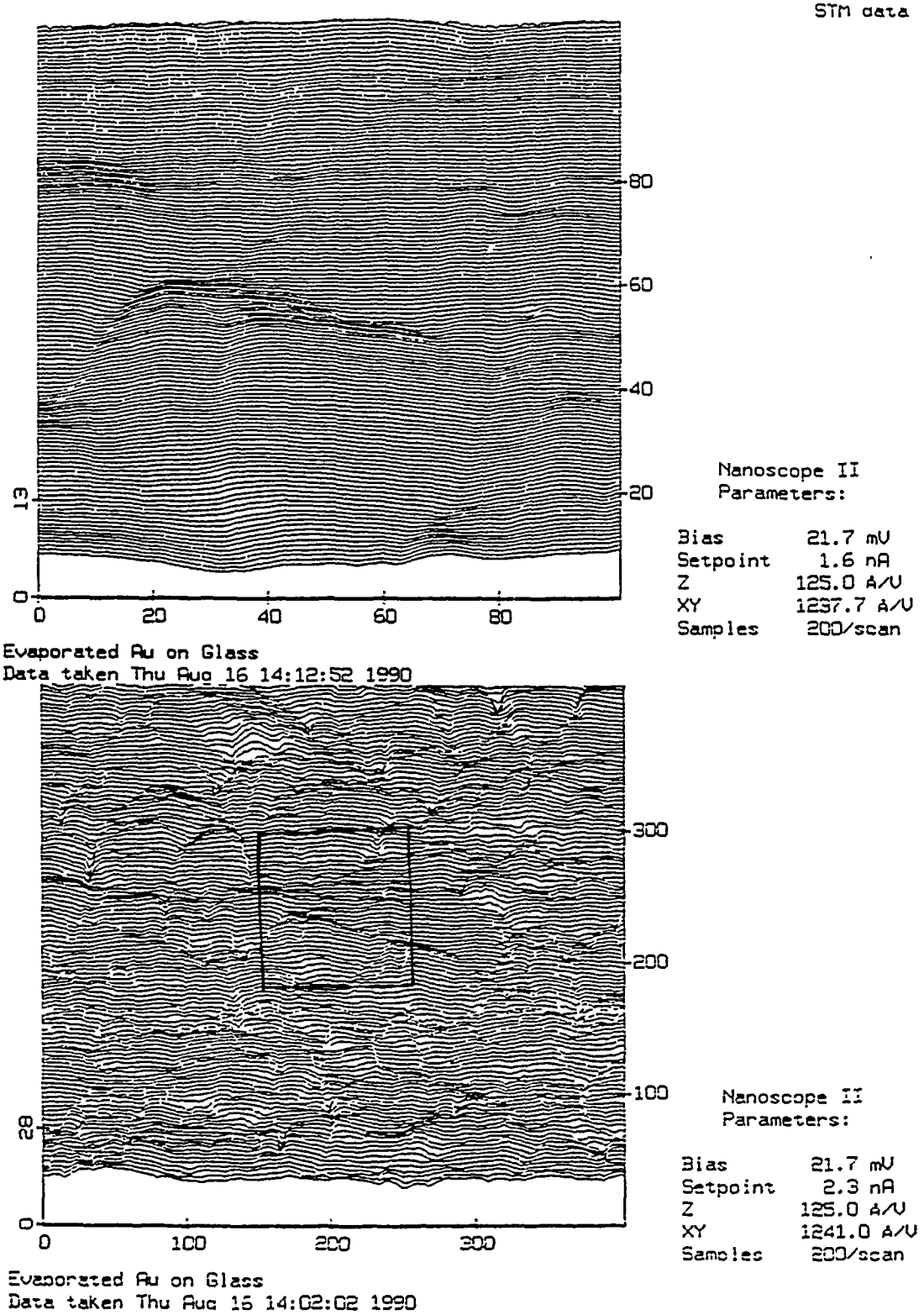
STM data
80
60
40
20
13
0
0
20
40
60
80
Nanoscope II
Parameters:
Bias 21.7 mV
Setpoint 1.6 nA
Z 125.0 A/V
XY 1237.7 A/V
Samples 200/scan
Evaporated Au on Glass
Data taken Thu Aug 16 14:12:52 1990
300
200
100
28
0
0
100
200
300
Nanoscope II
Parameters:
Bias 21.7 mV
Setpoint 2.3 nA
Z 125.0 A/V
XY 1241.0 A/V
Samples 200/scan
Evaporated Au on Glass
Data taken Thu Aug 16 14:02:02 1990

Figure 6

REFERENCES

Binnig,G.,H.Rohrer, "Scanning Tunneling Microscopy- From Birth to Adolescence," Rev. Mod. Phys., 1987, Vol. 59, No.3, pp. 615-625.

Hansma,P.K.,J.Tersoff, "Scanning Tunneling Microscopy,"J. Appl. Phys., 1987, Vol 61, No. 2, pp. R1-R23.

Kuk,Y.,P.J.Silverman, "Scanning Tunneling Microscope Instrumentation," Rev. Sci. Instrum., 1989, Vol. 60, No. 2, pp.165-180.

Dagata,J.A.,et. al., "Modification of Hydrogen-Passivated Silicon by a Scanning Tunneling Microscope Operating in Air," J. Appl. Phys., Vol. 64, No. 7, pp. 3516-3521.

Dagata,J.A.,et. al., "Selective-Area Epitaxial Growth of Gallium Arsenide on Silicon Substrates Patterned Using a Scanning Tunneling Microscope Operating in Air," presented at STM'90/NanoI Conference Baltimore, MD, July 1990.

Takahagi,T.,et al., "The Formation of Hydrogen Passivated Silicon Single-Crystal Surfaces Using Ultraviolet Cleaning and HF Etching,"J. Appl. Phys., 1988, Vol. 64, No.7, pp.3516-3521.

Nakagawa,Y.,et. al., " Scanning Tunneling Microscopy of Silicon Surfaces in Air: Observation of Atomic Images," J. Vac. Sci. Technol. A, 1990, Vol. 50, No. 24, pp. 1742-1744.

Sonnenfeld,R.,et. al., "Semiconductor Topography in Aqueous Environments: Tunneling Microscopy of Chemomechanically Polished (001) GaAs," Appl. Phys. Lett., 1987, Vol. 50, No. 24, pp 1742-1744.

1990 USAF-UES SUMMER FACULTY RESEARCH PROGRAM /

GRADUATE STUDENT RESEARCH PROGRAM

Sponsored by the

AIR FORCE OFFICE OF SCIENTIFIC RESEARCH

Conducted by the

Universal Energy Systems, Inc.

FINAL REPORT

EXPERIMENTAL METHOD, STUDY, & INVESTIGATION OF HIGH ENERGY ABSORBTION OF AS4/3502 GRAPHITE/EPOXY PANELS

Prepared by:	Magna Regina Altamirano
Academic Rank:	Graduate Student / Project Engineer
Department and University:	Mechanical Engineering University of New Orleans
Research Location:	WRDC/FIVST Flight Dynamics Laboratory Wright-Patterson AFB, OH 45433-6553
USAF Researchers:	Greg Czarnecki, Effort Focal Point
Date:	09/30/90
Work Unit No.:	24020261
Contract No.:	F49620-88-C-0053

Final Report

Experimental Method, Study, & Investigation of High Energy Absorbtion of AS4/3502 Graphite/Epoxy Panels

by

Magna Regina Altamirano

ABSTRACT

The study and investigation of high energy absorbtion of AS4/3502 graphite/epoxy panels is facilitated by the experimental method described in this report. Initially, the ballistic limit of the composite panel with a 1/2" steel sphere was determined. Seven different high energy levels with a repeatibility factor of four were chosen for this study. In order to properly assess damage and correlate NDT results with visual inspection, high energy composite damage definitions were added to describe the high velocity impact of composites, such as ply peeling, laminate cratering, and laminate breakage. A parametric energy study determined the experimental variables for theoretical and analytical investigation.

ACKNOWLEDGEMENTS

I wish to thank the Air Force Systems Command, the Air Force Office of Scientific Research, and Wright-Patterson Air Force Base for sponsorship of this research program.

My experience was beneficial and enriching with the positive influence of all the team players participating and contributing in the start up of this research effort. Greg Czarnecki provided support, encouragement, and an enjoyable working atmosphere as the effort focal point for every research phase. Adjusting to this environment was an easy transition with the orientation sessions and tours provided by Greg Czarnecki. Both Greg Czarnecki and Pat Pettit offered many valuable technical suggestions for this research effort. The advise of Dr. David Hui, my thesis advisor, and Dr. Arnold Mayer was also appreciated. The concern of Dr. R.S. Sandhu was also appreciated. The coordinating help from the following people bound our group project together; for this part, special thanks goes to:

James Hodges, Chief, Survivability Enhancement Branch

John Sparks, Chief, Technology Group

Bill Ibinson, Captain U.S. Air Force, ASRF Range Manager

Ricky Peters, Chief, Assessment Group

Joe Pokorski, Technical Manager FIBTA

Kevin Spitzer, Mechanical Engineer

John Daniels, Captain U.S. Air Force

Implementing this research effort could not have been accomplished without the support of the following team which was immensely appreciated:

Cliff Hitchcock, Strain Gage Technician

Raul Santiago, Coop. Engineering Student from University of Puerto Rico

Israel Martinez, Coop. Engineering Student from University of Puerto Rico

Jean Ay, High School Apprenticeship Program

Ron Studebaker, Range Safety Officer

SSgt. Richard Varady, Assistant Range Safety Officer

Larry Coulthard, Assistant Range Safety Officer

Tim Seymour, Range 1 Engineer

Marty Lentz, Principal Engineer, Survivability Enhancement Branch

Synergy team: Doug Coppess
Arvo Erikson
Gary Angel
Jack McCool

The day to day working environment was enhanced by the jovial, optimistic, and intellectual attitude of my office mates, Mike Bennett and John Murphy along with lunches from the members of the close-knit Survivability Enhancement Branch. The success of this research effort was the team spirit from everyone involved for this ten week period. To

coin an old cliche, "a chain is as strong as its weakest link." Most importantly, I wish to thank my parents for teaching me study habits and the value of independence at an early age along with the decision making processes and consequences that accompany this free thinking. Thanks to everyone who contributed to this success.

I. INTRODUCTION: Energy absorbed by composite panels during impact is an issue of vital concern relative to the vulnerability and survivibility of military aircraft during combat. Understanding the behavior of composite materials under extremely short duration time and intense loading contributes to an optimum design and/or improvement of future military aircraft through 'lessons learned' from experimentation. The Technology Group (FIVST) in the Survivability Enhancement Branch is particularly concerned with the incendiary functioning characteristics and penetration mechanics of Soviet API projectiles impacting graphite/epoxy composite panels with varying thicknesses.

My research interests have been in the area of designing systems to study and record a particular engineering phenomena with the appropriate analog to digital data acquisition system. In particular, solid mechanics and its application to real world problems is an area which maintains my interest. Teaching engineering undergraduates material, fluid, and thermodynamic laboratoratories was another contributing factor to my assignment at WPAFB. Developing guidelines for lab reports in the form of a sample format with valuable writing, engineering, investigative, and research suggestions contributed to their experimentation and time management skills and also for their future engineering careers. My diverse work experience in structural engineering, field engineering, project engineering, and finally engineering administration

/ management contributed to my assignment in the Technology Group (FIVST) of the Survivability Enhancement Branch at the Wright Research and Development Center at Wright-Patterson Air Force Base.

II. OBJECTIVES OF THE RESEARCH EFFORT: Currently, there does not exist a comprehensive data base in impact physics for the thorough investigation of high energy impact physics of composites with incendiary functioning characteristics and penetration mechanics of Soviet API projectiles impacting graphite/epoxy composite panels. A basic parametric study of this engineering phenomena without the incendiary functioning characteristics would help in the understanding of the composite fracture mechanics and the high energy absorbtion. Guidelines for conducting this basic parametric study for high energy absorbtion do not currently exist.

My assignment as a participant in the 1990 Summer Graduate Student Research Program was to develop, pursue, and implement an experimental procedure for the study and investigation of high energy absorbtion of AS4/3502 graphite/epoxy panels. An extensive literature search was undertaken to determine the work that currently exists and to avoid duplication of effort. The approach taken and its respective results for this research effort will be developed later in this report.

In order to have a comprehensive study and investigation of this engineering phenomena, additional

experimentation is being performed for an additional ten weeks at the Army Corps of Engineers, Cold Region Research and Engineering Laboratory (CRREL) in Hanover, New Hampshire. CRREL is also co-sponsoring this research effort. It should be emphasized that compression testing on the impacted composite panels will be performed along with ultrasonic immersion c-scans at WPAFB.

Due to the fast paced research effort, the data reduction of the raw data has not yet been reduced and analyzed.

This report will include the completion of Phase I or as outlined below:

I. Introduction

II. Objectives of the Research Effort

III. Theoretical Background

IV. Composite Panel Impact Testing

- A. Pre-Impact Procedures
- B. Impact Test
- C. Post-Impact Procedures

V. Preliminary Experimental Results

VI. Preliminary Conclusions

VII. Recommendations

VIII. Figures

IX. Tables

X. References

NOTE: This is a preliminary Phase I report for the ten week

research effort conducted in the 1990 USAF Summer Graduate Student Research Program. A Phase II interim report will also be written after completion of work performed at CRREL. A more thcrough report with theoretical formulations will be developed as Phase III in my Master of Science thesis from the University of New Orleans. Afterwards, as Phase IV, journal articles will be co-authored and submitted for publication.

III. THEORETICAL BACKGROUND. An extensive literature survey was conducted for this research effort to avoid duplication of work, and a summary of the survey is presented here for an understanding of this engineering phenomena.

The application of composites to a dynamically loaded system requires a knowledge and understanding of

* induced high energy absorbtion at impact
* dynamic loading
* induced wave propagation phenomena
* response of the composite material to produced high strain rates

Many factors contribute to the formulation of induced energy absorbtion at impact, such as

* kinetic energy
* shock and vibration energy
* heat transfer energy
* elastic strain energy
* plastic strain energy

As the projectile strikes the target, the composite material undergoes

* elastic deformation
* plastic deformation
* penetration/failure

During the impact, kinetic energy is produced, compressive waves initially spread into the sphere and composite material, and the reflection of the compressive wave causes a region of tensile stress. Above the yield point, the material response is both elastic and plastic and demonstrates the characteristics of

* Ductility: material able to withstand large strains without failure
* Brittleness: material fails after very little straining

In assessing damage and correlating the NDT results with visual inspection, Strong (1989) has defined several types of damage

* DELAMINATION - Separation of adjacent composite plies
* CRACK - Fractures in matrix and/or fibers
* DENT - A concave depression that does not rupture plies or debond the composite structure
* GOUGE - A special type of dent where some, but not all, composite plies are severed
* IMPACT DAMAGE - Damage from contact with foreign object
* PLY-STRIP PEELING - Outer surface plies peel off away

from impact damage hole in outside fiber direction

* PLY-STRIP CRATERING - At the exit side of the panel, a crater is ballooned outward in the direction of the exiting projectile. The hole at the apex of the crater is usually closed or very slightly opened but usually in a size smaller than the impacting projectile. See punch-through for another interpretation

* FRAGMENTED-PLY PETALING - At impact, a crater is ballooned outward, and plies break off. The speed of the impacting projectiles is rapid enough to break the apex fibers of the crater and cause fragmented-ply petaling.

* FRAGMENTED PUNCH-THROUGH - The impacting projectile has penetrated with enough speed to make and leave a hole with approximately the same size diameter or greater. The local area immediately surrounding the hole is interpenetrated by the projectile causing a crisp or brittle intraply breakage. If the penetration is described as a "punch-through ply-strip crater," then the apex hole created by the impacting projectile on the crater is approximately the size of the projectile diameter or greater.

IV. <u>COMPOSITE PANEL IMPACT TESTING</u>. This experiment is comprised of two main parts along with its set of logical sequential sections:

A. Pre-Impact Procedures

B. Impact Test

C. Post-Impact Procedures

Each section is detailed for the orderly execution of

the experiment. Refer to Table 1 for the equipment list, and refer to Table 2 for the test matrix for high velocity impact with steel spheres on a variety of panels along with the detailed scope of the work and its priority.

Safety precautions should be exercised when handling the composite material. When specimens are water jet cut (to minimize heat-affected zones) to the designed size, the cut edges should be smooth to insure splinters do not exist. Once testing is underway, extreme care with proper ventilation should be taken to prevent inhaling composite material debris. Also, the testing site should periodically be vacuumed to collect the composite material debris

IV.A. PRE-IMPACT PROCEDURES

Before this experiment is started, some pre-impact procedures must be conducted for a thorough investigation of the experimental results. The following steps for this evaluation are

1. Fabricate a test fixture assembly, as shown in Figures 1, 1A, 1B, 1C, and 1D for panel mounting

2. Perform an Ultrasonic Immersion C-Scan on the twenty-two 8" X 8" and 11" X 11" composite panels, and determine the quality of each panel by scanning the material with ultrasonic energy while monitoring the reflected energy for attenuation (diminishing) of the signal

3. Discard panels from the above composite panels that do not meet the quality assurance requirements of excellence. Based on the pre-impact c-scans, the panels

TABLE 1. EQUIPMENT LIST

ITEM NUMBER	EQUIPMENT NAME	QUANTITY	AVAILABILITY
1	Gas gun for high velocity impact	1 Range: 1000 fps to 12000 fps	Yes
2	Ultrasonic Immersion C-Scan	1	Yes
3	Hopkinson Bar Test	1	Yes CERL
4	Strain gages	1 per panel @ 100 panels = 400	
5	Thermocouples	1 per panel @ 100 panels = 100	
6	Graphite epoxy panels (AS3501/3502) SIZE: 8" x 8"	20	
7	Test fixture assembly * Fabricate from A36 steel & 1/4" thick	1 @ size 3"	
8	A/D software to convert signals from item 3 & 4 and plot this data digitally	1	
9	Camera - at test impact recording	1	
10	Rockwell Hardness testing machine	1	completed
11	Break paper to measure velocity	4 per panel @ 100 panels = 400	
12	Compression testing machine	1	
13	Projectiles - spheres SIZE: diam=1/2"	100	acquired

TABLE 2. TEST MATRIX FOR IMPACT EXPERIMENT WITH STEEL SPHERES

PRIORITY	MATERIAL	OBLIQUITY ANGLE (DEG)	NUMBER OF IMPACT VELOCITIES	IMPACT VELOCITIES (FPS)	REPETITIONS	TOTAL
1	Graphite/epoxy, AS4/3502 SIZE: 8" X 8" panels	0	6	ballistic limit 850 1250 2000 3000 4500 6500	4	28

were cut in sections where delamination (in the future area of projectile impact) does not exist. In other words, when the maximum percent at reflected energy for attenuation falls between 62% to 93% or the white-pink-red area. Delamination is seen to occur in the white-pink-red-yellow area but with a predominantly yellow area

4. Perform a random sample Rockwell Hardness Test on the spherical projectiles in order to determine its strength

5. Perform a Hopkinson Bar Test on each AS4/3502 5"X7" composite panel to determine the material's high strain rate behavior for compressive conditions (Experiment location: CRREL, Hanover, New Hampshire)

IV.B. IMPACT TEST

Once the initial condition of the composite panels has been determined and recorded, the actual impact testing for evaluation of the energy absorbed by the composite panel can begin. This projectile impact test involves the following steps

1. Place the break paper on the composite panel to measure terminal velocity of the projectile and also on an additional board behind the composite panel to measure the residual velocity of the projectile

2. Measure deflection by placing two strain gages back to back in a direction transverse to the outer fiber for peak strains as shown in Figure 2

3. Measure temperature by placing one thermocouple next to the strain gages as shown in Figure 2. (The

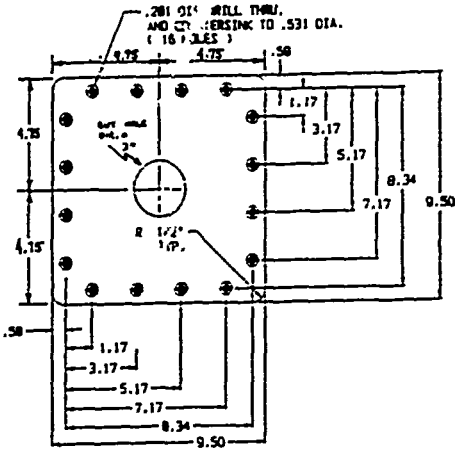

PANEL CLAMP FRAME
MATERIAL: 1/4" THK. x 10" STEEL FLAT

FIGURE 1. TEST FIXTURE ASSEMBLY

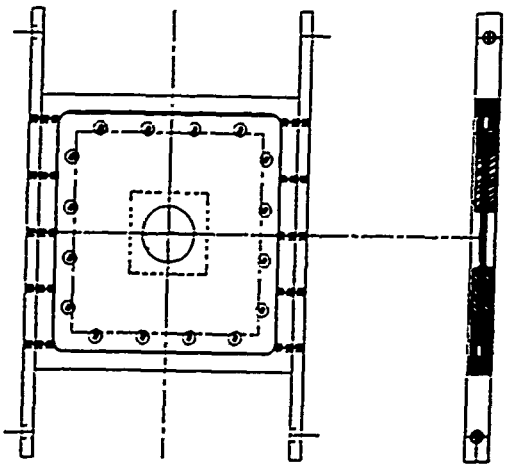

PANEL HOLDER ASSEMBLY

FIGURE 1A. TEST FIXTURE ASSEMBLY

thermocouple will be placed in 1/8" increments from center to search for the phenomena)

4. Connect the Analog-to-Digital hardware to the two strain gages and the thermocouple

5. Calibrate the Analog-to-Digital hardware and software to insure accurate readings

6. Assemble the composite panel on the test fixture assembly as shown Figure 3 to simulate partially clamped boundary conditions

7. Determine ballistic limit for the given test parameters. A minimum of six shots will be taken with

- the three lowest velocities for complete penetration
- the three highest velocities for partial penetration

Assess damage by visually inspecting for gouges, dents, and impact damage. At the transition point between partial and complete penetration, an average of the two velocities was taken to determine the ballistic limit. A recommended spread of 46 m/sec (150 fps) or less between shots is advisable

8. Prepare the gas gun for each set of projectiles, at the speeds specified below

- ballistic limit speed
- 800 fps
- 1000 fps
- 2000 fps
- 3000 fps
- 4500 fps

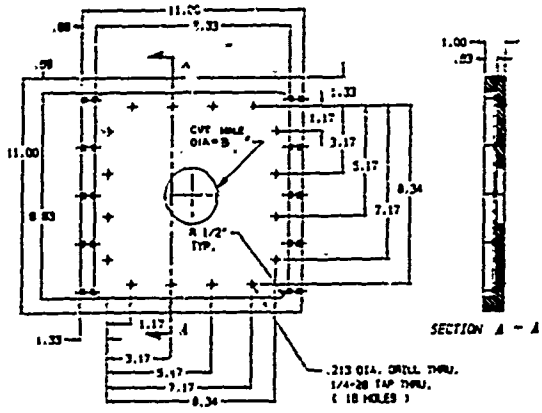

PANEL FRAME
4 REQUIRED
MATERIAL: 1" THK. x 11-1/2" x 11-1/2" STEEL PLATE

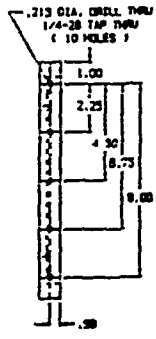

FIGURE 1B. TEST FIXTURE ASSEMBLY

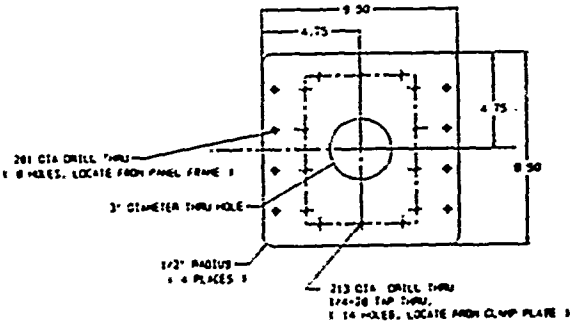

PANEL MOUNTING PLATE
MATERIAL 1/2" THICK STEEL PLATE

FIGURE 1C

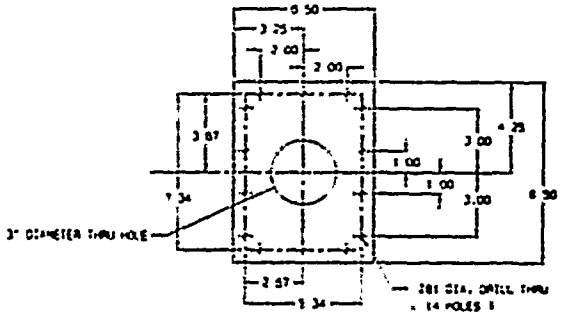

PANEL CLAMP PLATE
MATERIAL 1/4" THICK STEEL PLATE

FIGURE 1D

* 6000 fps

9. Collect the data for the spherical projectiles at each different speed and for the partially clamped boundary condition as outlined on the data sheet shown in Figure 4 and Table 3

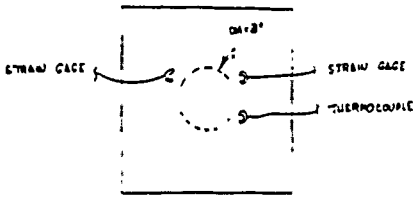

FIGURE 2. STRAIN GAGE AND THERMOCOUPLE MOUNTING DETAILS

REFER TO FIGURE 1. FOR DIMENSIONING DETAILS FOR 16 HOLES

IV.C. POST-IMPACT PROCEDURE

After the experiment is completed, some post-operation procedures must by performed, such as nondestructive testing (NDT) for detecting damage to composite parts. These steps are as follows

1. Shoot color photographs of the forward / back / profile impacted composite panel along with the

* test name description
* front / profile / back view
* accountibility number

2. Perform Ultrasonic Immersion C-Scan on the impacted composite panels

3. Perform a Compression Test (destructive test) on the impacted composite panels to determine the specimen strength of the material via strain gages and A/D hardware and software. Next, sketch a figure showing location.

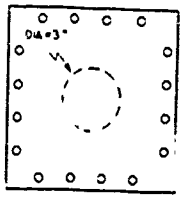

FIGURE 3. SET-UP FOR INITIAL BOUNDARY CONDITIONS

The parameters for the Compression Test are as follows:

A. Loading rate = 0.05 in/min

B. Fastest acquisition time for better resolution

C. Fastest sampling rate to capture the

correct data curve

D. Test an uninstrumented and undamaged panel at a loading rate of 0.05 in/min at the fastest acquistion time and fastest sampling rate, and record any buckling effects at this loading rate. If there is no buckling effect, then this will determine the loading rate for this test.

E. Perform a C-scan of the compressed composite panel. This will determine the best location for the strain gages for both the undamaged and impacted composite panels by finding the less compressed-damaged c-scan area. The instrumented undamaged panels will serve as the control specimen when comparing the results with the instrumented impacted composite panels.

F. Based on Step E, place the strain gages as shown on future sketch

G. Perform the Compression Test on both the instrumented undamaged and damaged panels. Refer to Table 4 for experiment data sheet.

H. Record and plot the data with the strain gage factors included in the plotting program, if this is possible. Store data on a disc in ASCII format if possible.

I. Record and plot the compression test data, and store on disc in ASCII format

J. Sketch the compression failure line for each specimen

K. Shoot photographs of the forward /

FIGURE 4 . DATA SHEET FOR COMPOSITE PANEL TEST

PRE-IMPACT TEST PHASE												IMPACT TEST PHASE						POST-IMPACT TEST PHASE				
BOUNDARY CONDITIONS	PROJECTILE SHAPE: SOURCE	PROJECTILE SHAPE: CODE	WEIGHT	ACCOUSTIC HARDNESS TEST	MATERIAL	COMPOSITE PANEL CHARACTERISTICS: ACCOUSTIC LOCATION	ULTRASONIC C-SCAN: SCANNING SYSTEM USED	ULTRASONIC C-SCAN: PANEL SCANNED	DATA ACQUISITION: TIME DATA ACQUISITION COMPLETED	DATA ACQUISITION: ULTRASONIC C-SCAN DATA ACQUISITION COMPLETED	TERMINAL ACCEPT VELOCITY (fps)	ACTUAL TERMINAL VELOCITY (fps)	RESIDUAL VELOCITY (fps)	STRAIN GAGE READING	THERMOCOUPLE READING	ULTRASONIC C-SCAN: PANEL SCANNED	ULTRASONIC C-SCAN: SCAN COMPLETED	TESTING TEST COMPLETED

profile / back compression tested composite panel along with the

- test name description
- front / profile / back view
- accountibility number

for the documented visual inspection.

L. Perform an ultrasonic immersion c-scan on the compression tested composite panels.

V. PRELIMINARY EXPERIMENTAL RESULTS

Due to the fast paced research effort, the raw data for this experiment has not been reduced or analyzed completely. Preliminary results with the Residual Energy Versus Impact Velocity are shown in Figure 5. The raw data from the 168 strain gages and 10 thermocouples is still being reduced and checked. The ultrasonic immersion c-scans for the impacted composite panels are in transit, and the experiment parameters for the post-impact compression test are currently being resolved. One specimen from each high energy group will be deplied to study the intraply (within or between ply layers) fracture mechanism.

VI. PRELIMINARY CONCLUSIONS

Preliminary results lead one to conclude that

- the thermocouple's response time was not rapid enough to capture the heat transfer during impact
- at all high velocity impacts, delamination and cracking exists

Table 3. Impact Data

ID NO.	WT. OF PLATE, PRE-IMPACT (G)	WT OF PLATE, POST-IMPACT (G)	PLUG WEIGHT (G)	VELOCITY, IMPACT (FPS)	VELOCITY, RESIDUAL (FPS)

DATE	PANEL #	IMPACT ENERGY (FT-LB)	FRONT PANEL DESCRIPTION & SKETCH	BACK PANEL DESCRIPTION & SKETCH

Table 4. Compression Test Data Sheet

Techniques for Battle Damaged Composite Surfaces. Technical Report AFWAL-TR-88-3086, Wright-Patterson Air Force Base, 1988.

Daniel, I.M. & T. Liber. Wave Propagation in Fiber Composite Laminates / Final Report - Part II. Technical Report NASA CR-135086 & IITRI D6073-III, 1976.

Jacobson, M.J. et al. Survivable Composite Integral Fuel Tanks. Technical Report AFWAL-TR-85-3085. Vol 1. Hawthorne, CA: Northrop Corporation, Aircraft Division, 1985.

Meguid, S.A. Engineering Fracture Mechanics. New York: Elsevier Science Publishing Co. Inc., 1989.

Pettit, Pat. High Energy Impact Physics of Composites / Task I / Incendiary Functioning Characteristics and Penetration Mechanics SovieteAPI Projectiles Impacting Graphite/Epoxy Composite Panels. Wright-Patterson Air Force Base: Test Plan, 1990

SACMA Recommended Test Method for Compression After Impact Properties of Oriented Fiber-Resin Composites. SRM 2-88 Arlington, VA: Suppliers of Advanced Composite Materials Association, 1988.

Schwartz, Dr. Charles S. et al. Safe Handling of Advanced Composite Materials Components: Health Information. Arlington, VA: Suppliers of Advanced Composite Materials Association, 1989.

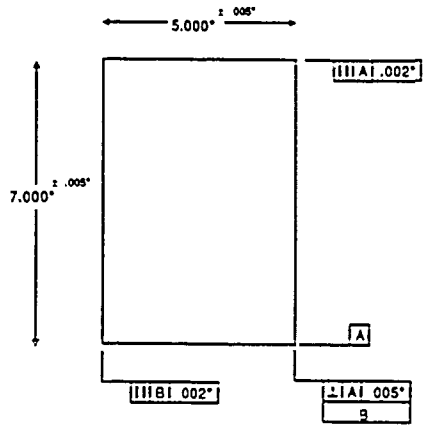

SPECIMEN DIMENSIONS ENERGY ABSORBTION GRAPHITE EPOXY PLATES FOR MAGNA R. ALTAMIRANO 24020261 11 JULY 1990	WRDC/FIBC COMPOSITES FACILITY

ROCKWELL C HARDNESS TEST

Rockwell C Hardness Test for 1/2 " Diameter Spheres

SPECIMEN NUMBER	ROCKWELL HARDNESS NUMBER
1	62C
2	60C
3	62C
4	62C
5	60C
6	60C
7	62C
8	60C
9	61C
10	61C
AVERAGE	61C

as energy increases, the damage or fracture mechanism appears to flow into two distinctive regimes, namely

- the lower velocity regime (370 - 1260 fps) with an equal amount of fragmented-ply petaling, ply-strip crater, and ply-peeling. No correlation can be made between the fracture mechanism and the high velocities or energies - only that fragmented punch-through does not occur in this region, and

- the higher velocity regime (2200 - 5890 fps) with the dominant damage mechanism of fragmented punch-through and ply-strip peeling. Likewise, at higher energy levels, the fracture mechanism trend is the later mode.

VII. RECOMMENDATIONS

Further testing is recommended for the lower velocity regime with a range incremented at a level where the transition between various types of fracture mechanisms can be easily distinguished. The repeatibillity factor of four should be increased to allow for repeatibilty in destructive testing. Also, a thermocouple with a faster response time is recommended.

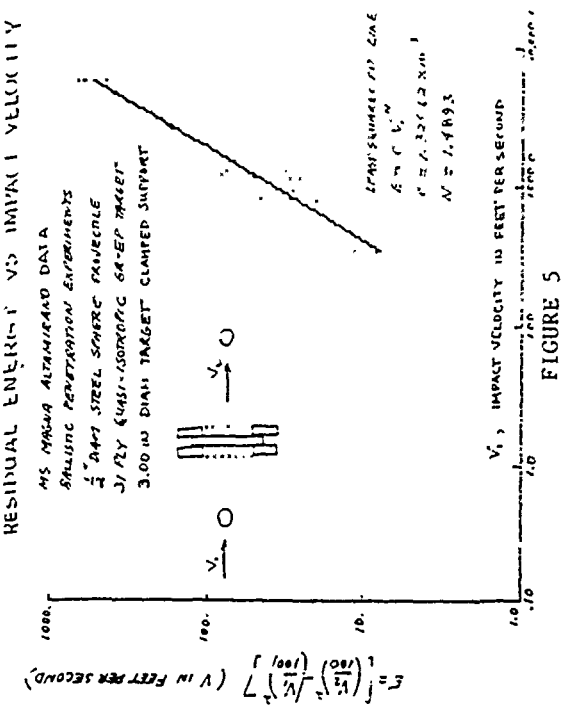

FIGURE 5

X. REFERENCES

Ball, Robert E. The Fundamentals of Aircraft Combat Survivability Analysis and Design. New York: American Institute of Aeronautics & Astronautics, Inc, 1985.

Czarnecki, Gregory. High-Speed Airflow Damage Attenuation

Standard Tests for Toughened Resin Composites - Revised Edition. NASA Reference Publication 1092, 1983.

Strong, Dr. Brent. Fundamentals of Composites Manufacturing. Dearborn, Michigan: Society of Manufacturing Engineers, 1989.

Zukas, Jonas A. et al. Impact Dynamics. USA: John Wiley & Sons, 1982.

1990 USAF-UES SUMMER FACULTY RESEARCH PROGRAM/

GRADUATE STUDENT RESEARCH PROGRAM

Sponsored by the

AIR FORCE OFFICE OF SCIENTIFIC RESEARCH

Conducted by the

Universal Energy Systems, Inc.

FINAL REPORT

Method of Characteristics applied to Supersonic/ Hypersonic Panel Flutter

Prepared by:	Frank R. Chavez
Academic Rank:	Graduate Student
Department and University:	Mechanical Engineering Arizona State University
Research Location:	Flight Dynamics Lab WRDC/FIBR Wright Patterson AFB Dayton, Ohio 45433-6553
USAF Researcher:	V. B. Venkayya
Date:	20 Sept. 1990
Contract No:	F49620-88-C-0053

Method of Characteristics applied to Supersonic/ Hypersonic Panel Flutter

by

Frank R. Chavez

ABSTRACT

The two-dimensional unsteady supersonic/hypersonic flow over an oscillating wedge with an attached oscillating shock for use in a panel flutter analysis is investigated by linearizing the unsteady two-dimensional Euler equations of motion, along with the Isentropic flow condition equation, about uniform flow behind an attached steady straight shock. The boundary condition on the wedge surface and the Rankine-Hugoniot shock boundary conditions are also linearized. The numerical Method of Characteristics is then applied to the set of linearized equations of motion in an attempt to solve for the unsteady pressure distribution over the oscillating wedge.

ACKNOWLEDGEMENTS

I wish to thank the Air Force Systems Command and the Air Force Office of Scientific Research for sponsorship of this research. Universal Energy Systems is also mentioned for their help to me in the administrative aspects of the program and for their interest in my personal concerns.

My experience was rewarding in other aspect than the research completed. The dedication to work and research I observed in the engineers at the Flight Dynamics Lab, especially in Dr. Venkayya, has given me renewd self-motivation in this and other research projects with which I am involved. Bill Johnson is also included for providing an enjoyable work envirinment and for relating his personal experiences to me concerning the engineering profession as a whole.

I. INTRODUCTION:

Several theories have been applied to the study of unsteady supersonic/hypersonic flow behind a shock for panel flutter analysis; ie., Linear Potential Theory using the Acceleration Potential (Ref. 1), Nonlinear Potential Theory (Ref. 2), Piston Theory (Ref. 3), and Unsteady Newtonian Theory (Ref. 4). These theories are characterized by the assumptions and/or idealizations made in their development. As a result of the assumptions and/or idealizations, there are restrictions on the applicability of the above theories. Linear Potential Theory does not account for thickness or rotationality attributed to the presence of the shock. Nonlinear Potential Theory also does not account for rotationality. Piston Theory, which is used quite extensively, is a one-dimensional theory whose applicable domain for supersonic/hypersonic flow is not well defined, and Newtonian Theory is limited to the upper hypersonic domain.

Because the present solution technique is an "exact" solution to the linearized equations, the only restrictions on the applicability are that the shock must be attached and that of small disturbances to the mean flow, which is also a common restriction to the above mentioned theories. The present solution is applicable for all range of Mach numbers in the supersonic/hypersonic domain; therefore, it can be considered a unified supersonic/hypersonic theory.

II. OBJECTIVE OF THE RESEARCH EFFORT:

The two-dimensional unsteady Euler equations of motion and the Isentropic flow condition equation are to be linearized by assuming that the flow variables can be written as a sum of two terms. The first term is the steady mean flow value and the second term is an unsteady small perterbation from the mean flow that is to be determined numerically by the Method of Characteristics. The linearization process results in a set of four equations for the four unknown perterbation flow variables; ie., pressure, density, and the two flow velocity components. Combining these equations properly results in a single linear partial differential equation for the perterbation pressure.

The boundary condition on the wedge surface is also linearized. This linearization process is straight forward and results in the same condition used for all other linear theories for unsteady flow.

The boundary conditions at the shock are determined by linearizing the Rankine-Hugoniot shock conditions. This linearization process results in a second set of four equations involving the unknown perterbation flow variables mentioned above and a fifth unknown variable which represents the unsteady shock motion; ie., f. This function is to be determined simultaneously with the flow variables as part of the solution procedure.

With the problem formulation complete; ie., determination of the linearized equations of motion and the linearized boundary conditions, the Method of Characteristics is now applied to determine the characteristic directions of the system; ie., the equations of motion. Along these characteristics, the partial derivatives become total derivatives and an "exact" solution can proceed along these directions. It turns out that the characteristics of the system are linear and the direction angle is not parallel to the mean shock angle. Because the characteristics of the system intersect the mean shock position, information from left running characteristics is reflected and propagated along right running characteristics. This is a consequence of the supersonic nature of the flow. At the shock boundary, the unknown shock function, f, is introduced and gives rise to a problem in solving the set of linear equations. There seems to be an indeterminacy for this function; ie., to many unknowns and not enough equations. Until this problem can be overcome, the pressure distribution can not be determined for this approach.

III.

a. The two-dimensional Euler equations and the Isentropic flow condition equation are written as

$$\frac{\partial \bar{\rho}}{\partial \bar{t}} + \frac{\partial}{\partial \bar{x}}(\bar{\rho}\,\bar{u}) + \frac{\partial}{\partial \bar{y}}(\bar{\rho}\,\bar{v}) = 0 \qquad 1$$

$$\frac{\partial \bar{u}}{\partial \bar{t}} + \bar{u}\frac{\partial \bar{u}}{\partial \bar{x}} + \bar{v}\frac{\partial \bar{u}}{\partial \bar{y}} = -\frac{1}{\bar{\rho}}\frac{\partial \bar{P}}{\partial \bar{x}} \qquad 2$$

$$\frac{\partial \bar{v}}{\partial \bar{t}} + \bar{u}\frac{\partial \bar{v}}{\partial \bar{x}} + \bar{v}\frac{\partial \bar{v}}{\partial \bar{y}} = -\frac{1}{\bar{\rho}}\frac{\partial \bar{P}}{\partial \bar{y}} \qquad 3$$

$$\frac{\partial}{\partial \bar{t}}\left(\frac{\bar{P}}{\bar{\rho}^{\gamma}}\right) + \bar{u}\frac{\partial}{\partial \bar{x}}\left(\frac{\bar{P}}{\bar{\rho}^{\gamma}}\right) + \bar{v}\frac{\partial}{\partial \bar{y}}\left(\frac{\bar{P}}{\bar{\rho}^{\gamma}}\right) = 0 \qquad 4$$

$\bar{P} \equiv$ flow pressure
$\bar{\rho} \equiv$ flow density
$\bar{u} \equiv$ flow velocity in the $\bar{x}$ direction
$\bar{v} \equiv$ flow velocity in the $\bar{y}$ direction

The coordinate system for the above equations along with the wedge and shock orientation is shown in fig.1. Following the work of Hui (Ref. 5), the above flow variables can be written in terms of a steady mean flow value and an unsteady small perterbation value; ie.,

$$\bar{P} = P_o(1 + \varepsilon P) \qquad 5$$

$$\bar{\rho} = \rho_o(1 + \varepsilon \rho) \qquad 6$$

$$\bar{u} = u_o(1 + \varepsilon u) \qquad 7$$

$$\bar{v} = u_o(\varepsilon v) \qquad 8$$

The length parameters $\bar{x}$ and $\bar{y}$ can be written as $\bar{x}=\bar{l}x$ and $\bar{y}=\bar{l}y$, where $\bar{l}$ is a reference length.

b. Substituting eq.'s 5 thru 8 into eq.'s 1 thru 4 and retaining only first order terms in epsilon gives the linearized equations of motion as

$$\frac{\partial \rho}{\partial t} + \frac{\partial \rho}{\partial x} + \frac{\partial u}{\partial x} + \frac{\partial v}{\partial y} = 0 \qquad 9$$

$$\frac{\partial u}{\partial t} + \frac{\partial u}{\partial x} + \frac{P_o}{\rho_o u_o^2}\frac{\partial P}{\partial x} = 0 \qquad 10$$

$$\frac{\partial v}{\partial t} + \frac{\partial v}{\partial x} + \frac{P_o}{\rho_o u_o^2}\frac{\partial P}{\partial y} = 0 \qquad 11$$

$$\left(\frac{\partial P}{\partial t} + \frac{\partial P}{\partial x}\right) - \gamma\left(\frac{\partial \rho}{\partial t} + \frac{\partial \rho}{\partial x}\right) = 0 \qquad 12$$

with $t = \frac{u_o}{\bar{l}}\bar{t}$

A single equation involving only the pressure P is now derived. Substituting eq.12 into eq. 9 for the density gives

$$\frac{1}{\gamma}\left(\frac{\partial P}{\partial t} + \frac{\partial P}{\partial x}\right) + \frac{\partial u}{\partial x} + \frac{\partial v}{\partial y} = 0 \qquad 9a$$

Differentiating eq. 9a with respect to x and t gives two equations

$$\frac{1}{\gamma}\left(P_{tx} + P_{xx}\right) + u_{xx} + v_{yx} = 0 \qquad 9b$$

$$\frac{1}{\gamma}\left(P_{tt} + P_{xt}\right) + u_{xt} + v_{yt} = 0 \qquad 9c$$

where the subscript refers to partial differentiation with respect to that variable. Now, differentiating eq. 10 with respect to x,

substituting into 9b for u_{xx} , and adding the resulting equation to 9c gives

$$P_{xx} + 2P_{xt} + P_{tt} - \frac{\gamma P_o}{\rho_o u_o^2} P_{xx} + \gamma(v_x + v_t)_y = 0 \qquad 13$$

Differentiating eq. 11 with respect to y and substituting into eq. 13 gives

$$\left(P_{xx} + 2P_{xt} + P_{tt}\right) - \frac{\gamma P_o}{\rho_o u_o^2}\left(P_{xx} + P_{yy}\right) = 0 \qquad 13a$$

Noting that $\frac{\gamma P_o}{\rho_o} = a_o$ (≡ mean flow speed of sound), eq. 13a is written as

$$(M_o^2 - 1)P_{xx} - P_{yy} + 2M_o^2 P_{xt} + M_o^2 P_{tt} = 0 \qquad 14$$

It is interesting to note that eq. 14 is the same equation for the perterbation velocity potential in subsonic and supersonic flow.

IV.

a. The boundary condition at the wedge surface is given as

$$\frac{\partial \bar{G}}{\partial \bar{t}} + \bar{u}\frac{\partial \bar{G}}{\partial \bar{x}} + \bar{v}\frac{\partial \bar{G}}{\partial \bar{y}} = 0 \qquad 15$$

where $\bar{G}(\bar{x},\bar{y},\bar{t})$ is the wedge surface equation given by

$$\bar{G}(\bar{x},\bar{y},\bar{t}) = \bar{y} - \varepsilon\bar{\delta}(\bar{x},\bar{t}) = 0 \qquad 16$$

and $\bar{\delta}(\bar{x}, \bar{t})$ is the known wedge surface oscillation function.

b. Substituting eq.'s 5 thru 8 into eq. 15 gives the linearized wedge surface boundary condition equation as

$$v(x,0,t) = \delta_t(x,t) + \delta_x(x,t) \qquad 17$$

V.

a. The Rankine-Hugoniot shock conditions in terms of (x,y,t) are given as

$$\left[\rho\left(u_o \frac{\partial F}{\partial t} + \vec{V}\bullet\nabla F\right)\right]_{\infty}^{+s} = 0 \qquad 18$$

$$\left[\vec{V}\bullet\vec{\tau}\right]_{\infty}^{+s} = 0 \qquad 19$$

$$\left[\rho\left(u_o \frac{\partial F}{\partial t} + \vec{V}\bullet\nabla F\right)^2 + (\nabla F)^2 P\right]_{\infty}^{+s} = 0 \qquad 20$$

$$\left[\frac{1}{2}\left(u_o \frac{\partial F}{\partial t} + \vec{V}\bullet\nabla F\right)^2 + (\nabla F)^2 h\right]_{\infty}^{+s} = 0 \qquad 21$$

where (∞) refers to the left side of the shock and (+s) refers to the right side of the shock inside the region of interest. In the above equations, the flow variables at (∞) are written as P_∞ , ρ_∞ , $\vec{V}_\infty$,and at (+s) the flow variables are given by eq.'s 5 thru 8. The vectors are expressed in terms of the (x,y) coordinate system and $\vec{\tau}$ is a vector in

the tangential direction to the shock. The function F is the shock shape function given by

$$F(x,y,t) = y - x\tan\varphi - \varepsilon f(x,t) = 0 \qquad 22$$

b. Expanding the above shock equations and retaining only first order terms in epsilon results in two sets of four equations, one set for the steady mean flow values and one set for the unsteady perterbation flow values along with the unknown shock function f. The two sets are written as

$$\rho_o u_o \sin\varphi = \rho_\infty U_\infty \sin\beta \qquad 23$$

$$u_o \cos\varphi = U_\infty \cos\beta \qquad 24$$

$$P_o + \rho_o u_o^2 \sin^2\varphi = P_\infty + \rho_\infty U_\infty^2 \sin^2\beta \qquad 25$$

$$h_o + \frac{1}{2}u_o^2 = h_\infty + \frac{1}{2}U_\infty^2 \qquad 26$$

and

$$u\tan\varphi - v + \rho\tan\varphi = \left(\frac{\rho_\infty}{\rho_o} - 1\right)\frac{\partial f}{\partial t} + \left(\frac{\rho_\infty}{\rho_o} - 1\right)\cos^2\varphi\frac{\partial f}{\partial x} \qquad 27$$

$$u + v\tan\varphi = \left(1 - \frac{\rho_o}{\rho_\infty}\right)\sin\varphi\cos\varphi\frac{\partial f}{\partial x} \qquad 28$$

$$u\tan\varphi - v + \frac{1}{2}P\frac{1}{\gamma M_o^2}\frac{1}{\sin\varphi\cos\varphi} + \frac{1}{2}\rho\tan\varphi = 0 \qquad 29$$

$$u + P\frac{1}{(\gamma-1)M_o^2} - \rho\frac{1}{(\gamma-1)M_o^2} = \left(\frac{\rho_o}{\rho_\infty} - 1\right)\sin\varphi\cos\varphi\frac{\partial f}{\partial t} \qquad 30$$

Equations 23 thru 26 are solved for the mean flow values in terms of the undisturbed flow parameters at (∞). Equations 27 thru 30 are the linearized boundary conditions for the unsteady perterbation flow variables evaluated at the mean shock position; ie., $y = x\tan\varphi$. Note that the unknown shock function, f, is not expressed explicitly but in derivative form.

VI.

a. The disturbance at the wedge surface is assumed to be periodic; ie., $\delta(x,t) = \Delta(x)e^{ikt}$. The linear nature of the problem allows the flow parameters also to be assumed periodic of the same form. Equations 9 thru 12 can be written as

$$\frac{1}{\gamma}(ikP + \frac{\partial P}{\partial x}) + \frac{\partial u}{\partial x} + \frac{\partial v}{\partial y} = 0 \qquad 31$$

$$iku + \frac{\partial u}{\partial x} + \frac{P_o}{\rho_o u_o^2}\frac{\partial P}{\partial x} = 0 \qquad 32$$

$$ikv + \frac{\partial v}{\partial x} + \frac{P_o}{\rho_o u_o^2}\frac{\partial P}{\partial y} = 0 \qquad 33$$

where the density has been elliminated by combinig eq.'s 9 and 12. If eq.'s 31 thru 33 are written in the matrix form

$$\frac{\partial \vec{z}}{\partial x} + [A]\frac{\partial \vec{z}}{\partial y} + \vec{b} = \vec{0} \qquad 34$$

where $\vec{z} = [u,v,P]^T$ and [A] is a constant matrix, then the Method of Characteristics can be applied as follows.

$$\vec{w}_i^T\left[\frac{d\vec{z}}{dx} + \vec{b}\right] = 0 \qquad i = 1,2,3 \qquad (35)$$

where the total derivative is taken along the characteristic directions given by $dy = \lambda_i dx$. The $\vec{w}_i$ are the left-eigenvectors and the λ_i are the eigenvalues of the matrix [A].

b. The characteristic directions are constant and are determined to be

$$\lambda_1 = -\frac{1}{\beta}, \quad \lambda_2 = 0, \quad \lambda_3 = \frac{1}{\beta} \quad \text{with} \quad \beta = \sqrt{M_o^2 - 1}$$

Along these directions the equations of motion can be writen as

$$\frac{dv}{dx} - \frac{\beta}{\gamma M_o^2}\frac{dP}{dx} + ik\left(\frac{1}{\beta}u + v - \frac{1}{\gamma\beta}P\right) = 0 \qquad \text{along } \lambda_1 \qquad (36)$$

$$\frac{du}{dx} + \frac{1}{\gamma M_o^2}\frac{dP}{dx} + iku = 0 \qquad \text{along } \lambda_2 \qquad (37)$$

$$\frac{dv}{dx} + \frac{\beta}{\gamma M_o^2}\frac{dP}{dx} + ik\left(-\frac{1}{\beta}u + v + \frac{1}{\gamma\beta}P\right) = 0 \qquad \text{along } \lambda_3 \qquad (38)$$

The above equations can now be approximated by a second-order accurate (in Δx) numerical scheme along the three characteristic directions. This results in a set of three equations for the three

unknow flow parameters at a point in the region of interest; ie., the intersection of the three characteristic direction lines, as a function of the values upstream of the characteristic directions. At the intersections of the left and right-running characteristics and the mean shock position, the unknown shock function, f,is introduced and there is now an extra unknown in the set of three equations. The interior region; ie., the region bounded by the shock and the wedge surface, can not be determined until this unknown function, f, can be evaluated.

VII. RECOMMENDATIONS:

Three ideas are presented here as suggestions for determining the unknown function, f, at the shock boundary.

a. The sets of equations at each interior point along with the sets of equations involving the unknown function, f, along the mean shock position can be written in matrix form. This matrix equation can then be solved for all the unknowns simultaneously. This method would result in the decomposition or inversion of a very large matrix which would negate the advantages of differentiating and moving along the characteristic directions.

b. A continuity condition on f; ie., that f and its derivatives are continuous, along the mean shock position based on physical and/or

geometrical arguments can yield another equation with which to solve for the four unknows at the shock boundary.

c. Equation 14 can be used to yield another equation to solve for the four unknowns at the shock boundary. Because eq. 14 was derived from the same equations used to determine the characteristic equations, this might introduce redundant information.

A proposal to AFOSR will be prepared in order to obtain a Mini-Grant to continue the present research in an effort to determine a method by which the shock shape function, f, can be evaluated. After a proper method has been determined, the pressure distribution over the wedge surface can be solved. With the pressure distribution known, a Panel Flutter analysis can be performed.

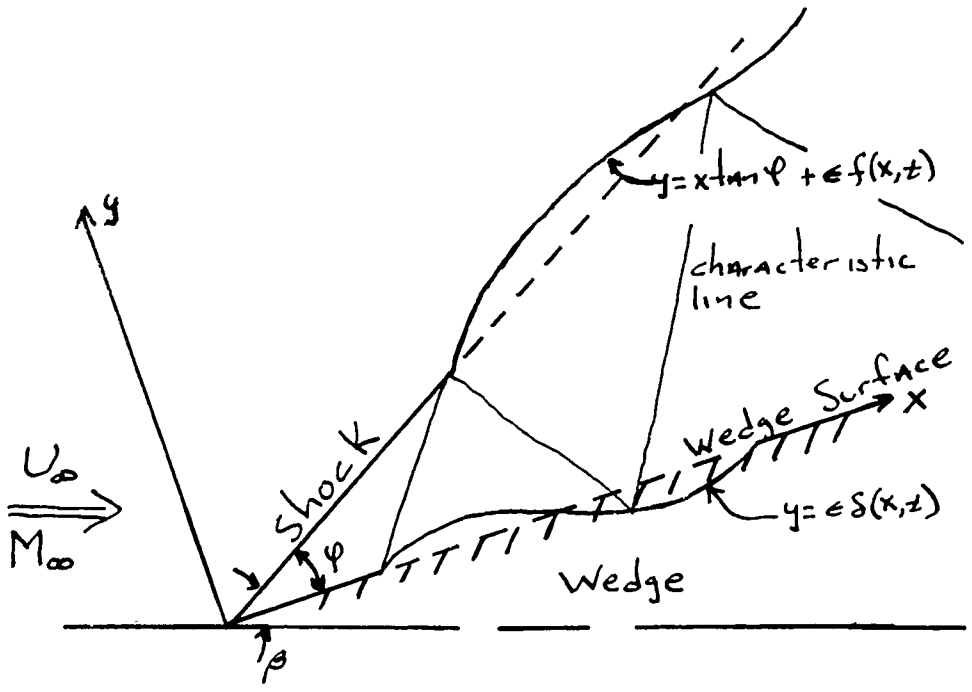

FIGURE 1. Wedge and Shock Coordinate System

REFERENCES

1. Cunningham, H. J., "Flutter Analysis of Flat Rectangular Panels Based on Three-Dimensional Supersonic Potential Flow," AIAA Journal, Vol. 1, No. 8, August 1963, pp.1795-1801.

2. Landahl, M. T., "Unsteady Flow Around Thin Wings at High Mach Numbers," Journal of Aerospace Sciences, January 1957, pp. 33-38.

3. Ashley, H. and Zartarian, G., "Piston Theory-A New Aerodynamic Tool for the Aeroelastician," Journal of the Aeronautical Sciences, Vol. 23, No. 13, December 1956, pp. 1109-1118

4. Hui, W. H. and Tobak, M., "Unsteady Newton-Busemann Flow Theory, Part I: Airfoils," AIAA Journal, Vol. 19, No. 3, 1981, pp. 311-318

5. Hui, W. H. , "Perterbation Theory for Hypersonic Flow," Phd. Thesis University of Southhampton,1968

1990 USAF-UES SUMMER FACULTY RESEARCH PROGRAM/

GRADUATE STUDENT RESEARCH PROGRAM

Sponsored by the

AIR FORCE OFFICE OF SCIENTIFIC RESEARCH

Conducted by the

Universal Energy Systems, Inc.

FINAL REPORT

PRELIMINARY INVESTIGATION OF THE STRUCTURAL DURABILITY OF AIRCRAFT TIRES

Prepared by:	Patrick M. Fourspring
Academic Rank:	Graduate Student
Department and University:	Engineering Science and Mechanics The Pennsylvania State University
Research Location:	Wright-Patterson Air Force Base Wright Research and Development Center Flight Dynamics Laboratory Vehicle Subsytems Division Aircraft Launch and Recovery Branch
USAF Researcher:	Gary J. Migut

Date:	27 August 1990
Contract No:	F49620-88-C-0053

PRELIMINARY INVESTIGATION OF THE STRUCTURAL DURABILITY OF AIRCRAFT TIRES

by

Patrick M. Fourspring

ABSTRACT

To better analyze the operational life of a tire, the United States Air Force has established the Tire Life Durability Predictor Strategy. The Strategy calls for the development of an analytical model(computer program) to predict tire life durability. To validate the analytical model, the Strategy also includes tire testing.

The objective of the research effort described in this report was to perform a preliminary investigation of structural failure processes of cord-rubber materials as a first step to model aircraft tire durability. The approach used to investigate these processes was uniaxial tension testing of aircraft tire representations.

This report presents quantitative and qualitative results from the testing.

I. INTRODUCTION:

Tire failure categorization is based on the time required for the failure mechanism to act. Short term failure mechanisms cause tire failure almost immediately. Examples of short term failure mechanisms are tire punctures and manufacturing defects as well as over speed excursions. In contrast long term failure mechanisms lead to failure after many operating cycles. Long term failure mechanisms for tires include tread wear, structural deterioration, and material aging. Aside from short term failure mechanisms for tires, long term failure mechanisms define the operational life of a tire.

To better analyze the operational life of a tire, the United States Air Force has established the Tire Life Durability Predictor Strategy. The Strategy calls for the development of an analytical model(computer program) to predict tire life durability. To validate the analytical model, the Strategy also includes tire testing.

Note, "life durability" refers to the long term failure mechanisms for tires as opposed to short term failure mechanisms that can also define tire life.

Improved analysis of the operational life of an aircraft tire may allow the Air Force to begin condition dependent tire replacement instead of time dependent replacement. Condition dependent operational procedures for aircraft tire replacement would fully use each tire and thus reduce costs. In addition the study of tire life durability may result in tire design

improvements.

The research effort described in this report initiates a proposed, larger research program to model aircraft tire durability. This proposed research program aligns with the Tire Life Durability Predictor Strategy.

My interest is solid mechanics. Beyond my solid mechanics knowledge, however, I had no specific knowledge about tires or specifically aircraft tires. Yet, I was able to assist Dr. B. L. Lee who has extensive tire and composite material knowledge with this research effort.

II. OBJECTIVE OF THE RESEARCH EFFORT:

The objective of this research effort was to perform a preliminary investigation of structural failure processes of cord-rubber materials as a first step to model aircraft tire durability.

III. APPROACH:

The approach used to investigate structural failure processes of aircraft tires was to uniaxially tension test representations of an aircraft tire.

IV. TESTING:

Actual aircraft tire testing simulates tire loading with specialized testing machines. As expected, actual tire testing is expensive. Furthermore, sensoring or observing individual phenomena during actual tire testing is difficult since tires are unsymmetrically shaped when loaded, multiaxially

loaded, and anisotropic. Moreover, the presently available data from testing only applies to the particular tire tested under the applied loading and provides no general conclusions about the · ıctural durability of aircraft tires. Finally, present tire manufacturing technology leads to varying mechanical properties between tires and thus distorts the testing results.

To avoid these difficulties, testing tire samples and tire specimens instead will isolate various structural failure phenomena and thus ease structural durability analysis.

Tire samples are cuttings from specified locations of an actual aircraft tire with a known loading history. The curved tire samples can fit into typical material testing machines allowing normal uniaxial tension and compression, torsion, and flexure tests.

Similar in size to tire samples, tire specimens are constructed to represent the cord-rubber tire material. Tire specimens are flat and thus simplify testing.

Even though testing tire samples and tire specimens is straightforward, the relevance of the resulting data to actual aircraft tires is less clear. Hysteretic heating is a key parameter in the structural durability of a tire. Yet tire samples and tire specimens poorly represent the heat transfer characteristics of an actual tire. Actual tires have one external surface and one surface exposed to contained air. In addition tire samples and tire

specimens when tested fail to represent the multiaxial loading and the boundary conditions of an actual aircraft tire.

On the other hand, the individual structural failure processes observed in the tire samples and tire specimens are representative of the processes in an actual aircraft tire.

The research effort described in this report used two configurations of a tire specimen. Drawing 1.0 shows these configurations.

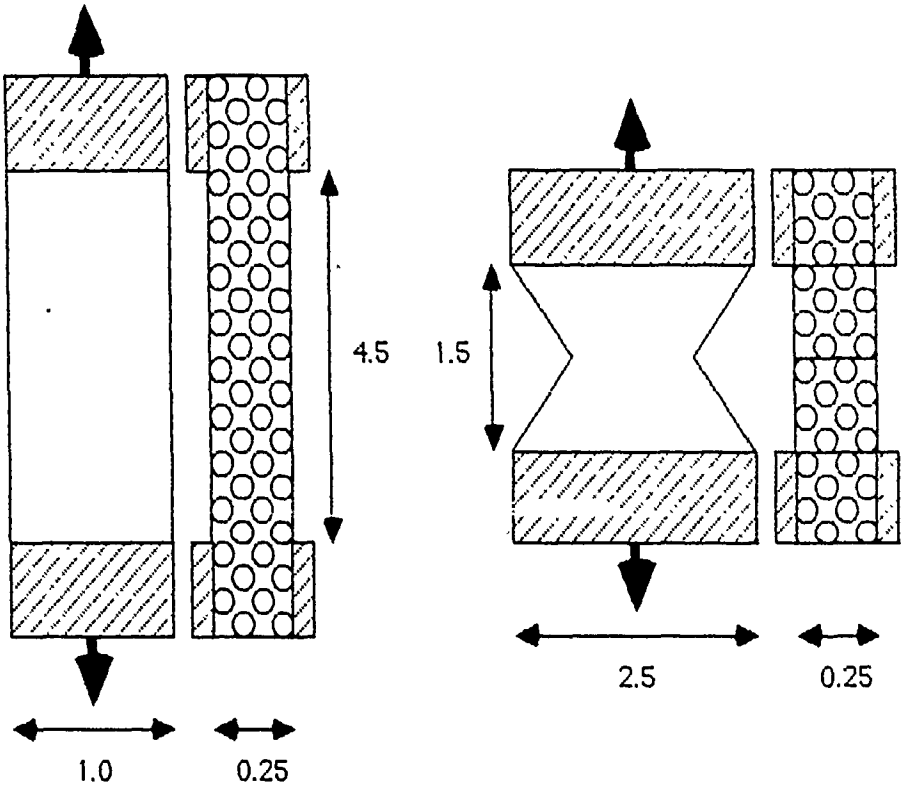

NOTE:
Dimensions are in inches and are nominal
Tab region

Drawing 1.0 Specimen Configurations

Tire specimens with the Type I configuration were manufactured using steel, nylon, and aramid cords. Tire specimens with the Type II were manufactured using only nylon cords. Note, the nylon cord specimens best represent aircraft tires since they are normally nylon cord reinforced. Table 1.0 lists the specifications of each specimen.

Cord Material	Cord Angle	Matrix Material
1260/2 Nylon	+/- 38°	Proprietary Rubber Compound
Wrapped, Twisted Steel, 1.36 mm Dia	+/- 19°	Natural Rubber Based Compound
Aramid	n/a	n/a

Table 1.0 Specimen Specifications

The tire specimen testing for this research effort included four loading regimens. Briefly, one loading regimen was static, tensile loading and another was cyclic, tensile/tensile loading. A third loading regimen was static, tensile reloading after static, tensile loading. The fourth and final loading regimen was static, tensile reloading after cyclic, tensile/tensile loading. Table 2.0 describes each loading regimen.

Regimen	Constants	Outputs
Static Loading	•Displacement Rate	•Displacement/Load •Periodic Pictures •Acoustical Emission
Cyclic Loading	•Load Controlled	•Displacement/Cycle •Temperature/Cycle •Periodic Pictures
Static Reloading	•Displacement Rate	•Displacement/Load •Periodic Pictures •Acoustical Emission
Cyclic Loaded, Static Reloading	•Load Controlled, •Displacement Rate	(All previous outputs)

Table 2.0 Testing Regimens

Note, only the steel cord specimens were tested under all four testing regimens. The nylon cord specimens were only tested under the static loading regimen, and the aramid cord specimens remain untested.

V. RESULTS:

Analog data and picture based data resulted from the testing. The picture based data are distances measured from tire specimen photographs taken periodically during testing.

The tire specimens have hand drawn lines that appear on the pictures of each specimen. Distances measured from the pictures between these lines or between the lines and edges of the specimens represent deformations. Using ratios of these distances to calculate strains and cord angles disconnects the resulting values from the unknown, absolute distances measured from the pictures. The implicit assumption used in calculating the strains and cord angles is that the distance between the camera and the specimen is constant.

Table 2.0 indicates the general outputs available from each testing regimen, but Table 3.0 lists the specific output series available.

Loading	Output Series
Static	•Displacement, Load •Displacement, Load, Interlaminar Shear Strain, Longitudinal Strain, Cord Angle
Cyclic	•Maximum Displacement, Minimum Displacement, Surface Temperature •Maximum Displacement, Minimum Displacement, Surface Temperature, Interlaminar Shear Strain, Longitudinal Strain

Table 3.0 Available Output Series

In addition, Table 4.0 lists the accuracy of the analog data.

Loading	Output	Accuracy
Static	•Displacement	•+/- 0.01 inch
	•Loading	•+/- 25 pound
Cyclic	•Displacement	•+/- 0.02 inch
	•Loading	•Exact, Load Controlled
	•Temperature	•+/- 5°F
	• Cycles	•Exact, from Counter

Table 4.0 Data Accuracy

Photocopies of the hard copy form of the analog data are available. Copies of the computer files in ASCII, tab delimited format of the manually digitized analog data and picture based data are also available.

Note, the Type II tire specimens failed in the tab region during testing. Therefore, the Type II tire specimen configuration is unsuitable for uniaxial

tension testing.

The quantitative results from this research effort group as follows:

- Strain Plots (Figures 1.0-2.0)
- Failure Cycle Plots (Figures 3.0-4.0)
- Displacement Rate and Temperature Rate Plots (Figures 5.0-6.0).

The relations shown in Figures 1.0-6.0 may represent intrinsic material properties and thus provide tire durability analysis tools.

Beyond the graphical quantitative results, two qualitative conclusions emerged.

First, cyclic loading caused permanent deformation of the steel cord tire specimen before failure. Permanent deformation then can provide an indicator of impending failure.

Several observations indicate permanent deformation of the specimens. To begin, all the cyclic loaded, unfailed specimens had visual signs of permanent deformation. Next, after a cyclic loading halt, the specimens resumed the same deformations as before the testing halt after a short transient. Moreover, cyclic preloading reduced specimen stiffness. The reduced stiffness indicates permanent deformation caused by the cyclic loading.

Second, debonding was the dominate fatigue failure processes that occurred in the steel cord tire specimens. Delamination occurred in several of the specimens resulting from a cyclic loading change. The relation between the cyclic loading change and the delamination is uncertain.

Yet, the debonding failure process was visually clear on the failure surface of each specimen. The cords pulled out of the rubber and left a detailed imprint of the cord on the rubber. The cord imprint on the rubber indicates debonding between the cord and the rubber. Furthermore, the cords of the two interior laminates were in general cleaner of rubber than the cords of the exterior laminates. The cleaner interior cords indicates more complete debonding due higher interior temperatures.

VI. RECOMMENDATIONS:

Tire sensoring technology and tire nondestructive evaluation(NDE) technology are perhaps the greatest barrier to increasing aircraft tire knowledge. Therefore, a thorough review of available tire sensoring and NDE technologies and then the development of promising new technologies could remove this barrier.

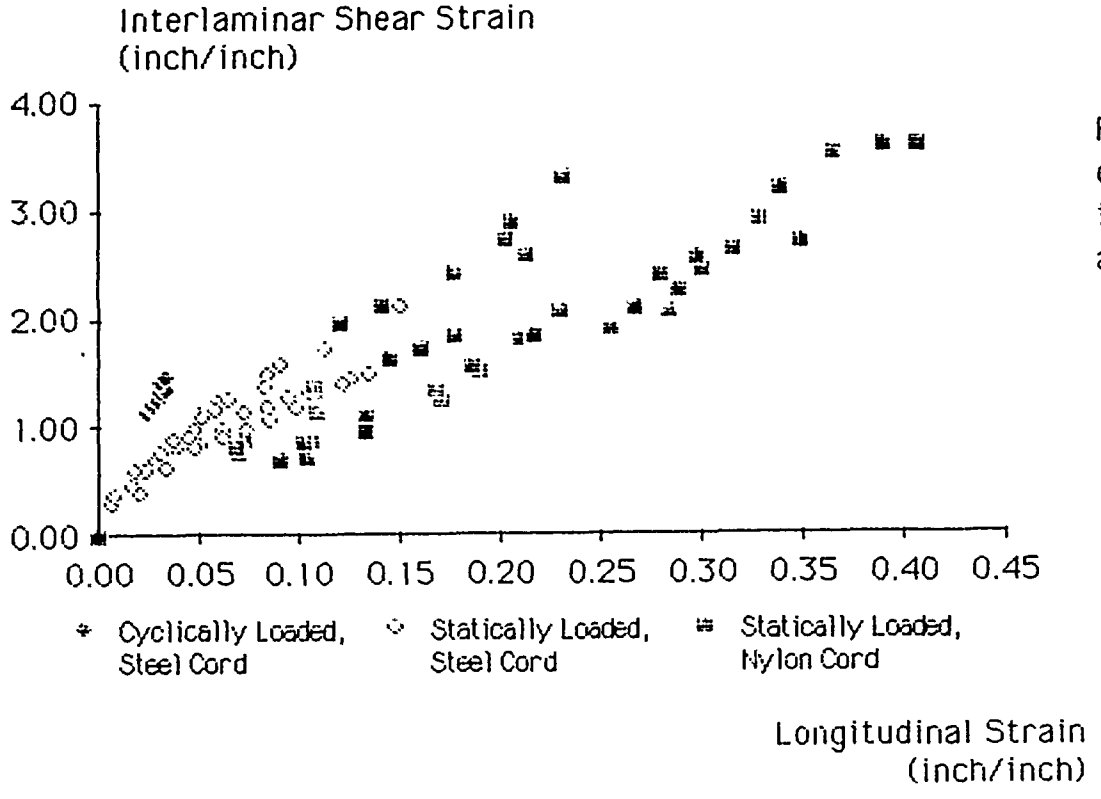

Figure 1.0 indicates a dependence between interlaminar shear strain and longitudinal strain.

Figure 1.0 Interlaminar Shear Strain vs. Longitudinal Strain

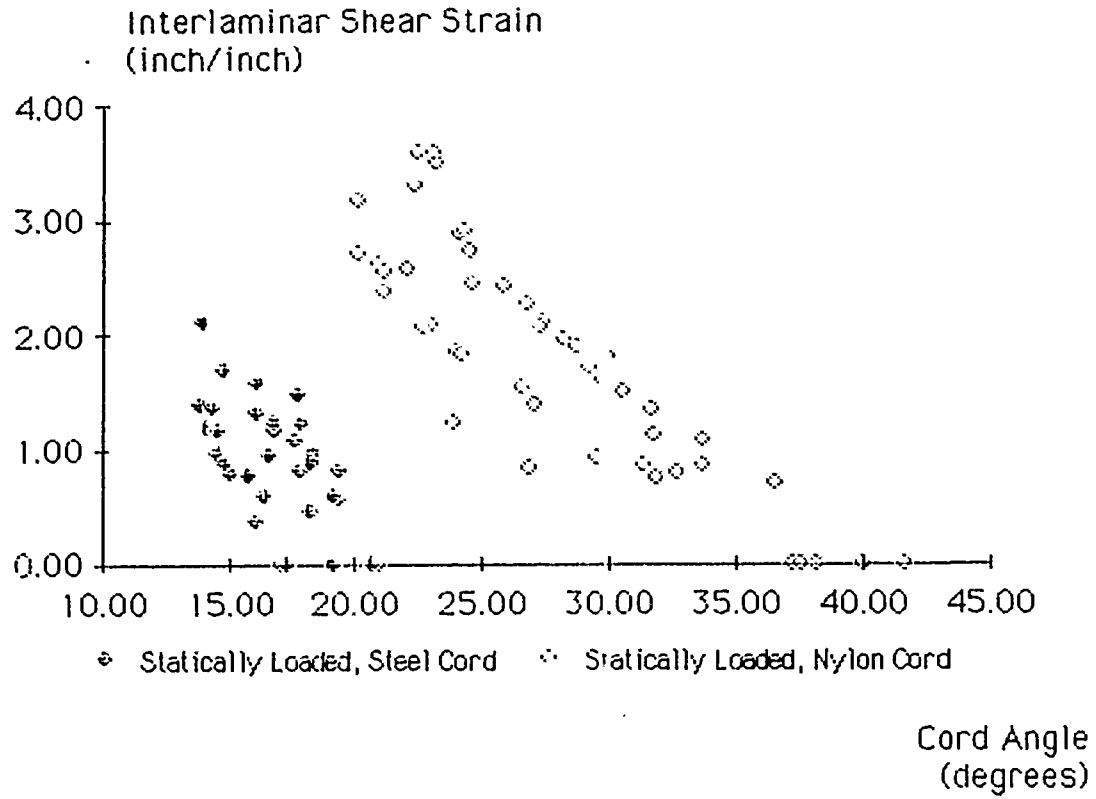

Figure 2.0 indicates a dependence between interlaminar shear strain and cord angle change.

Figure 2.0 Interlaminar Shear Strain .vs. Cord Angle

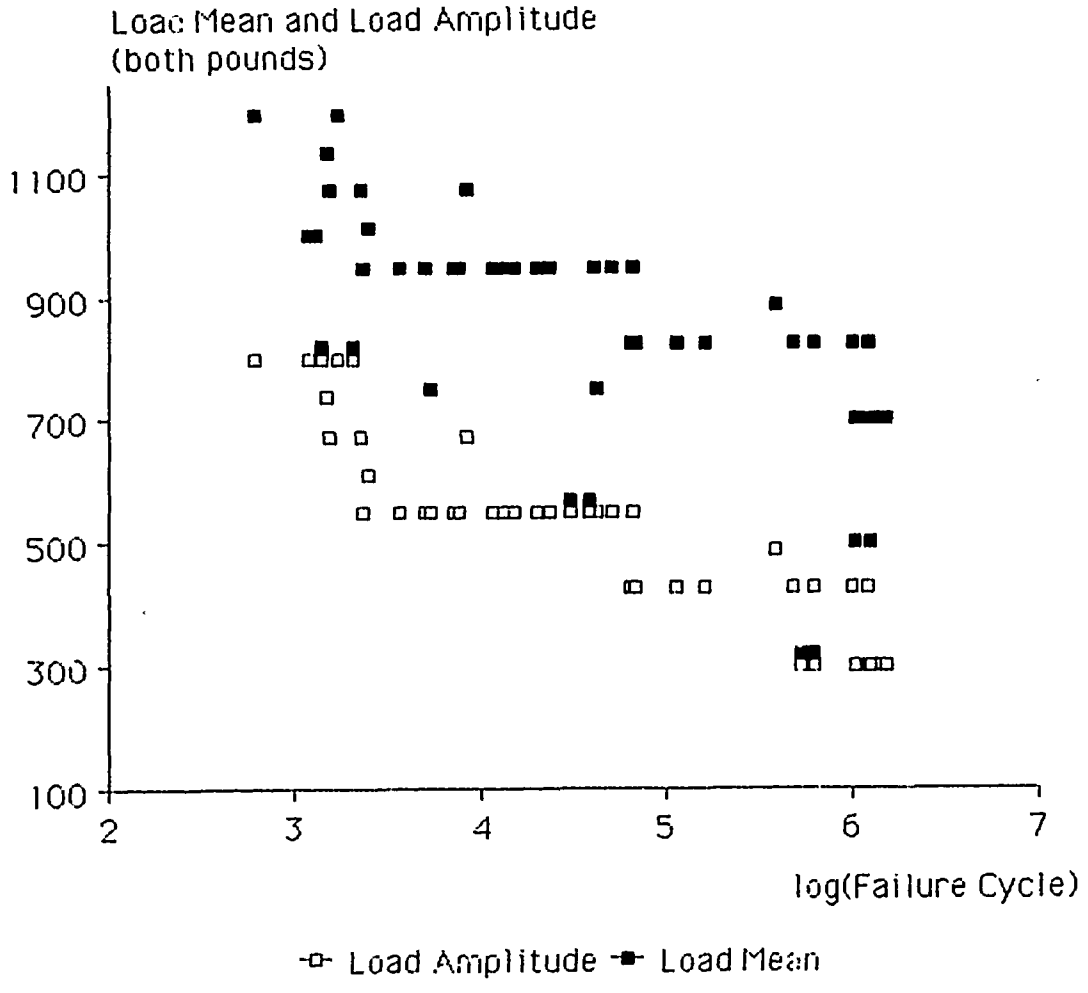

Figure 3.0 shows that an endurance limit.exits for the specimen.

Note, as appropriate for initial testing, the loading frequency varied for the data shown.

Figure 3.0 Load Mean and Load Amplitude .vs. log(Failure Cycle)

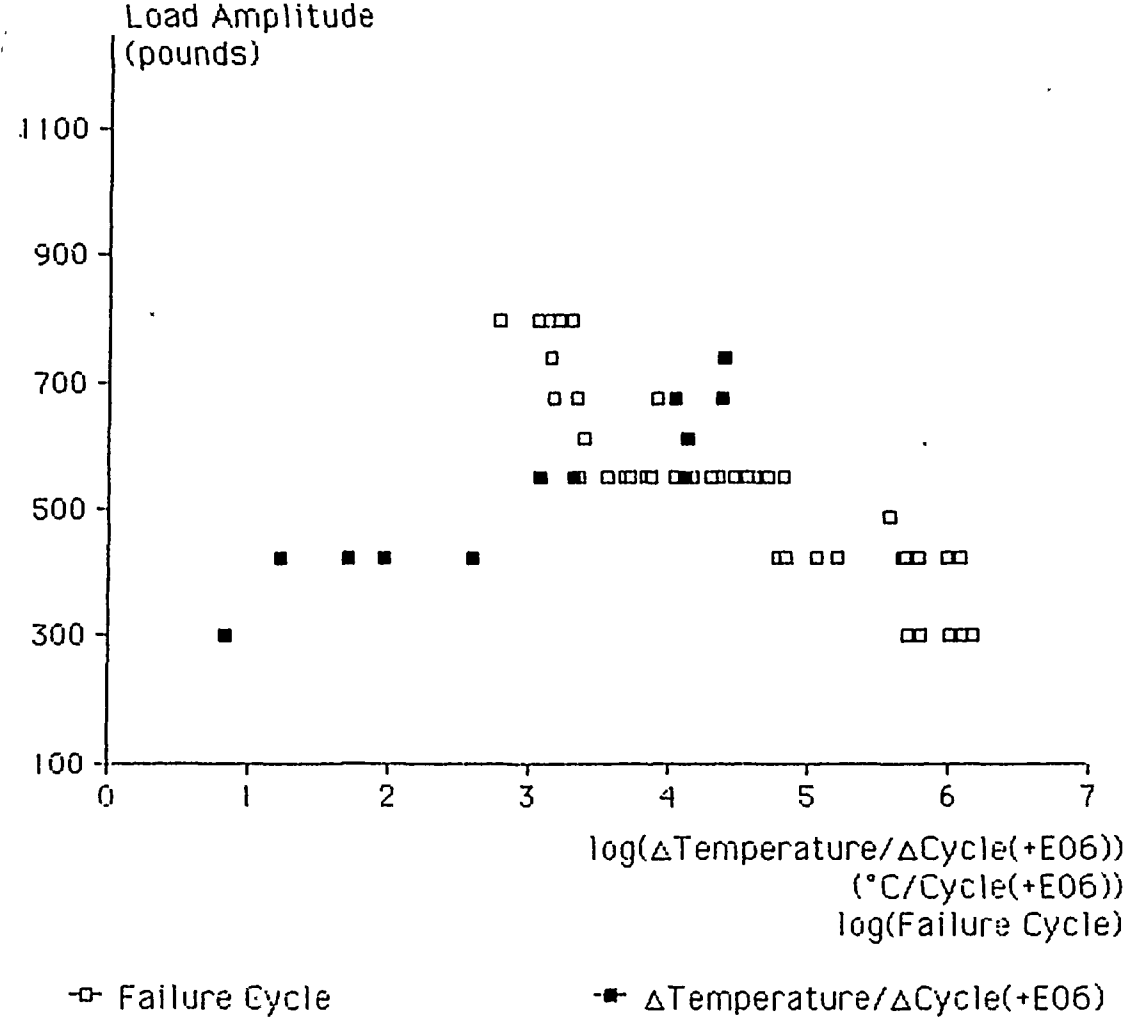

Figure 4.0 shows the that the temperature rate change is almost zero for load amplitudes near the endurance limit. Whereas, above the endurance limit, the temperature rate change increases dramatically.

Note, as appropriate for initial testing, the loading frequency and the load mean varied for the data shown.

Figure 4.0 Load Amplitude vs. Temperature Rate and Failure Cycle

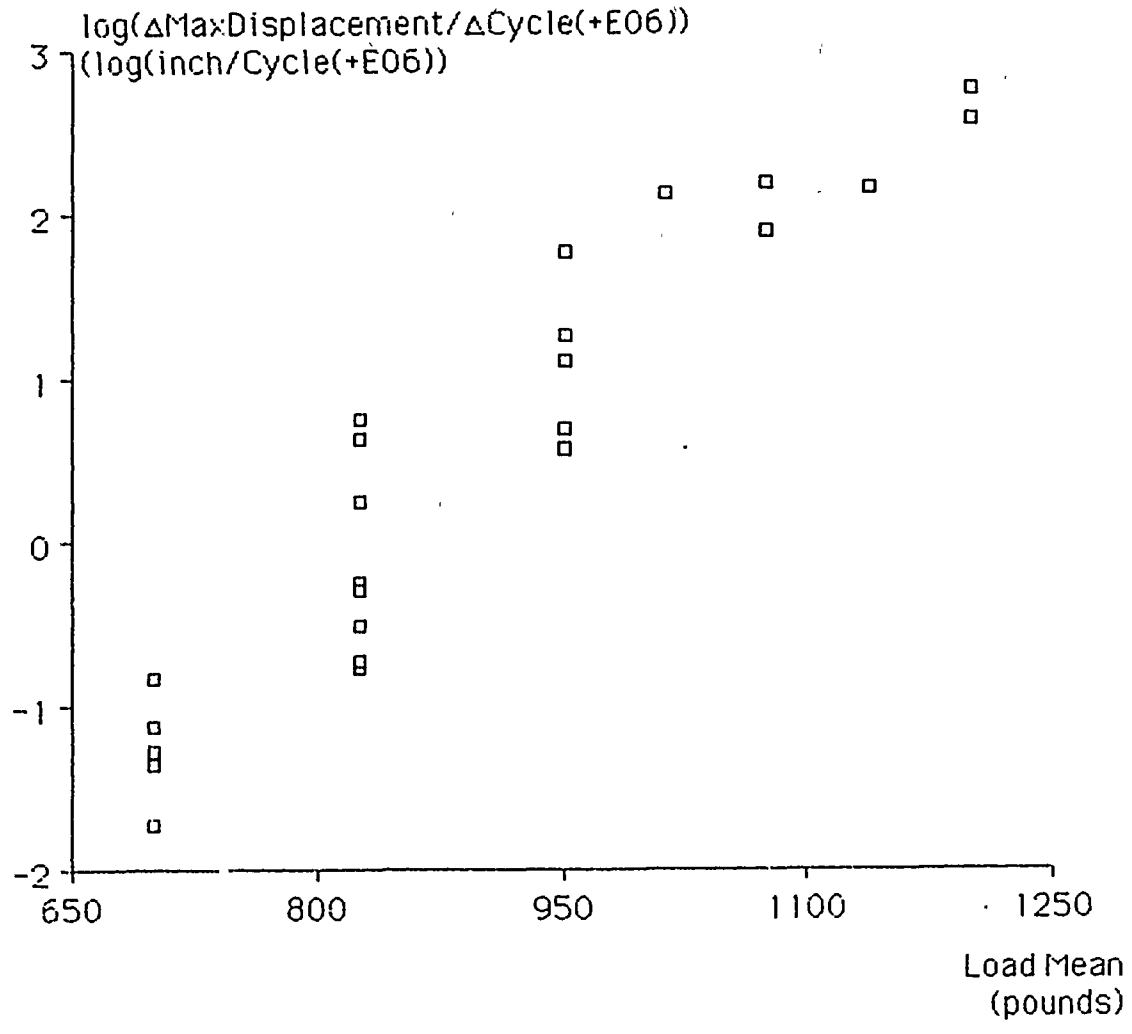

Figure 5.0 shows that the nonzero mean load leads to creep deformation.

Note, as appropriate for initial testing, the loading frequency and the load amplitude varied for the data shown.

Figure 5.0 Creep Deformation

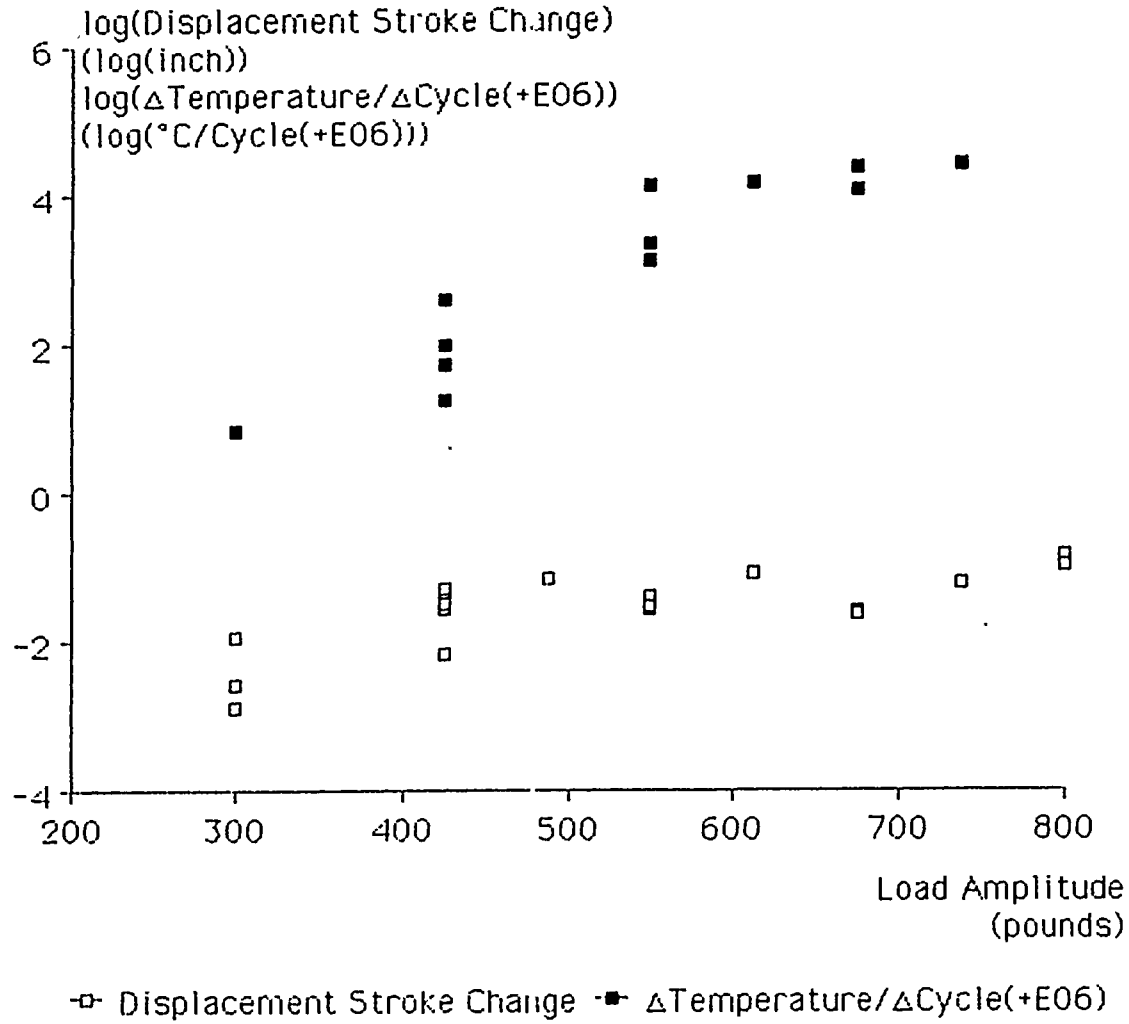

Figure 6.0 shows that the cyclic loading as measured by load amplitude leads to cyclic softening. Figure 6.0 plots the change in the difference between the maximum displacement and the minimum displacement against the load amplitude. Finally, Figure 6.0 shows that the temperature rate change increases as the load amplitude increases.

Note, as appropriate for initial testing, the loading frequency and the load mean varied for the data shown.

Figure 6.0 Displacement Stroke Change and Temperature Rate .vs. Load Amplitude

ACKNOWLEDGMENTS

The following groups sponsored the research effort described in this report.

- Air Force Systems Command
- Air Force Office of Scientific Research
- Wright Research and Development Center, Flight Dynamics Laboratory, Vehicle Subsystems Division, Aircraft Launch and Recovery Branch.

The folks at the Aircraft Launch and Recovery Branch were especially helpful by answering questions and discussing ideas.

In addition, the following individuals supported the research effort:

- Dr. G. P. Sendeckyj, Wright Research and Development Center, Flight Dynamics Laboratory, Structures Division, Structural Integrity Branch
- Dr. J. M. Whitney and Dr. R. Y. Kim(University of Dayton Research Institute), Wright Research and Development Center, Materials Laboratory, Nonmetallic Materials Division, Mechanics and Surface Interactions Branch.

Harold Stalnaker at the Structural Integrity Branch and Ron Esterline (University of Dayton Research Institute) and John Camping (University of Dayton Research Institute) at the Mechanics and Surface Interactions Branch provided excellent support by performing the various specimen testing.

Finally, I would like to thank Dr. B. L. Lee at the Pennsylvania State University for allowing me to participate in the initial phase of the aircraft tire durability research program.

REFERENCES

(None)

Same as Prof. Matzen

Submitted as Technical Memorandum

1990 USAF-UES SUMMER FACULTY RESEARCH PROGRAM/
GRADUATE STUDENT RESEARCH PROGRAM

Sponsored by the

AIR FORCE OFFICE OF SCIENTIFIC RESEARCH

Conducted by the

Universal Energy Systems, Inc.

FINAL REPORT

STUDY OF IMPACT OF CARBON GRAPHITE COMPOSITE PLATES

Prepared by:	John Thomas Dees Lair
Academic Rank:	Graduate Student
Department and	Civil Engineering Department
University:	University of New Orleans
Research Location:	WRDC/FIVST
USAF Researcher:	Pat Pettit
Date:	25, September, 1990
Contract No.:	F49620-88-C-0053

STUDY OF IMPACT OF CARBON GRAPHITE COMPOSITE PLATES

by

John Thomas Dees Lair

ABSTRACT

Panels of composite materials and aluminum plates are impacted with 12.7 mm API projectiles. Thickness of the panels and plates are varied as are the obliquity angles. The initial velocity, residual velocity, and change in weight of the projectiles are recorded. Panel and plate initial and final weights are recorded. Changes in surface strain is recorded by use of strain gauges.

Acknowledgements

I wish to thank the Air Force Systems Command and the Air Force Office of Scientific Research for sponsorship of this research. Universal Energy Systems has been most helpful in administrative matters and all other areas in which they could be of assistance.

I extend special thanks to Dr. Arnold Mayer and Dr. David Hui for their direction and support of this project. I am grateful to Greg Czarnecki, Marty Lentz and Pat Pettit for their excellent technical advice and support. Ron Studebaker provided outstanding support in his operation of the test facilities. John Sparks, Gary Angel and Doug Coppess performed most meritoriously in helping acquire supplies and solving technical problems.

I. INTRODUCTION

The behavior of composite materials in high speed impact by projectiles differs from that of metals such as aluminum due to the anisotropic nature of composites and differences in hardness and ductility. These factors affect the results of the impact such as residual velocity and damage size. The Survivability Enhancement Branch of the Flight Dynamics Laboratory at Wright Patterson Air Force Base is concerned with the survivability of aircraft. The results of projectile impact directly affects the survivability of aircraft constructed of composite materials prompting their interest in the matter.

My graduate studies have been primarily dealing with the behavior of materials and related subjects. I have had work experience with installation and analysis of results of strain gauges.

II. OBJECTIVES OF THE RESEARCH EFFORT:

Impact phenomena of composite materials in the ballistic velocity range is not widely covered in the literature. Although the phenomena of metal impact is quite well covered it has not been shown that this data relates well to composite materials. Conclusions about effects of projectile impacts on composites based on the studies of metal impacts therefore are suspect. The areas of interest include residual velocity, change in panel weight, and damage area. These parameters are based on impact velocity, projectile size, impact obliquity, panel ply orientation and panel thickness.

My project in the 1990 Summer Fellow graduate Student Research Program was to compare the effects of impacting composite panels to the impacting of aluminum plates. This was an add on to a existing program concerning functioning of API projectiles being carried out by Pat Pettit of the Survivability Enhancement Branch.

My initial objectives for the project was to obtain residual velocities, change in panel weight due to impact, and surface strain history for composite panels at various thicknesses and obliquity angles and compare these to aluminum plates of equal areal weight. This would reveal if it were practical to use metal impact equations to describe impacts on composite materials.

The original test matrix proposed by Ms Pettit was composed of variations of the following graphite epoxy panel thicknesses, obliquity angles and impact velocities. There were to be twenty tests of 32 ply panels, at 2500 feet per second projectile velocity, four shots at each obliquity angle of 0, 30, 45, 60 and 70 degrees. Forty test of 48 ply panels were to be made divided equally between 1500 and 2500 feet per second projectile velocity, four shots at each

obliquity angles of 0, 30, 45, 60 and 70 degrees. Twenty test were to be made of 64 ply panels all at a projectile velocity of 2500 feet per second four at each obliquity angles of 0, 30, 45, 60 and 70 degrees. All test panels were to be eight inches square.

Modifications were made to the original test plan to obtain data required for my project. Aluminum plates were added to the test matrix. Additional break papers were placed to determine residual velocity and strain gauges were placed on the panels and plates to determine strain wave velocity in the materials and strain wave form. Due to time constraints in the testing facility the 1500 feet per second tests and the obliquities other than 0 degrees for the aluminum plates thicker than 0.091 inches were not performed during my project.

Graphite epoxy panels in 32, 48 and 64 ply thicknesses in a quasi-isotropic lay up were chosen based on availability, uniform strength in 0, 45 and 90 degree directions and the fact the material is currently in use. Plates of aluminum alloy 2024 T3 in thicknesses of 0.091", 0.142" and 0.192" taken from available stock were used as these most closely matched the weight per square inch of the composite panels. The selection of alloy 2024 T3 was based on the fact that is has been reviewed in the literature (Malick 1969).

A review of the literature on the subject of impact of plates was conducted as the first course of action. This study reveled that although there was a substantial body of information concerning impact of metals such as steel, aluminum and to a lesser degree titanium very little was uncovered regarding the impact of composite plates. One notable exception is a document which concludes that formulas for impact of metals do not coincide with available

data for composite materials (Pettit 1989). The most accurate models currently available for metals are empirical formulas based on method of coefficients (Malick 1969). This indicates that the theory of impact was not fully developed at the time of publication and that previous successful models have relied on curve fitting to a body of data. Most models studied have relied on a plugging phenomenon occurring (Zukas 1982). This phenomenon is based on a ring of target material reaching the plastic state and allowing a "plug" of target material to be ejected out the back of the plate. It is not clear if this process can occur in composite material based on its brittle type stress strain diagram.

Initially a flash X-ray camera was to be used to capture two images of the projectile as it exited the panel to determine the time the projectile took to pass through the panel. It was however determined that the operation of the X-ray flash devices would set up a magnetic field which would disrupt the strain measurement by strain gauges.

Break papers were fitted in front of and to the test fixture and monitored by two methods. Counters were place in line to measure velocity as was a nine track tape with a 100 Kilohertz clock signal feed into one channel. The counters were direct read instruments and the nine track tapes were printed all tracks simultaneously to a plotter and the time between break paper activations were measured as a function of the 100 Kilohertz signal trace. Four break papers at three foot spacing were set up in front of the target one break paper was placed on the target and three were placed after the target at two foot spacing.

The panels were instrumented with strain gauges initially with two gauges per panel. At this time the strain gauges were sensed using a 500,000 cycle per second Nicolet digital

oscilloscope. New Kontron digital oscilloscope/computer instruments with four channel capability and computer readable output became available after the first couple of tests panels. The remainder of the panels were instrumented with four strain gauges, two per side. These were arranged in pairs on opposing faces of the panels so that when viewed from one face their centerlines overlapped. This was to measure any bending moment in the panel during impact. They generally were arranged radially on a face with a one inch spacing between centerlines in order to measure wave speed.

The panels were weighed and their thickness measured using a micrometer; the weights and thicknesses were recorded. They were then fitted in to a steel frame constructed for Ms Pettit's project. The above mentioned break papers and strain gauges were fitted and connected to recording devices. They were then impacted with 12.7 API projectiles using a conventional powder gun. The projectiles were retrieved using a bundle of Celotex panels. The panels were weighed and the weights recorded again at this time. This procedure provided data on initial velocity, panel weight and projectile weight also residual velocity, panel weight and projectile weight. The data recorded from the strain gauges provided a strain history of the surface of the panel.

The residual velocity data from the graphite epoxy panels proved to be an enigma. Although a general trend could be shown of decreasing velocity as obliquity angle increased no such trend could be shown for increasing the thickness of the panel. The data contained several anomalies such as the change in velocity being greater at a obliquity angle of 0 for a single panel thickness than at greater obliquity angles. Other panel thicknesses did not exhibit this phenomenon.

The change in panel weight gave more stable results. The loss of composite panel weight increased with thickness and obliquity angle as expected. The comparison with aluminum plates showed that at thinner thicknesses the composites lost more material, based on change in weight, than the aluminum plates but that at greater thicknesses the composites lost less material than the aluminum plates. In all cases the loss of material was less than two percent of the original weight of the plate or panel.

Change in projectile weight seemed to be more a question of incendiary function than of loss of projectile material due to impact. Losses of 284 grains were common whenever the incendiary functioned fully. When the incendiary did not function the projectile weight loss was less than one percent of projectile initial weight.

Preliminary analysis of the surface strain history provided by the strain gauges indicates that as expected elastic waves in composites travel faster along the fiber direction than across it. Further analysis is pending decoding the output files of the data acquisition equipment to a form usable by a personal computer.

IV. RECOMMENDATIONS:

a. Further investigation into the anomalies in the residual velocities is recommended. Other methods of obtaining velocities without obstructing other aspects of the test program should be investigated. As function of the incendiary was a part of this program the use of a ballistic pendulum and use of high speed photography was ruled out and break papers were used.

b. Studies of the strain data obtained during this test

sequence shall be conducted and reported on at a latter time.

c. A test sequence of different projectile sizes, impact velocities and composite panel lay up schemes is planned by WRDC/FIVST. This effort will produce sufficient data to show the above parameter's effect on residual velocity and damage size, which is expected to deviate greatly from available metal impact formulas.

REFERENCES

Pettit, P., Incendiary Functioning Characteristics of Soviet API Projectiles Impacting Graphite/Epoxy Composite Panels, WRDC/FIVST report, 6, September, 1989

Malick, D., The Resistance of Aluminum Alloy Targets to Perforation by Small-Caliber, Armor-Piercing Projectiles (U), BAL Technical Report No. 70, Jan. 1969

Zukas, J.A., Impact Dynamics, John Wiley & Sons, 1982

1990 USAF-UES SUMMER FACULTY RESEARCH PROGRAM/

GRADUATE STUDENT RESEARCH PROGRAM

Sponsored by the

AIR FORCE OFFICE OF SCIENTIFIC RESEARCH

Conducted by the

Universal Energy Systems, Inc.

FINAL REPORT

DELAMINATION OF LAMINATED COMPOSITES

Prepared by:	Kristina Pawlikowski
Academic Rank:	Graduate Research Associate
Department and University:	Civil Engineering Department The Ohio State University
Research Location:	WRDC/FIBCA Wright Patterson AFB OH 45433
USAF Researcher:	Dr. Raghbir S. Sandhu
Date:	30 Sep 90
Contract No:	F49620-88-C-0053

DELAMINATION OF LAMINATED COMPOSITES

by

Kristina Pawlikowski

ABSTRACT

In previous summer faculty and graduate summer research program appointments we have looked at the initiation of damage in laminated composites subjected to low velocity impact. A review of the literature as well as an analysis of our own tests showed that a significant mode of failure resulting from the impact event is delamination. A prediction of the extent of delamination requires an evaluation of interlaminar stresses and the material properties governing delamination.

In the research performed during this summer's appointment, an analytical investigation of the tendency for delamination as predicted by the delamination moment coefficient originally defined by Sandhu was performed. The effects of ply orientation and laminate thickness on the calculated delaminating stresses was determined.

Acknowledgements

I wish to thank the Air Force Systems Command and the Air Force Office of Scientific Research for sponsorship of the Summer Faculty Research Program. The project was administered by Universal Energy Systems Inc. Their help throughout the summer is appreciated.

I am grateful to all who have helped me during this past summer. In particular, I want to thank to Mr. George Holderby, group leader of FIBCA for most of the summer, who made the work environment so conducive to success and to Dr. Raghbir S. Sandhu who was been my technical monitor. Dr. Sandhu was always willing to share his ideas and never tired of teaching.

I. INTRODUCTION

The behavior of laminated composites that have been impacted at low velocities is of great concern to designers of high performance aircraft. These events which may result from a maintenance accident or debris impact during takeoff or landing can significantly degrade aircraft performance and even cause structural failure without detectible surface evidence of the event. A large number of researchers have studied the delamination problem both analytically and experimentally. However, i· spite of considerable effort, current predictive capabilities are limited. The research

conducted during this graduate student summer research appointment consisted of an analytical investigation of the tendency of particular configurations of graphite/epoxy composites to delaminate. For this study we used as a predictor the delaminating moment coefficient which was originally proposed by Sandhu (1).

II. OBJECTIVES OF THE RESEARCH EFFORT

The work described in this report is a continuation of previous summer faculty research program appointments (4-6) in which the initiation of damage in laminated composites subjected to low velocity impact was studied. Those efforts showed that, during the impact event, a significant cause of failure is ply delamination. A prediction of the extent of delamination requires an evaluation of interlaminar stresses. The development of such a capability is underway in a companion graduate summer research program (3), in which a stress based plate theory is being used to determine the magnitude and distribution in inplane shear stresses as well as out of plane normal stresses.

In addition to an understanding of the stress field, any prediction of the extent of delamination requires an evaluation of the governing material properties. The main objective of this summer's research was to identify ply orientations in which delamination was the sole mode of failure so that test specimens suitable for use in determining

interlaminar strength properties could be designed.

To accomplish this objective, the delaminating moment coefficients were determined for a large number of plate thicknesses and fiber orientations.

III. RESULTS OF WORK EFFORT

3.1 Preliminary Numerical Studies:

There has been a considerable amount of research conducted over the past three decades on the behavior of composite materials. Much of the work has been in the area of laminated plate theory which has, in recent years, focussed on ply-by-ply analyses. Reviews of previous work have been presented by several investigators including the SFRP technical monitor of this project in Sandhu (1) and Sandhu and Sendeckyj (2).

Sandhu (1) reported that most investigators have identified interlaminar normal stresses as the primary cause of ply delamination. He observed that a number of attempts had been made to evaluate the magnitude of the interlaminar normal stresses due to inplane loads. In several of these studies expressions for delamination tendency were based on an assumed distribution of interlaminar normal stresses. In his work, Sandhu observed that these assumed distributions of interlaminar normal stresses were not necessary for determining the ply orientations most prone to delaminate.

Sandhu defined a delaminating moment coefficient (DMC), and showed that delamination could be expected when the DMC reached a critical value. This delaminating moment coefficient given in terms of the average axial stress is presented as equation 1.

$$DMC_s = \frac{DM}{\sigma_o} = m(4m+n)\left(\frac{t^2}{2}\right)\frac{\sigma^{\theta}_{y}}{\sigma_o} \qquad \text{Eq. 1}$$

where:

DM = delaminating moment at the mid-surface of the laminate

m = number of 90^0 plies

n = number of θ^0 plies

t = ply thickness

σ^{θ}_{y} = transverse stress in the θ plies

σ_o = average axial stress

Subsequent work by Sandhu and Sendeckyj (2) identified the critical value of the DMC as being a function of, plate thickness and ply orientation. They observed that laminated graphite/epoxy composites with DMCs greater than 10×10^{-5} in^3 delaminated, whereas plates with ply orientations resulting in DMCs less than 8×10^{-5} in^3 did not delaminate. They speculated

that the DMC could be considered to be a material parameter capable of defining the delamination tendency of composite of different material systems.

An analysis of the effects of different ply orientations on the value of Sandhu's delamination moment coefficient was performed for plates of several thicknesses with off-axis ply orientations varying from 0 to 90 degrees. Figure 1 shows the results of these calculations. It is apparent that, for the graphite/epoxy system studied, a critical angle for the off-axis plies between 40 and 50 degrees can be defined. It is also clear from Figure 1 that the DMC and therefore delamination tendencies increase with increasing laminate thickness. Sandhu and Sendeckyj have shown that although coupons made with the angle of the off-axis plies slightly greater than 40 degrees delaminated, they also experienced axial strains greater than 4000 uin/in prior to the onset of delamination. Since the failure strain of the epoxy matrix is approximately 4000 uin/in, any delamination in these specimens would be accompanied by matrix cracking and consequently not be just a simple opening mode failure. Therefore it was determined that for the finite element studies to be conducted in this program, only laminates with the off-axis plies oriented at 40 degrees to the long axis of the test coupon would be examined.

3.2 Finite Element Studies:

Using the results of the above preliminary numerical studies, a finite element analysis of the specimens with the greatest tendency to delaminate without experiencing matrix cracking during in-plane loading was undertaken. In this section, we present the results of these studies which were conducted to identify the state of stress and thereby the tendency for delamination in graphite/epoxy plates of six different thicknesses. As was done in the preliminary studies, each plate was modelled as having two 90 degree plies located at the midplane of the specimen. The outer plies all consisted of fibers oriented at ± 40 degrees. The number of pairs of ± 40 degree plies placed symmetrically about the 90 degree plies ranged from one, $[\pm 45/90]_s$, to six, $[(\pm 45)_6/90]_s$. The results of the computer simulations of the tensile tests are shown in Figures 2 through 7. Note in each of the figures the clear tendency for peeling as well as stretching at the free surface of the specimen. The stress contours plotted for each of the coupons studied shows that the interlaminar normal stresses are considerably larger and the gradients steeper for the thicker specimens than for the thinner ones, thus verifying the finding of Section 3.1 that the likelihood of delamination increases with the thickness of the panel. The distribution of interlaminar normal stress normalized by the mean axial stress for each of the coupon thicknesses tested is presented in Figure 8.

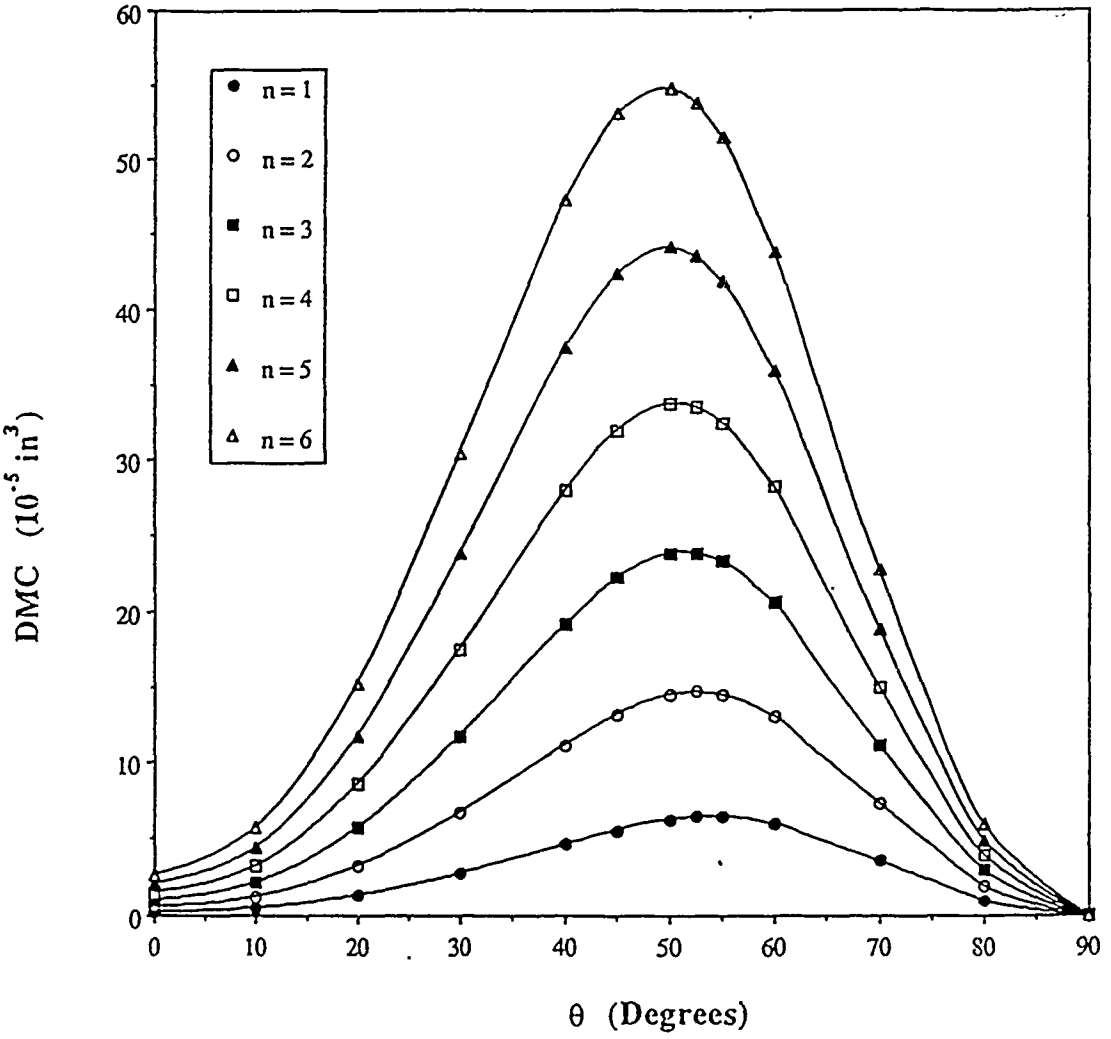

Figure 1: Variations of Delamination Moment Coefficient (DMC) in $[(\pm\theta)_n / 90]_S$ Laminates

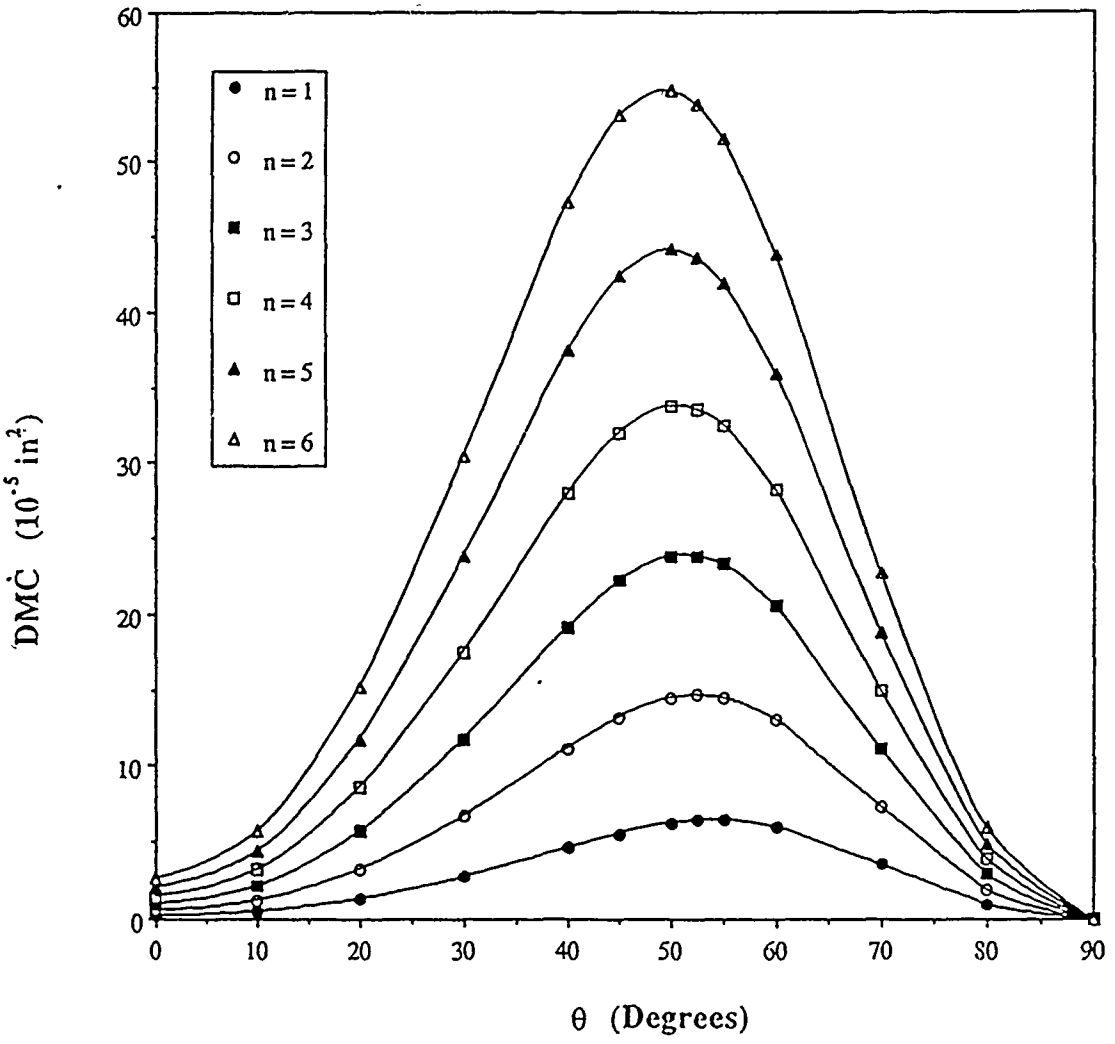

Figure 1: Variations of Delamination Moment Coefficient (DMC) in $[(\pm\theta)_n / 90]_s$ Laminates

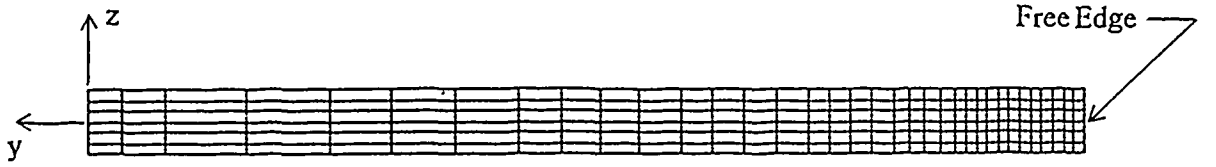

a. Undeformed Finite Element Mesh.

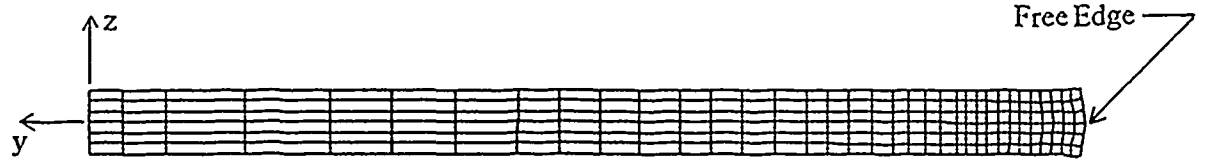

b. Deformed Finite Element Mesh under 100 psi Axial Stress.

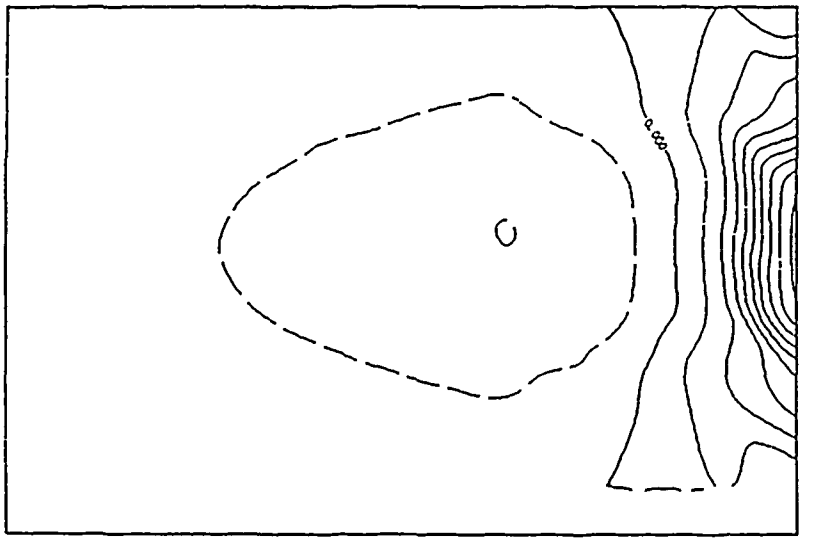

c. Interlaminar Normal Stress Distribution, σ_Z, at Free Edge.

Figure 2: 6 Ply Laminate, $[\pm 40/90]_S$

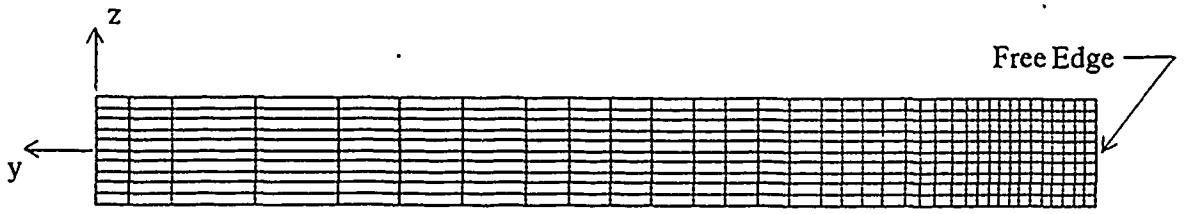

a. Undeformed Finite Element Mesh.

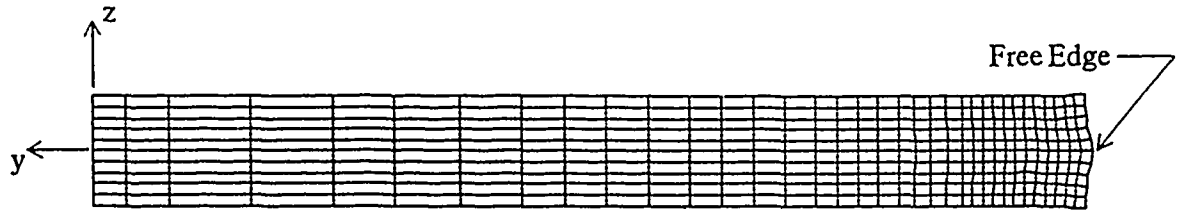

b. Deformed Finite Element Mesh under 100 psi Axial Stress.

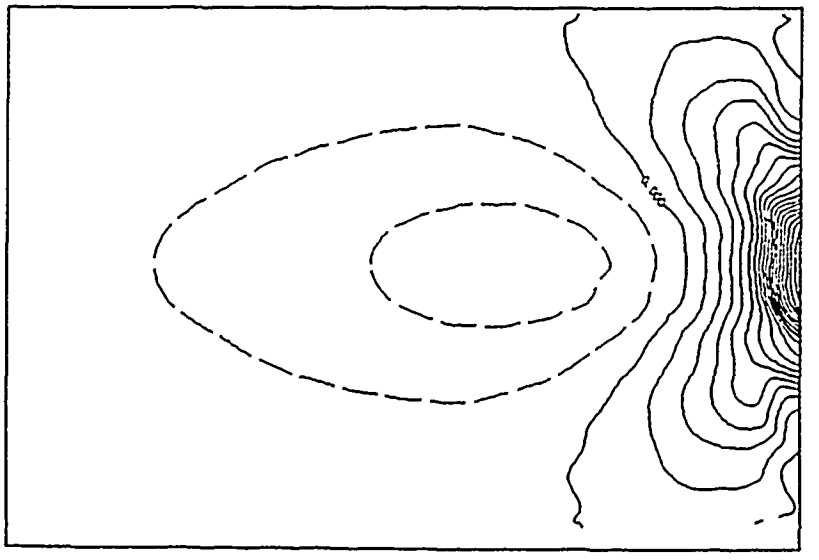

c. Interlaminar Normal Stress Distribution, σ_z, at Free Edge.

Figure 3: 10 Ply Laminate, $[(\pm 40)_2 / 90]_S$

a. Undeformed Finite Element Mesh.

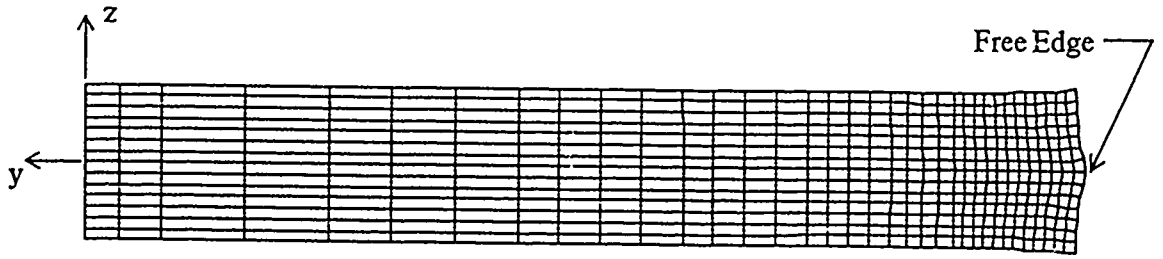

b. Deformed Finite Element Mesh under 100 psi Axial Stress.

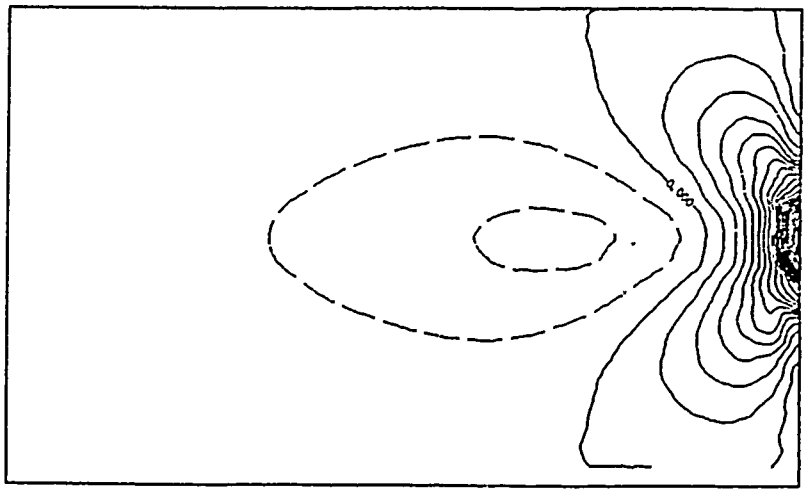

c. Interlaminar Normal Stress Distribution, σ_Z, at Free Edge.

Figure 4: 14 Ply Laminate, $[(\pm 40)_3 / 90]_S$

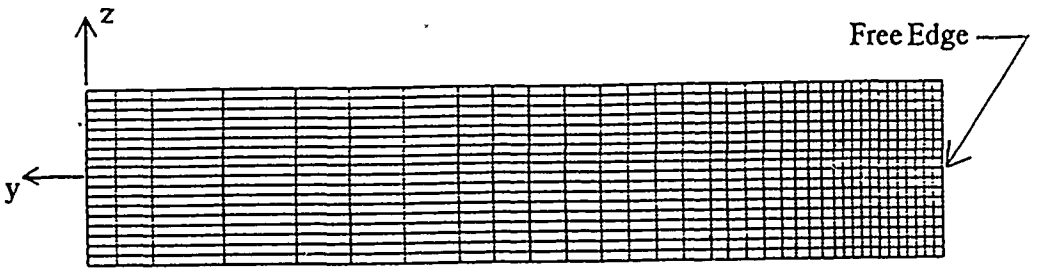

a. Undeformed Finite Element Mesh.

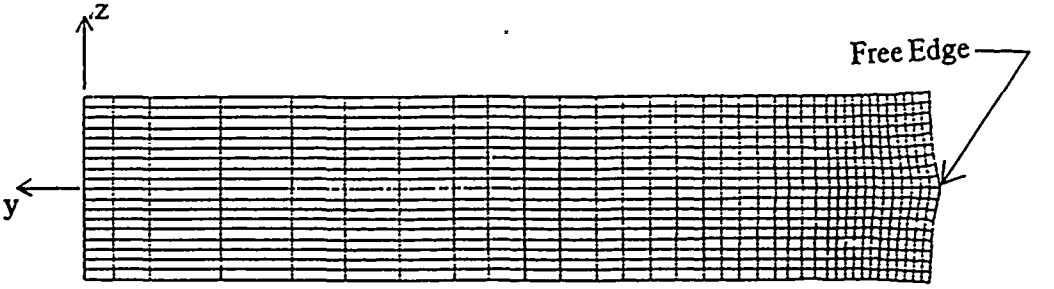

b. Deformed Finite Element Mesh under 100 psi Axial Stress.

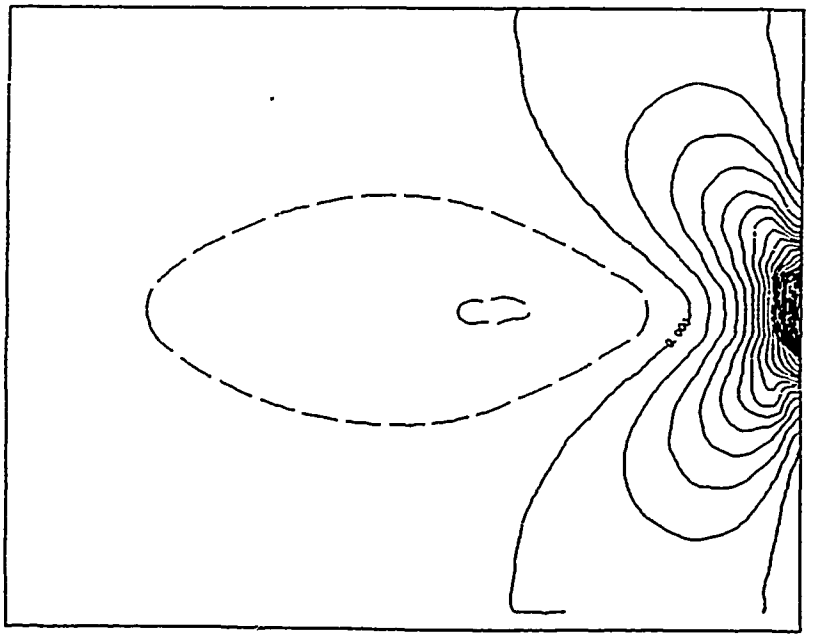

c. Interlaminar Normal Stress Distribution, σ_Z, at Free Edge.

Figure 5: 18 Ply Laminate, $[(\pm 40)_4 / 90]_S$

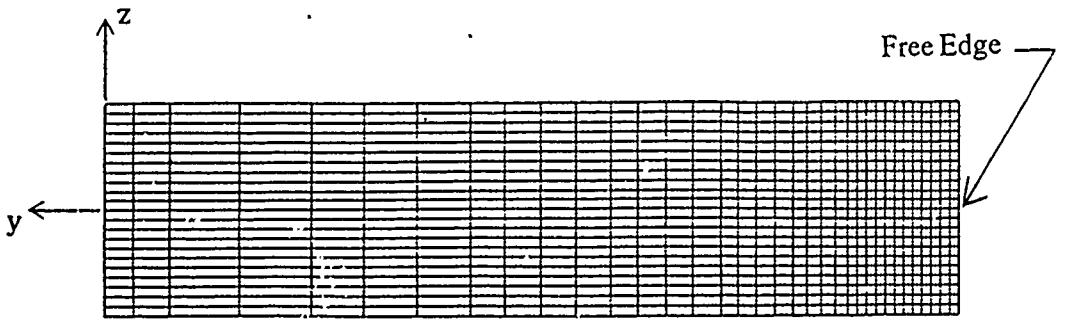

a. Undeformed Finite Element Mesh.

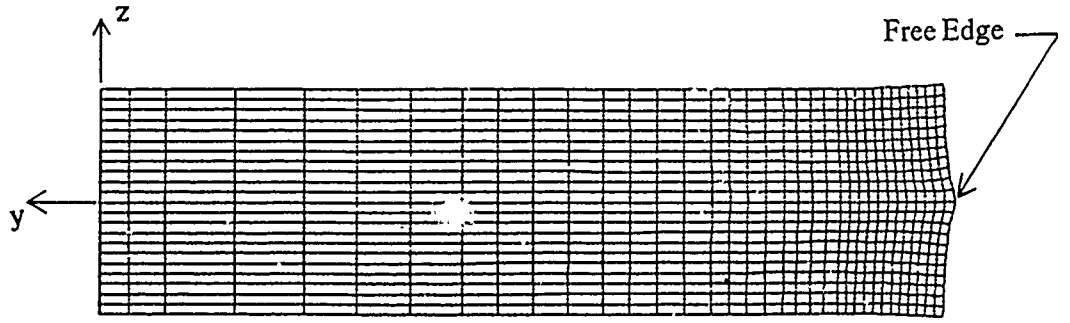

b. Deformed Finite Element Mesh under 100 psi Axial Stress.

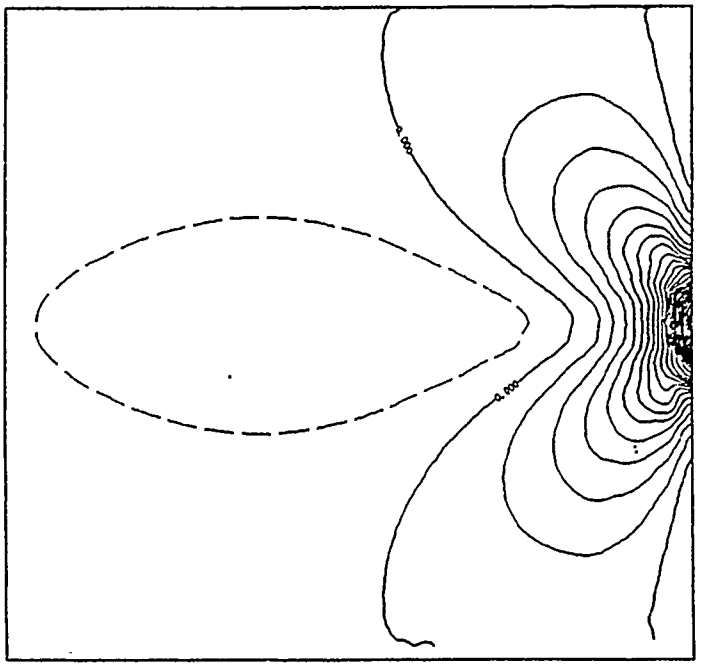

c. Interlaminar Normal Stress Distribution, σ_Z, at Free Edge.

Figure 6: 22 Ply Laminate, $[(\pm 40)_5 / 90]_S$

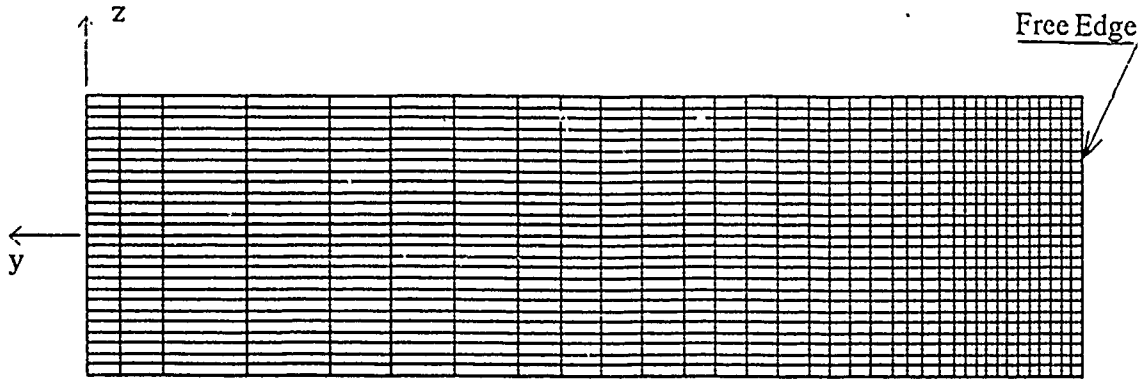

a. Undeformed Finite Element Mesh.

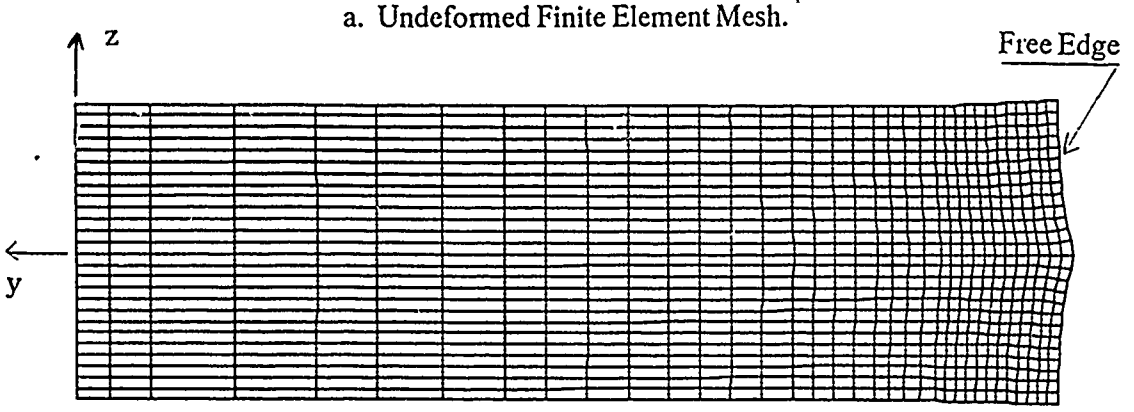

b. Deformed Finite Element Mesh under 100 psi Axial Stress.

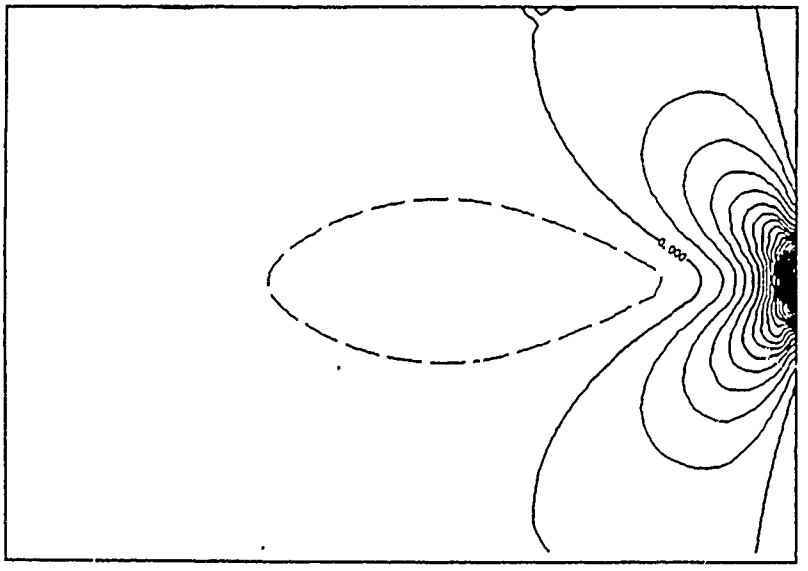

c. Interlaminar Normal Stress Distribution, σ_z, at Free Edge of Specimen.

Figure 7: 26 Ply Laminate, $[(\pm 40)_6 / 90]_s$

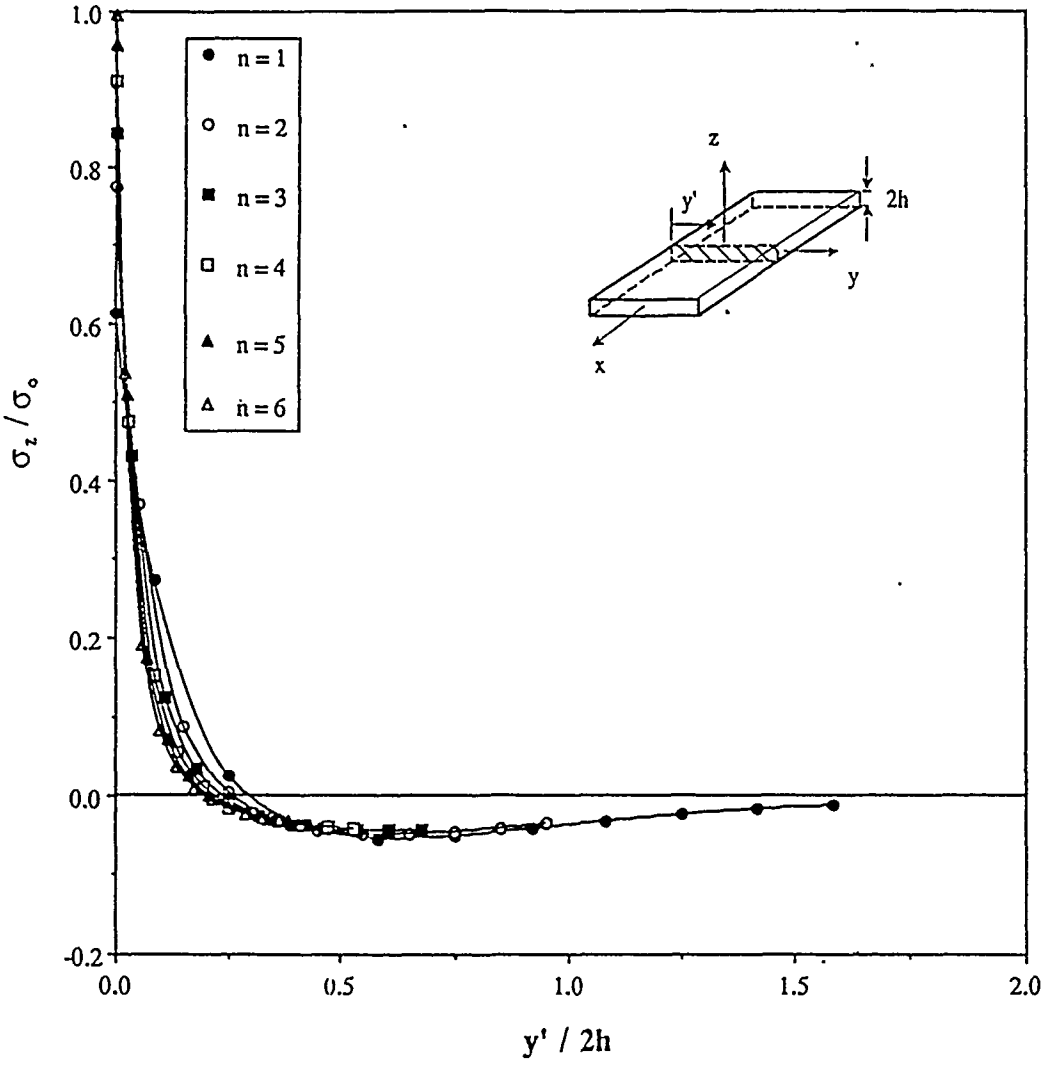

Figure 8: Interlaminar Normal Stress Distribution along Midplane of $[(\pm 40)_n / 90]_S$ Laminates

IV. RECOMMENDATIONS

The numerical studies conducted during the summer research program have shown that an evaluation of a composite laminate's tendency to delaminate may be made by identifying a material property, originally proposed by Sandhu (1), the delaminating moment coefficient (DMC). By designing laminates with the maximum DMC, different composite systems can be made to delaminate without simultaneously undergoing complicating additional failure modes. Proposed follow-on studies should include:

1) an experimental program designed to verify the utility of the DMC in predicting the failure mode. For the graphite/epoxy system studied in this effort, we suggest specimens of several thicknesses each with off axis plies oriented at $\pm 40^0$ be fabricated and tested;
2) additional numerical investigations of different materials to identify the effects of other system properties on the DMC.

REFERENCES

1. Sandhu, R.S., "Analytical-Experimental Correlation of the Behavior of 0^0, $\pm 45^0$, 90^0 Family of AS/3501-5 Graphite Epoxy Composite Laminates under Uniaxial Tensile Loading," AFFDL-TR-79-3064, Wright-Patterson Air Force Base, Ohio, May, 1979.

2. Sandhu, R.S. and Sendeckyj, G.P., "On Delamination of $(\pm\theta_m/90_{n/2})_s$ Laminates Subjected to Tensile Loading, "AFWAL-TR-87-3058, Wright-Patterson Air Force Base, Ohio, July, 1987.

3. Schoeppner, G.A., Composite Laminate Stress Fields During Dynamic Loading, Final Report, USAF-UES Summer Graduate Student Research Program, September, 1990.

4. Wolfe, W.E., Low Velocity Impact of Graphite/Epoxy Plates, Final Report, USAF-UES Summer Faculty Research Program, September, 1987.

5. Wolfe, W.E., Damage in Graphite/Epoxy Plates Subjected to Low Velocity Impact, Final Report, USAF-UES Summer Faculty Research Program, September, 1988.

6. Wolfe, W.E. and Schoeppner, G.A., Low Velocity Impact of Composite Materials, Final Report, Grant Nos. S-760-7MG-102 and S-210-9MG-082, Universal Energy Systems, Dayton, Ohio, February, 1990.

1990 USAF-UES SUMMER FACULTY RESEARCH PROGRAM/

GRADUATE STUDENT RESEARCH PROGRAM

Sponsored by the

AIR FORCE OFFICE OF SCIENTIFIC RESEARCH

Conducted by the

Universal Energy Systems, Inc.

FINAL REPORT

H_∞ Design Based on Loop Transfer Recovery and Loop Shaping

Prepared by:	Chin S. Hsu, Ph.D.	Jenny L. Rawson
Academic Rank:	Associate Professor	Graduate Student
Department and University:	Department of Electrical Engineering and Computer Science Washington State University	
Research Location:	Flight Dynamics Laboratory WRDC/FIGC Wright-Patterson AFB, OH 45433	
USAF Researcher:	Siva S. Banda, Ph.D.	

Date:	17 Aug 90
Contract No:	F49620-88-C-0053

Same Report as
Prof. Chin Hsu
(Report # 101)

1990 USAF-UES SUMMER FACULTY RESEARCH PROGRAM/

GRADUATE STUDENT RESEARCH PROGRAM

Sponsored by the

AIR FORCE OFFICE OF SCIENTIFIC RESEARCH

Conducted by the

Universal Energy Systems, Inc.

FINAL REPORT

Parallel Implementation of Structural Analysis and Control Synthesis Algorithms

Prepared by:	Keith A. Redmill
Academic Rank:	M.S. Candidate
Department and	Electrical Engineering
University:	The Ohio State University
Research Location:	USAF/WRDC/FIBRA
	Wright Patterson AFB
	Dayton OH 45433
USAF Researcher:	Vipperla Venkayya
Date:	22 Sept 1990
Contract No:	F49620-88-C-0053

Parallel Implementation of Structural Analysis and Control Synthesis Algorithms

by

Keith A. Redmill

ABSTRACT

The design and analysis of large scale structures often involves linear models with hundreds or thousands of degrees of freedom. The resulting computations require large quantities of computer time and memory, and can be either infeasable or prohibitively expensive on commonly available single processor computer systems. We are interested in implementing analysis routines such as linear systems solvers and eigenvalue estimators, which arise in finite element analysis, and Riccati equation solvers, which arise in many control synthesis techniques, on MIMD parallel processing architectures such as the Intel IPSC Hypercube.

In this report we describe the results of a literature search concerning the solution of the matrix eigenvalue problem, a literature search concerning the solution of the matrix Riccati equation, and the implementation of several routines for matrix factorization and the solution of linear system on a 32 node Intel IPSC/1 Hypercube multiprocessor.

I. INTRODUCTION:

The analysis and control of large scale systems is usually carried out using models derived from either finite element analysis programs or finite difference approximations of differential equations derived for the system. In either case, the end result is a large, often sparse set of matrices which model the dynamic behavior of the system. The solution of the various large matrix problems which arise when studying these systems often requires a large quantity of computing resources. In addition, the large size of these problems may result in numerical instabilities.

The Analysis and Optimization Branch of the Flight Dynamics Lab/Wright Research and Development Center at Wright-Patterson Air Force Base created and maintains a large scale finite element structural analysis and optimization program called ASTROS. They are also currently involved in developing new optimization algorithms, and are interested in the control of large space structures.

My research interests concern numerical algorithms and applied mathematics, control theory, and novel computer architectures, particularly architectures for parallel computation. My training in applied mathematics and control theory, as well as my interest in parallel computers, combined

with the research and technical experience of the Analysis and Optimization Branch, produced a mutually enriching experience for all parties involved.

II. OBJECTIVES OF THE RESEARCH EFFORT:

My objectives as a participant in the 1990 Graduate Summer Research Program were three fold. First, a literature survey of various techniques for solving the large generalized eigenvalue problem, involving both sparse and dense matrices, which I began last year, was to be completed, and potential useful results were to be identified for possible implementation, either during the summer or at a later date. Second, a literature survey of the currently available solution techniques for the matrix algebraic Riccati equation and the generalized algebraic Riccati equation was to be undertaken. Again, potentially useful results or techniques, as well as areas open for addition research, were to be identified. Finally, a library of useful linear algebra routines was to be implemented for the Intel IPSC Hypercube parallel computer, and the performance of these algorithms was to be characterized.

This research project is to continue throughout the academic year, and will hopefully result in useful results and algorithms for analysis and control system synthesis.

III. THE EIGENVALUE PROBLEM:

Solution methods for the eigenvalue problem can be grouped into classes based on the matrix properties they employ. The most popular algorithms, at least for single processor computers, are those which use similarity transforms to reduce the matrix to a standard form. The best known example of this technique uses Householder transformations to generate a tridiagonal matrix, from which the eigenvalues and eigenvectors can be extracted.

A second popular technique relies on the fact that the eigenvectors of a matrix are invariant under the matrix. These methods are variously called power methods, vector iterations, or invariant subspace iterations. The best known algorithms in this class are forward iteration, which converges to the eigenvalue of largest magnitude, and inverse iteration, which converges to the eigenvalue of smallest magnitude. In each case, the routine can be made to converge to any desired eigenvalue by applying the appropriate shift before iterating.

A third technique uses the Sturm Sequence properties of the characteristic polynomials of the leading principle minors of a matrix to approximately locate an eigenvalue. A technique such as bisection can be used to locate the desired eigenvalue to any desired precision.

Finally, there are a variety of other algorithms, including Cuppen's algorithm, which uses rank one tearing to transform the original eigenvalue problem into a set of smaller eigenvalue problems, and the Lanczos' algorithm, which iteratively generates a series of tridiagonal matrix whose extreme eigenvalues quickly converge to those of the original matrix.

Most of these techniques have been implemented on a parallel multiprocessor. Techniques based on similarity transformations perform very poorly on parallel computers, and are rarely used in practice. Speedups in the range of 6-10 on a 32 node Intel Hypercube have been reported for subspace iteration algorithms. Cuppen's algorithm, when the computational load is properly balanced among all processors, has shown speedups as high as 30. Bisection algorithms also perform well on parallel processors, so long as the eigenvalue estimates are not required to be too precise. Finally, Lanczos' algorithm performs rather poorly in parallel implementations, showing speedups of only 2-4, but the method deserves some consideration because of its inherent speed. In practice, it is often the fastest algorithm. [2-4]

IV. THE RICCATI EQUATION:

Many techniques have been proposed for solving the matrix Riccati equation. The current method of choice, both in terms of speed and numerical stability, is the Schur vector method, which involves expressing the Riccati equation as a Hamiltonian matrix and reducing the matrix to an ordered real Schur form. This method has been implemented on a parallel multiprocessor, but the highest speedup obtained was 6, regardless of the number of processors. [5] Alternate methods include various optimization schemes, foe example algorithms based on a Newton iteration, doubling or interval partitioning techniques, parametric embedding techniques, and special case analytic solutions. [6] A special case of the doubling strategy, utilizing the matrix sign function, has been implemented on a hypercube multiprocessor, and speedups of almost 30 have been obtained on large problems. [7]

V. A LIBRARY OF LINEAR ALGEBRA FUNCTIONS ON THE HYPERCUBE:

Several basic algorithms from linear algebra were chosen for implementation on a hypercube multiprocessor, based upon my expectation of their usefulness in the eigenvalue and Riccati equation solvers which will be implemented at a later time. In addition to standard linear algebra functions such as matrix-vector and matrix-product operations, LU decomposition with

partial pivoting [8], a wavefront algorithm for linear systems [9], and a conjugate gradient algorithm for linear systems [10] were implemented.

All algorithms were implemented using a column wrapped storage scheme. Selecting timing results for each of these major algorithms, as run on a 32 node Intel IPSC/1 Hypercube with vector arithmetic boards (no vectorization was employed in the code), are presented in Tables 1-3. Speedup results are presented in Figures 1-2.

VI. RECOMMENDATIONS:

Having implemented most of the needed basic linear algebra algorithms, we are ready to begin implementing solvers for the eigenproblem and the matrix Riccati equation. At least one efficient eigenvalue routine will be needed in order to implement solution algorithms for the Riccati equation. We shall implement the matrix sign function algorithm and the Schur vector algorithm first, to serve as benchmarks. We will then to explore the parallel implementation of parametric embedding techniques, as well as the possibility of iterative optimization techniques.

FIGURE 1

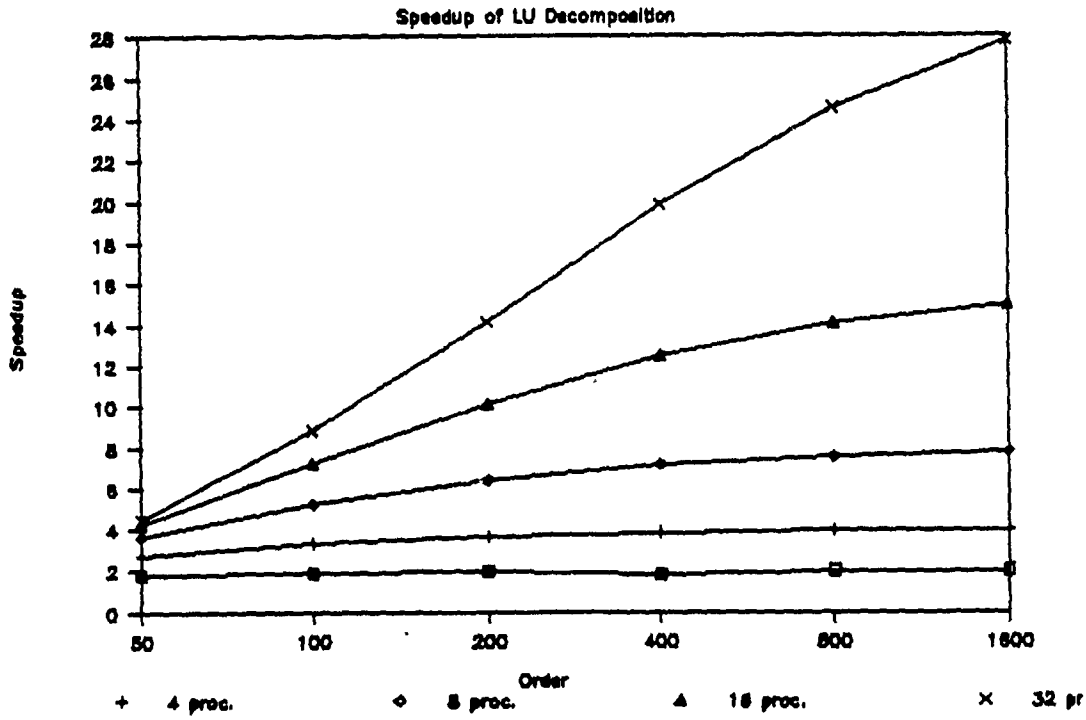

FIGURE 2

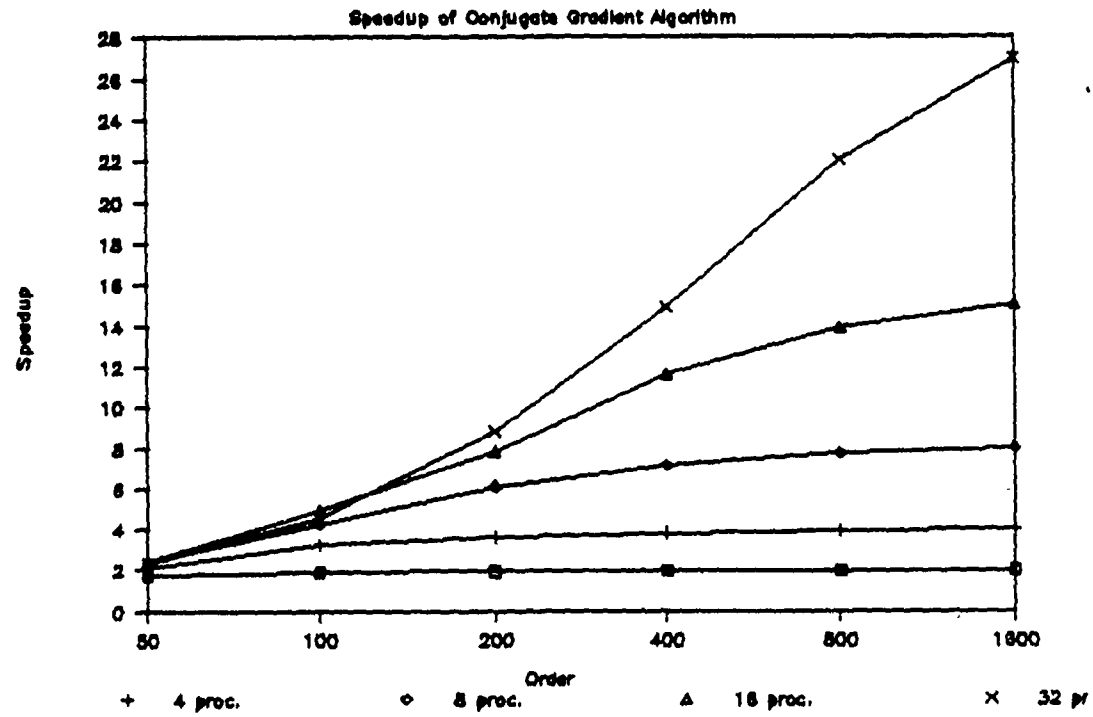

TABLE 1
Computation Times
LU Decomposition
(seconds)

Order	1 Processor	32 Processors
50	3.34	.75
100	24.17	2.76
200	183.52	12.99
400	1429.51	72.12
800	11282.99	459.36
1600	89654.51	3223.78

TABLE 2
Computation Times
Wavefront Linear Solver
(seconds)

Order	1 Processor	32 Processors
50	.68	.32
100	1.67	.66
200	4.69	2.04
400	14.82	6.48
800	51.52	16.85
1600	190.70	63.34

TABLE 3
Iteration Times
Conjugate Gradient Solver
(milliseconds)

Order	1 Processor	32 Processors
50	187	79
100	769	152
200	2969	307
400	10524	712
800	41696	2825
1600	165990	6176

Acknowledgements

I wish to thank the Air Force Systems Command and the Air Force Office of Scientific Research for their sponsorship of this research, as well as Dan Danishek and Universal Energy Systems for their administrative efforts. I also wish to thank Dr. Thomas Hartrum and the Department of Electrical Engineering at the Air Force Institute of Technology for providing access to their 32 Node Intel IPSC/1 Hypercubes, as well as Rick Norris, the system administrator, who kept the machines and I on speaking terms, and was always available to answer my technical questions. I very much appreciate the support of the staff of the Flight Dynamics Lab, Analysis and Optimization Branch, who shared their resources, and their own research efforts, with me. Finally, I wish to thank Dr. Umit Ozguner, my advisor at The Ohio State University, who, though not officially sponsored by this program, frequently came to Dayton to direct my research and study.

REFERENCES

1. Noor, A.K., "Parallel Processing in Finite Element Structural Analysis," Engineering Computation, 3:4 (1988), pp. 225-41.

2. Dongarra, D.J. and D.C. Sorenson, "A Fully Parallel Algorithm for the Symmetric Eigenvalue Problem," Siam Journal of Scientific and Statistical Computing, 8:2 (1987), pp. 5199.

3. Ipsen, Ilse C.F. and Elizabeth R. Jessup, "Two Methods for Solving the Symmetric Tridiagonal Eigenvalue Problem on the Hypercube," 1987 Hypercube Multiprocessing Conference, pp. 627-638.

4. Storaasli, O., S. Bostic, M. Patrick, U. Mahajan, and S. Ma, "Three Parallel Computation Techniques for Structural Vibration Analysis," Proceedings of the 29th Structures, Dynamics, and Materials Conference, 1988, p. 1401-1411.

5. Geist, G.A., R.C. Ward, G.J. Davis, and R.E. Funderlic, "Finding Eigenvalues and Eigenvectors of Unsymmetric Matrices using a Hypercube Multiprocessor," Third Conference on Hypercube Concurrent Computers and Applications, 1988.

6. Jamshidi, M., "An Overview on the Solutions of the Algebraic Matric Riccati Equation and Related Problems," Large Scale Systems: Theory and Applications, 1:3 (1980), pp 167-192.

7. Gardiner, Judith D. and Alan J. Laub, "Matrix Sign Function Implementation on a Hypercube Multiprocessor," Proceedings of the 29th Conference on Decision and Control, 1988, pp. 1466-1471.

8. Geist, G,A, and C.H. Romine, "LU Factorization Algorithms on Distributed-Memory Multiprocessor Architectures," SIAM Journal of Scientific and Statistical Computing, 9:4 (1988), pp. 639-649.

9. Heath, M.T. and C.H. Romine, "Parallel Solution of Triangular Systems on Distributed-Memory Multiprocessors," SIAM Journal on Scientific and Statistical Computing, 9:3 (1988), pp. 550-588.

10. Aykanat, C., F. Ozguner, F. Ercal, and P. Sadayappan, "Iterative Algorithms for Solution of Large Sparse Systems of Linear Equations on Hypercubes," IEEE Transactions on Computers, 37:12 (1988), pp. 1554-1567.

1990 USAF-UES SUMMER FACULTY RESEARCH PROGRAM/

GRADUATE STUDENT SUMMER SUPPORT PROGRAM

Sponsored by the

AIR FORCE OFFICE OF SCIENTIFIC RESEARCH

Conducted by the

Universal Energy Systems, Inc.

FINAL REPORT

COMPOSITE LAMINATE STRESS FIELDS DURING DYNAMIC LOADING

Prepared by:	Gregory A. Schoeppner
Academic Rank:	Graduate Research Associate
Department and University:	Civil Engineering Department The Ohio State University
Research Location:	WRDC/FIBCA Wright Patterson AFB OH 45433
USAF Researcher:	Dr. Raghbir S. Sandhu
Date:	30 Sept 90
Contract No:	F49620-88-C-0053

Composite Laminate Stress Fields During Dynamic Loading

by

Gregory A. Schoeppner

ABSTRACT

The derivation of a stress based laminate plate theory for describing the dynamic behavior of composite laminate plates was continued. The basic assumption of the theory is a linear through-the-thickness distribution of in-plane stresses. The transverse components of the stress tensor are derived from the equations of motion, constitutive equations and kinematic conditions. The governing field equations are subsequently derived from a Hamiltonian type variational formulation which has been extended to include inertia terms. The governing equations are manipulated to produce a self-adjoint form and a consistent set of boundary conditions which is favorable for a Ritz type finite element implementation are obtained. The governing function for describing the dynamic behavior of laminated plates is determined. It has been shown that satisfaction of the governing equations and the boundary conditions minimizes the functional.

ACKNOWLEDGEMENTS

The author wishes to thank the Air Force Systems Command and the Air Force Office of Scientific Research for sponsorship of the research during this summer appointment. The project was administered by Universal Energy Systems and their help during my summer stay was appreciated.

I want to thank the administration of the Flight Dynamics Laboratory, WRDC, for allowing me to participate in the Summer Graduate Student Research Program at their facility. The talent and knowledge of their personnel contributed greatly toward this research effort.

I am particularly grateful to my program monitor, Dr. R. S. Sandhu and group leader, Mr. G. R. Holderby, who provided the technical background and work environment to make this summer a successful experience. Appreciation and thanks are extended to my faculty advisor Dr. W. E. Wolfe for his valuable discussions and continued support throughout this research.

I. INTRODUCTION

The research described in this report is a continuation of an ongoing effort by the author and his faculty advisor Dr. William E. Wolfe in the Flight Dynamics Laboratory, WRDC. Previous low velocity impact studies on composite laminates performed by the author have demonstrated that predictive capabilities using empirical or semi-empirical models are limited [1,2]. However, these models are necessary since our level of understanding of the behavior of these material systems under dynamic transient loading is extremely limited. These experimental data based models offer the designer and user of composite laminates a qualitative as well as a quantitative set of rules or guidelines which define the expected behavior of composite laminates under certain specialized service loading conditions.

In an effort toward determining an appropriate theory for implementation into a computer program the author conducted an extensive survey of the available literature. It was determined that no existing theories were able to model the specifics of the stress field to the extent that the author felt necessary for laminated plates subjected to transient loading. Therefore, it was determined that an existing stress based theory which accurately describes the stress field in laminated plates for static loading would be most suitable for extension to dynamics. Toward this effort, a stress based laminated plate theory which includes inertia effects was begun during a recent project sponsored by AFOSR through UES and was reported in Reference [3].

II. OBJECTIVES OF THE RESEARCH EFFORT

The objective of the summer research program was to continue development and modification of the stress based theory previously presented [3]. The primary focus was to derive a self-adjoint set of governing field equations and a consistent set of boundary conditions. Having found a self-adjoint form of the governing equations, the finite element formulation using a Ritz type approach could be derived using established variational methods [4].

Along with the continued development of the new plate theory, a survey of the recent literature as a supplement to an earlier review [3] was conducted to determine the state-of-the-art in the determination of dynamic stress fields in laminated plates. The amount of work which has been published in the past two years on the analysis of laminated composite plates is a testament to the need in the research community to understand the behavior of this material system. Although much of the new literature are applications of existing theories, some new developments and progress in understanding this material have been made. Although a review of all the recently published work on this subject is not appropriate here, the cited references are selected to review various theories and are not necessarily the only significant contributions on the subject.

III. REVIEW OF LITERATURE

Much of the recent research in the area of laminated plates has been toward understanding the behavior of laminates on a ply-by-ply basis. Since the mechanism of damage initiation is a local response to loading, the local response must be investigated and determined for applications that require survivability, damage assessment, damage threshold and damage growth type studies. Also, as an interest to designers of composite structures, design tolerances are based on such studies of localized behavior.

3.2 First Order Shear Deformation Theories (FSDT)

An investigation by Noor [5] compared Classical Plate Theory (CPT) and FSDT for the prediction of natural frequencies of vibration for laminated plates. He found that although the stress predictions using FSDT where not accurate, the prediction of the low frequency global behavior of thick laminates was acceptable.

An impact study by Cairns and Lagace [6] used a Rayleigh-Ritz method to solve the FSDT governing equations. They found that to characterize the impact problem, using a local contact model where the influence of the structural behavior is neglected or using a global model where local phenomenon are neglected is incorrect since both local and global contributions occur.

Using a FSDT [7] and a Higher Order Shear Deformation Theory (HSDT) [8], a technique first suggested by Murthy [9] was employed by Engblom and Ochoa to determine a better estimate of interlaminar stresses. Although FSDT gave good predictions of in-plane stress

distributions, its prediction of transverse shear stresses and its neglect of transverse normal stress was unacceptable for determining localized behavior. Therefore, having determined an accurate estimate of in-plane stress components, the transverse stress components are found by integrating the three-dimensional equilibrium equations i.e. in the transverse direction z, such that

$$\sigma_{13,3} = -(\sigma_{11,1} + \sigma_{12,2})$$

$$\sigma_{23,3} = -(\sigma_{12,1} + \sigma_{22,2}) \qquad (1)$$

$$\sigma_{33,3} = -(\sigma_{13,1} + \sigma_{23,2})$$

The prediction of transverse stress components using this procedure was found to compare favorably to elasticity solutions.

Expanding upon this approach a predictor-corrector approach was used by Noor and Burton [10] to determine an improved prediction of interlaminar stresses. Their technique used FSDT to determine in-plane stresses and Murthy's method of integrating the equilibrium equations to determine an estimate of transverse stress components. New estimates of the shear correction factors are obtained by comparing the transverse shear strain energy calculated from FSDT and the transverse strain energy calculated by the strain associated with integrating the equilibrium equations. A new FSDT analysis is performed using the improved shear correction factors. The authors found that the use of this two-phase approach extends the range of validity of FSDT to fairly thick multilayered plates which otherwise are highly dependent on the selected shear correction factor [11].

3.2 Higher Order Shear Deformation Theories (HSDT)

Fuehne and Engblom [12] presented a displacement based approach in which all three displacement components were represented by a linear distribution through-the-thickness direction. As in previous work, the in-plane stresses were computed using the constitutive relations while the transverse stress components were calculated by integrating the equilibrium equations.

A theory by Murthy [9] where the in-plane displacements were approximated by cubic polynomials in the transverse direction and the transverse displacement was assumed to be constant through-the-thickness enforced the vanishing of the transverse shear strains on the top and bottom surfaces of the plate. This approach was latter adopted by Bhimaraddi and Stevens [13] and Reddy and Phan [14]. Since the transverse displacement component was assumed to be constant through-the-thickness, the transverse normal stress was neglected. Interlaminar shear stresses were determined from in-plane stress results using equilibrium equations.

To provide for an arbitrary variation of in-plane displacements through-the-thickness, a generalized plate theory by Krishna Murty [15] used the following displacement field to describe the vibration of thick plates.

$$u = u_o - zw_{o,x} + \sum_{n=1,2,3,..} p_n \phi_n$$

$$v = v_o - zw_{o,y} + \sum_{n=1,2,3,...} p_n \psi_r \qquad (2)$$

$$W = W_o$$

where midplane displacement and phi and psi are independent of z and are included in order to provide for arbitrary variation of in-plane displacements across the thickness. Also

$$p_n = \xi^{2n+1} - \frac{2n+1}{2^{2n}}\xi \tag{3}$$

$$\xi = \frac{z}{t}$$

Extending this approach to laminated plates, the authors [16] enforced zero shear strains at the top and bottom of the plate for the symmetric laminate which gave

$$\bar{U} = -zw_{o,x} - \sum_{n=3,5,\ldots} p^{(n)}(\xi)\, u_n$$

$$\bar{V} = -zw_{o,y} - \sum_{n=3,5,\ldots} p^{(n)}(\xi)\, v_n \tag{4}$$

$$\bar{W} = w_o + \sum_{n=2,4,\ldots} q^{(n)}(\xi)\, w_n$$

where

$$p^{(n)}(\xi) = \xi\left(1 - \frac{\xi^{n-1}}{n}\right) \tag{5}$$

and

$$q^{(n)}(\xi) = (1 - \xi^n) \tag{6}$$

giving a parabolic transverse displacement distribution. However, Krishna Murty and Vellaichamy [16] found that the estimates of transverse stresses where in error. Therefore, they used Murthy's approach to generate estimates of transverse stress components.

3.3 Discrete Laminate Theories

Discrete laminate theories were introduced not to obtain improved predictions of global responses, which are predicted well by SDT, but to determine the layer-wise local stresses and strains.

Owen and Li [17] assumed that each layer of the laminate is represented as having a linear through-the-thickness distribution of in-plane displacements and a constant distribution of transverse displacement. Although their predictions of displacement and frequency response were close to exact solutions, the prediction of transverse stress was not acceptable. The displacement field implies that the transverse normal stress is zero while the interface transverse shear stresses are discontinuous.

The only theory known to the author that uses a HSDT on a layer-wise basis is given by Cho, et.al. [18]. Using a cubic distribution through-the-thickness of in-plane displacement and a quadratic distribution of transverse displacement for each layer, continuity of the displacements and transverse stress components at interfaces is enforced. In-plane stress and transverse shearing stress distributions were found to be in good agreement with FSDT using stress equilibrium equations and with HSDT.

3.4 Other Displacement Based Approaches

Hinrichsen and Palazotto [19] represented the in-plane displacement distribution through-the-thickness by spline functions. The displacement field was written as

$$u_\alpha = \tilde{u}_\alpha + \hat{u}_\alpha$$
$$u_3 = \tilde{u}_3 \tag{7}$$

where tilde variables are functions of the in-plane coordinates and the hat variables which are cubic splines are functions of all three coordinates. Since the transverse displacement is assumed constant through-the-thickness, the transverse strains are neglected. The finite element results predicted in-plane stresses close to the exact solution, however, the critical transverse normal stress was not addressed.

Accounting for variation of transverse displacement through the thickness, Bogdanovich and Yarve [20,21] also used spline functions to represent displacement distributions. The displacement field which was written as

$$u_x(x,y,z,t) = \sum_i u_i(x,y,t)\phi_i(z)$$
$$u_y(x,y,z,t) = \sum_i v_i(x,y,t)\phi_i(z) \tag{8}$$
$$u_z(x,y,z,t) = \sum_i w_i(x,y,t)\phi_i(z)$$

where the spline functions in z are a linearly independent set. The authors employed both linear and quadratic spline-approximations. They found that the transverse stress components at the interfaces between the physical layers, having different characteristics, maintain certain discontinuities. The criteria for accuracy for their technique is the magnitude of the discontinuities.

3.5 Stress Based Theories

The only stress based theory for laminated plates is due to Pagano [22] in which he used Reissner's linear variation of in-plane stresses. The transverse stress components are obtained by integrating the equilibrium equations. The theory has been used to analyze the free edge stresses in composite laminate coupons. The high stress gradients near the free edge were closely modelled using this approach. The theory however has not been extended to include inertia effects. It is presumed that the theories ability to accurately model high stress gradients while ensuring continuity of stresses at interfaces will be a valuable tool for analyzing stress fields in laminates subjected to transient loading if inertia effects are incorporated into the theory.

IV. RESULTS

A recent report submitted to UES [3] includes in part the initial development of the stress based laminate theory. The theory which is a generalization of Pagano's stress based theory for statics [22] has a linear distribution of in-plane stresses through-the-thickness. Using this assumption along with the three-dimensional equations of equilibrium, the transverse stress components are obtain. This procedure is presented in Reference [3] along with a derivation of the governing equations. An alternative derivation to obtain a self-adjoint set of governing equations is presented here.

An energy formulation using the principle of stationary potential energy extended to dynamics is used to derive the governing

equations. The volume of the body is represented by V and the surface of the body is represented by S. let the portion of the boundary where traction is prescribed be denoted by S_s and the portion of the boundary where the displacement is prescribed be represented by S_u. The surface S_u and S_s are disjoint sets of S, such that $S_u \cup S_s = S$. The boundary conditions for the problem are

$$\begin{aligned} u_i &= s_i \quad on \quad S_u \\ \eta_i \sigma_{ij} &= t_i \quad on \quad S_s \\ \acute{u}_i &= \acute{g}_i \quad on \quad \acute{S}_u \\ \eta_j \acute{\sigma}_{ij} &= \acute{h}_i \quad on \quad \acute{S}_s \end{aligned} \tag{9}$$

where the primes indicate surfaces of jump discontinuities. The total energy of the body at any instant in time greater than or equal to time zero, is the integral over time of the kinetic energy minus the potential energy. This can be represented as

$$J = \int_0^t (T - \Pi) dt \tag{10}$$

The potential energy functional governing the problem of small deformation of an elastic body allowing for jump discontinuities is

$$\begin{aligned} \Omega = \int_V [u_i(\sigma_{ij,j} + f_i) + \epsilon_{ij}(E_{ijkl}\epsilon_{kl} - \sigma_{ij}) + \sigma_{ij}(u_{i,j} - \epsilon_{ij})]\, dV \\ + \int_{S_u} (u_i - 2s_i)\eta_j \sigma_{ij} dS - \int_{S_s} (\eta_j \sigma_{ij} - 2t_i) u_i dS \\ + \int_{\acute{S}_u} (\acute{u}_i - 2\acute{g}_i)\eta_j \sigma_{ij} dS - \int_{\acute{S}_s} (\eta_j \acute{\sigma}_{ij} - 2\acute{h}_i) u_i dS \end{aligned} \tag{11}$$

The complementary form of this equation can be written as

$$\Pi = \int_V [u_i(\sigma_{ij,j}+2f_i) + \sigma_{ij}(-u_{i,j}+S_{ijkl}\sigma_{kl})\,dV$$

$$+\int_{S_u} (u_i-2s_i)\eta_j\sigma_{ij}dS - \int_{S_s}(\eta_j\sigma_{ij}-2t_i)\,u_i dS \qquad (12)$$

$$+\int_{\acute{S}_u} (\acute{u}_i-2\acute{g}_i)\eta_j\sigma_{ij}dS - \int_{\acute{S}_s}(\eta_j\acute{\sigma}_{ij}-2\acute{h}_i)\,u_i dS$$

Writing the strain energy density as

$$W = \frac{1}{2}\sigma_{ij}S_{ijkl}\sigma_{kl} \qquad (13)$$

the complementary form for a linear elastic body can be extended as

$$\Pi_I = \int_V [u_i f_i - \frac{1}{2}\sigma_{ij}(u_{i,j}+u_{j,i}) + W]\,dV + \int_{S_u}(u_i-s_i)\eta_j\sigma_{ij}dS$$

(14)

$$+\int_{S_s} t_i u_i dS + \int_{\acute{S}_u}(\acute{u}_i-\acute{g}_i)\eta_j\sigma_{ij}dS + \int_{\acute{S}_s}\acute{h}_i u_i dS$$

The kinetic energy functional for an elastic body can be written as

$$T = \int_V [p_i\dot{u}_i - \frac{1}{2\rho}p_i p_i]\,dV \qquad (15)$$

where

$$\dot{p}_i = \rho\ddot{u}_i \qquad (16)$$

Assuming that the mass density is constant with time, we can write

$$T = \int_V [\rho\dot{u}_i\dot{u}_i - \frac{1}{2\rho}\rho\dot{u}_i\dot{u}_i]\,dV = \int_V \frac{1}{2}\rho\dot{u}_i\dot{u}_i dV \qquad (17)$$

Thus expressions for the kinetic and potential energies have been determined.

Taking the variational of the total energy expression where the variables subject to variation are the stress and displacement components gives

$$\delta J = \int_0^t [\frac{d}{d\dot{u}_i} T_R \delta \dot{u}_i - (\frac{\partial}{\partial \sigma_{ij}} \Pi_R \delta \sigma_{ij} + \frac{\partial}{\partial u_i} \Pi_R \delta u_i + \frac{\partial}{\partial u_{i,j}} \Pi_R \delta u_{i,j})]\, dt = 0 \qquad (18)$$

Substituting the potential and kinetic energy expressions into this equations and performing the differentiation we get

$$\delta J = \int_0^t \iint_V \{\rho \dot{u}_i \delta \dot{u}_i - [(\frac{u_{i,j}+u_{j,i}}{2} - \frac{\partial W}{\partial \sigma_{ij}}) \delta \sigma_{ij} + f_i \delta u_i - \sigma_{ij} \delta u_{i,j}]\} dV dt$$

$$+ \int_0^t \iint_{S_u} (u_i - s_i)\, \delta (\eta_j \sigma_{ij})\, dS dt + \int_0^t \iint_{S_\sigma} t_i \delta u_i dS dt \qquad (19)$$

$$+ \int_0^t \iint_{S_u} (\dot{u}_i - \dot{g}_i)\, \delta (\eta_j \sigma_{ij})\, dS dt + \int_0^t \iint_{S_\sigma} \dot{h}_i \delta u_i dS dt = 0$$

Using integration by parts, applying the Green-Gauss theorem and making some trivial manipulations, this equation becomes.

$$\delta J = \int_0^t \iint_V \{[\frac{u_{i,j}+u_{j,i}}{2} - \frac{\partial W}{\partial \sigma_{ij}}] \delta \sigma_{ij} - (\sigma_{ij,j} + f_i - \rho \ddot{u}_i)\, \delta u_i\} dV dt$$

$$+ \int_0^t \iint_{S_u} (u_i - s_i)\, \delta (\eta_j \sigma_{ij})\, dS dt - \int_0^t \iint_{S_\sigma} [\eta_j \sigma_{ij} - t_i]\, \delta u_i dS dt \qquad (20)$$

$$+ \int_0^t \iint_{S_u} (\dot{u}_i - \dot{g}_i)\, \delta (\eta_j \sigma_{ij})\, dS dt - \int_0^t \iint_{S_\sigma} [\eta_j \dot{\sigma}_{ij} - \dot{h}_i]\, \delta u_i dS dt$$

$$- \int_V (\rho \dot{u}_i \delta u_i) \Big|_0^t dV = 0$$

This is the functional which is used to derive the governing field equations for the anisotropic elastic medium under consideration. Consider a laminated body composed of N layers, the volume of which are represented by V_k (k=1,2,3,...,N). Both traction and displacement continuity at the interfaces are considered. Observe that the surface S involves the cylindrical boundary, edges of the layers, as well as the top of the Nth layer and the bottom of the first layer. Then the governing functional for the case of a laminate can be expressed as

$$\delta J = \sum_{k=1}^{N} \int_0^t \int_{V_k} \{ [\frac{u_{i,j}+u_{j,i}}{2} - \frac{\partial W}{\partial \sigma_{ij}}] \delta \sigma_{ij} - (\sigma_{ij,j}+f_i-\rho \ddot{u}_i) \delta u_i \}^{(k)} dV_k dt$$

$$-\sum_{k=1}^{N} \int_{V_k} \rho [\dot{u}(x_j, t) \delta u_i(x_j, t) - \dot{u}_i(x_j, 0) \delta u_i(x_j, 0)]^{(k)} dv_k$$

$$+\int_0^t \int_{S_u} (u_i - s_i) \delta (\eta_j \sigma_{ij}) dS dt - \int_0^t \int_{S_s} [\eta_j \sigma_{ij} - t_i] \delta u_i dS dt \qquad (21)$$

$$+\sum_{k=1}^{N} \int_0^t \int_{\dot{S}_{u_k}} [(\dot{u}_i - \dot{g}_i) \delta (\eta_j \sigma_{ij})]^{(k)} dS dt$$

$$+\sum_{k=1}^{N} \int_0^t \int_{\dot{S}_{s_k}} \{[\eta_j \sigma_{ij} - \dot{h}_i] \delta u_i\}^{(k)} dS dt = 0$$

The vanishing of the volume-time integrals requires satisfaction of the kinematic and constitutive relations as well as the equations of motion for each layer. Vanishing of the volume integrals requires satisfaction of the initial conditions. The vanishing of the area-time integrals on S_s, S_u, S_s' and S_u' require

that one term of each of the products in the integral be prescribed at each point on the internal and external boundaries.

Having determined the stress tensor in Reference [3], substitution into the governing functional and performing the variation, yields the governing field equations and numerous natural boundary conditions. Upon manipulation of these equations a self-adjoint form of the governing equations can be obtain. The self-adjoint system consists of twenty three field variables and a like number of field equations. The consistent boundary terms, consistent in the sense of the convolution bilinear mapping, for the self-adjoint equations were then determined. In preparation of finite element implementation, the required differentiability and smoothness of the field variables have been determined based on the equilibrium, constitutive and interface continuity equation requirements. The governing functional for the theory has been written and it has been shown that the Gateaux differential of the functional vanishes for satisfaction of the governing equations, the interface continuity conditions and the boundary conditions.

V. RECOMMENDATIONS

The development outline above clearly shows that the consistent theory is well suited for describing stress field in laminated plates subjected to transient loading. Additional extensions for reducing the number of field variables will enhance the employment of the theory. It is proposed that the following steps in the continuing development of the theory be performed:

a) a finite element formulation be written and implemented;

b) the solution to a simple problem whose exact solution is known be analyzed for exactness of the theory;

c) after verification of the theory, implement a stress based failure criterion to model delamination behavior.

It is felt that further extensions and development of the theory could result in an understanding of the failure mechanisms associated with low velocity impact of laminated plates. With future extensions the theory should be able to predict damage initiation as well as damage history and presumably eliminate the need for low velocity empirical evaluation of new materials and laminate geometries. Therefore, it is recommended that the development and extension of the theory continue.

REFERENCES

1. Schoeppner, G. A., **Damage in Graphite/Epoxy Plates Subjected to Low Velocity Impact**, Final Report, USAF-UES Summer Graduate Student Research Program, 1988

2. Schoeppner, G. A., **Low Velocity Impact of Graphite/Epoxy Plates**, Final Report, USAF-UES Summer Graduate Student Research Program, 1987

3. Wolfe, W. E. and Schoeppner, G. A., **Low Velocity Impact of Composite Materials**, Final Report, Grant Nos. S-760-7MG-102 and S-210-9MG-082, Universal Energy Systems, Dayton, OH., 1990

4. Sandhu, R. S. and Salaam, U.,"Variational Formulation of Linear Problems with Nonhomogeneous Boundary Conditions and Internal Discontinuities," Comp. Meth. in Appl. Mech. Eng., Vol. 7, 1975, pp. 75-91

5. Noor, A. K.,"Free Vibration of Multilayered Composite Plates," AIAA Journal, Vol. 11, No. 7, 1973, pp. 1038-1039

6. Cairns, D. S. and Lagace, P. A.,"Transient Response of Graphite/Epoxy and Kevlar/Epoxy Laminates Subjected to Impact," AIAA Journal, Vol. 27, No. 11, 1989, pp. 1590-1596

7. Engblom, J. J. and Ochoa, O. O.,"Finite Element Formulation Including Interlaminar Stress Calculations," Computers and Structures, Vol. 23, No. 2, 1986, pp. 241-249

8. Engblom, J. J. and Ochoa, O. O.,"Through-the-thickness Stress Predictions for Laminated Plates of Advanced Composite Materials," IJNME, Vol. 21, 1985, pp. 1759-1776

9. Murthy, M. V. V., **An Improved Transverse Shear Deformation Theory for Laminated Plates**, NASA Technical Paper 1903, 1981

10. Noor, A. K. and Burton, W. S.,"Stress and Free Vibration Analysis of Multilayered Composite Plates," Composite Structures, Vol. 11, 1989, pp. 183-204

11. Chatterjee, S. N. and Kulkarni, S. V.,"Shear Correction Factors for Laminated Plates," AIAA Journal, Vol. 17, No. 5, 1979, pp. 498-499

12. Fuehne, J. P. and Engblom, J. J.,"A Shear Deformable Finite Element Penalty Formulation for Predicting Transverse Stresses in Thick Composite Structures," **Proc. Am. Soc. for Comp., Fourth Tech. Conf.**, Blacksburg, VA., 1989, pp. 224-233

13. Bhimaraddi, A. and Stevens, L. K.,"A Higher Order Theory for Free Vibration of Orthotropic, Homogeneous, and Laminated Rectangular Plates," J. Appl. mech., Vol. 51, 1984, pp. 195-198

14. Reddy, J. N. and Phan, N. D.,"Stability and Vibration od Isotropic, Orthotropic and Laminated Plates According to a Higher-Order Shear Deformation Theory," J. Sound Vibration, Vol. 98, No. 2, 1985, pp. 157-170

15. Krishna Murty, A. V.,"Higher Order Theory for Vibrations of Thick Plates," AIAA Journal, Vol. 15, No. 12, 1977, pp. 1823-1824

16. Krishna Murty, A. V. and Vellaichamy, S.,"On Higher Order Shear Deformation Theory of Laminated Composite Panels," Composite Structures, Vol. 8, 1987, pp. 247-270

17. Owen, D. R. J. and Li, Z. H.,"A Refined Analysis of Laminated Plates by Finite Element Displacement Methods - II. Vibration and Stability,"Computers and Structures, Vol. 26, No. 6, 1987, pp. 915-923

18. Cho, K. N., Striz, A. G. and Bert, C. W.,"Bending Analysis of Thick Bimodular Laminates by Higher-Order Individual-Layer Theory," Composite Structures, Vol. 15, No. 1, 1990, pp. 1-24

19. Hinrichsen, R. L. and Palazotto, A. N.,"Nonlinear Finite Element Analysis of Thick Composite Plates Using Cubic Spline Functions," AIAA Journal, Vol. 24, No. 11, 1986, pp. 1836-1842

20. Bogdanovich, A. E. and Yarve, E. V.,"Numerical Solutions of a Two-dimensional Problem of Nonsteady Deformation of Laminated Media," Mech. of Comp. Matl., Vol. 24, No. 1, 1989, pp. 31-38

21. Bogdanovich, A. E. and Yarve, E. V.,"Numerical Analysis of Laminated Composite Plates Subjected to Impact Loading," **Proc. Am. Soc. for Comp., Fourth Tech. Conf.**, Blacksburg, VA., 1989, pp. 399-409

22. Pagano, N. J.,"Stress Fields in Composite Laminates," Int. J. Solids Structures, Vol. 14, 1978, pp. 385-400

1990 USAF-UES SUMMER FACULTY RESEARCH PROGRAM

Sponsored by the

AIR FORCE OFFICE OF SCIENTIFIC RESEARCH

Conducted by the

UNIVERSAL ENERGY SYSTEM, INC.

FINAL REPORT

Influence of Static and Dynamic Aeroelastic Constraints on the Optimal Structural Design of Flight Vehicles

Prepared by:	Dr. Franklin E. Eastep and Anne Stephenson
Academic Rank:	Professor Graduate Student
Department and University:	Aerospace Engineering University of Dayton
Research Location:	Flight Dynamics Laboratory, Structures and Dynamics Division, Analysis/Optimization Branch
USAF Researcher:	Dr. Vipperla B. Venkayya
Date:	1 November 1990
COntract No.:	F49620-88-C-0053

Same Report as
Prof. Franklin Eastep
(Report # 99)

1990 USAF-UES SUMMER FACULTY RESEARCH PROGRAM/

GRADUATE STUDENT RESEARCH PROGRAM

Sponsored by the

AIR FORCE OFFICE OF SCIENTIFIC RESEARCH

Conducted by

Universal Energy Systems, Inc.

FINAL REPORT

A COMPARISON OF THE ANALYTICAL AND NUMERICAL SOLUTIONS OF THE NONLINEAR DIFFUSION EQUATION AND A PRELIMINARY INVESTIGATION INTO A SPECIFIC CASE OF SECOND HARMONIC GENERATION

Prepared by:	Brian D. Cull
Academic Rank:	Graduate Student
Department and University:	Physics Department Kent State University
Research Location:	WRDC/MLPO WPAFB Dayton, OH 45433
USAF Researcher:	Dr. Patrick M. Hemenger
Date:	August 13, 1990
Contract No.:	F49620-88-C-0053

A COMPARISON OF THE ANALYTICAL AND NUMERICAL SOLUTIONS OF THE NONLINEAR DIFFUSION EQUATION AND A PRELIMINARY INVESTIGATION INTO A SPECIFIC CASE OF SECOND HARMONIC GENERATION

by

Brian D. Cull

ABSTRACT

A numerical solution of the nonlinear heat diffusion equation with a laser source term was found using the forward-time centered-space difference method. Good agreement was found in the 10^{-6}m--10^{-4}m range of penetration depths when this solution was compared to the analytical result previously obtained by Hemenger and Moroi. Good agreement was also found in this same range when the numerical and analytical solutions of the constant coefficient case were compared.

A start was made in the study of nonlinear optical properties of materials. Maxwell's equations were solved for a specific case in which the existing incident E and B field vectors were known, and progress was made toward the generation of the second harmonics.

ACKNOWLEDGEMENTS

I would like to extend thanks to the Air Force Office of Scientific Research, the Air Force Systems Command, the Wright Research and Development Center, and the Materials Laboratory for sponsoring this research project. I would also thank Universal Energy Systems for the opportunity they provided me.

Thanks go to the Physics Department at Kent State University for allowing me time to complete this work. I appreciate all the help that the people in the Materials Lab gave me: Ron Perrin for his assistance with the computer system, and Dr. Patrick Hemenger for providing me with whatever was needed. And thanks also go, of course, to Dr. David Moroi, who helped and guided me through this project with patience and understanding.

I. INTRODUCTION

Semiconductor devices made of a material such as GaAs are fabricated by ion implantation using the method of pulsed laser annealing. The electrical properties of these devices are determined by the final dopant profile, which can be predicted by solving a temperature-dependent dopant diffusion equation that has been coupled with a nonlinear heat conduction equation. It is essential to obtain a temperature profile of the doped semiconductor device. Development and optimization of the electrical characteristics of these devices are important to the Materials Laboratory of the Wright Research and Development Center at Wright Patterson Air Force Base.

A study of nonlinear optics is important to the understanding of such phenomena as optical phase conjugation, distortion-free transmission of data, and other interesting effects. Theoretical research involving Maxwell's equations is necessary to fully explore the possible applications of the above-mentioned phenomena.

My interest in solid state physics and higher mathematics, as well as my programming proficiency, aided me in my work on this project.

II. OBJECTIVES OF THE RESEARCH EFFORT

One goal of this research was to develop a numerical solution to the nonlinear diffusion equation with source term. Moroi and Hemenger[1] developed an analytical solution of this equation, and it was necessary to test the accuracy of this method by means of comparing the analytical results with those obtained numerically. My assignment as part of the 1990 Summer Graduate Student Research Program was to develop the numerical solution and use it to obtain the error inherent in the analytical result. It was also necessary to find the error inherent in the numerical result, and so the numerical solution was compared to the exact analytical in the constant coefficient case.

The work in nonlinear optics was directed at solving Maxwell's equations for a specific case of second harmonic generation. More work is necessary on this project because time constraints prevented completion of this phase of the research.

III. COMPARISON OF ANALYTICAL AND NUMERICAL SOLUTIONS OF THE NONLINEAR DIFFUSION EQUATION WITH SOURCE TERM

The nonlinear heat diffusion equation with source term may be written as

$$\rho(T)c(T)\frac{\partial T}{\partial t} = \frac{\partial}{\partial z}\left(K(T)\frac{\partial T}{\partial z}\right) + I(1-R(T_s))\alpha(T)\exp\left(-\int_0^z \alpha(T)dz\right) \qquad (1)$$

where $T(z,t)$ is the temperature and $T_s = T(0,t)$. The boundary and initial conditions are

$$\frac{\partial T}{\partial z} = 0 \quad \text{at } z=0 \tag{2}$$

$$T(\infty,t) = 0 \tag{3}$$

$$T(z,0) = 20°C \tag{4}$$

The temperature dependent terms in the above equations are:

ρ -- mass density

c -- specific heat

K -- thermal conductivity

α -- absorption coefficient

R -- reflectivity

The intensity I of the laser source was considered to be constant.

Moroi and Hemenger have been able to transform Eq. (1) by introducing the variables

$$\tau = \tau(z,t) = \int_0^t dt\, \alpha^2\{T(z,t)\}\, K\{T(z,t)\}/\rho c\{T(z,t)\} \tag{5}$$

$$\zeta = \zeta(z,t) = \int_0^z dz\, \alpha\{T(z,t)\} \tag{6}$$

$$\Theta(T) = \Theta(\zeta,\tau) = \int_{T_{ambient}}^{T} \alpha(T)K(T)dT \tag{7}$$

thus generating the simple quasi-linear equation

$$\frac{\partial \Theta}{\partial \tau} = \frac{\partial}{\partial \zeta}\frac{\partial \Theta}{\partial \zeta} + I(1-R)\exp(-\zeta) \tag{8}$$

with corresponding boundary and initial conditions

$$\frac{\partial \Theta}{\partial \zeta} = 0 \text{ at } \zeta=0 \tag{9}$$

$$\Theta(\infty,\tau) = 0 \tag{10}$$

$$\Theta(\zeta,0) = 0 \tag{11}$$

The analytical solution of Eq. (8) was found to be

$$\Theta(\zeta,\tau) = I(1-R)\{2\sqrt{\frac{\tau}{\pi}}\exp(-\frac{\zeta^2}{4\tau}) + \frac{1}{2}\exp(\zeta+\tau)\operatorname{erfc}(\sqrt{\tau}+\frac{\zeta}{2\sqrt{\tau}})$$

$$+ \frac{1}{2}\exp(-\zeta+\tau)\operatorname{erfc}(\sqrt{\tau}-\frac{\zeta}{2\sqrt{\tau}}) - \exp(-\zeta) - \zeta\operatorname{erfc}(\frac{\zeta}{2\sqrt{\tau}})\} \quad (12)$$

Computer code was written which found the roots ζ and τ of this equation and then calculated the real variables z and t (see Appendix I). The task of this researcher was to develop code which would generate the numerical solution of Eq. (1), and then compare that result to the analytical answer.

In the numerically explicit forward-time centered-space (FTCS) difference method,[2,3,4] temperature values are calculated using previously obtained results. Applying this method, the partial derivatives in Eq. (1) are transformed as follows:

$$\frac{\partial T}{\partial t} = \frac{T(z,t+\Delta t) - T(z,t)}{\Delta t} \quad (13)$$

$$\frac{\partial}{\partial z}(K(T)\frac{\partial T}{\partial z}) = \frac{1}{2(\Delta z)^2}[(K\{T(z+\Delta z,t)\} + K\{T(z,t)\})\,(T(z+\Delta z,t) - T(z,t)) \quad (14)$$

$$- (K\{T(z-\Delta z,t)\} + K\{T(z,t)\})\,(T(z,t) - T(z-\Delta z,t))]$$

Thus, Eq. (1) becomes

$$\{T(z,t+\Delta t) - T(z,t)\}/\Delta t = \frac{1}{2(\Delta z)^2}[(K\{T(z+\Delta z,t)\} + K\{T(z,t)\})\,(T(z+\Delta z,t)-T(z,t))$$

$$- (K\{T(z+\Delta z,t)\} - K\{T(z,t)\})\,(T(z,t)-T(z-\Delta z,t))] \quad (15)$$

$$+ I(1-R)\alpha\{T(z,t)\}\exp(-\int_0^z \alpha\{T(z,t)\}dz).$$

Rearranging this equation we obtain

$$T(z,t+\Delta t) = T(z,t) + \frac{\Delta t}{2(\Delta z)^2}[(K\{T(z+\Delta z,t)\} + K\{T(z,t)\})\,(T(z+\Delta z,t) - T(z,t))$$

$$- (K\{T(z-\Delta z,t)\} + K\{T(z,t)\})\,(T(z,t) - T(z-\Delta z,t)) \qquad (16)$$

$$+ I(1-R)\alpha\{T(z,t)\}\exp(-\int_0^z \alpha\{T(z,t)\}dz$$

where $T(z-\Delta z,t)$, $T(z,t)$, and $T(z+\Delta z,t)$ are previously calculated values that allow us to obtain $T(z,t+\Delta t)$, the temperature at position z at the next highest time step.

To ensure the stability of the numerically explicit method, the following condition must be met[5]:

$$\Delta t \leq \frac{1}{2}\frac{\rho c(\Delta z)^2}{K} \qquad (17)$$

A space step of any size may be chosen in order to generate the desired number of data points, but the time step must then correspond to Eq. (17) to ensure stability. In this case a space step of one micrometer (10^{-6}m) was chosen, and the time step necessary for stability was $.5790 \times 10^{-12}$s.

The boundary condition represented by Eq. (2) was achieved by setting

$$T(-z,t) = T(z,t) \qquad (18)$$

after each calculation for a particular time step. This condition thus affects the boundary-level temperature of the next highest time step. Eq. (3) can be approximately fulfilled by choosing an outermost space limit, then dividing that number by the space step size to determine the number of steps necessary, and then setting that outermost position to zero.

In the present case, an outermost limit of 10^{-3}m was chosen. Because the space step size was 10^{-6}m, this meant approximately 1100 positions were necessary, and T(1100,t) was set equal to zero after each calculation. The coding for the numerical solution can be found in Appendix II.

IV. RESULTS OF COMPARISON OF ANALYTICAL AND NUMERICAL METHODS

Plots of temperature versus penetration depth for the nonlinear diffusion equation with temperature-dependent coefficients can be seen in Figs. (1), (2), and (3). The maximum error in the analytical result as compared to the numerical is shown for selected regions in the table below:

Penetration Depth Range (m)	Temperature Range (°C)	Maximum Error (%)
10^{-6} -- 10^{-5}	1400--1150	+0.14
10^{-5} -- 10^{-4}	1150--250	-7.36
10^{-4} -- 10^{-3}	250--20	-12.9

As can be seen from Fig. (3), the numerical solution crosses the analytical at a penetration depth of approximately 8.5×10^{-6}m. From there it steadily diverges from the analytical, and the error steadily increases. One explanation of this is that the method used led to an accumulation of roundoff error.[6] The use of double precision variables in the source code was offset by the large number of space and time steps necessary to generate the desired graph. In the

forward explicit method used, previously-calculated temperatures in both time and space are used to generate the next highest temperature, and the roundoff error accumulates over many steps. Attempts were made at finding a totally implicit method, but the boundary condition in Eq. (18) prevented the use of such methods. It may be argued that, in this case, the numerical solution should be closer to the true answer than the analytical approximation. Therefore the exact analytical solution should lie between the two curves and the error between the analytical approximation and the exact analytical answer must be less than the error between the numerical and analytical solutions.

A comparison was also made in the case of constant coefficients where the temperature-dependent coefficients were evaluated at 20°C (see Figs. (4), (5), and (6)). The analytical answer was exact and the numerical was compared to give the error inherent in that method. The maximum error of the numerical method in selected regions follows:

Penetration Depth Range (m)	Temperature Range (°C)	Maximum Error (%)
10^{-6} -- 10^{-5}	1400--1380	-1.36
10^{-5} -- 10^{-4}	1380--1100	-5.6
10^{-4} -- 10^{-3}	1100--20	-10.7

These errors may also be attributed to the accumulation of roundoff error due to the number of steps involved and the forward method.

V. A SPECIFIC CASE IN THE GENERATION OF SECOND HARMONICS

Starting with the source-free Maxwell equations in the CGS system[7]

$$\nabla \cdot D = 0 \tag{19}$$

$$\nabla \cdot B = 0 \tag{20}$$

$$\nabla \times E = -\frac{1}{c}\frac{\partial B}{\partial t} \tag{21}$$

$$\nabla \times B = \frac{\mu}{c}\frac{\partial D}{\partial t} \tag{22}$$

it is possible to generate second harmonics given the proper initial assumptions. In this case let us assume that

$$E_x^{(0)} = E_y^{(0)} = 0 \tag{23}$$

$$E_z^{(0)} \neq 0 \tag{24}$$

and

$$E_y^{(2)} = 0 \tag{25}$$

so

$$E^{(2)} = (E_x^{(2)}, 0, E_z^{(2)}) \tag{26}$$

and

$$B^{(2)} = (0, B_y^{(2)}, 0) \tag{27}$$

If in general[8]

$$D_i^{(1)} = \sum_k \varepsilon_{ik} E_k^{(1)} + 4\pi \sum_{jk} \chi_{ijk}^{(2)}(-\omega;-\omega,2\omega) E_j^{*(1)} E_k^{(2)} \tag{28}$$

$$D_i^{(2)} = \sum_k \varepsilon_{ik} E_k^{(2)} + 4\pi \sum_{jk} \chi_{ijk}^{(2)}(-\omega;-\omega,2\omega) E_j^{(1)} E_k^{(1)} \tag{29}$$

$$\text{and } \varepsilon_{ik}(\omega) = \varepsilon_{ii}^{(L)}(\omega)\delta_{ik} + 8\pi \sum_j \chi_{ijk}^{(2)}(-\omega;0,\omega) E_j^{(0)} \tag{30}$$

then the specific values of D and ε can be found for given initial assumptions. From Eqs. (28) and (30) and our initial assumptions it can be shown that

$$D_x^{(1)} = D_z^{(1)} = 0 \tag{31}$$

$$\text{and } D_y^{(1)} = \varepsilon_{22}(\omega) E_y^{(1)} + 4\pi \chi_{223}^{(2)}(-\omega;-\omega,2\omega) E_y^{*(1)} E_z^{(2)} \tag{32}$$

and from Eqs. (29) and (30) that

$$D_x^{(2)} = \varepsilon_{11}(2\omega)E_x^{(2)} \tag{33}$$

$$D_y^{(2)} = 0 \tag{34}$$

$$D_z^{(2)} = \varepsilon_{33}(2\omega)E_z^{(2)} + 4\pi\chi_{322}^{(2)}(-2\omega;\omega,\omega)[E_y^{(1)}]^2 \tag{35}$$

Thus we can write Maxwell's equations for the second harmonic as

$$(\nabla\times E)_x^{(2)} = \frac{\partial E_z^{(2)}}{\partial y} - \frac{\partial E_y^{(2)}}{\partial z} = i\frac{2\omega}{c}B_x^{(2)} \tag{36}$$

$$(\nabla\times E)_y^{(2)} = \frac{\partial E_x^{(2)}}{\partial z} - \frac{\partial E_z^{(2)}}{\partial x} = i\frac{2\omega}{c}B_y^{(2)} \tag{37}$$

$$(\nabla\times E)_z^{(2)} = \frac{\partial E_y^{(2)}}{\partial x} - \frac{\partial E_x^{(2)}}{\partial y} = i\frac{2\omega}{c}B_z^{(2)} \tag{38}$$

and

$$(\nabla\times B)_x^{(2)} = \frac{\partial B_z^{(2)}}{\partial y} - \frac{\partial B_y^{(2)}}{\partial z} = -i\mu\frac{2\omega}{c}D_x^{(2)} \tag{39}$$

$$(\nabla\times B)_y^{(2)} = \frac{\partial B_x^{(2)}}{\partial z} - \frac{\partial B_z^{(2)}}{\partial x} = -i\mu\frac{2\omega}{c}D_y^{(2)} \tag{40}$$

$$(\nabla\times B)_z^{(2)} = \frac{\partial B_y^{(2)}}{\partial x} - \frac{\partial B_x^{(2)}}{\partial y} = -i\mu\frac{2\omega}{c}D_z^{(2)} \tag{41}$$

Given Eqs. (26) and (27), Eqs. (36) and (38) yield that

$$E_x^{(2)} = E_x^{(2)}(x,z) \tag{42}$$

$$E_z^{(2)} = E_z^{(2)}(x,z) \tag{43}$$

Using Eqs. (36) through (38), Eqs. (39) and (41) can be rewritten

$$\frac{\partial}{\partial z}\frac{\partial E_x^{(2)}}{\partial z} - \frac{\partial}{\partial x}\frac{\partial E_z^{(2)}}{\partial z} = -\mu\left(\frac{2\omega}{c}\right)^2\varepsilon_{11}E_x^{(2)} \tag{44}$$

$$\frac{\partial}{\partial x}\frac{\partial E_x^{(2)}}{\partial z} - \frac{\partial}{\partial x}\frac{\partial E_z^{(2)}}{\partial x} = \mu\left(\frac{2\omega}{c}\right)^2[\varepsilon_{33}E_z^{(2)} + 4\pi\chi_{322}^{(2)}(E_y^{(1)})^2] \tag{45}$$

A third equation is provided by

$$\nabla\cdot D^{(2)} = 0 \tag{46}$$

$$\frac{\partial D_x^{(2)}}{\partial x} + \frac{\partial D_y^{(2)}}{\partial y} + \frac{\partial D_z^{(2)}}{\partial z} = 0 \tag{47}$$

$$\varepsilon_{11}\frac{\partial E_x^{(2)}}{\partial x} + \varepsilon_{33}\frac{\partial E_z^{(2)}}{\partial z} + 4\pi\chi_{322}^{(2)}\frac{\partial}{\partial z}[E_y^{(1)}]^2 = 0 \tag{48}$$

If we assume that

$$E_x^{(2)} = E_x^{(2)}(x,z) = E_x(z)\exp(2ikx) \tag{49}$$

and
$$E_z^{(2)} = E_z^{(2)}(x,z) = E_z(z)\exp(2ikx) \tag{50}$$

where the coefficients E_x and E_z are complex, then Eqs. (44), (45), and (48) become

$$\frac{\partial}{\partial z}\frac{\partial E_x}{\partial z} + \mu\left(\frac{2\omega}{c}\right)^2\varepsilon_{11}E_x - i2k\frac{\partial E_z}{\partial z} = 0 \tag{51}$$

$$\left[2ik\frac{\partial E_x}{\partial z} + 4k^2E_z - \mu\left(\frac{2\omega}{c}\right)^2\varepsilon_{33}E_z\right]\exp(2ikx) = 4\pi\chi_{322}(E_y^{(1)})^2 \tag{52}$$

$$\left[\varepsilon_{11}2ikE_x + \varepsilon_{33}\frac{\partial E_z}{\partial z}\right]\exp(2ikx) = -4\pi\chi_{322}\frac{\partial}{\partial z}(E_y^{(1)})^2 \tag{53}$$

But Maxwell's equations arise from the relation

$$\nabla\times\nabla\times E = \mu\left(\frac{2\omega}{c}\right)^2 D \tag{54}$$

and so, using a familiar vector identity,

$$\nabla\cdot(\nabla\times\nabla\times E) = \mu\left(\frac{2\omega}{c}\right)^2\nabla\cdot D = 0 \tag{55}$$

we see that, to ensure linear independence, only two of Eqs. (51) through (53) may be used to solve this system. Choosing Eqs. (51) and (53), first we solve Eq. (51) for $\frac{\partial E_z}{\partial z}$:

$$\frac{\partial E_z}{\partial z} = \frac{1}{2ik}\left[\frac{\partial}{\partial z}\frac{\partial E_x}{\partial z} + \mu\left(\frac{2\omega}{c}\right)^2\varepsilon_{11}E_x\right] \tag{56}$$

Substituting this result into Eq. (53) and rearranging,

$$\frac{\varepsilon_{33}}{2k}\frac{\partial}{\partial z}\frac{\partial E_x}{\partial z} + E_x\left[\frac{\varepsilon_{33}\mu\varepsilon_{11}}{2k}\left(\frac{2\omega}{c}\right)^2 - \varepsilon_{11}2k\right] = -i4\pi\chi_{322}\frac{\partial}{\partial z}(E_y^{(1)})^2\exp(-2ikx) \tag{57}$$

Now let's solve Eq. (53) for E_x:

$$E_x = \frac{i}{\varepsilon_{11}2k}\left[\varepsilon_{33}\frac{\partial E_z}{\partial z} + 4\pi\chi_{322}\frac{\partial}{\partial z}(E_y^{(1)})^2\exp(-2ikx)\right] \tag{58}$$

Substituting into Eq. (51) and rearranging,

$$\frac{\varepsilon_{33}}{\varepsilon_{11}}\frac{\partial}{\partial z}\frac{\partial}{\partial z}\frac{\partial E_z}{\partial z} + \frac{\partial E_z}{\partial z}\left[\mu\left(\frac{2\omega}{c}\right)^2\varepsilon_{33} - 4k^2\right] =$$

$$-4\pi\chi_{322}\exp(-2ikx)\left[\frac{1}{\varepsilon_{11}}\frac{\partial}{\partial z}\frac{\partial}{\partial z}\frac{\partial}{\partial z}(E_y^{(1)})^2 + \mu\left(\frac{2\omega}{c}\right)^2\frac{\partial}{\partial z}(E_y^{(1)})^2\right] \tag{59}$$

Eqs. (57) and (59) are nonlinear, nonhomogeneous partial differential equations that must be solved.

Eq. (57) resembles a differential equation that is solvable using the method of variation of parameters. Applying that technique to a rearranged Eq. (57),

$$\frac{\partial}{\partial z}\frac{\partial E_x}{\partial z} + E_x[\mu(\frac{2\omega}{c})^2\varepsilon_{11} - \frac{4k^2\varepsilon_{11}}{\varepsilon_{33}}] = -i\frac{2k}{\varepsilon_{33}}4\pi\chi_{322}\frac{\partial}{\partial z}(E_y^{(1)})^2\exp(-2ikx) \tag{60}$$

Setting

$$\alpha^2 = \mu\varepsilon_{11}(\frac{2\omega}{c})^2 - \frac{4k^2\varepsilon_{11}}{\varepsilon_{33}} \tag{61}$$

we see that the general solution to Eq. (57) is

$$E_x = A_1\exp(i\alpha z) + A_2\exp(-i\alpha z) \tag{62}$$

where A_1 and A_2 are constants to be determined by fitting the particular boundary conditions.

The particular solution of Eq. (57) due to the nonhomogeneity is

$$(E_x)_{particular} = C_1(z)\exp(i\alpha z) + C_2(z)\exp(-i\alpha z) \tag{63}$$

where the Wronskian is

$$W = -i\alpha - i\alpha = -2i\alpha \tag{64}$$

and so

$$C_1(z) = \int_0^z \frac{i2k}{2i\varepsilon_{33}}4\pi\chi_{322}(E_y^{(1)})^2\exp(-2ikx)\exp(-i\alpha z)dz \tag{65}$$

$$\text{and } C_2(z) = \int_0^z \frac{i2k}{2i\varepsilon_{33}}4\pi\chi_{322}(E_y^{(1)})^2\exp(-2ikx)\exp(i\alpha z)dz \tag{66}$$

so E_x in terms of $E_y^{(1)}$ is

$$E_x = A_1\exp(i\alpha z) + A_2\exp(-i\alpha z) + \exp(i\alpha z)\frac{4\pi k\chi_{322}}{\varepsilon_{33}}\exp(-2ikx)\int_0^z (E_y^{(1)})^2\exp(-i\alpha z)dz$$
$$+ \exp(-i\alpha z)\frac{4\pi k\chi_{322}}{\varepsilon_{33}}\exp(-2ikx)\int_0^z (E_y^{(1)})^2\exp(i\alpha z)dz \tag{67}$$

Progress was still being made toward solving Eq. (59) for E_z in terms of $E_y^{(1)}$ when the research period came to an end.

V. RECOMMENDATIONS

The program Expnum, which generated the numerically explicit results, is presented in Appendix II. The program is written in FORTRAN 77 and is documented to provide guidance for its use and modification. All runs were done on a Microvax III. It should be noted that, in its present form, the program takes approximately 140 hours to run due to the small size of the time and space steps and the range of positions under analysis.

Error analysis showed that the numerical solution had an acceptable inherent error (less than 5.6 percent) over the region 10^{-6}m -- 10^{-4}m. Analysis also showed that when the analytical solution was compared to the numerical there was an error of less than 7.4 percent over the same region. In both cases the maximum error in the region 10^{-4}m -- 10^{-3}m was greater than 10 percent, which suggests that the analytical approximation yields reasonably good results for a penetration depth of less than 10^{-4}m.

The work involving the generation of second harmonics was only a beginning, and much remains to be done. More involved cases could be examined which would more closely describe real-world situations.

REFERENCES

[1]D. Moroi, P. Hemenger, "Model Calculations for Pulsed Laser Annealing," unpublished.

[2]W. Press, B. Flannery, S. Teukolsky, W. Vetterling, Numerical Recipes: The Art of Scientific Computing, Cambridge University Press, 1986.

[3]M. L. James, G. M. Smith, J. C. Wolford, Applied Numerical Methods for Digital Computation with FORTRAN, International Textbook Co., 1986.

[4]D. U. von Rosenberg, Methods for the Numerical Solution of Partial Differential Equations, American Elsevier Publishing Co., 1969.

[5]Curtis Gerald, Applied Numerical Analysis, 2nd ed., Addison-Wesley Publishing Co., 1978.

[6]Louis Kelly, Handbook of Numerical Methods and Applications, Addison-Wesley Publishing Co., 1967.

[7]D. J. Griffiths, Introduction to Electrodynamics, 2nd ed., Prentice-Hall, 1989.

[8]Y. R. Shen, The Principles of Nonlinear Optics, John Wiley & Sons, 1984.

Figures and Appendix

may be obtained

from the Author or

UES

1990 USAF-UES SUMMER FACULTY RESEARCH PROGRAM/GRADUATE STUDENT RESEARCH PROGRAM

Sponsored by the

AIR FORCE OFFICE OF SCIENTIFIC RESEARCH

Conducted by the Universal Energy Systems, Inc.

FINAL REPORT

Eddy Current Testing in Nondestructive Evaluation

Prepared by:	Thomas J. Haas, B.S.E.E., B.S. Physics
	P.K. Kadaba, PhD.
Academic Rank:	Graduate Student (M.S.E.E.)
	Professor, University of Kentucky
Department and	Electrical Engineering
University:	University of Kentucky
Research Location:	WRDC/MLLP
	WPAFB
	Dayton, OH 45433
USAF Researcher:	P.K. Bhagat
Date:	31 Aug 90
Contract No:	F49620-88-C-0053

Same Report as
Prof. Prasad Kadaba
(Report # 113)

1990 USAF-UES SUMMER FACULTY RESEARCH PROGRAM/

GRADUATE STUDENT RESEARCH PROGRAM

Sponsored by the

AIR FORCE OFFICE OF SCIENTIFIC RESEARCH

Conducted by the

Universal Energy systems, Inc.

FINAL REPORT

MICROCRACK INITIATION AND GROWTH DURING FATIGUE CYCLING BY SURFACE ACOUSTIC WAVE SCATTERING

Prepared by:	Margo McDowell
Academic Rank:	Graduate Student
Department and	Civil Engineering
University:	University of Nebraska
Research Location:	WRDC/MLLN Building 655, Rm. 23 Wright Patterson AFB, OH 45433
USAF Researcher	Theodore Nicholas, Ph.D.
Date:	30 September 1990
Contract No.:	F49620-88-C-0053

Microcrack Initiation and Growth During Fatigue Cycling by Surface Acoustic Wave Scattering

by

Margo R. McDowell

ABSTRACT

A surface acoustic wave non-destructive evaluation method was used to detect the nucleation of surface microcracks in highly stressed regions of hourglass-shaped 6061 and 2024 aluminum alloy specimens during fatigue cycling. The experiment progressed in blocks of 2K cycles after which measurements were taken aided by two contacting wedge transducers. The incoming signal was converted into a surface wave which traveled away from the transducer, reflected off the microcrack, was received by the second transducer, and then amplified to become the crack reflection signal monitored on an oscilloscope.

ACKNOWLEDGEMENTS

I wish to thank primarily the Air Force Systems Command and the Air Force Office of Scientific Research for giving me the opportunity to do research in their facility. I would also like to express my appreciation to Universal Energy System for their concern and help in all administrative and directional aspects of this program.

My experience was rewarding and enlightening because of many different influences. A special acknowledgement is due to Dr. Ted Nicholas for providing me with support, encouragement and a truly friendly working atmosphere. I would also like to extend my gratitude to Rick Klysmith for a great deal of assistance in operating the equipment and for providing me with access to an electropolisher.

I. INTRODUCTION:

Early detection of crack nucleation and growth has many applications in the design, maintenance and manufacture of high performance structures. Specifically, advanced metallic alloys, such as titanium aluminide, are susceptible to premature failure due to the presence of microscopic surface cracks produced by conventional fabrication techniques.

The Nondestructive Evaluation Branch of the Wright Research and Development Center is particularly concerned with the creation of practical techniques to measure damage in materials important to the mission of the Air Force both under laboratory conditions and on structures operating in the field.

As a research assistant, directed under Dr. Resch, my interests have been focused on gaining knowledge of the surface acoustic wave scattering theory. And to become familiar with the techniques used to investigate the growth behavior of surface microcracks. Preceding this period, little opportunity has been available to me for researching the SAW method of nondestructive evaluation, in that my experience has been in the area of stress analysis. However, through my efforts at Wright Patterson Research and Development Center, I plan to further my assistance and study concerning the SAW method for nondestructive evaluation of the nucleation and growth of small surface cracks.

II. OBJECTIVES

Currently, optical scanning is the only reliable method for nondestructive evaluation of the nucleation of surface microcracks, in hourglass-shaped specimens, available for fatigue crack initiation studies in the High Temperature Metals and Ceramics Branch of the Wright Research and Development Center. This process, however, is extremely time consuming and exhibits uncertainties concerning the exact amount of tensile stress needed to cause adjacent crack faces to become traction free.

My assignment as a participant in the 1990 Summer Graduate Student Research program was to assist Dr. Michael Resch in the utilization of the SAW scattering technique for the in-situ measurement of crack opening behavior during cycling. The proposed investigation was to include but not be limited to the following:

1. Acquiring the skills involved in preparation of aluminum alloy specimens.

2. The creation of an algorithm to be used on a HP28S calculator which computes the amplitude of the reflection wave as well as back calculates to determine crack depth.

3. To operate efficiently the controlled testing equipment available, namely Mate 223 systems and then to integrate the machine control with the computerized controlled ultrasonic measure.

4. To perform fatigue cycling test and to acquire the ability to recognize cracks in their initial stages.

III. METALLOGRAPHY

The aluminum alloy specimens upon which the experiments centered were T-2024 and T-6061. These specimens were cut in an hourglass-shape so as to control the location of crack initiation. A mirror-like finish was then given to their surface along the high stress region of the neck. Thus making the detection of microcracks and photographs using a metallographic microscope possible, as well as reducing noise picked up by the transducers. To achieve such a surface, grit paper was administered followed by either diamond polish, using 30 micron through 1 micron, or use of an electropolisher.

IV. SAW SCATTERING THEORY

Using an empirical approach to the ultrasonic surface acoustic wave theory for evaluating crack size and growth during fatigue cycling provides valuable insight into fatigue behavior for the special conditions incorporated into the experiment performed. However, such calculations are complex and result in a rigorous time-consuming task. Thus, to eliminate the possibility of

miscalculations and to save time, I created an algorithm to be administered on an HP28S hand calculator. By inputting the material characteristic parameters of Young's Modulus, Possions Ratio and density, and also inputting the ultrasonic acoustic wave frequency, the program formulates the required amplitude of the reflection wave or back calculates to determine crack depth.

The fundamental equation upon which the algorithm revolves is a polynomial of the form:

$$V_2 = \rho [A_0 a^3 + 2 A_1 B a^4 + A_2 B^2 a^5 \qquad (1)$$

(A Graphical interpretation of eq 1 is illustrated via Fig. A)

The constants A_0, A_1 and A_2 have been evaluated numerically as described in Ref. 1 and Ref. 2. Using the results of Ref. 3, for a material with a Possion Ratio V = 1/3, A_0 = 1.8137, A_1 = .83842 and A_2 = .4435,

B is determined through equation (2) for which $k = 2\pi/(V_r/f)$

$$B/k = \frac{[2(V_s/V_r)^2 - 1][1-(V_r/V_s)^2]^{.5} - \left[1 + \frac{[2(V_s/V_r)^2 - 1]}{2[1-(V_s/V_L)^2]}\right][1-(V_r/V_L)^2]^{.5}}{2[1-(V_s/V_L)^2]} \qquad (2)$$

where V_s, V_r and V_l are respectively the shear, Rayleigh, and longitudinal wave velocities in the material.

To determine the ζ factor equation (3) can be used; however, a more efficient method is to back calculate using known values of reflection wave amplitude V2, crack depth a and B.

$$\zeta^2 = \frac{1-(V_r/V_s)^2(V_s/V_L)^2}{1-(V_r/V_s)^2} \qquad (3)$$

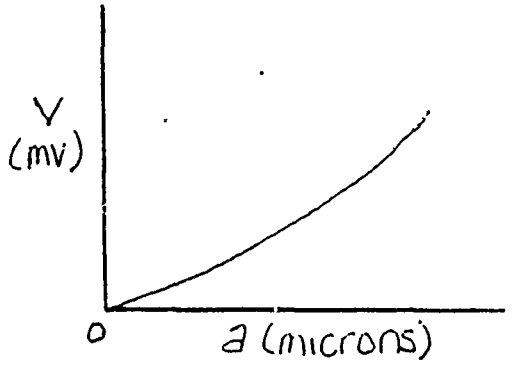

Fig. A

General illustration of reflection wave amplitude (V) vs. crack depth (a)

V. COMPUTER CONTROLLED TESTING/CRACK INITIATION AND DETECTION

Microscopic cracks were produced at the surface of metallographically prepared specimens of 6061 and 2024 aluminum alloy through fatigue cycling. The tests were performed on a servohydraulic MTS machine operating in displacement control.

To initiate a microcrack on the specimen's surface, cycles were administered with the aid of the Mate 223 system in blocks of 2K cycles. At the completion of a block, a maxium axial loading was implemented and at which time an ultra-sonic measurement was taken using the surface acoustic wave method of nondestructive evaluation. The test proceeded with the removal of the load and a cycling block increase.

The surface acoustic wave measurement system was the fundamental component in microscopic crack detection. A schematic diagram of its major components is shown in Figure B. The incoming signal produces a longitudinal wave which is converted to a surface wave on the specimens' surface. The wave packet then travels away from the transducer in a narrow beam. The beam reflects from the microcrack, is received by the second transducer, and is then amplified the crack reflection signal monitored on the oscilloscope.

Unfortunately, the presence of backscattered signals (noise) from microstructural features such as grain boundaries and inclusions partially obscure the acoustic reflection from the crack, denoting the beginning of the opening of adjacent crack faces. However, as cycling proceeds and crack growth occurs, the reflection amplitude from the microcrack emerges. Figure C is an example of a typical oscilloscope reading in which the microscopic crack is depicted by the wave with the largest amplitude.

Once a microcrack was believed to exist, cycling was ceased and a check performed. This was administered by slowly loading the specimen and observing, in real time, any amplitude gains that occur at the supposed crack location. If the wave amplitude does increase, the specimen is removed and the crack examined and measured under a metallographic microscope, else cycling is continued.

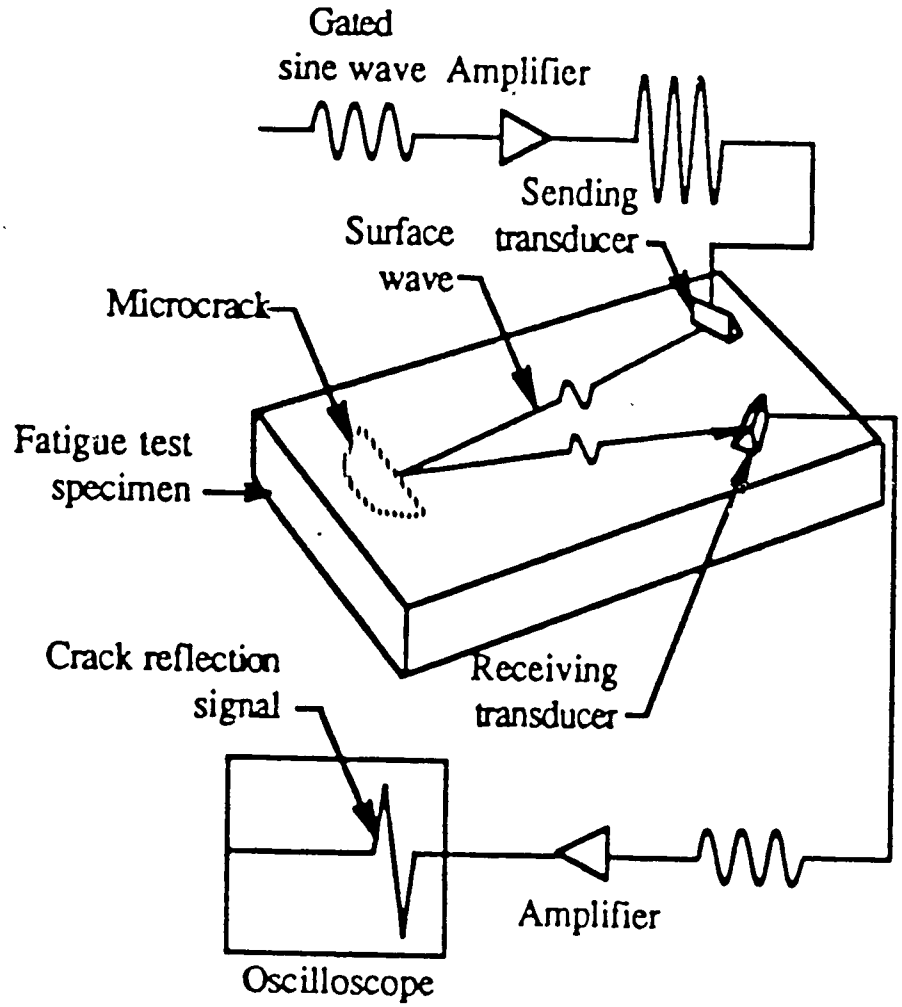
Gated
sine wave
Amplifier
Sending
transducer
Surface
wave
Microcrack
Fatigue test
specimen
Crack reflection
signal
Receiving
transducer
Amplifier
Oscilloscope

(Fig. B)

(Fig. B)

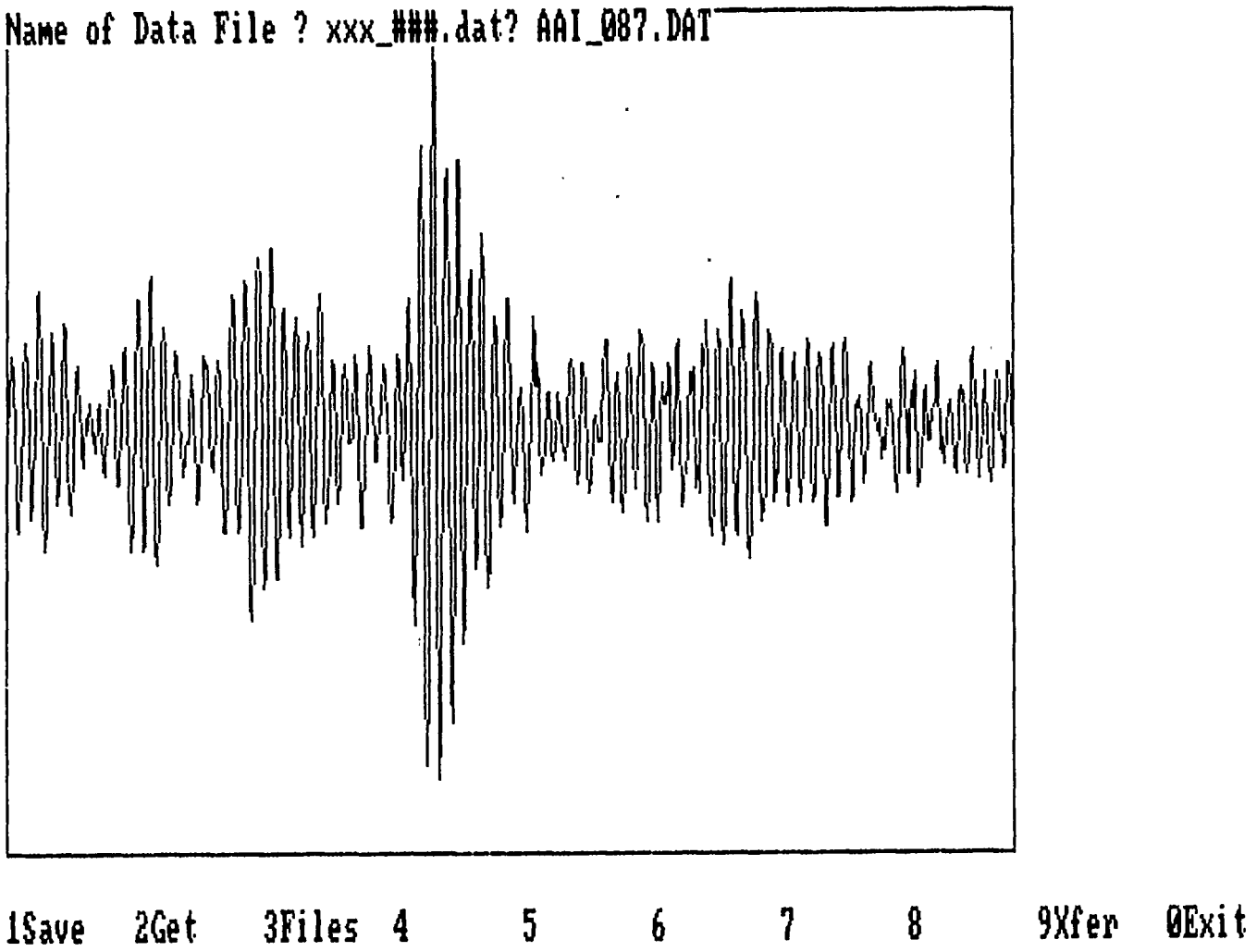
Name of Data File ? xxx_###.dat? AAI_087.DAT
1Save 2Get 3Files 4 5 6 7 8 9Xfer 0Exit

(Fig. C)

(FIG. C)

VI. RECOMMENDATIONS

The efficiency of the SAW scattering technique to provide useful information concerning the size and opening behavior of surface microcracks in metals during fatigue is well documented. However, its usefulness as a viable tool in fatigue research is currently limited by:

1. The inavailability of wedge transducers small enough to transmit and receive surface acoustic waves on extremely small hourglass-shaped specimens.
2. The reduction of noise on specimens other than aluminum.

The first of these limitations is easily rectified. The second, however, demands more consideration. Uncertainties lie in developments to the signal processing algorithm in that when grain boundaries and other inclusions produce greater noise, crack initiation and growth are still detectable.

REFERENCES

Resch, M.T., Nelson, D.V., Yuce, H.H., and Ramusat, G.F., "A Surface Acoustic Wave Technique for Monitoring the Growth Behavior of Small Surface Fatigue Cracks," Journal of Nondestructive Evaluation, Vol. 5, No. 1, 1985, pp. 1-7.

Resch, M.T., Nelson, D.V., Yuce, H.H., and London, B.D., "Use of Nondestructive Evaluation Techniques in Studies of Small Fatigue Cracks," Basic Questions in Fatigue, Vol. I, ASTM STP 924, J.T. Fong and R.J. Fields, eds., American Society for Testing and Materials, Philadelphia, 1988, pp. 323-336.

Kapur, P., Shanker, P.M., Rose, J.L., and Newhouse, U.L., "Split Spectrum Processing: Optimizing the Processing Parameters Using Minimization," Ultrasonics, Butterworth Scientific, Vol. 25, July 1987, pp. 204-208.

Resch, M.T., Khuri-Yukub, B.T., Kino, G.S., and Shyne, J.C. "The Acoustic Measurement of Stress Intensity Factors," Appl. Phys. Lett. Vol. 34, No. 3, American Institute of Physics, 1979, pp. 181-184.

1990 USAF-UES SUMMER FACULTY RESEARCH PROGRAM/GRADUATE STUDENT RESEARCH PROGRAM

Sponsored by the

AIR FORCE OFFICE OF SCIENTIFIC RESEARCH

Conducted by the

Universal Energy Systems, Inc.

FINAL REPORT

The Effect of Evaporated Aluminum Overlayers on the Compressive Strength of High-Performance Polymer Fiber Poly-(p-phenylene benzobisthiazole)

Prepared by:	Keith E. Newman
Academic Rank:	Doctoral Candidate
Department and University:	Materials Science and Engineering - Metals Science and Engineering Program, The Pennsylvania State University
Research Location:	WRDC/MLBP Wright-Patterson AFB, OH 45433-6533
USAF Researcher:	Charles Y-C. Lee, Ph.D.
Date:	27 Aug 1990
Contract No:	F49620-88-C-0053

The Effect of Evaporated Aluminum Overlayers on the Compressive Strength of High-Performance Polymer Fibers Poly-(p-phenylene benzobisthiazole)

by

Keith E. Newman

ABSTRACT

The compressive strength of the high-performance polymeric fiber, poly-(p-phenylene benzobisthiazole) or PBZT has been evaluated using the recoil test method. In addition preliminary tensile and compressive results are reported for as-spunPBO fiber spun at the Polymer Branch, WRDC. Fiber tensile and compressive strengths were 410 ksi and 30-40 ksi respectively (PBZT), and 550 ksi and 45-60 ksi respectively(PBO). PBZT was coated with high-purity, zero-valent aluminum of varying thicknesses, ranging from 30 to 2500Å. Results indicate no improvement in compressive strength is obtained from having aluminum overlayers present during testing. However, this result is complicated by the inability to observe the location of failure, i.e. kink bands, until gross fiber kinking has occurred. This is due to the aluminum overlayer rendering the fiber opaque to the transmitted light used to detect kink bands. High-resolution field emission microscopy of the fiber-metal interface indicates no penetration of metal into the fiber interior and poor interfacial bonding.

I. INTRODUCTION:

There is no accepted model for the development of compressive failure in rigid-rod heterocyclic aromatic, or any other, polymer fibers. Several proposed models for the initiation of buckling modes of failure in fibers have been discussed(1). In general, they may be broadly categorized as either macroscopic fiber buckling or microscopic fibrillar buckling. If the cause of compressive failure is by regions of localized fiber buckling, called kink band formation, originating at the fiber surface and proceeding into the fiber interior, then the application of a shell of material around the fiber should improve fiber compressive strength(2). If the cause of failure is fibrillar buckling at the location of least support from neighboring fibrils, then a surface coating most likely would not contribute to improving fiber compressive strength since the primary unit responsible for failure is not influenced by the applied shell of material.

The Polymer Branch of the Non-Metallic Materials Division at Wright Research and Development Center, Wright-Patterson Air Force Base is particularly concerned with this problem since poly-(p-phenylene benzobisthiazole) PBZT, poly-(p-phenylene benzobisoxazole) PBO, and their variants were developed in this lab and show excellent promise as a reinforcing material in composite systems. At present their potential application is limited by their poor compressive strength. Therefore, any means to improve fiber compressive strength would be a significant step towards commercial application of these polymers.

My research interests are in the incorporation of PBZT into an aluminum alloy matrix using liquid metal infiltration methods. My work on the effect of molten metal contact on PBZT fiber tensile properties as a function of metal temperature and time of immersion contributed to my assignment to the Polymer Branch of the Non-Metallic Materials Division at WRDC.

II. OBJECTIVES OF THE RESEARCH EFFORT:

The application of high-strength polymeric fibers as reinforcement in epoxy or other matrices is limited by the tensile and compressive strength of the fiber. It has been known for years that Kevlar™ possesses high tensile strength but poor compressive strength. This same behavior holds true for all high performance polymeric fibers currently being developed for use in composite systems. In particular, fibers of the heterocyclic aromatic polymer system, PBX(X=O, S, NH), possess tensile properties which meet or exceed most graphite fibers(3) yet possess compressive properties only ten percent of their tensile properties. Currently, efforts are aimed at improving the compressive strength of these polymers using a variety of techniques(4).

My assignment as a participant in the 1990 Summer Graduate Student Research Program was to determine if the application of a coating of aluminum metal to the surface of PBZT and PBO would improve fiber compressive strength through either, infiltration of metal into the fiber interior thus binding the fibrils together, or the coating acting as a rigid outer support to prevent fiber buckling at the outer surface.

III. EXPERIMENTAL TECHNIQUES

Materials

The 200 filament PBZT fiber tow used in all experiments was spun at the DuPont Experimental Station under contract from the Polymer Branch-WRDC. The tow was spun by the dry-jet wet spun process, dried, and heat treated at approximately 575°C for 10 seconds under a nitrogen shield gas. Nominal fiber diameter was determined from measurement of 50 filaments as 15.9±0.9μm. An optical micrograph of a representative PBZT fiber is shown in Figure 1a.

The PBO fiber used was spun from dope supplied by Dow Chemical in the processing laboratory of the Polymer Branch-WRDC. This fiber was tested in the as-spun condition as fabricated . An optical micrograph of a representative fiber is shown in Figure 1b; these fibers have a nominal diameter of 58.1±1.5μm.

Recoil Test

A variety of test techniques are currently available to determine fiber compressive strength, with no agreement on which one is the best. In general though, the recoil test(5) is becoming accepted as the best technique available. A schematic of the recoil test apparatus used at the Polymer Branch is found in Figure 2. The test is based on the principal that the application of a controlled tensile pre-load to the fiber, followed by rapid breakage of the fiber(induced by cutting), results in a tensile stress wave travelling from the break, up the fiber length, until the wave reaches the rigid fiber end. At this point the tensile wave changes to an equal but opposite magnitude compressive wave. If the compressive stress generated is higher than the compressive strength of the fiber, the fiber fails. In high performance polymeric fibers, the fiber failure is manifested by kink band formation. These kink bands are observed optically using transmitted light as dark bands, Figure 3a, or gross

translation of the fiber, Figure 3b. This process is repeated using new specimens until a lower tensile stress is found below which no kink bands are observed after specimen failure.

Evaporative Metal Coating of PBZT

Samples of fiber were coated with high-purity aluminum(99.999%) by vacuum evaporation at ambient temperature. Prior to coating, fiber samples were mounted onto the "rotisserie" used to rotate the fibers during deposition, thus maintaining a uniform layer of metal onto the fiber. A schematic of the fiber rotisserie unit used can be seen in Figure 4. Coating occurred in a large bell jar maintained at 10^{-7} - 10^{-8} torr. The pure aluminum wire was held in a tungsten filament basket which was resistively heated until the aluminum vaporized at which time a shutter was opened and the aluminum vapor entered the chamber. Coating thickness was monitored by an oscillating quartz-crystal.

Mechanical Testing

After coating, the fibers were removed from the rotisserie and mounted on paper tabs of 1" gauge section using 5-Minute Epoxy©. Once the epoxy cured, but prior to testing, the fiber diameter was measured in three places and averaged, using a filar eyepiece on an optical microscope. All reported tensile and compression values are the result of a minimum of twenty tests. Tensile and compression testing was performed on a benchtop Instron tensile machine. For tensile testing of PBZT and PBO fibers a 500 gram capacity load cell was used. A 50 gram capacity load cell was used for compression testing of PBZT fibers and a 500 gram capacity load cell used for compression testing PBO fiber. Pneumatic air grips were used to prevent sample slippage during testing.

Scanning Electron Microscopy

In order to examine the metal-polymer interface, metal-coated fibers were peeled in half down their length and a Hitachi S-900 high-resolution field-emission scanning electron microscope operated at 2.3 kV accelerating voltage was used to observe the interface.

IV. RESULTS

Mechanical Properties

Results from tensile testing PBZT fiber at The Pennsylvania State University are summarized in Table 1, along with results of compression tests on PBZT and tensile and compression tests of PBO fiber obtained during this investigation at the Polymer Branch-WRDC. Fiber tensile properties for both PBZT and PBO are within the limits of previously reported values.

As can be seen in Figure 5, the compressive strength of PBZT fiber does not increase as the coating thickness approaches 2500Å. The usual method to detect compressive failure in polymer fibers is to observe the fiber optically for kink bands. It was not possible to see through the fibers possessing 1035 and 2500Å thick aluminum coatings and detect the same level of kink bands as could be resolved on the transparent fibers, i.e. the as-received or 30Å Al-coated fibers, therefore the compressive strengths reported for these cases must be considered as upper limits. This result has significant implications to any future work on measuring the compressive strength of coated fibers. Others have not accounted for this in their published results(6). Therefore, to establish if the fiber is indeed kinked in coated fiber systems may require other techniques aside from optical inspection, as is currently the practice.

The as-spun PBO fiber exhibited a compressive strength of 45-60 ksi which is within the limits found using other samples of PBO fiber fabricated both at the Polymer Branch and elsewhere.

Field emission microscopy shows the metal-polymer interface to be poor as evidenced by the large amount of cracking in the coating and the appearance that the coating simply lays on the fiber surface, Figure 6. Adhesion measurements made of aluminum coated PBZT films indicates no appreciable adhesion exists between the metal and polymer as observed by the entire aluminum coating coming off when peeled with scotch tape(7). Additionally, Figure 7 shows the aluminum coating to be a microcrystalline aggregate of average crystallite size 144±0.3nm. The rough surface could act as a stress concentrator, either in tension or compression. Therefore it would be desirous to have a microscopically smooth, uniform coating to eliminate this possible influence.

V. RECOMMENDATIONS:

The coating of rigid-rod polymer fibers with aluminum overlayers of thickness up to 2500Å has no significant influence on fiber compressive strength. Extreme care must be exercised during the coating process in order that damage may not be produced in the fiber prior to testing and which would subsequently influence the final properties.

Further research on the use of coatings to improve fiber compressive strength, or any other work which affects the optical detection of fiber defects(which is the current means to measure fiber integrity), requires alternative detection methods be devised. This would be an area for further research effort.

Another result from this study is the fact that it is not possible to incorporate another material inside these polymer fibers once the fiber is in the dried and heat treated condition. In order to incorporate a coupling agent between the fibrils, which may be one of the best means to improve fiber compressive strength(8), the material must be infiltrated while the fiber structure is still open and permeable; this is the case while the fiber is wet, immediately after spinning the fiber. A process of slowly replacing the water between the fibrils with a liquid having the required coupling agent, followed by a process that reduces the material to its final form, called sol-gel, has been performed previously. No systematic study of various candidate materials that could act as a coupling agent between the fibrils has been carried out. This could be an area of very fruitful research.

ACKNOWLEDGEMENTS

I wish to thank the Air Force Systems Command, Air Force Office of Scientific Research and WRDC/MLBP for their support during the course of this investigation. I appreciate the warmth and hospitality afforded me by the members of the Polymer Branch-WRDC during my stay. Special thanks go to Mr. Unnikrishnan Santhosh for his help in introducing me to compression testing, performing the recoil tests, and his friendship, Mr. Gary Price for his assistance in performing the field-emission microscopy, and Mr. Morley Stone for his optical micrographs of the PBZT and PBO fiber. Finally, thanks to Charles Y-C. Lee for his effort in bringing me to the facility and our discussions regarding the nature and results of this investigation.

REFERENCES

1. Lee, C. Y-C., and Santhosh, U., WRDC-TR-90-4023 1990.
2. Moalli, J., and McGarry F.J., Specialty Polymers '90, Johns Hopkins University, Baltimore, MD, August 7-12, 1990.
3. Adams, W.W., and Eby, R.K., MRS Bulletin 1989.
4. Lee, C. Y-C., Private communication.
5. Allen, S.R., J. Mater. Sci., **22**,(1987), p.853.
6. Moalli, J., and McGarry F.J., Specialty Polymers '90, Johns Hopkins University, Baltimore, MD, August 7-12, 1990.
7. Newman, K.E., unpublished research.
8. Lee, C. Y-C., and Santhosh, U., WRDC-TR-90-4023 1990.

Table I
Mechanical Properties of PBZT and PBO Fiber

Fiber	Tensile Strength (ksi)	Elastic Modulus (Msi)	Strain-to-failure	Compressive Strength (ksi)
HT-PBZT	410	43.5	1.5	30-40
As-spun PBO	550	19.4	6	45-60

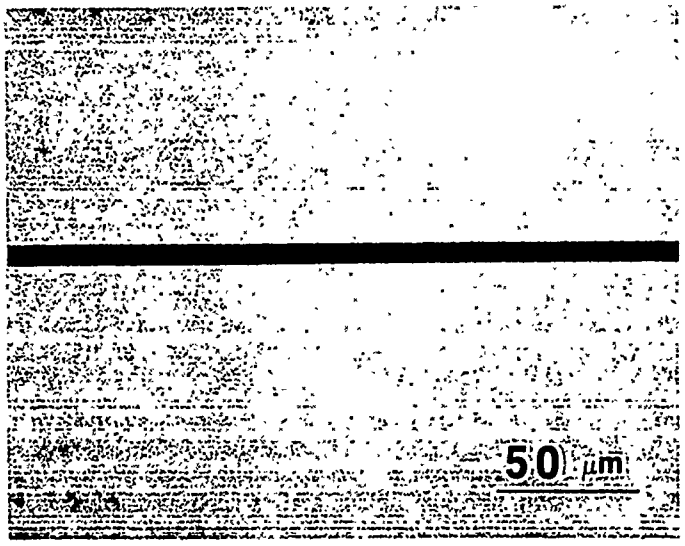

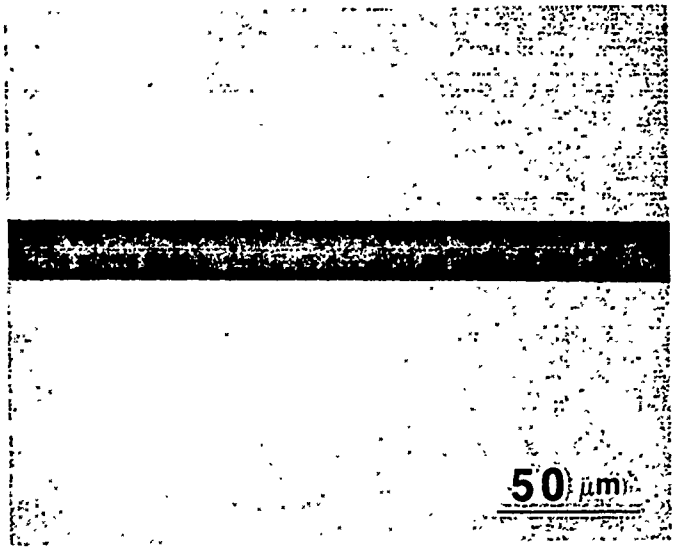

Figure 1 - Optical micrographs using transmitted light of; a) heat treated PBZT, b) as-spun PBO fiber.

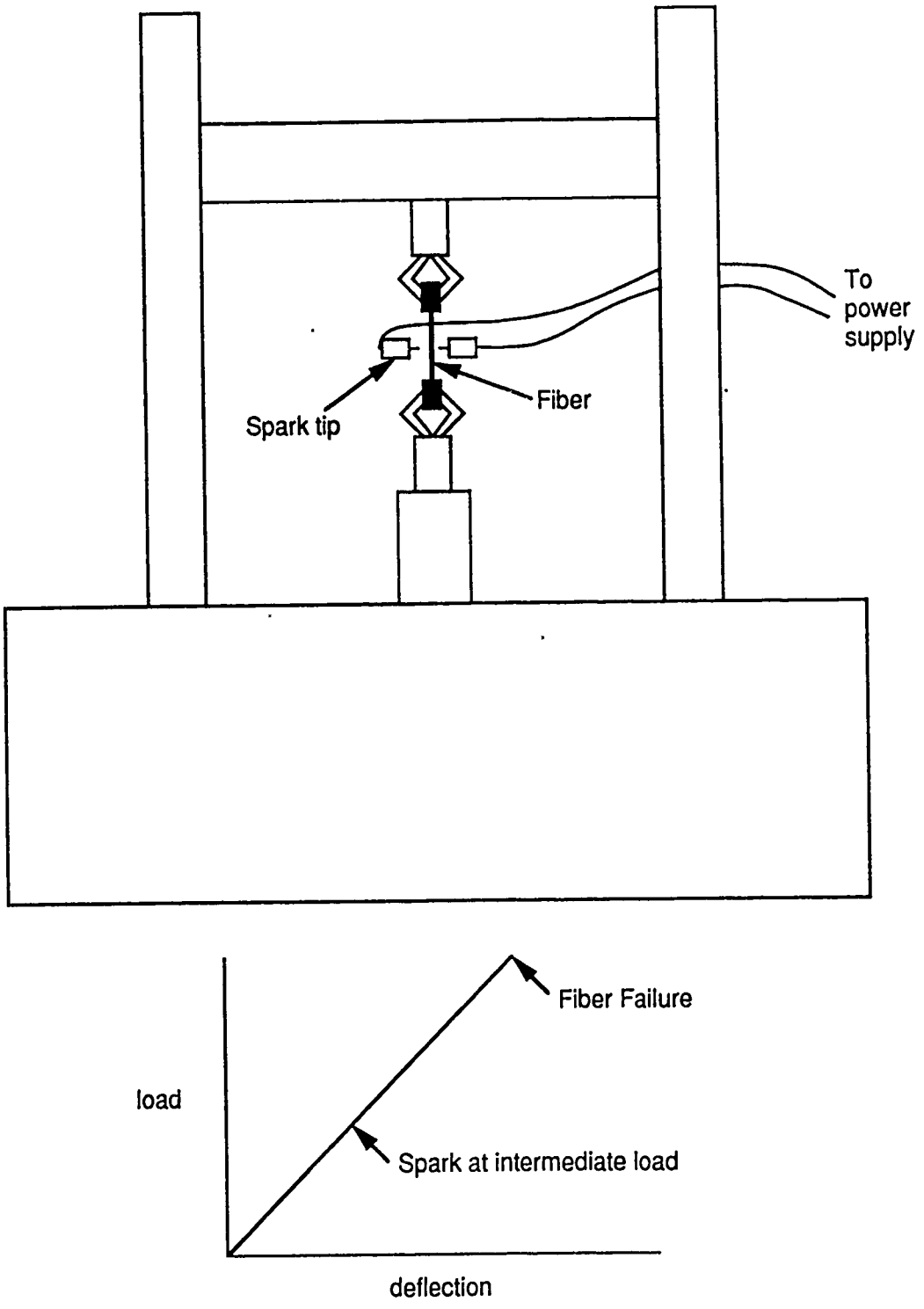

Figure 2 - Schematic of the recoil test apparatus used at WRDC/MLBP.

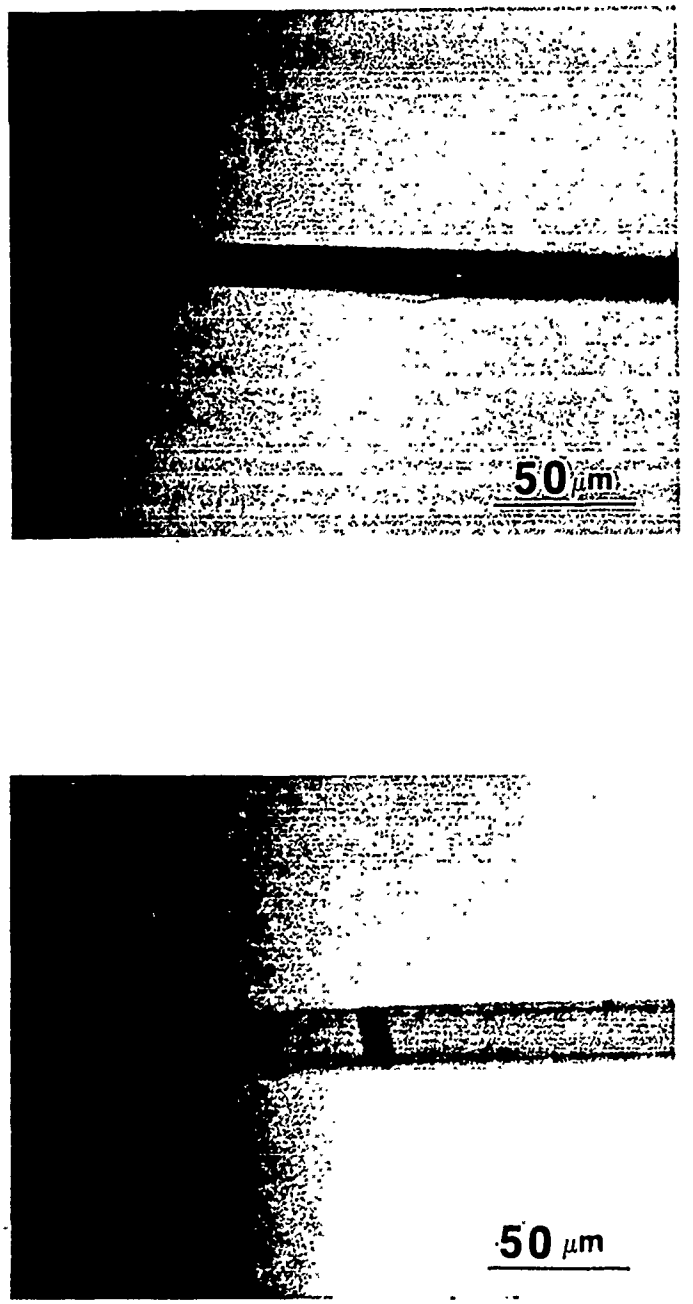

Figure 3 - Optical micrographs taken of as-spun PBO fiber showing a) kink band that would be considered sample failure, b) gross fiber translation caused by a large kink band.

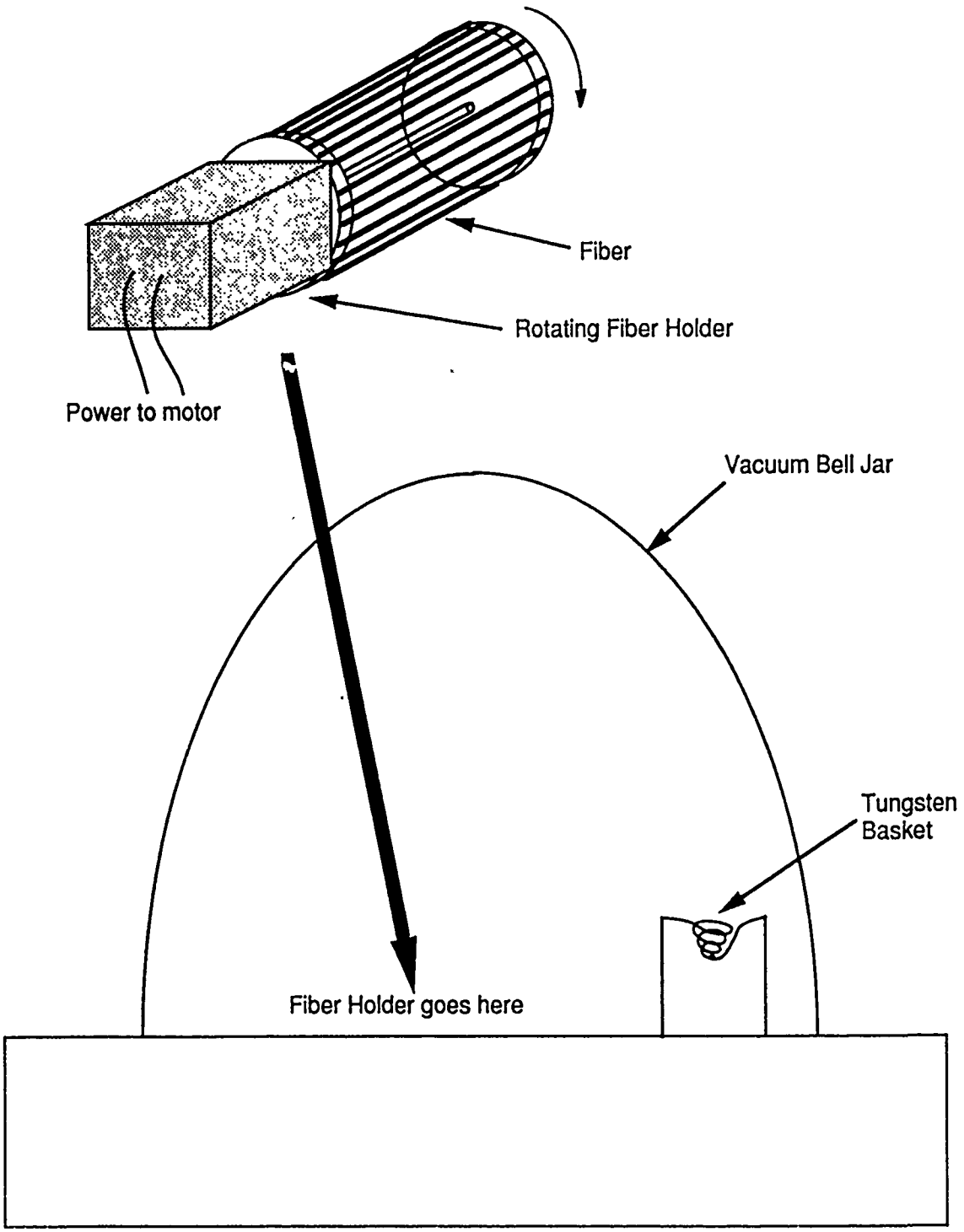

Figure 4 - Schematic of the apparatus used at Penn State to do vacuum evaporation of metals onto fiber.

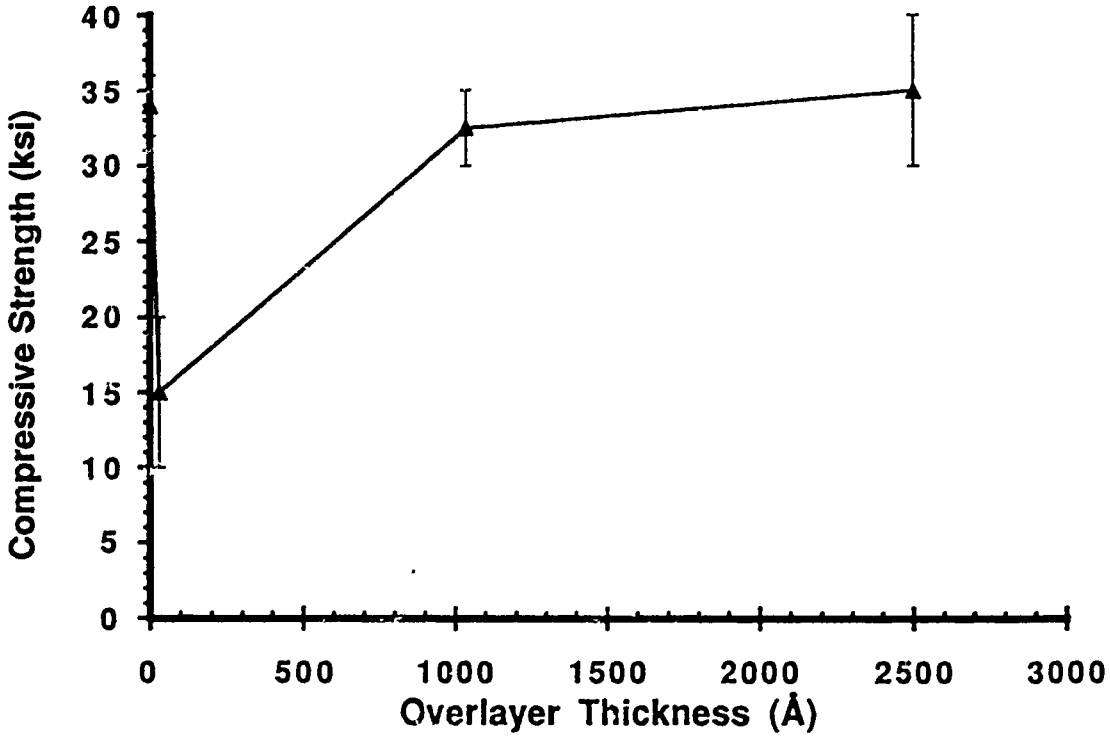

Figure 5 - Plot of PBZT fiber compressive strength as a function of aluminum overlayer thickness.

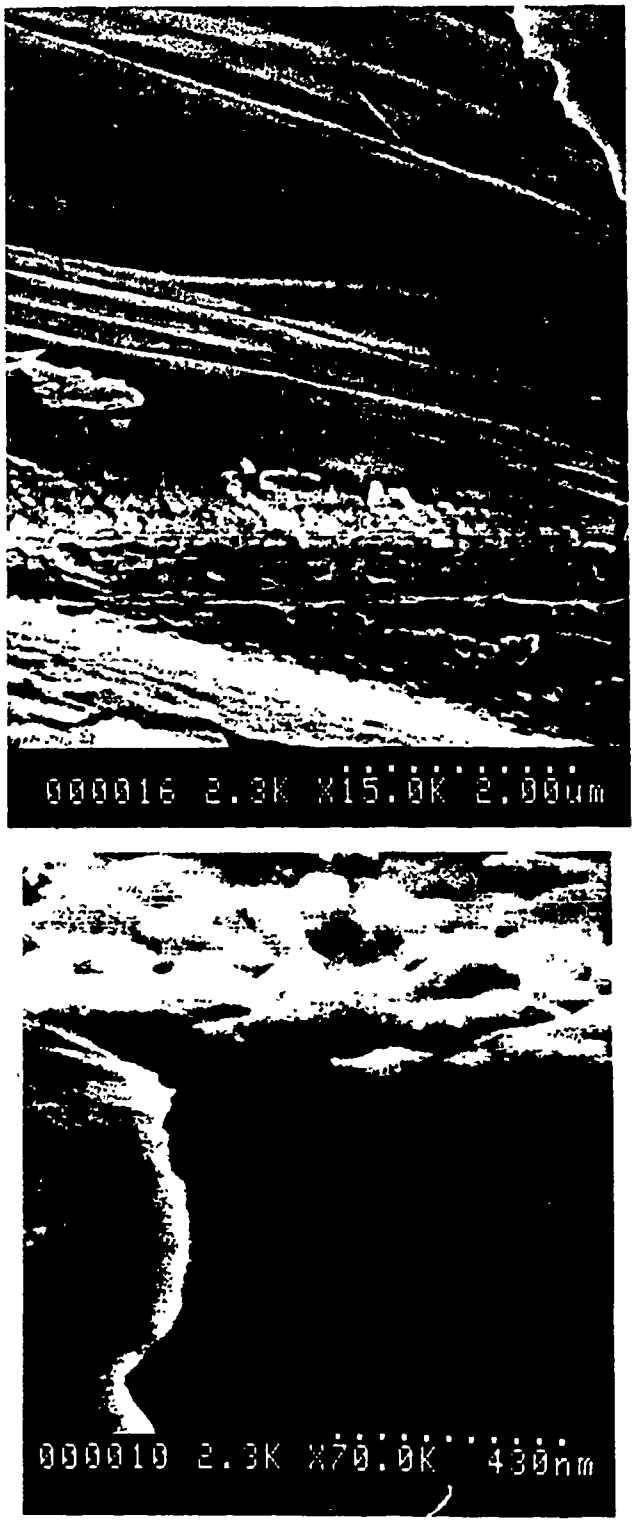

Figure 6 - High resolution scanning electron micrograph of an aluminum coated PBZT fiber that has been peeled along its length revealing the lack of metal infiltration into the sample interior, and the appearance of the coating simply resting on the fiber surface.

Figure 7 - High resolution scanning electron micrograph of the aluminum coating applied onto a fiber surface. The average microcrystallite size is 144 nm.

1990 USAF-UES SUMMER FACULTY RESEARCH PROGRAM/

GRADUATE STUDENT RESEARCH PROGRAM

Sponsored by the

AIR FORCE OFFICE OF SCIENTIFIC RESEARCH

Conducted by the

Universal Energy Systems, Inc.

FINAL REPORT

LOADING RATE EFFECTS ON DUCTILE-PHASE TOUGHENING IN IN-SITU NIOBIUM SILICIDE - NIOBIUM COMPOSITES

Prepared by:	JOSEPH D. RIGNEY
Academic Rank:	GRADUATE STUDENT
Department and University:	MATERIALS SCIENCE AND ENGINEERING, CASE WESTERN RESERVE UNIVERSITY
Research Location:	WRIGHT-PATTERSON AIR FORCE BASE WRDC/MLLM, DAYTON OH
USAF Researcher:	DENNIS M. DIMIDUK
Date:	30 NO 1990
Contract No.:	F49620-88-C-0053

LOADING RATE EFFECTS ON DUCTILE-PHASE TOUGHENING IN IN-SITU NIOBIUM SILICIDE-NIOBIUM COMPOSITES

by

Joseph D. Rigney

ABSTRACT

Brittle silicide intermetallics such as Nb_5Si_3 have been significantly toughened by Nb particles incorporated during in-situ processing techniques. Ten-fold increases in toughness as well as resistance-curve behavior have been realized at nominal testing rates with these ductile Nb particles. Under more rapid loading rates the efficiency of the body-centered cubic Nb particles in enhancing the toughness may be affected due to the strain-rate sensitivity of the Nb and/or the possible strain-rate sensitivity of interfacial debonding. Toughness tests conducted at loading rates ($\dot{K}_Q$ - rate of increase in stress intensity) of 0.035 to >200 MPa$\sqrt{m}$/sec have indicated a significant sensitivity to testing rate, with a drop in fracture toughness from 28 to 9 MPa$\sqrt{m}$ over this range accompanied by a change in fracture mode from primarily ductile to cleavage failure in the Nb.

ACKNOWLEDGEMENTS

This work was partially supported by a Graduate Research Assignment at Wright Research and Development Center (WRDC) through the Air Force Systems Command, Air Force Office of Scientific Research (AFOSR)/Graduate Student Research Program (GSRP) under contract F49620-85-C-0013. Universal Energy Systems, Inc. requires acknowledgement for all administrative aspects of this program. Additional support at Case Western Reserve University (CWRU) is provided by AFOSR 89-0508. I would like to thank Dr. Madan G. Mendiratta (UES), Dr. Dennis M. Dimiduk (WRDC/MLLM) and Dr. John J. Lewandowski (CWRU) for their guidance, encouragement and useful discussions throughout the duration of this project. The technical assistance in the sample preparation/characterization and mechanical testing laboratories while in residence at WPAFB is also gratefully appreciated.

This work was conducted during a June 4th through August 15th (1990) assignment at WPAFB/WRDC/MLLM.

I. INTRODUCTION:

Silicides and silicide-based composites provide a number of attractive features for potential high temperature service.[1-5] One system of recent interest is based on the binary Nb-Si system,[1-5] where the line compound Nb_5Si_3 has a melting point of 2757 K and is expected to possess high temperature strength, stiffness and creep resistance. However, a low value of fracture toughness (≈3 MPa$\sqrt{m}$) and inadequate ambient ductility[4] limit its application. A composite toughening approach, accomplished through processing in the Nb rich end of the Nb-Si binary phase diagram[6] (i.e., Nb-10 at.% Si), by vacuum arc casting followed by extrusion and heat treatment, has been designed to incorporate elongated primary and secondary ductile refractory niobium (≈0.8 at.% Si) solid solution particles within a Nb_5Si_3 matrix. The silicide and refractory metal are virtually immiscible up to 1943 K,[7] and differ in thermal expansion coefficient by ≈$1x10^{-6}$/K,[4] providing a degree of thermal (chemical) and mechanical compatibility in these in-situ formed composites to high temperatures.

The incorporation of Nb particles into the silicide matrix has increased the room temperature fracture initiation toughness of Nb_5Si_3[1-4] to values exceeding 20 MPa$\sqrt{m}$ and provided an increase in fracture toughness with crack extension or resistance(R)-curve behavior.[8] Other brittle matrix composite systems have realized toughening as a result of dispersed ductile phases such as Al_2O_3/Al,[9,10] SiC/Al,[11] TiAl/(Nb or NbTi)[12] in addition to model systems such as glass/Pb[13] and glass/(Al or Ni).[14] As described in several analyses,[13,15,16] ductile phase toughening is accomplished via ductile bridging of intact ligaments behind the crack tip along the fracture plane. The degree of toughening in these analyses depends primarily on the stress-strain behavior of each ductile ligament - yield stress and extent of plastic stretching before failure (or in other words, the area underneath the stress-strain curve) - with a constraint imposed by the surrounding elastic matrix. The degree of constraint or matrix-ductile phase debonding will affect the stress-strain behavior of the ligaments. The toughening is also proposed to be related to the area fraction and radius of the ligaments in the fracture plane and the length of the bridged zone; recent work[8] has begun to measure the extent of bridging and its effects on resultant R-curve behavior in this system.

Although it has been demonstrated that incorporation of ductile particles is effective in enhancing toughness under quasi-static conditions, it is not clear how changes in loading rate will affect such processes. It is possible that changes in loading rate may affect the

yield strength and ductility of the ductile phase as well as the degree of interface debonding, thereby affecting the magnitude of toughening. While conventional fracture toughness testing procedures[17] require that notch tip loading rates at failure lie in the range of 0.55 to 2.75 MPa$\sqrt{m}$/sec, actual loading rates in service may be appreciably higher or lower. It is well documented that loading rate significantly affects the ambient fracture behavior and subsequent fracture resistance of body-centered cubic (bcc) materials, especially under the constraint of a notch (i.e., ferritic steels).[18,19] For example, impact rates can promote cleavage and reduced fracture toughness in structural steels by raising the material's brittle-to-ductile transition temperature (BDTT). However, no such similar studies exist for refractory metals. The fracture resistance as measured by the critical stress intensity factor, K_{IC}, or R-curve behavior, of Nb_5Si_3/Nb ductile-phase toughened composite materials may also be affected by changes in loading rate via the resulting changes in deformation and fracture behavior of the Nb phase and interfacial regions in the composite. The present work was undertaken to investigate and quantify the effects of loading rate on ductile phase toughening in silicides toughened with Nb, although the rates of loading utilized were not in the range of impact rates.

II. OBJECTIVES OF THE RESEARCH EFFORT:

Composite materials have been fabricated based on the Nb_5Si_3 matrix incorporating niobium particles increasing the toughness by the mechanism of ductile-phase toughening. Previous fracture toughness tests conducted at conventional rates of testing have indicated that significant toughening and resistance-curve behavior can be obtained. In service applications, however, these materials can observe rates of loading in excess of those used in conventional tests. In this investigation, as stated above, fracture toughness tests were conducted over a range of testing rates to determine the influence of the rate on the measured fracture initiation toughness and the fracture behavior of the composite. Because the toughening is dictated by the stress-strain behavior of the niobium, any change in fracture behavior or extent of interfacial debonding with changes in loading rate will be noted and observations related to the change in toughness.

III. EXPERIMENTAL PROCEDURES:

The materials investigated were initially vacuum arc-cast with a composition of Nb-10 at.% Si (Westinghouse, Inc., Pittsburgh PA). Secondary processing such as hot extrusion (in Mo cans at 5.5:1 and 1923 K: Wright-Patterson Air Force Base, Dayton OH) and

vacuum heat treatment (1773 K for 100 h) was utilized to change the morphology and fracture behavior of the primary and secondary Nb contained within the Nb_5Si_3 matrix. Notched three point bend bars were then electro-discharge machined (EDM) from the extrusions such that the notch was perpendicular to the extrusion direction. The notch root radii were measured to be 170μm. Samples typically had height(W)-by-thickness(B) dimensions of 9 x 6 mm and crack depth-to-height ratios(a/W) between 0.2 and 0.4. Samples were tested with span(S)-to-height(W) ratios of ≈4/1 in accordance with standard testing procedures.[17] The sides of the samples were polished to a 1μm finish to later examine the extent and nature of damage accumulated during crack growth.

Mechanical tests were conducted over a range of crosshead displacement rates (0.00042 to 8.47 mm/sec) either on screw-driven Instron or servohydraulic MTS equipment. Strip chart recorders and storage oscilloscopes were used to record load versus time traces for the various tests that were conducted. The peak loads (P_Q) recorded were used in the following equation,[17] to determine the fracture toughness of the sample, where f(a/W) is a geometrical factor related to the initial crack depth ratio:

$$K_Q = \left(\frac{P_Q S}{B W^{3/2}}\right) \cdot f\left(\frac{a}{W}\right)$$

Time (t) to peak load was also recorded and used to calculate the average rate of increase in stress intensity factor, $\dot{K}_Q$ (MPa√m/sec), at the notch tip before failure:

$$\dot{K}_Q = \frac{K_Q}{t}$$

The fracture surfaces of the fastest and slowest tested samples were examined on a JEOL 840A scanning electron microscope (SEM) operated in the secondary electron mode. Figure 1 shows a schematic of the regions analyzed. Two adjacent 200X micrographs were taken in the plane strain region (i.e., center of the sample), while the change in fracture surface morphology was documented from the notch to the back face of the specimen. A Zeiss Videoplan Optical Comparitor equipped with a quantitative metallography program was used to determine the area fraction of cleaved primary niobium on each micrograph. Several SEM micrographs were also taken using back scattered electrons (BEI) and metallographic techniques were used to determine the area fraction of primary niobium.

IV. RESULTS AND DISCUSSION:

The typical extruded and heat treated microstructure of the Nb/Nb_5Si_3 composite is presented in Figure 2 along with a schematic showing the orientation of the notched three point bend specimens with respect to the elongated Nb particles. The large primary niobium particles occupy 51.3% by volume in the composite and long axes oriented perpendicular to crack propagation in the mechanical tests. The continuous dark phase in the microstructure is the Nb_5Si_3 matrix.

The results of the testing rate on the fracture initiation toughness (i.e., K_Q) are plotted in Figure 3a and 3b as a function of crosshead displacement rate (mm/sec) and rate of increase in stress intensity at the notch tip (MPa$\sqrt{m}$/sec), respectively. From these graphs, it is apparent that there is an effect of testing rate on the toughness. Increasing the rate from 0.035 to 135 MPa$\sqrt{m}$/sec produces a slight decrease in K_Q from ≈26 to 19 MPa$\sqrt{m}$, while rates >200 MPa$\sqrt{m}$/sec produced fracture toughness values of 9 MPa$\sqrt{m}$, a factor of 3 lower than those at the slowest rates tested.

The fracture surfaces of the two extreme toughness specimens (i.e., 28 and 9 MPa$\sqrt{m}$) representing slow (0.035 MPa$\sqrt{m}$/sec) and fast (200 MPa$\sqrt{m}$/sec) tests, respectively, were analyzed in the SEM. Figures 4a through 4d show the fracture appearance near the notch (a/W≈0.25) and near the specimen mid-section (a/W≈0.6) for these two extreme cases. In the slow test, extensive plastic stretching and debonding of primary Nb is observed near the notch (Figure 4a), while some cleavage is observed at approximately 2x the notch root radius (≈350μm) below the notch tip. Near the specimen mid-plane, the percentage of cleavage has increased significantly (Figure 4b). In comparison, at the faster testing rate, the percentage of cleavage near the notch (Figure 4c) is significantly higher and again increases in proportion with distance from the notch (Figure 4d). Figure 5 shows the percentage of primary Nb cleavage as a function of crack position (a/W) and loading rate and suggests that both loading rate and crack velocity affect the ductility of the primary Nb particles as discussed below. For the test conducted slowly, the percentage of cleavage varied from a low of 7% at the notch, increased to 42% near the specimen center, and returned to 7% at the end of the specimen. At the faster rate, the fraction of cleavage at the notch was 23% and increased to ≈60% over most of the specimen, but returned to the low value of 7% at the back face.

Experimental and theoretical work[20] have shown that loading cracked specimens under

fixed grips (stroke-controlled) conditions, the velocity of the crack will increase to a maximum with distance from a notch (depending the initial crack size), then decrease to rest after further propagation. The profile of cleavage versus location on the fracture surface in both slow and fast tests in this study suggests that the increase in cleavage events resulted from an increase in crack velocity or essentially, an increase in strain rate ahead of the crack tip; a decrease in the proportion of cleavage with crack depth similarly is believed to accompany the crack deceleration. When the velocity of the crack is low (i.e. at the notch tip in the slow test), the primary Nb particles are able to deform and the interface to debond therefore providing high toughening. As the crack velocity increases (i.e., the strain rate increases), the Nb particles do not debond from the matrix and cleave before extensive plastic extension. The increase in strain rate may affect the brittle-to-ductile transition of the bcc Nb particles consistent with that found for other bcc materials such as steels,[21,22] and/or affect ability of the Nb/Nb_5Si_3 interface to debond. In the higher rate tests, the initial crack velocity is higher than that at the slow loading rate, and higher percentage of cleavage and lower degree of debonding near the notch is concurrent with lower observed toughness.

The decrease in fracture toughness of the composites in this study is concurrent with the observation of brittle behavior of the Nb increasing with testing rate and crack velocity. From the models that have been proposed[13,15,16] the toughening and R-curve behavior of ductile-bridging toughened composites depends on the stress-strain behavior of the ductile bridging ligaments. Because the Nb tested at the fast rates in these composites apparently does not attain the degree of plasticity as in the slower tests, for reasons discussed above, the degree of toughening is less. The R-curve behavior may also be affected by the testing rate, as the percentage of cleavage increases with crack extension; however, this has not yet been examined.

V. CONCLUSIONS:

The initiation toughness of in-situ processed ductile-phase toughened Nb_5Si_3/Nb composites is affected by the rate of testing. Toughnesses decreased from 28 to 19 $MPa\sqrt{m}$ by increasing the loading rate from 0.035 to 135 $MPa\sqrt{m}$/sec. Toughnesses as low as 9 $MPa\sqrt{m}$ were obtained for tests conducted at notch tip loading rates near 200 $MPa\sqrt{m}$/sec. The samples tested at the lowest rates exhibited a low percentage of cleavage of primary Nb particles near the notch tip, while higher loading rates produced a higher percentage of cleavage near the notch. Regions near the specimen mid-plane consistently

exhibited higher proportions of cleavage in comparison to the notch regions, regardless of test speed. The increased percentage of cleavage may result from the strain-rate sensitivity of Nb while the effects of loading rate on interfacial debonding are under investigation.

VI. RECOMMENDATIONS FOR FURTHER WORK

This research has given insight into the rate effects on the initiation toughness of these ductile-phase toughened materials. Significantly lower fracture toughness values have been observed at rates of loading that are higher than those used in conventional fracture toughness testing procedures but those that are not in the range of impact rates. These results are of engineering importance. The decreased toughness is believed to be controlled by either one or both of two factors:

(a) The strain-rate sensitivity (yield strength changes or brittle-to-ductile transition) of the constrained niobium particles and possible grain size dependence of this phenomenon; and/or:

(b) The strain-rate sensitivity of Nb/Nb_5Si_3 interfacial debonding events which will dictate the contriant on the Nb and, therefore, degree of toughening possible according to established models.

Further experimental work should focus on delineating these two effects. One way to establish (a) is to conduct tests on similarly processed (arc cast, extruded and heat treated) constrained Nb solid solution material, either on notched three point bend fracture toughness or notched tensile specimens, over a similar range of effective strain rates used in the tests reported on in this investigation. With the notched tensile tests, the possible changes in yield strength, plastic extension as well as ductile-to-brittle transition of constrained niobium with increased strain rate can be determined in the absence of interfaces found in the composite. Notched or precracked fracture toughness tests will similarly provide evidence of change in fracture mode in addition to fracture toughness as a function of rate.

Interfacial debonding rate-dependent effects (b) can be determined using cocentric layered cylindrical tensile specimens with Nb wire surrounded by the brittle Nb_5Si_3. In these tests, samples, similar to those used in another investigation,[13] are precracked through the silicide to the Nb/Nb_5Si_3 interface with the Nb intact and undeformed. These specimens can be pulled in tension over a range of strain rates and the degree of Nb/Nb_5Si_3

debonding as well as changes in Nb yield strength and plastic extension can be determined simultaneously at each strain rate.

Because the length of bridged zones also affects the amount toughening, it would also be worth while to measure the steady state bridge lengths established at various rates of testing or crack velocities. J-integral tests of resistance-curve behavior over this range of rates will also provide information on how the slope of the resistance curve may change.

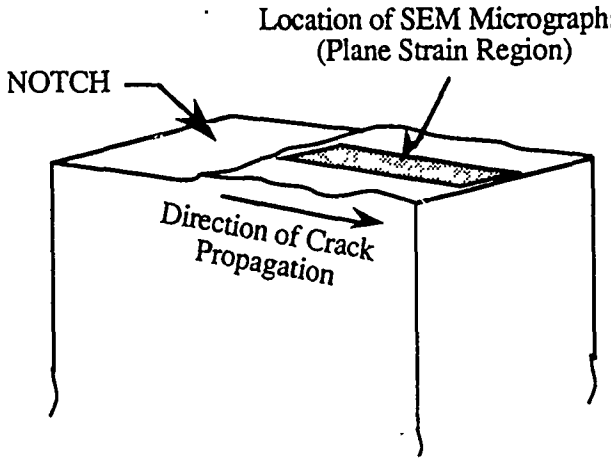

Figure 1: Schematic showing the location of micrographs taken for fractographic analysis.

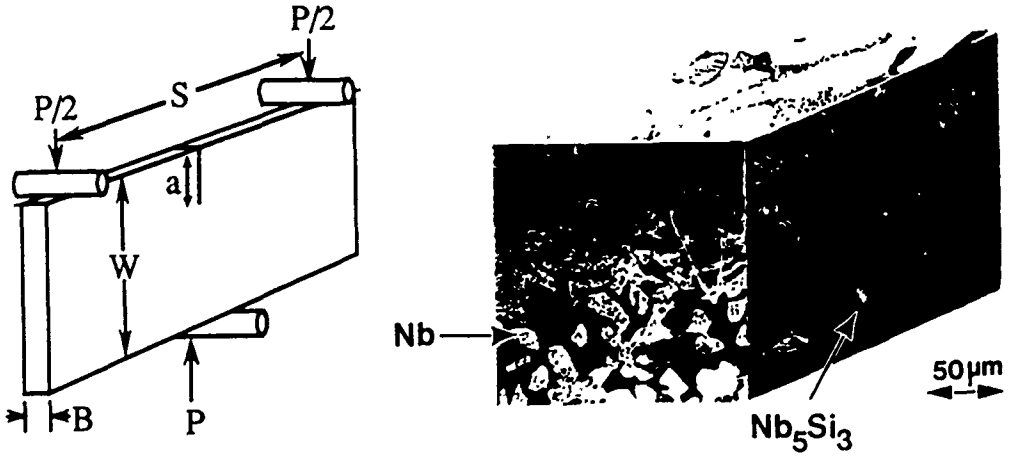

Figure 2: Microstructure of the extruded and heat treated Nb_5Si_3/Nb composite (Nb_p is 51.3% by volume) and the orientation of the notch in the mechanical tests with respect to the microstructure.

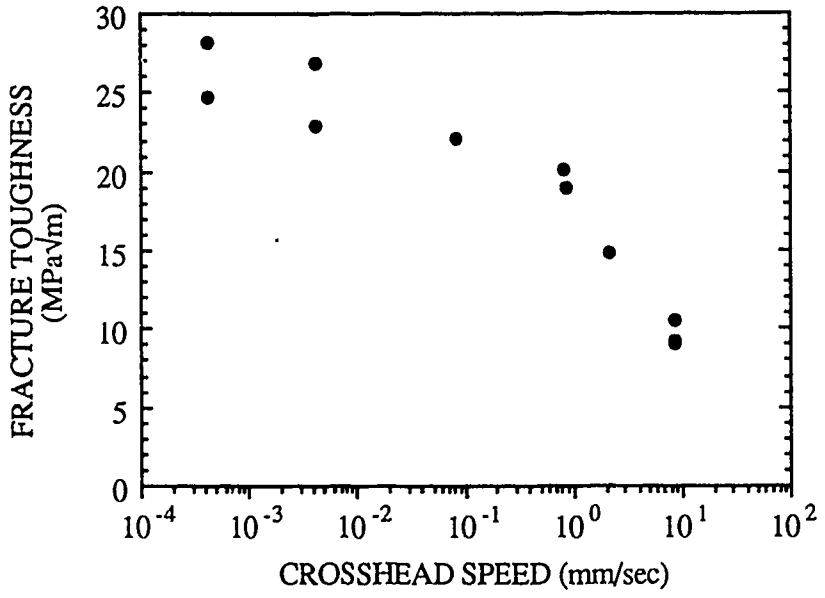

Figure 3a: Measured fracture toughness values (MPa√m) as a function of Crosshead Displacement Rate (mm/sec).

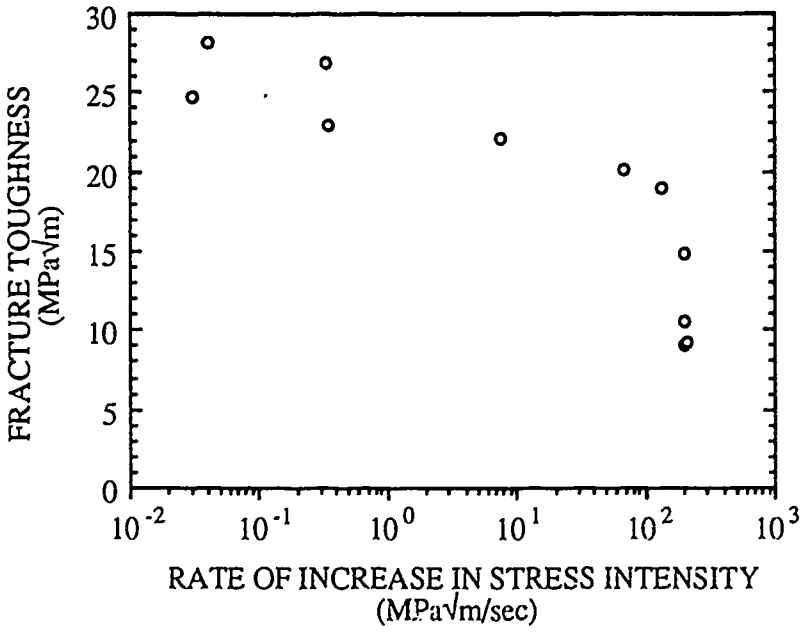

Figure 3b: Measured fracture toughness values (MPa√m) as a function of Rate of Increase in Stress Intensity (MPa√m/sec).

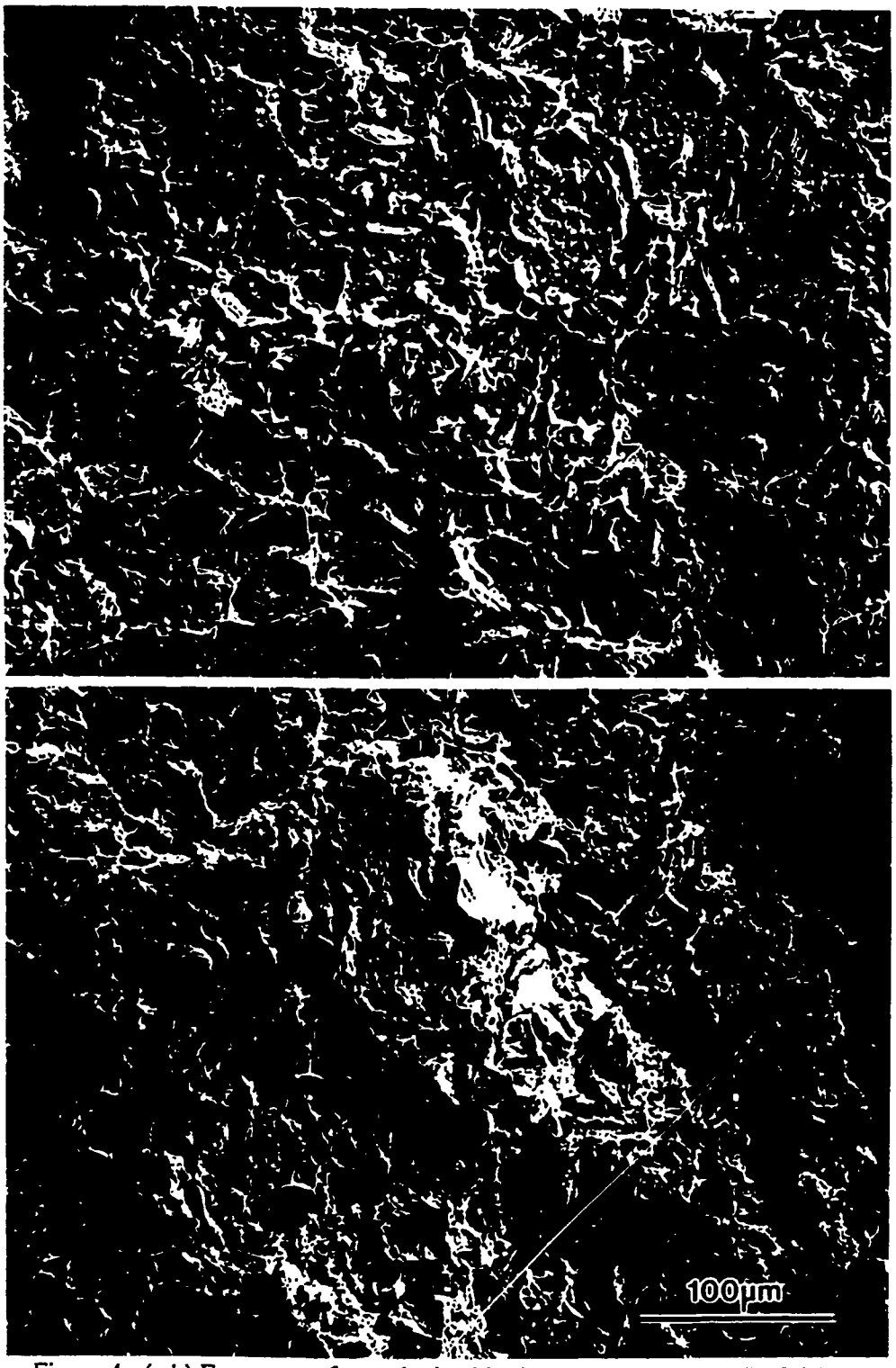

Figure 4: (a,b) Fracture surfaces obtained in the (a) near-notch (a/W≈0.25) and (b) the near mid-plane (a/W≈0.6) regions in a specimen tested at a slow rate (0.035 MPa√m/sec) [Fracture initiation toughness, 28 MPa√m].

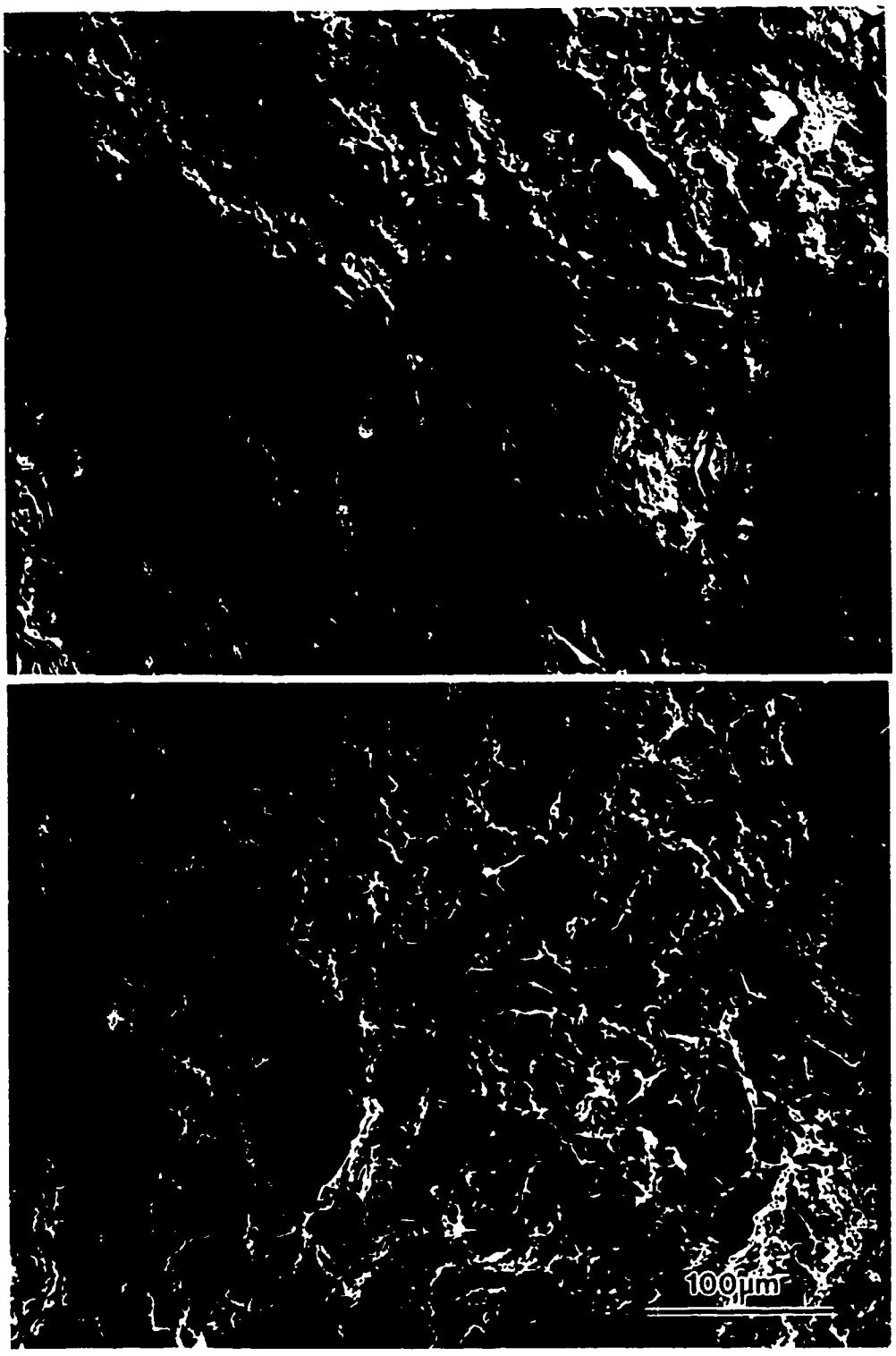

Figure 4: (c,d) Fracture surfaces obtained in the (a) near-notch (a/W=0.25) and (b) the near mid-plane (a/W=0.6) regions in a specimen tested at a fast rate (200 MPa√m/sec) [Fracture initiation toughness, 9 MPa√m].

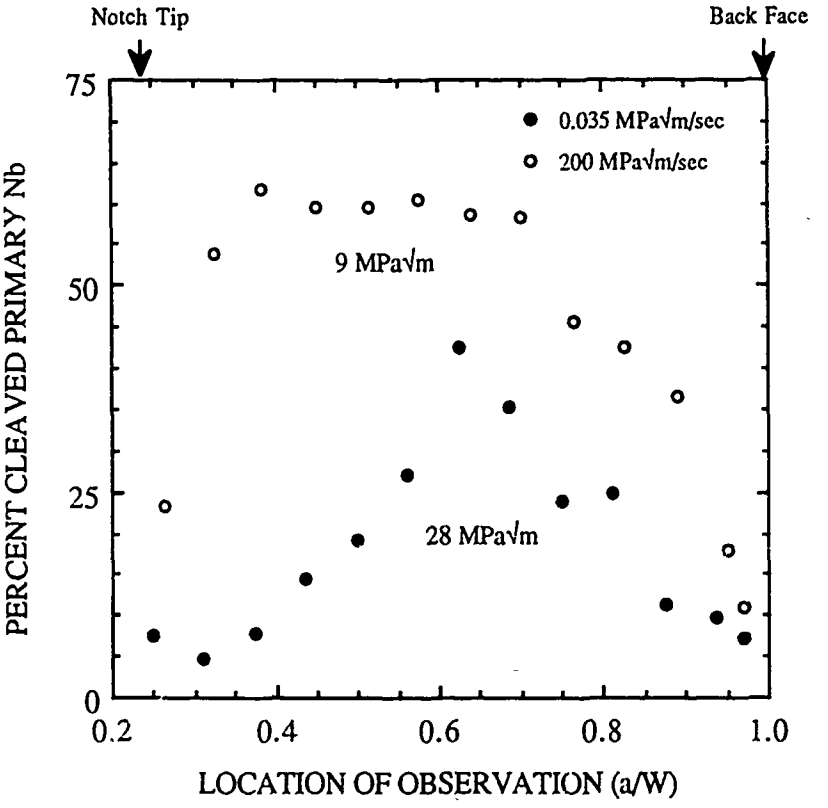

Figure 5: Fracture surface observations of percentage of primary Nb cleavage in Nb_5Si_3/Nb composites. Effects of loading rate and location of observation (a/W) are shown.

REFERENCES

[1] J.J. Lewandowski, D.M. Dimiduk, W. Kerr and M.G. Mendiratta, Mat. Res. Soc. Symp. Proc., **120**, 103 (1988).

[2] M.G. Mendiratta and D.M. Dimiduk, Mat. Res. Soc. Symp. Proc., **133**, 441 (1989).

[3] M.G. Mendiratta, J.J. Lewandowski and D.M. Dimiduk, to be published in Metall. Trans. A (1990).

[4] R.M. Nekkanti and D.M. Dimiduk, Mat. Res. Soc. Symp. Proc.: Intermetallic Composites, to be published, Spring Meeting, San Francisco CA (1990).

[5] R.L. Fleisher, J. Mater. Sci., **22**, 2281 (1987).

[6] T.B. Massalski, ed., Vol. 2: Binary Alloy Phase Diagrams, American Society for Metals, Metals Park OH (1986).

[7] M.G. Mendiratta and D.M. Dimiduk, to be published in Scripta Metall. (1990).

[8] J.D. Rigney and J.J. Lewandowski, Proc. Am. Ceram. Soc. Symp. on Composite Interfaces, Orlando FL (Nov. 1990).

[9] B.D. Flinn, M. Rühle and A.G. Evans, Acta Metall., **37**, 3001 (1989).

[10] L.S. Sigl, P.A. Mataga, B.J. Dalgleish, R.M. McMeeking and A.G. Evans, Acta Metall., **36**, 945 (1988).

[11] M. Manoharan, L. Ellis and J.J. Lewandowski, Scripta Metall., **24**, 1515 (1990).

[12] H.C. Cao, B.J. Dalgleish, H.E. Déve, C.K. Elliot, A.G. Evans, R. Mehrabian and G.R. Odette, Acta Metall., **37**, 2969 (1989).

[13] M.F. Ashby, F.J. Blunt and M. Bannister, Acta Metall., **37**, 1847 (1989).

[14] V. Krstic and P.S. Nicholson, J. Am. Ceram. Soc., **64**, 499 (1981).

[15] B. Budianski, J.C. Amazigo and A.G. Evans, J. Mech. Phys. Solids, **36**, 167 (1988).

[16] P.A. Mataga, Acta Metall., **37**, 3349 (1989).

[17] ASTM Standard E399, Annual Book ASTM Standards, Vol. 03.01, ASTM, Philadelphia, PA, 519 (1984).

[18] G.E. Dieter, Mechanical Metallurgy, 3rd Edition, McGraw-Hill (1986).

[19] J.F. Knott, Fundamentals of Fracture Mechanics, Butterworths, London (1973).

20 B.R. Lawn and T.R. Wilshaw, Fracture of Brittle Solids, Cambridge University Press, London (1975).

21 A.K. Shoemaker and S.T. Rolfe, Eng. Fract. Mech., **2**, 319 (1971).

22 D.A. Curry, Mater. Sci. Eng., **43**, 135 (1980).

1990 USAF-UES SUMMER FACULTY RESEARCH PROGRAM

GRADUATE STUDENT RESEARCH PROGRAM

Sponsored by the

AIR FORCE OFFICE OF SCIENTIFIC RESEARCH

Conducted by the

Universal Energy Systems, Inc.

FINAL REPORT

Analysis of Interlaminar Shear Failures in Brittle-Matrix Composite Flexure Specimens

Prepared by:	Scott R. Short
Academic Rank:	Doctoral Candidate
Department and	Grad. Chemical and Materials Egr.
University:	University of Dayton
Research Location:	WRDC/MLBM
	WPAFB, Ohio 45432
USAF Researcher:	Dr. James M. Whitney
Date:	8 Aug 90
Contract No.:	F49620-88-C-0053

Analysis of Interlaminar Shear Failures in Brittle-Matrix Composite Flexure Specimens

by

Scott R. Short

ABSTRACT

An inexpensive method has been developed to determine the approximate initiation site and monitor the propagation of an interlaminar shear failure in a fiber-reinforced composite flexure specimen. The method involves the use of electrical sensors attached to one side of a coupon-type flexure specimen in areas where the shear failure propagates. A two megasample-per-second Nicolet Model 2090 digital storage oscilloscope, along with a specially designed signal multiplexer box is used to record the data. Results of four-point flexural testing of unidirectional graphite-epoxy laminated composite beams indicate that the interlaminar shear failures initiate between a load and support, propagate in both directions along the beam length simultaneously, and reach very high crack propagation speeds.

ACKNOWLEDGEMENTS

The author wishes to acknowledge the support and assistance of the Summer Research Technical Focal Point, Dr. James M. Whitney, the Air Force Systems Command, the Air Force Office of Scientific Research, WRDC/MLBM, WRDC/MLBC, and John D. Camping, of University of Dayton Research Institute. Mr. Camping's expertise in the areas of electronic technology and mechanical testing proved very helpful in the successful completion of the research.

I. INTRODUCTION

Many of the common design features in today's laminated composite structures involve out-of-plane loads resulting in interlaminar stresses that can initiate and promote delamination growth from either manufacturing defects or inservice damage (Browning et al. 1986). Delamination is a general term used to describe the tendency of laminated materials to separate (debond) in the plane of the laminate, often at the interface between individual laminae. Delaminations, along with other modes of failure in laminated composite materials, can be related to the low "secondary" (matrix-dominated) properties of brittle-matrix composites. Brittle-matrix composites can be defined as those composite materials with matrix phases of relatively low ductility that experience catastrophic fracture rather than gross plastic deformation when subjected to loadings of low strain rate. Delaminations are a fundamental issue in the evaluation of laminated composite structures for both durability and damage tolerance. They are prone to rapid propagation and are inherently related to catastrophic failure and the strength of laminates. For the successful design of composite structures, it is therefore imperative that the level and type of stress required to produce delaminations be determined for the various composite materials used in engineering.

In order to characterize a laminated material's resistance to delamination, its strength must be assessed. A common method of analyzing the strength of a material is through the use of strength failure criteria. This method is based on the underlying principle that the strength of a material in specific directions can be measured with simple tests. Although most experimental determinations of strength are based on uniaxial stress states, practical

problems generally involve combined stress states. Failure criteria provide the analytical relation for strength under combined stresses. However, because of the various characteristics unique to laminated composites, problems exist with the various methods used to determine the strength of a material in specific directions. In particular, test methods routinely used to provide an estimate of the interlaminar shear strength of laminated composites have recently been shown to provide questionable results at best (Whitney et al. 1984).

Along with the need for the determination of interlaminar shear strength for use in the development of various failure criteria, knowledge of the interlaminar shear strength is essential in the study of fiber/matrix interfacial bonding and matrix failure of composites. Determination of the interlaminar shear strength is also a requirement in the investigation of free-edge effects in laminated anisotropic materials. In addition, accurate limiting values of the interlaminar shear stress are important in the area of fracture mechanics and in research involving impact resistance of composite materials.

Several methods have been proposed to determine the interlaminar shear strength of laminated composites. Many have their roots in the metallurgical or the adhesive testing fields. Each has its own particular drawbacks, however. For example, on a theoretical basis, a tubular specimen provides an excellent means for the characterization of the shear properties of fiber-reinforced materials. Difficulties with this method include expense and requirement of specialized testing equipment including gripping systems. Therefore, it is most common for materials engineers to consider the use of flat specimens (coupons) for characterization of interlaminar shear properties of composite materials. However, methods utilizing coupon-type specimens are affected by nonuniform or unknown stress states in the test section of the specimen, in addition to the presence of stress concentrations.

One of the most popular and routinely-used test methods for providing an estimate of the interlaminar shear strength of laminated composites is the short-beam shear test method as prescribed by ASTM D2344. The test method is simple to perform and uses a minimum of material. However, several studies (Sattar et al. 1969; Berg et al. 1972; Whitney et al. 1985) have shown that a complex state of stress exists in the vicinity of the point of loading. This stress concentration is responsible for suppression of interlaminar shear failures. Closer inspection of short-beam shear test specimen failures show evidence of buckling and microcracking in the region of loading. In order that a flexure test, like the short-beam shear test, be a viable method for determining the interlaminar shear strength of laminated composite materials, modification of the basic test method must occur. The ideal quantitative interlaminar shear test method should provide a region of pure, uniform shear stress. For accurate determination of the shear stress-strain response, the test section should be one of maximum shear stress relative to all other regions of the specimen. In addition, the test section should maintain this stress state during nonlinear material behavior up to the time of failure.

In the case of a mode II, interlaminar shear failure produced during flexure of a beam, several theories have been proposed by investigators in the metals, timber, and advanced composites industries concerning the initiation site of the shear failures. Some have suggested that the failures initiate at the end of the beam where a discontinuity exists. Some suggest that the shear failures initiate somewhere between a load and support. Others suggest that compression damage beneath a load anvil is responsible for crack initiation.

II. OBJECTIVES OF THE RESEARCH EFFORT

The author has been involved in an ongoing effort to develop an improved test method for the determination of the interlaminar shear strength of brittle-matrix laminated composite materials. Recently, a new interlaminar shear test method based on modification of the standard short-beam shear test has been developed (Short 1990). The method minimizes the stress concentration in the specimen near the region of loading and is capable of consistently producing interlaminar shear failures in coupon-type, laminated composite specimens. Along with the capability of producing mode II-type interlaminar shear failures in laminated composite flexure specimens, comes the question concerning the initiation site and propagation characteristics of such shear failures. The present research project, in conjunction with the United States Air Force Office of Scientific Research, addresses this question. An attempt will be made to determine the initiation site, direction of crack propagation, and crack propagation speed of the interlaminar shear failure of a coupon-type laminated composite flexure specimen.

III. EXPERIMENTAL PROCEDURE

Unidirectional graphite-epoxy beams, 50 plies thick, 1/2 in wide, and 6 in long were prepared and assembled in a specially designed test fixture. The test fixture was developed by the author to allow four-point flexural testing of composite beam specimens while preventing damage to the specimen near the point of loading. Previous investigations have shown that graphite-epoxy beam specimens contained within the test fixtures fail in interlaminar shear while not experiencing surface damage near the region of loading (Short 1990). The failures consist of a shear crack extending from one of the points of loading to the end of the specimen farthest away. The failures occur

approximately on the neutral plane of the beam (See Figure 1). When the specimen fails during flexural testing, a loud pop is heard, and the shear crack forms instantaneously.

The possibility of video taping the shear failure has been suggested. However, high-speed video taping equipment would be required. Such equipment is not readily available. In addition, the total duration of the film magazine for ultra high-speed video is only 1 and 3/4 seconds. If no method is available to "trigger" the camera, the event may easily be missed. It is possible that the shear failure propagates at such a high speed that an attempt to video tape its initiation and propagation might be futile. Therefore, an alternative method of monitoring the shear crack is required.

A method that does not rely on video recording has been devised to monitor the general crack behavior. Sensing elements are attached to the side of the flexure specimen at specific intervals along the length. The progress of the crack is monitored electronically as the sensing elements ("triggers") are broken by growth of the crack. A two megasample-per-second Nicolet Model 2090 digital storage oscilloscope is used to record the data. Since the oscilloscope is a two-channel instrument, only two sensing elements can be monitored in a given test. This does not provide sufficient information to determine the initiation site of the crack or its direction of propagation. In order to gather more information from each specimen tested, an eight-input signal multiplexer box was designed and constructed (Camping 1990). This device converts up to eight separate on/off signals from sensing elements attached to the specimen to a single voltage signal that can be recorded by the digital oscilloscope. The signal multiplexer circuitry is based on a high-speed, eight-bit, digital-to-analog converter. Each of the eight bits is connected to a sensing element. When activated, each bit changes the voltage in the circuit by a specific amount. The circuit is adjusted to span a 20-volt range from +10 volts DC to -10 volts DC. Each sensing element represents a voltage that is a binary fraction of 20 volts.

Therefore, since the eight bits are related in binary sequence, even if two or more sensing elements fail simultaneously, proper determination of which elements failed can always be made. The multiplexer circuit, in conjunction with the digital oscilioscope, produces a time versus voltage curve from which the failure sequence of the sensing elements can be determined. By measuring the location of each sensing element along the length of the flexure specimen, the general behavior of the shear failure, including the average crack propagation speed between any two sensing elements, can be determined.

A simplified block diagram of the circuitry of the signal multiplexer box is illustrated in Figure 3. The circuitry consists of an input conditioning circuit, a high-speed digital-to-analog converter, an output amplifier, a trigger circuit, and a power supply. All components are contained in a small chassis box along with a power switch, fuse, input and output connectors, indicator lights, and an "ARM" push button. The total cost of the crack monitoring system is less than $200.00 which makes it a particularly attractive laboratory instrument.

Specialized crack propagation gages were considered for use as the sensing elements. They were rejected however, because readily available gages are too large to be conveniently attached to the side of the flexure specimen. These gages are also fairly expensive. Standard foil-type gages are a cheaper alternative. Duplicate test fixtures were instrumented with several standard strain gages. The gages were bonded to the side of the test specimen along the length. The outputs of the gages are the inputs to the crack detection circuit described above.

Another type of sensing element was also used and consists of thin strips of electrically conductive paint applied to one side of the test specimen. A "wire" is effectively painted between two terminals and acts as a "trigger" on the specimen side. This form of sensing

element covers a very narrow region along the specimen length. In addition, the conductive paint dries to a brittle state and fractures easily when a crack propagates beneath it. Because the composite test specimens contain electrically conductive graphite fibers, a thin layer of epoxy adhesive is applied in a narrow strip on the specimen side at each trigger location. This coating acts as an insulator, isolating the circuits of the signal multiplexer box from the specimen and testing machine. After the epoxy has cured (room-temperature), small loops of copper wire are glued to the insulated surface near the top and bottom surfaces of the specimen. The conductive paint is applied between the loops to complete the electrical connection (See Figure 4). After the specimen is instrumented, the trigger wires are connected to the input connector of the multiplexer box using 36 gage insulated magnet wire. Such fine wire prevents breakage of the trigger wire connections by the shock accompanying failure of the specimens. False indications of crack propagation are thereby prevented.

Six replicate specimens were instrumented with the conductive-paint triggers. Two different configurations of trigger locations were used. Four replicates were instrumented as shown in Figure 1. These tests will provide the general characteristics of the crack, i.e., site of initiation, direction of crack propagation, and approximate crack propagation speed. Figure 2 illustrates the configuration of the triggers for the other two replicates. This configuration of triggers will hopefully allow for more precise identification of the shear failure initiation site.

IV. RESULTS

All specimens failed in shear as expected. (Success of the test-fixture method of interlaminar shear testing of coupon-type composite specimens has been documented by Short 1990.) No results were obtained for the specimens employing standard strain gages as sensing elements. Problems were encountered with breakage of these gages. On the other hand, specimens instrumented with the conductive-paint triggers produced excellent results. The flexure specimens experienced interlaminar shear failure as shown in figures 6 and 7. Typical voltage-drop versus elapsed-time plots, as obtained from the oscilloscope and signal multiplexer box data, are shown in Figures 8 and 9. From the voltage-drop versus elapsed-time data, along with measurement of the location of each trigger along the length of the specimen, the sequence of trigger-breaks can be determined for each specimen. With the known location of each sensor, the average crack propagation speed between any two triggers can be determined. Analysis of the results for all specimens indicates that the shear failures initiate between a load and support and propagate simultaneously in both directions along the length of the beam. The crack increases in speed as it propagates outward toward the end of the specimen. Speeds of over 10,000 ft/sec are possible near the end of the specimen. The crack also propagates inward toward the middle of the specimen length but at much slower speeds; 2,000 ft/sec. The crack is arrested near the point of loading farthest away from the cracked end.

V. DISCUSSION OF RESULTS

Problems were encountered with the standard foil-type strain gages used as sensing elements. The backing of the gages is relatively ductile and prevents the strain gage from breaking when a crack propagates beneath it. Closer inspection of the gages after testing reveals that the ductile backing wrinkles rather than fractures when subjected to shear deformation at the neutral plane of the beam.

The method employing conductive-paint triggers as sensing elements worked well. The conductive paint dries to a brittle state and fractures easily when a crack propagates beneath it as shown in Figure 5. The oscilloscope and signal multiplexer circuitry have sufficient speed and resolution to determine the general behavior of the shear failure. The different trigger locations allow identification of the general area of shear failure initiation. It is determined that the shear failures initiate between a load and support near either end of the beam rather than at the end of the beam. Moreover, the shear failures initiate between the load and support in some general area rather than immediately beneath a load or support anvil. It is theorized that the shear stress between a load and support causes a coalescence of microscopic "shear voids" in this area, which upon reaching a critical size, instantaneously propagates as a shear failure. Once a shear failure initiates, the state of stress at the crack tip is complex and the crack driving force varies dynamically. Consequently, the rate of crack propagation varies greatly along the specimen length. It is interesting to note that the crack propagation rate is highest near the end of the specimen.

VI. CONCLUSIONS

An inexpensive method has been developed to monitor the initiation and propagation of a shear failure in a fiber-reinforced composite flexure specimen. The method involves the use of electrical sensors attached to the side of a coupon-type flexure specimen in areas where the shear failure propagates. Propagation of a shear failure activates the sensors. A high-speed, analog-to-digital circuit, along with an oscilloscope records the data. The data can be used to determine the general location of shear failure initiation, direction of crack propagation, and average crack propagation speed between any two sensors.

Application of the crack monitoring system to fiber-reinforced composite flexure specimens indicates that the shear failure initiates in the region of high shear stress between a load and support, propagates simultaneously in either direction along the length of the beam, and reaches very high crack propagation speeds near the end of the specimen. It is also concluded that due to the extremely high crack propagation speeds, video taping of such shear failures would be impossible.

VII. RECOMMENDATIONS

Recommendations for further work include additional testing of replicate specimens, along with testing of other laminates and materials. Also, the circuitry of the multiplexer box can be improved by the use of a faster D/A converter, etc.. Of course, improvements of this type would result in greater expense. Finally, it is desirable to perform a detailed stress analysis of the flexure problem from the standpoint of the theory of elasticity. This will allow conclusions to be made as to the effect of the stress field on the initiation site of the shear failure.

REFERENCES

Berg, C. A., Tirosh, J., Israeli, M., "Analysis of Short Beam Bending of Fiber Reinforced Composites", Composite Materials: Testing and Design ASTM STP 497, 1972.

Browning, C. E., Schwartz, H. S,, "Delamination Resistant Composite Concepts", Composite Materials: Testing and Design (Seventh Conference) ASTM STP 893, 1986.

Camping, J. D., "A Device for Measuring High-Speed Crack Propagation", Internal Technical Document, University of Dayton Research Institute, 1990.

Sattar, S. A., Kellogg, D. H., "The Effect of Geometry on the Mode of Failure of Composites in Short-Beam Shear Test", Composite Materials: Testing and Design ASTM STP 460, 1969.

Short, S. R., "Determination of the Interlaminar Shear Strength of Brittle-Matrix Composites", Ph.D. dissertation, University of Dayton, 1990.

Whitney, J. M., Browning, C. E., "Materials Characterization for Matrix-Dominated Failure Modes", Effects of Defects in Composite Materials ASTM STP 836, 1984.

Whitney, J. M., Browning, C. E., "On Short-Beam Shear Tests for Composite Materials", Experimental Mechanics, 25, No. 3, 1985.

Whitney, J. M., "Elasticity Analysis of Orthotropic Beams under Concentrated Loads", Composites Science and Technology, 22, 1985.

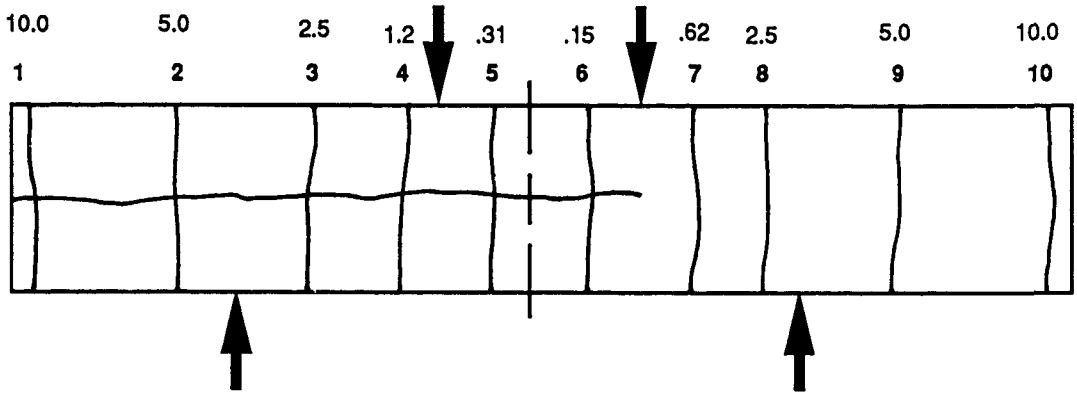

Figure 1. Illustrates location and voltage drop of "triggers" for specimens of first set of tests. Integers correspond to trigger number; decimal numbers correspond to voltage drop of the trigger.

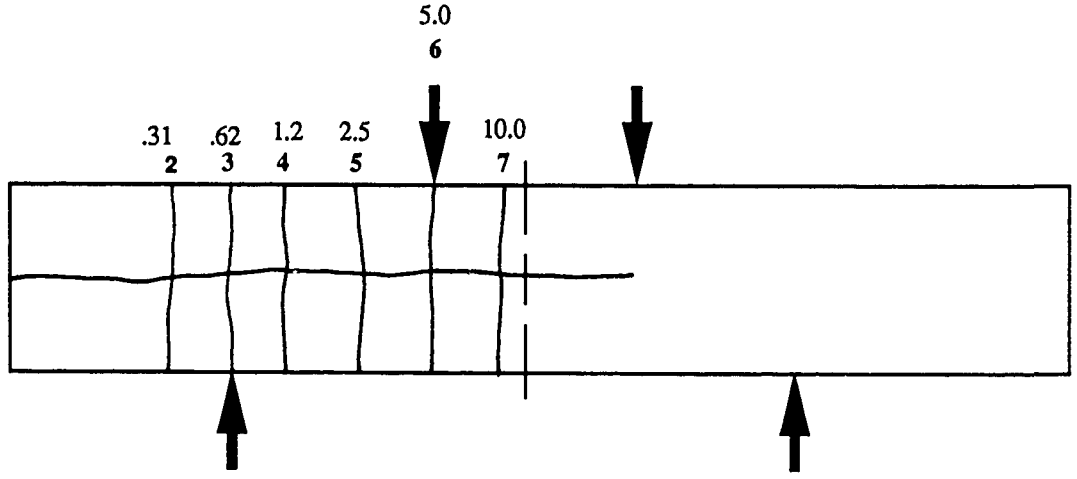

Figure 2. Illustrates location and voltage drop of "triggers" for specimens of second set of tests. Integers correspond to trigger number; decimal numbers correspond to voltage drop of the trigger.

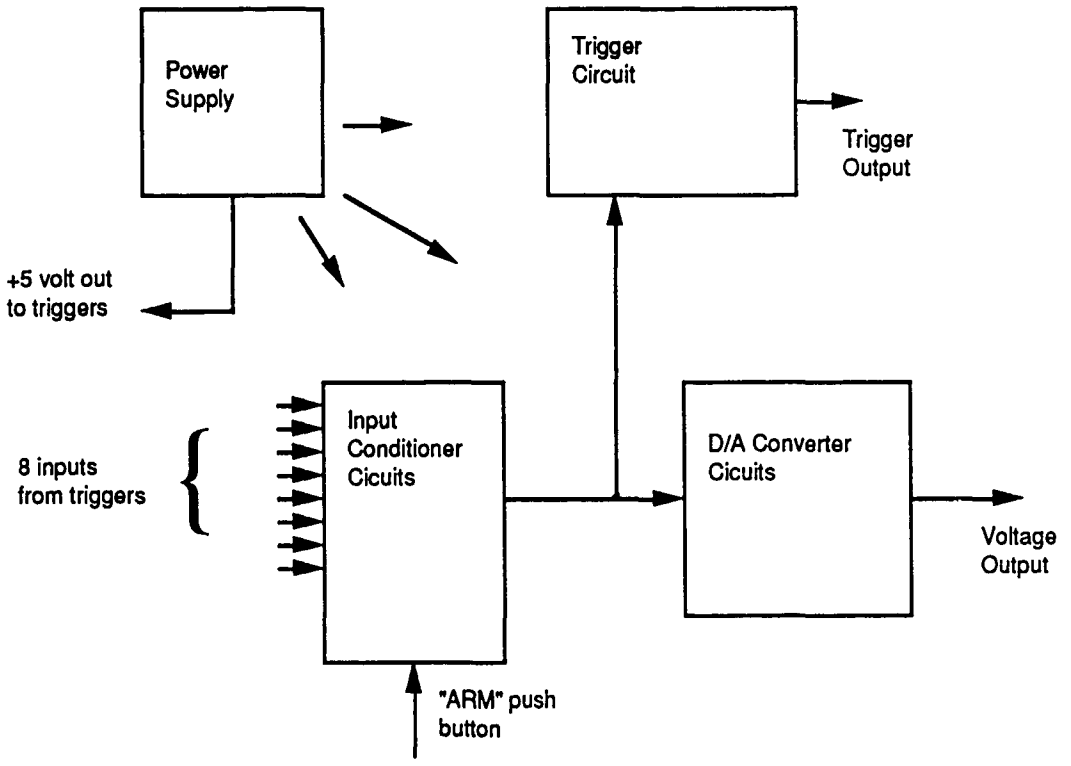

Figure 3. Simplified block diagram of circuitry of signal multiplexer box.

Figure 4. Shows connection between conductive paint and wire. 38X

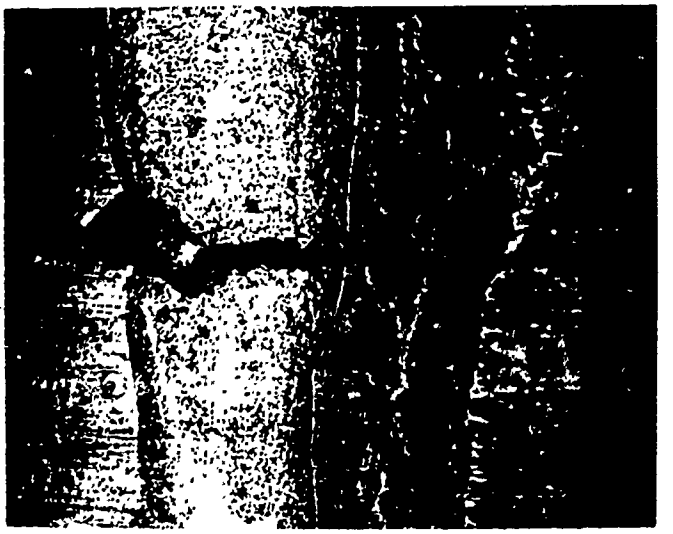

Figure 5. Shows crack in conductive paint. 38X

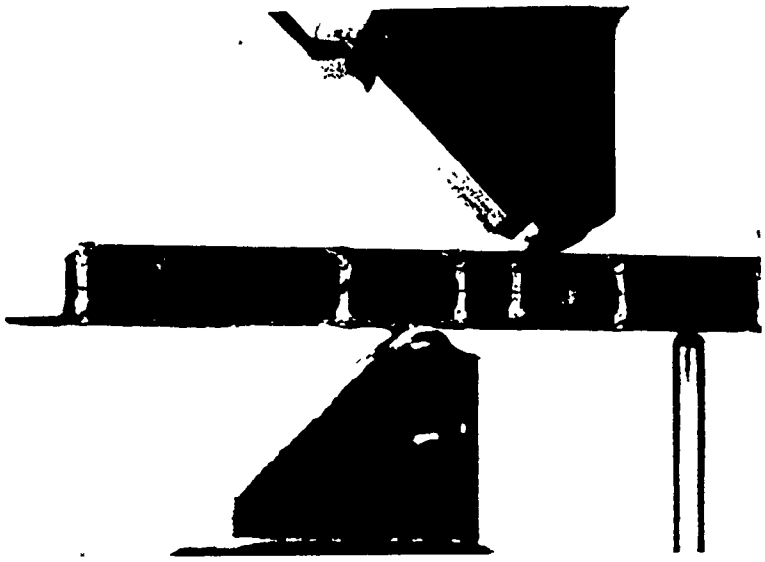

Figure 6. Shows typical specimen failure.

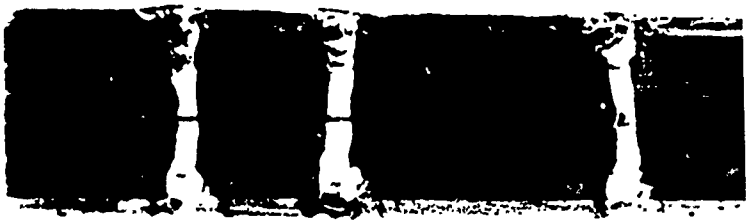

Figure 7. Shows typical specimen failure.

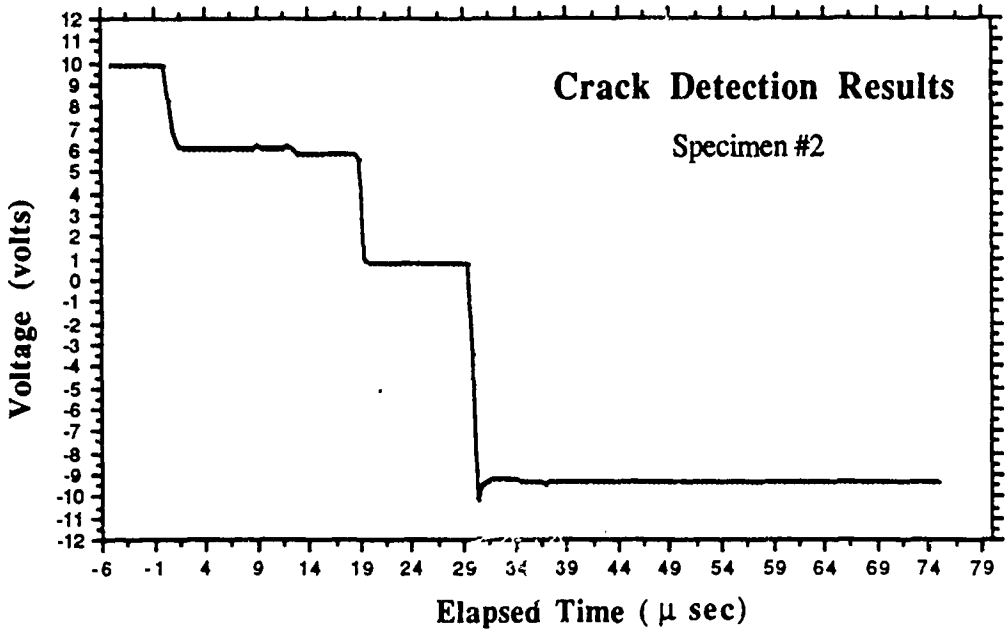

Figure 8. Oscilloscope data.

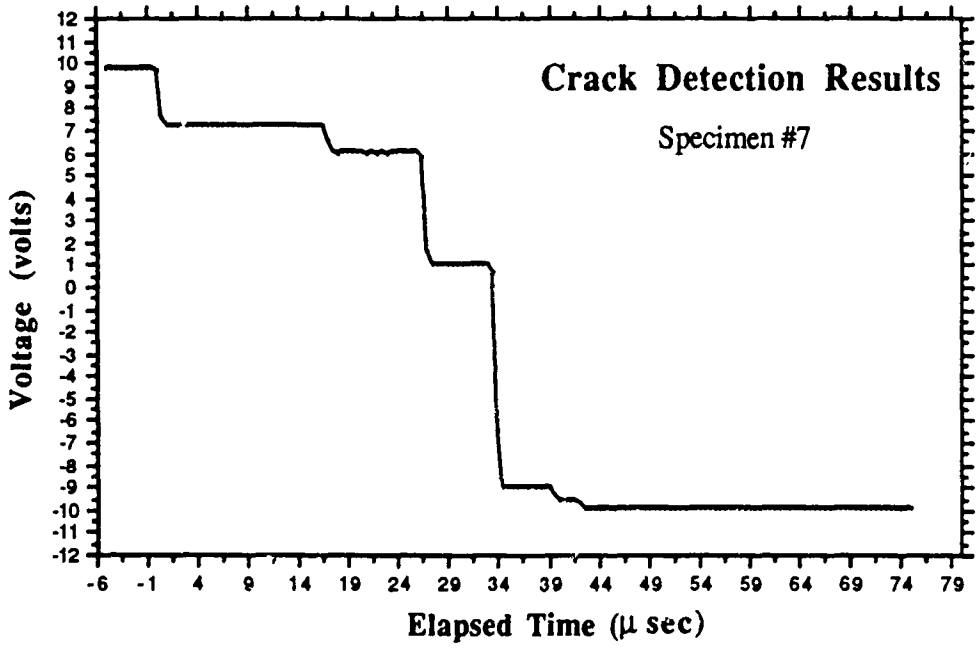

Figure 9. Oscilloscope data.